Downloaded from orbit.dtu.dk on: May 04, 2023

DTU Library

Microfluidics for single cell analysis

Jensen, Marie Pødenphant

Publication date:
2015

Document Version
Publisher's PDF, also known as Version of record

Link back to DTU Orbit

Citation (APA):
Jensen, M. P. (2015). *Microfluidics for single cell analysis*. DTU Nanotech.

General rights
Copyright and moral rights for the publications made accessible in the public portal are retained by the authors and/or other copyright owners and it is a condition of accessing publications that users recognise and abide by the legal requirements associated with these rights.

- Users may download and print one copy of any publication from the public portal for the purpose of private study or research.
- You may not further distribute the material or use it for any profit-making activity or commercial gain
- You may freely distribute the URL identifying the publication in the public portal

If you believe that this document breaches copyright please contact us providing details, and we will remove access to the work immediately and investigate your claim.

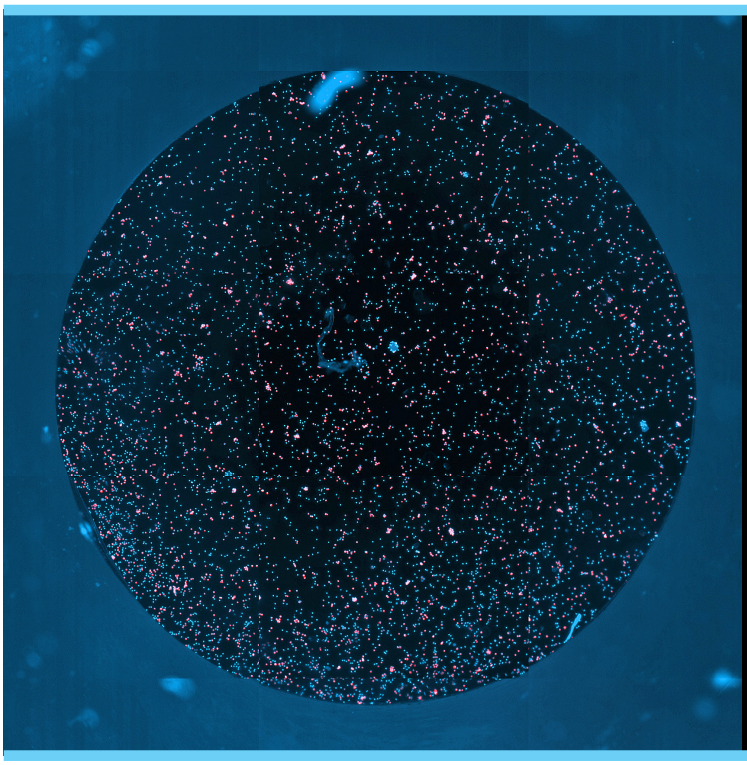

Microfluidics for single cell analysis

Marie Pødenphant Jensen
PhD Thesis September 2015

DTU Nanotech
Department of Micro- and Nanotechnology

DTU Nanotech
Department of Micro- and Nanotechnology

Ph.D. Thesis

Microfluidics for single cell analysis

Marie Pødenphant Jensen

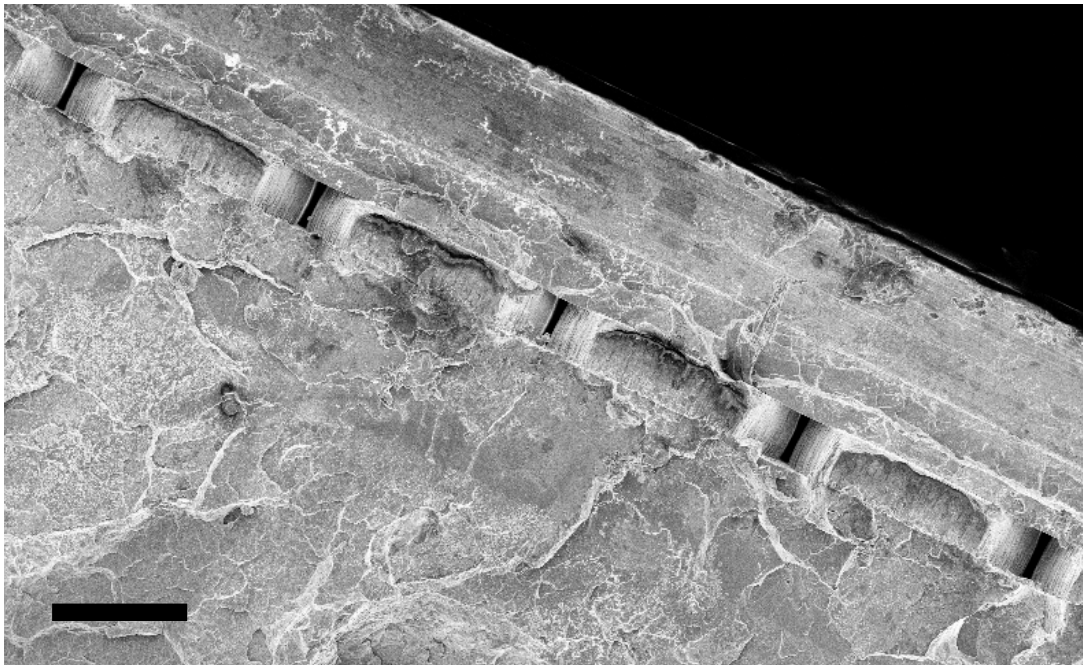

Supervisor: Associate Professor Rodolphe Marie
Co-supervisor: Professor Anders Kristensen

Department of Micro- and Nanotechnology
Technical University of Denmark

14 September 2015

Front page illustration:
Scanning electron microscope image of a fractured cell trapping chip showing the trap dimensions. The scale bar is 100 μm.

Preface

This thesis is submitted in partial fulfilment of the requirements for obtaining the Philosophiae Doctor (Ph.D.) degree at the Technical University of Denmark (DTU). The work presented here has been carried out at the Department of Micro and Nanotechnology (DTU Nanotech) in the Optofluidics group, in the DTU Danchip clean room facilities, and at the Cancer and Immunogenetics group at The Weatherall Institute of Molecular Medicine, Oxford UK. The work was performed in the period from 15 September 2012 to 14 September 2015. The project was funded by the European Commission under the Seventh Framework Programme (FP7/2007−2013) under grant agreements number 278204 (Cell-O-Matic).

The project was supervised by associate professor Rodolphe Marie from the Optofluidics group at DTU Nanotech and co-supervised by Professor Anders Kristensen, group leader of Optofluidics. I am very grateful for their support, help and encouragement during the past three years. I would like to thank my colleagues at the Optofluidics group for keeping my motivation high and for improving the daily life both inside and outside the lab.

I would also like to thank Sir Walter Bodmer for letting me visit his lab in Oxford, and to thank the members of his group for making me feel welcome at their lab and teaching me a great deal about working with cells.

Furthermore I would like to thank the other project partners who have been involved in my work. NIL Technology for providing the shims, and Tom and Sanne from Unisensor for valuable ideas and input to my project.

Thanks to all my friends, who have made my life outside DTU very enjoyable. Also thanks to my friends at DTU, especially the members of the cake club, who have contributed with many interesting discussions and always left me in a positive mood, and the Friday bar team for many fun times at late hours.

Finally I would like to thank my family and especially Jesper for always being there for me, and for their patience and support.

Marie Pødenphant Jensen
Kgs. Lyngby
14 September 2015

Abstract

Isolation and manipulation of single cells have gained an increasing interest from researchers because of the heterogeneity of cells from the same cell culture. Single cell analysis can ensure a better understanding of differences between individual cells and potentially solve a variety of clinical problems. In this thesis lab on a chip systems for rare single cell analysis are investigated. The focus was to develop a commercial, disposable device for circulating tumour cell (CTC) analysis. Such a device must be able to separate rare cells from blood samples and subsequently capture the specific cells, and simultaneously be fabricated and operated at low costs and be user-friendly. These challenges were addressed through development of two microfluidic devices, one for rare cell isolation based on pinched flow fractionation (PFF) and one for single cell capture based on hydrodynamic trapping. Both devices were fabricated by injection moulding with a nickel master.

CTC isolation was realised using PFF, which is a passive, size-based microfluidic technique. The focus was mainly on experimental work; however designs were based on flow calculations and analysed with numerical simulations to support experimental results. Devices were extensively characterised and tested with fluorescent nano- and microspheres, and with cancer cells and blood cell samples. It was demonstrated that the separation not only relies on size, but that differences in cell deformability are also exploited, which enabled a successful separation with an efficiency of over 90%.

Single cell capture was realised using hydrodynamic cell trapping, which is based on flow and cell interactions with microstructures. The criteria for hydrodynamic single cell capture were investigated and clarified through development of several devices with increasingly optimized designs. The final design provides the possibility of parallel single cell DNA extraction for subsequent off-chip investigations. Because the devices are sensitive to small changes of the structures, the injection moulding process was optimized to improve replication of the structures from the nickel master.

A novel method based on freeze-fracture was used to investigate and improve the bonding process used for sealing device microchannels. Structures were intentionally altered by bonding at high temperatures, and the resulting channel cross sections were visualized in a scanning electron microscope. It was demonstrated that chips with the altered structures had an increased capture efficiency.

Finally low cost mass-production of the devices was realised using injection moulding in thermoplastics from a nickel master. With this process the price per device rapidly decreases for higher numbers of fabricated devices. In addition devices were fabricated on a Luer-platform that ensures easy connection to external equipment. The devices were used by collaborators in a cancer research lab, which demonstrates their commercial potential.

Dansk resumé

Isolering og manipulering af enkeltceller har opnået en stigende interesse fra forskere pga. heterogeniteten af celler fra samme cellekultur. Analyse af enkeltceller kan medføre en bedre forståelse af forskellene mellem individuelle celler, og potentielt løse en række kliniske problemer. I denne afhandling undersøges lab-on-a-chip-systemer til analyse af sjældne enkeltceller. Fokus var på at udvikle kommercielle enheder til analyse af cirkulerende tumorceller (CTC'er) til engangsbrug. Sådanne enheder skal kunne separere sjældne celler fra blodprøver og efterfølgende fange de udvalgte celler, samtidig med at de skal kunne fabrikeres og opereres ved lave omkostninger og være brugervenlige. Disse udfordringer blev behandlet ved at udvikle to mikrofluid-enheder, en til isolation af sjældne celler baseret på en metode kaldet "pinched flow fractionation" (PFF), og en til indfangning af enkeltceller vha. hydrodynamiske indsnævringer. Begge enheder blev fabrikeret ved sprøjtestøbning med en nikkelform.

CTC isolation blev opnået ved brug af PFF, som er en passiv, størrelsesbaseret mikrofluid-teknik. Fokus var primært på eksperimentelt arbejde, dog blev design baseret på beregninger af flow og analyseret med numeriske simuleringer for at understøtte eksperimentelt opnåede resultater. Enhederne blev karakteriseret og testet udførligt med fluorescerende nano- og mikrokugler, og med kræftceller og blodprøver. Det blev demonstreret at separationen ikke kun afhænger af størrelse, men at forskelle i cellestivhed også kan udnyttes, hvilket muliggjorde en succesfuld separation med en effektivitet på over 90 %.

Enkeltceller blev fanget vha. hydrodynamiske indsnævringer. Indfangningen er baseret på væskestrømninger og cellevekselvirkninger med mikrostrukturer. Kriterierne for hydrodynamisk celleindfangning blev undersøgt og præciseret gennem udvikling af flere generationer af enheder med gradvist forbedrede design. Det endelige design muliggør parallel DNA-udtrækning på enkeltceller til efterfølgende undersøgelser uden for enheden. Da enhederne er følsomme over for små ændringer af indsnævringerne, blev sprøjtestøbningsprocessen optimeret for at forbedre gengivelsen af strukturerne fra nikkelformen.

En ny metode baseret på "freeze-fracture" blev brugt til at undersøge og forbedre forseglingsprocessen, der blev brugt til at tætne enhedernes mikrokanaler. Strukturerne blev bevidst ændret ved forsegling med høje temperaturer, og de resulterende tværsnit af kanalerne blev visualiseret i et scanningselektronmikroskop. Det blev demonstreret at enheder med de ændrede strukturer havde en forhøjet indfangningseffektivitet.

Endelig blev masseproduktion ved lave omkostninger realiseret med sprøjtestøbning i termoplastik fra en nikkelform. Med denne proces falder prisen pr. enhed hurtigt jo flere enheder der fabrikeres. Derudover blev enhederne fabrikeret på en "Luer"-platform der sikrer nem tilslutning til eksternt udstyr. Enhederne blev brugt af samarbejdspartnere i et kræftforskningslaboratorium, hvilket demonstrerer deres kommercielle potentiale.

List of publications

Journal papers

Paper I
Marie Pødenphant, Rodolphe Marie, Tom Olesen, Marco Matteucci and Anders Kristensen. *Injection molded pinched flow fractionation device for enrichment of somatic cells in cow milk*, Microelectronic engineering, 2014 **124** 53-57.
Contributions: All experiments were performed by me during the studies for my master thesis. Parts of the data analysis and all manuscript writing was done during my Ph.D. work. I am first author of the paper.

Paper II
Marie Pødenphant, Neil Ashley, Kamila Koprowska, Kalim U. Mir, Maksim Zalkovskij, Brian Bilenberg, Walter Bodmer, Anders Kristensen and Rodolphe Marie. *Separation of cancer cells from white blood cells by pinched flow fractionation*, submitted for publication at Lab on a Chip.
Contributions: I am first author of the manuscript, did parts of the fabrication, and performed all experiments and data analysis.

Paper III
Marie Pødenphant, Brian Bilenberg, Anders Kristensen and Rodolphe Marie. *Optimization of thermally sealed all-polymer microfluidic devices for single cell trapping*, submitted for publication at AIP Advances.
Contributions: I am first author of the manuscript, did parts of the fabrication, and performed all experiments and data analysis.

Conference contributions

Marie Pødenphant, Neil Ashley, Walter Bodmer, Jonathan Beckett, Kalim Mir, Rodolphe Marie and Anders Kristensen. *Injection moulded pinched flow fractionation device for cell separation*, poster presented at The 39th International Conference on Micro and Nano Engineering (MNE), London, UK (2013).

Marie Pødenphant, Rodolphe Marie, Tom Olesen, Marco Matteucci and Anders Kristensen. *Injection molded microfluidic device for enrichment of somatic cells in cow milk*, talk given at The 1st International Conference on Polymer Replication on Nanoscale (PRN), Copenhagen, Denmark (2014).

Contents

List of abbreviations

CCD	charge coupled device
COC	cyclic olefin copolymer
CTC	circulating tumour cell
DFF	Dean flow fractionation
DLD	deterministic lateral displacement
DNA	deoxyribonucleic acid
EDTA	ethylenediaminetetraacetic acid
EMCCD	electron multiplying charge coupled device
EpCAM	epithelial cell adhesion molecule
FDA	Food and Drug Administration
FWHM	full width at half maximum
HEPA	high-efficiency particulate air
HF	hydrofluoric acid
ISET	isolation by size of epithelial cells
KOH	potassium hydroxide
LoC	lab-on-a-chip
PBS	phosphate-buffered saline
PDMS	polydimethylsiloxane
PFF	pinched flow fractionation
PMMA	poly(methyl methacrylate)
RBC	red blood cell
RNA	ribonucleic acid
RNase	ribonuclease
RPM	revolutions per minute
SEM	scanning electron microscope
TX	Triton-X 100
UV	ultraviolet
WBC	white blood cell
WIMM	Weatherall Institute of Molecular Medicine

1 Introduction

This chapter covers the motivation behind the work carried out for this thesis and introduces the basic cell biology and the microfluidic techniques used throughout the chapters. The focus is on state-of-the-art results and challenges yet to be solved.

Contents

1.1 Motivation

The scope of this thesis is to demonstrate lab-on-a-chip (LoC) systems for rare cell isolation and single cell trapping. LoC systems scale down one or more laboratory functions on a single chip. This miniaturisation has many advantages: it reduces costs by reducing the consumption of expensive reagents, the fluid flow is easy to control because the small dimensions often result in laminar flows, and the small dimensions also enable handling of small particles like single cells or strands of DNA.

This thesis was part of the Cell-O-Matic EU project[1], which is a four year project running from January 2012 to December 2015. The overall goal of Cell-O-Matic is development of a chip-based technology for processing DNA from single cells, and development of methods that enable whole chromosome lengths of DNA to be mapped. To process DNA from single cells they must first be isolated from the sample they are contained in, and then be trapped individually in a way that enables extraction of their DNA. The combination of

[1]The official website is found at: http://www.cellomatic.eu/

cell isolation and single cell trapping creates a powerful analysis tool that enables a better understanding of differences between individual cells.

Substantial evidence has demonstrated heterogeneity of individual cells within a genetically identical population. Methods that use average responses from a population will consequently overlook differences between individual cells. In this thesis and in the Cell-O-Matic project, the device application was directed towards circulating tumour cells (CTCs), which are cancer cells that circulate in the blood of cancer patients, and are believed to be responsible for metastasis, which is when a new tumour is created. It is hypothesised that only a fraction of CTCs are capable of initiating new tumours, and by targeting these cells the effectiveness of cancer treatment can be increased. Analysis of DNA from single CTCs is therefore expected to increase the general knowledge of cancer with the long-term goal of improved cancer treatment.

In this thesis, cell separation and capture are achieved using hydrodynamic principles, where the device functionality depends on flow conditions and particle interactions with microstructures. The separation and capture are based purely on physiological characteristics of the different cell populations. Hydrodynamic devices are advantageous because they can be operated solely with flow controllers, and samples do not need labelling. This combination ensures device user-friendliness and easy setup in any cell research lab.

All devices were fabricated by injection moulding, which is an industrial technique used to fabricate most plastic parts today. In brief, injection moulding works by injecting a molten polymer into a cavity, with a structured master. The master transfers a microscale pattern onto the polymer, and after cooling, the cavity is opened and the polymer chip is released. The master can be reused to mould thousands of polymer devices, and in this way LoC systems can be mass-produced at low costs. The cavity can be shaped to enable easy connection between the on-chip microchannels and external equipment used to control the flow. Low costs and easy connection ensures the potential for widespread use of the chips in research labs worldwide.

1.2 Physical characteristics of cells

Some basic knowledge of human blood cells, CTCs and cancer cells in general is necessary to understand the principles behind different separation and trapping techniques, and their challenges. The different cell types used in this thesis are described below.

Whole blood

Human blood from a healthy person consists of red blood cells (RBCs), white blood cells (WBCs) and platelets suspended in approx. 55 % plasma. Whole blood is a non-Newtonian fluid [1], which makes it challenging to work with. Often this problem is solved simply by diluting the blood with a buffer fluid.

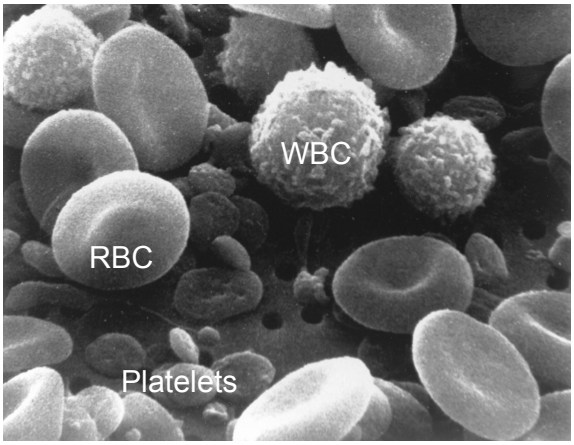

Figure 1.1: SEM image of blood cells from The National Cancer Institute [3].

Red blood cells

The most abundant blood cells are the RBCs. They are disc-shaped with an average diameter of $7.2\,\mu$m and the thickest part is $2.2\,\mu$m. There are between 4.2×10^9 and 5.4×10^9 RBCs pr. mL of blood and they form approximately 99 % of the total number of cells. Their mass density varies from $1.089\,\mathrm{g\,cm^{-3}}$ to $1.100\,\mathrm{g\,cm^{-3}}$ [2].

White blood cells

WBCs are spherical and have diameters ranging from $6\,\mu$m to $10\,\mu$m and mass densities of $1.055\,\mathrm{g\,cm^{-3}}$ to $1.085\,\mathrm{g\,cm^{-3}}$ [2]. There are between 4×10^6 and 11×10^6 WBCs pr. mL of blood. WBCs can be split into three overall types: granulocytes, lymphocytes and monocytes. The latter is the largest type, but also the least abundant of the three. WBCs are closer to CTCs in size, shape and density than the other blood cells and are thus the most difficult to remove.

Platelets

Finally there are the platelets, which have sizes of only $2\,\mu$m to $4\,\mu$m and concentrations of $2.1 \times 10^8 - 5 \times 10^8$ pr. mL of blood [2]. A scanning electron microscope (SEM) image of a blood sample from a healthy person can be seen in Figure 1.1.

Circulating tumour cells

CTCs are cells that have detached from a primary tumour of a cancer patient and then circulate in the blood. From there they can interact with blood components, access nutrients and travel around inside the body through the bloodstream. They can then penetrate the tissue surrounding the blood vessels and grow a secondary tumour somewhere else in the body. This process is called metastasis [4]. Metastasis causes approximately 90 % of all cancer-related deaths [5] and the detection of CTCs is very important for

detection and diagnosing of cancer [6]. CTCs are heterogeneous and it has been suggested that only some stem-cell-like CTCs can initiate new tumours [7]. It is important for the understanding of metastasis to be able to analyse single CTCs. To do this the CTCs must first be separated from the blood cells, which is a challenge since only 1-1000 CTCs are found in 1 mL of patient blood depending on the advancement of the disease [8]. A few methods quickly remove some of the blood cells. RBC lysis buffer can be used to remove RBCs while leaving the WBCs and CTCs intact. Another method is centrifugation with a density gradient, which divides the blood into three layers: 1. Plasma and platelets, 2. Lymphocytes, monocytes and CTCs if any, 3. Granulocytes and RBCs. Thus CTCs have a density close to that of lymphocytes and monocytes. While centrifugation with density gradients effectively removes RBCs, platelets and about half the WBCs, the CTCs are still very rare compared to the remaining cells. The size of cancer cells varies greatly, but measurements on 20 different cancer cell lines showed that on average more than 90 % cells had a mean diameter greater than 8 μm [9], which means that a few of them overlap in size with WBCs.

Cell lines

Often whole blood or WBCs spiked with cultured cancer cells are used to test separation devices. It is more practical to use cell lines because they are more accessible. Also their concentration can be controlled, they can be stained with a fluorescent marker, so they can be distinguished from the blood cells, and properties, like their size distribution, can be measured prior to experiments. In this study human colon adenocarcinoma LS174T cells are used to model CTCs [10]. This cell line was simply chosen because it was available at one of the Cell-O-Matic partner's lab and the partners had prior experience working with it. Measured sizes of WBCs and LS174T cells are showm in Figure 1.2. They have average sizes of 7.1 μm and 13.6 μm respectively, but it can be seen that the sizes overlap. According to the measured cell sizes, 2 % of the WBCs have a diameter larger than 8 μm and 1.5 % of the cancer cells have a diameter smaller 8 μm. In the figure there is approximately an equal amount of both cell types, but with 10^6 times more WBCs than cancer cells the overlap becomes more significant. Details on how the cell sizes were measured are found in Section 3.4.

There are many challenges that need to be solved to obtain CTC separation and capture. The CTCs are rare compared to all other blood cells even after use of RBC lysis or density gradients. A large number of cells have to be processed within a reasonable time frame with a high recovery of CTCs and a high removal of blood cells. It is very difficult to get a good separation since the WBCs and CTCs have a small overlap in both size and density. After separation the cells should be collected for further analysis, so they must still be viable with the same characteristics as before separation. For single cell analysis, single CTCs must be captured in separate traps and then be retrieved separately to avoid cross contamination.

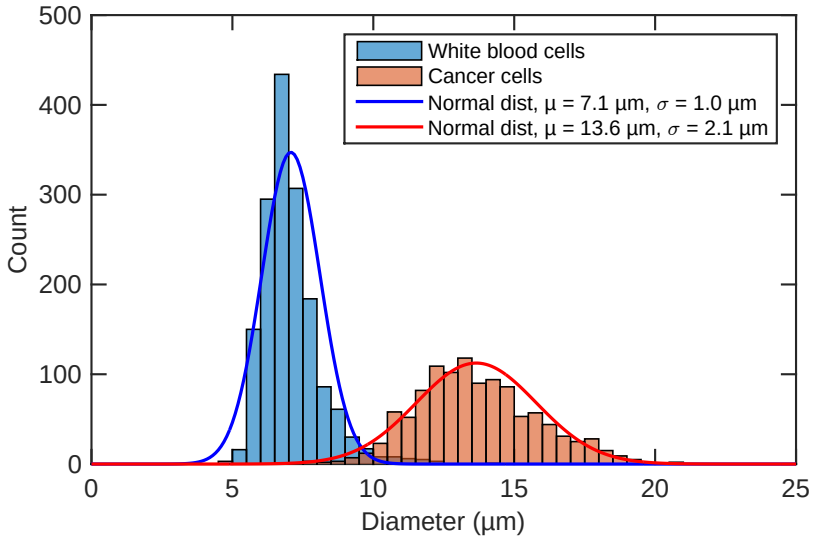

Figure 1.2: Measured sizes of WBCs and LS174T cancer cells with fitted normal distributions.

1.3 State-of-the-art cell sorting methods

A wide range of techniques for CTC enrichment and isolation has been developed. The techniques exploit the biological or physical properties specific for CTCs, including size shape and deformability. This section is divided into two subsections: one describing the rare cell isolation techniques that are already available in biology labs or are being developed for commercial applications, and one describing developments in continuous LoC techniques.

Commercial techniques

Most of the commercially available devices utilise immunological capture using antibodies targeting tumour-associated antigens, like the epithelial cell adhesion molecule (EpCAM), or common WBC-associated antigens, like CD45 [11]. The only Food and Drug Administration (FDA) approved technology for clinical monitoring of CTCs in cancer patients is the CellSearch® system from Janssen Diagnostics. This system is based on immunomagnetic enrichment of EpCAM-positive cells and the subsequent CTC counting is done using fluorescent microscopy to detect DAPI-positive, cytokeratin-positive and CD45-negative cells [12]. Microfluidic systems utilizing antibody-based capture also exist. The herringbone-chip combines antibody-coated walls with passive mixing of cells though generation of microvortices [13]. Another system called the CTC-iChip combines immunomagnetic selection, hydrodynamic cell sorting and inertial focusing to separate CTCs from diluted whole blood [14]. All antibody-based capture technologies have limitations as they might capture only a subpopulation of the CTCs. Furthermore, most of them have high initial and running costs and require user specialisation.

CTCs can also be isolated by use of filtration. An example is isolation by size of

epithelial cells (ISET), where diluted whole blood spiked with tumour cells is pushed through a membrane with 8 μm cylindrical pores [15]. Another example is the ScreenCell® device that can filter live cells that are able to grow in culture after the enrichment [16]. It has filters with a size of 6.5 μm. Finally Tang *et al.* used conical shaped filters, also with a size of 6.5 μm [17]. They tested the filters on three cell lines and showed that the capture efficiency depends on the size of the rigid cell nucleus. The problem with the filtration techniques is that some WBCs are retained in the pores and eventually the filters will be clogged. Also the cancer cells are stuck in the filters and cannot be further processed for example for single cell capture or DNA extraction.

These are just some of the systems that are commercially available or being developed for commercial use. A more thorough review can be found in [18].

Continuous LoC techniques

Various microfluidic continuous separation techniques exist and have been used to separate polymer beads of different sizes or to enrich biological samples. The separation techniques can be split into two different types: Active and passive. The active separation rely on an externally applied field to separate the particles, whereas the passive use interactions between particles, microchannel structures and flow fields. The passive separation method Pinched Flow Fractionation (PFF) was studied in this thesis, and focus of this state-of-the-art will be on similar passive methods. Both active and passive techniques as well as devices combining both have already been extensively described in several excellent reviews [19–22]. Instead follows here a short list of active techniques and a thorough description and comparison of separation results gained with passive methods.

The active separation methods include flow cytometry, dielectrophoresis, magnetophoresis and acoustophoresis [23–26]. The disadvantage of the active methods is that the particles must have differences in electrical, magnetic or acoustic properties, which limits the samples that can be used. Otherwise the particles must be labelled, which might alter their physical properties. Also active devices require more expensive fabrication processes such as integration of electrodes.

The passive devices can be fabricated solely in thermoplastics and require a less complicated experimental setup. One of the first on-chip separation methods was microfiltration, which is very similar to the commercial filters. Filtration can be realized by placing micro-pillars in arrays with small spacing which only allows small cells to pass [27], or by driving the flow through a narrow planar slit [28]. These devices are very ineffective because cells are trapped in the flow direction, as in the commercial filters. Instead the filters can be arranged perpendicular to the flow direction so the smallest particles are continuously removed. Cross-flow filters were used by Sethu *et al.* to remove WBCs from whole blood [2]. They isolated approx. 50 % of the RBCs, while depleting more than 97 % of the WBCs. The method is limited by the flow rate, because when increased to above 5 μL/min. they observed a large increase in WBCs that deformed and passed through the filter. A sketch of the design is shown in Figure 1.3A.

Another passive method is called Deterministic Lateral Displacement (DLD). The devices consist of channels with micro-posts placed in arrays such that particles with

different sizes follow different flow patterns as illustrated in Figure 1.3B. Loutherback *et al.* used DLD to separate MDA-MB-231 breast cancer cells from diluted whole blood [29]. The main advantage of DLD is the sample flow rate, which can be up to 10 mL/min. However the measured separation efficiencies are relatively low because cancer cells deform when they hit the posts and thus follow the same flow patterns as smaller particles.

A method called hydrodynamic filtration was suggested by Yamada *et al.* [30]. In their design, samples are pumped through a main channel with several side branches so a small amount of liquid continuously leaves the main channel. Particles are thus directed towards the sidewalls and the smallest particles are removed. Yamada *et al.* used hydrodynamic filtration to enrich WBCs from diluted whole blood. They measured a final WBC purity of 3.6 % after two rounds of filtration. With this method some particles will never migrate to the side of the main channel and it is impossible to completely remove all small particles from a sample, as indicated on Figure 1.3C.

A similar method is hydrophoretic separation, where slanted obstacles are placed at the top and bottom of a main channel. The obstacles create a flow perpendicular to the direction of the main flow, so that the large particles migrate to the channel sidewalls, whereas the small particles can move more freely through the obstacle gabs, as shown in Figure 1.3D. Choi *et al.* used this method to separate platelets from diluted whole blood [31], and to separate RBCs from WBCs [32]. They isolated the WBCs with a purity of 58 %. Their device is limited by the deformability of the large cells, which enables them to migrate towards the outlet for small particles, and therefore Choi *et al.* measured a loss of 15 % of the WBCs.

Bhagat *et al.* investigated shear-modulated inertial migration of particles in rectangular channels with high aspect ratios [33]. They showed that at high flow rates, particles align at specific equilibrium positions because of lift forces, as seen in Figure 1.4A. Lift forces depend on particle size and deformability, and can thus be used for cell separation. This was demonstrated by Hur *et al.* who separated SAOS-2 osteosarcoma cells and MCF-7 breast carcinoma cells with increased metastatic potential (modMCF-7) from diluted whole blood [34]. The separation was mainly size-based, but they showed that the more deformable modMCF-7 cells had an equilibrium position further away from the blood cells because of their high deformability, as illustrated in Figure 1.4B. This yielded an enrichment ratio of 5.4, instead of 3.2 for the stiffer SAOS-2 cells. The lateral position of the cancer cells overlapped with the position of the WBCs, so while they obtained a recovery of 96 % - 97 % they only removed 71 % - 83 % of the WBCs.

Bhagat *et al.* also used inertial microfluidics for cancer cell separation. They made a design with contraction–expansion regions along the main microchannel length for improved inertial focus, and were able to separate MCF-7 cells from diluted whole blood at a throughput of 10^8 cells/min. [35]. Because of the improved inertial focus they were able to remove more than 99 % of both RBCs and WBCs, with a cancer cells recovery of 84.5 %. They observed that the large cancer cells disturb the flow field and make a few blood cells follow them into the cancer cell outlet, as sketched in Figure 1.4C.

It was demonstrated by Geislinger *et al.* that viscous forces can also be used for cell separation, and they used it to separated RBCs from platelets [36]. However purely viscous lift forces only appear in low flow rate regimes, which greatly limits the sample throughput.

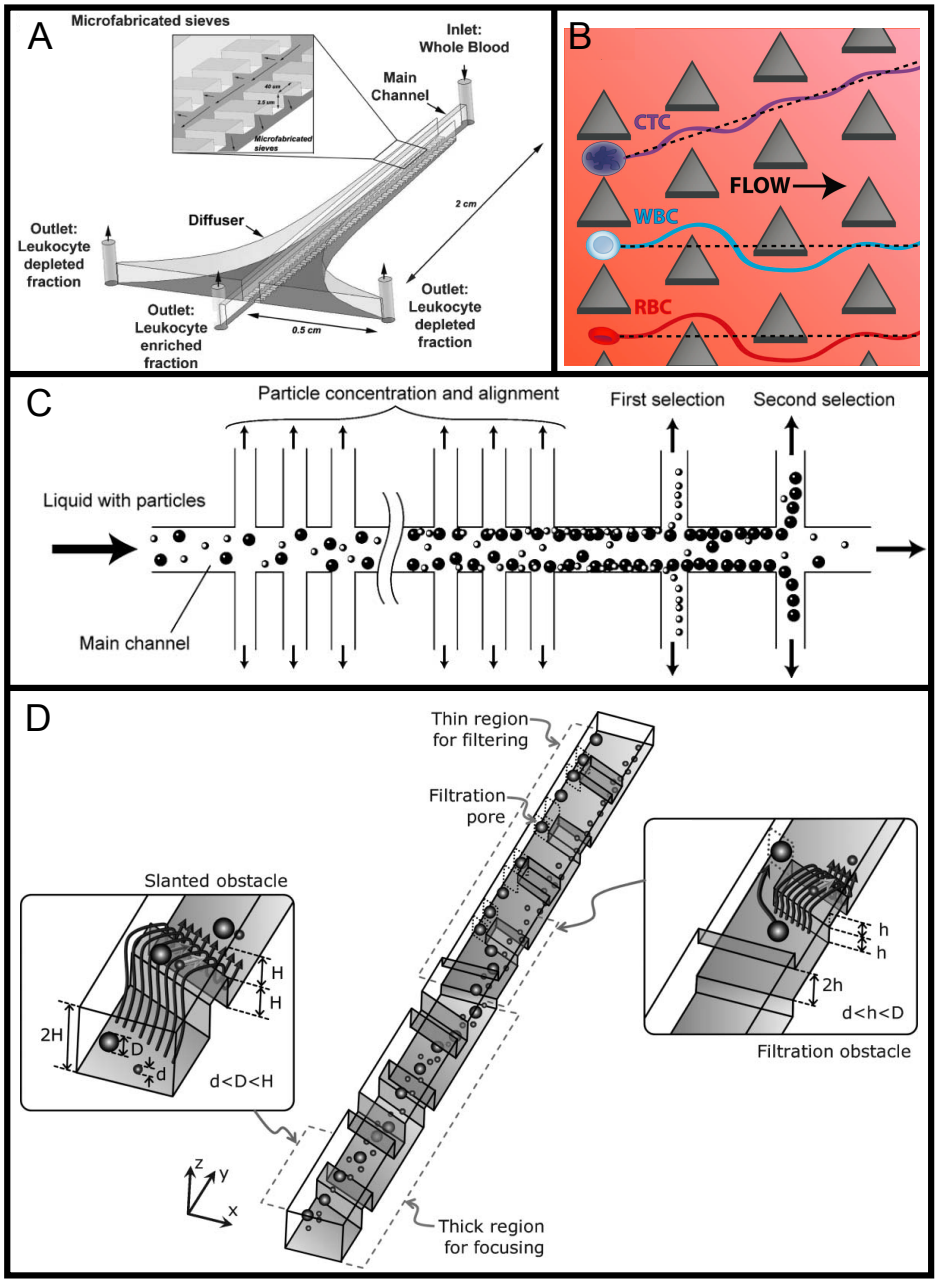

Figure 1.3: (A) Design from [2] with 40 μm×2.5 μm sieve structures. (B) DLD principle from [29]. (C) Hydrodynamic cell sorting chip from [30]. The dimensions are optimised to bring particles close to the side branches. Next small particles are removed, and then the large particles. A few particles will not be sorted and go towards the waste outlet with the remaining fluid.(D) Slanted obstacles in the hydrophoretic separation device from [32]. First all particles are focused to one side of the main channel, and then large particles are moved to the other side while small particles flow above/below the obstacles and keep their position.

Another way to exploit lift forces is to use on-chip microvortices to first capture the targeted cells and then release them. The devices consist of microvortices that capture cells in reservoirs on the chips. Large particles experience a large shear-gradient lift force at the vortex and are trapped in the vortex center, whereas small particles experience a weak lift force and are flushed out of the trapping region. Hur *et al.* made a microvotex chip for isolation of cancer cells from blood [37], shown in Figure 1.4D. They separated HeLa cervical cancer cells and MCF-7 cells from diluted RBC-lysed blood at sample flow rates of 4 mL/min. However they only measured a cancer cell recovery of 10 % for HeLa cells and 23 % for MCF-7 cells. They claim this is due to deformability of the cells, which then experience an additional lift force towards the center of the main channel, i.e. away from the vortices.

A method called Dean Flow Fractionation (DFF) combines Dean drag forces with inertial microfluidics. The Dean drag forces arise from the centrifugal acceleration of fluid flow in curved channels. Depending on size the cells will either experience a stronger Dean drag force or a stronger inertial lift force and migrate towards the inner side wall or the center of the curved channel. Sun *et al.* made a double spiral DFF device shown in Figure 1.4E. The device was tested with HeLa cells mixed with diluted whole blood [38], and high separation efficiencies were measured at flow rates of 1 mL/min. Hou *et al.* tested a single spiral DFF device on clinical samples from lung cancer patients [39]. The initial CTC concentrations were unknown, however after separation the ratio of CTCs to WBCs was an impressive 1:9.

It is clear that a lot of cell separation techniques exists because of the high interest in CTC isolation. To compare all mentioned passive separation techniques, some parameters describing the separation performance are listed in Table 1.1. The parameters include recovery of cells of interest and removal of other cells. Recovery is calculated as the number of collected targeted cells divided by the total number of processed targeted cells. Similarly the removal is calculated as the number of removed untargeted cells divided by the total number of processed untargeted cells. Ideally both recovery and removal should be 100 %. Recovery and removal were chosen instead of enrichment or purity because they are independent of the initial mixture ratio of the sample. Another listed parameter is sample throughput, which was chosen because it takes dilution of samples into account as opposed to the sample flow rate. Most of the numbers were stated by the authors, while some are based on simple calculations. An example is throughput which is calculated as sample flow rate times concentration. If the removal is not stated it is determined from the recovery and the enrichment ratio.

None of the techniques yield efficiencies over 98 % for both cell types simultaneously although it should be possible based on the measured cell sizes. In the published papers they used other cell lines than the LS174T cells used in this project, however their cell lines are not expected to have a larger size overlap with the WBCs. It is difficult to determine exactly why some cells are not separated correctly, especially because it is common to measure the amount of cells in each outlet after separation, but not the cell sizes. Different effects can have an influence on the separation. For the filtration methods and DLD higher flow rates leads to lower efficiencies. The reason is that high flow rates cause cells to deform and move through filters, or in flow patterns similar to smaller particles. For

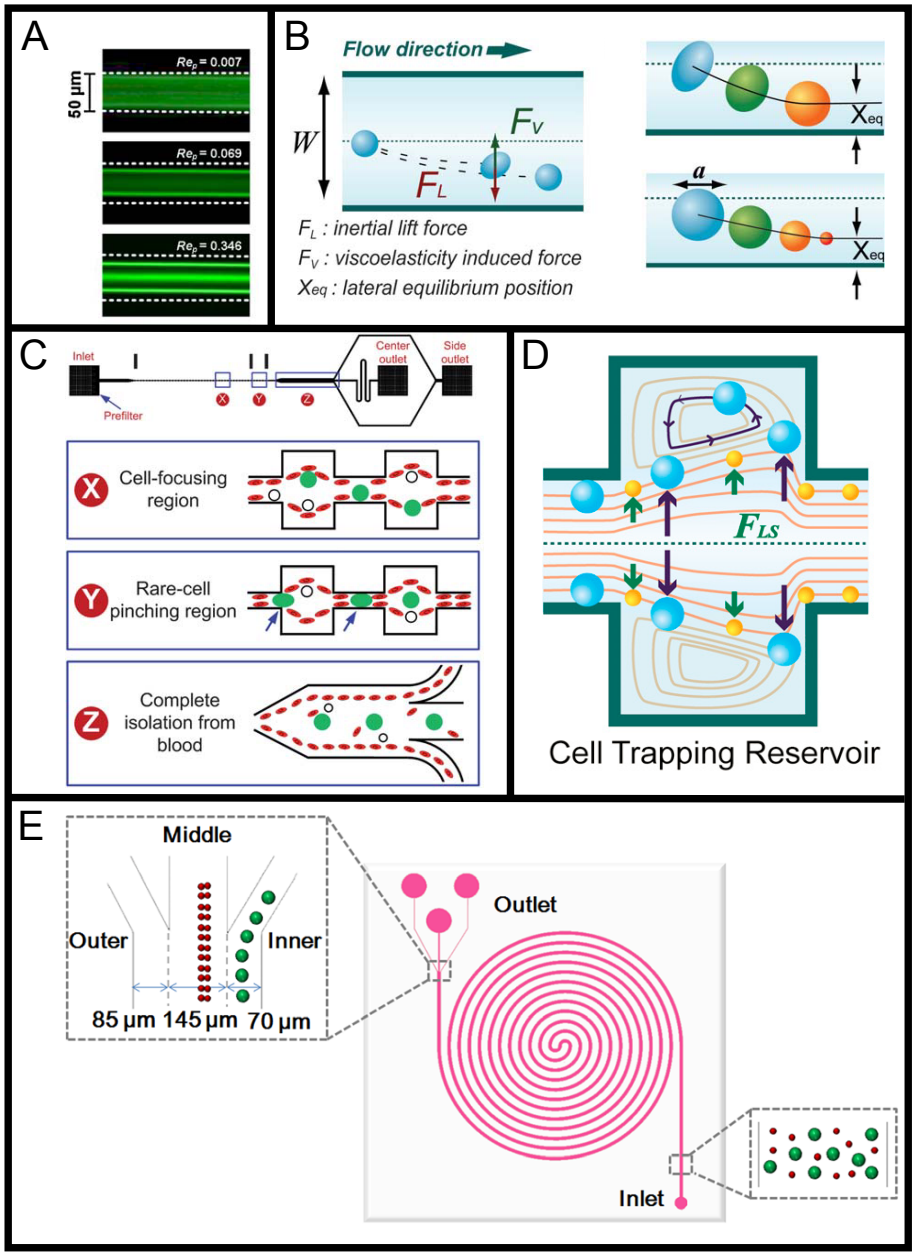

Figure 1.4: (A) Distribution of 4.2 μm particles in a rectangular channel at increasing flow rates. The image is taken from [33]. (B) Principle of inertial sorting from [34]. The intertial forces depend on particle size and deformability. (C) Contraction-expansion chip from [35]. (D) Chip with microvortices. First the cells are aligned at their equilibrium positions. Then they reach the reservoirs, where large (and deformable) cells experience larger shear-gradient lift forces and are pushed towards the vortex, whereas small (and stiff) particles are flushed out [37]. (E) DFF chip with a double spiral from [38]. The particles experince different lift and drag forces, which determine their equilibrium positions.

Table 1.1: Comparison of separation results gained with different passive state-of-the-art microfluidic cell sorting techniques.

Method	Sample	Throughput [cells/min]	Recovery [%]	Removal [%]
Microfiltration [2]	Whole blood (WBC removal)	2.5×10^7	∼50	>97
DLD [29]	MDA-MB-231 cells (5 %) spiked in 20x diluted whole blood	2×10^8	86	77.9
Hydrodynamic filtration [30]	10x diluted whole blood (WBC enrichment)	1×10^7	∼100	96.2
Hydrophoretic separation [32]	20x diluted rat blood (WBC enrichment)	2.5×10^5	85	99.8
Inertial lift forces [34]	SAOS-2 cells (1.4 % compared to WBCs) mixed with 10x diluted whole blood. Only the WBC removal was measured.	1.1×10^4	97	70.6
Inertial microfluidics [35]	MCF-7 cells (10^{-5} %) spiked in 20x diluted whole blood	1×10^8	84.5	>99
Microvortex [37]	HeLa or MCF-7 cells (1 %) spiked in diluted RBC-lysed blood	4.5×10^8	10-23	>99
DFF [38]	HeLa cells (∼3 cells/mL) mixed with 20x diluted whole blood	2.5×10^8	80	91.3

these methods a compromise between throughput and recovery/removal must be made. The methods that exploit inertial forces are generally operated at higher throughputs and with high efficiencies, especially when the lift forces are combined with other effects like in the contraction–expansion chip made by Bhagat *et al.* and in the DFF devices. However inertial forces also depends on deformability. The deformability of cancer cells can be used as a marker for their metastatic potential [40]. While metastatic cancer cells have an increased deformability, it is believed that most cancer cells are more rigid than WBCs. This causes problems for the LoC techniques using lift forces, as deformable cells will act like larger rigid cells and the deformability of WBCs thus decrease the separation efficiency. A method using the high deformability of WBCs combined with size separation would thus have an advantage and could potentially increase the separation efficiency even further. Microfilters already separate cell based on both size and deformability [41, 42, 17]. However these filters still have issues with clogging and the cells are caught in the filters where they cannot be used for subsequent investigations. In this thesis PFF was used for cell separation. The separation is mainly size-based, but it will be shown that the higher

deformability of the WBCs can be used as an advantage to obtain cancer cell separation at high efficiencies.

1.4 Pinched flow fractionation

PFF is a continuous passive size separation technique first presented by Yamada *et al.* [43]. The principle of PFF is shown in Figure 1.5. A sample containing particles of different sizes is placed in one inlet and a buffer solution is placed in the other. Pressure is applied at both inlets, and the solutions are pushed through the device and meet in a narrow channel called the pinched segment. Here the particles get aligned against the side wall due to high flow from the buffer solution, and they follow streamlines according to the position of their center of mass. The pinched segment is split into two or more outlet channels, and particles go towards specific outlets depending on their size.

The PFF technique was first used to separate polymer beads of different sizes using increasingly advanced designs. Takagi *et al.* made a device with multiple outlet channels and used it to separate 1.0 μm and 2.1 μm beads [44]. They also made a simple model for predicting which outlet particles of a certain size will go to. Sai *et al.* made a device with microvalves used to control the flow rate through some of the outlet channels. They used it to separate submicron sized beads at efficiencies around 90 % [45]. Recently Lu *et al.* used inertially induced lift forces to enhance the separation of microbeads at sample flow rates of 150 μL/h [46]. PFF has also been applied to biological samples and was used for

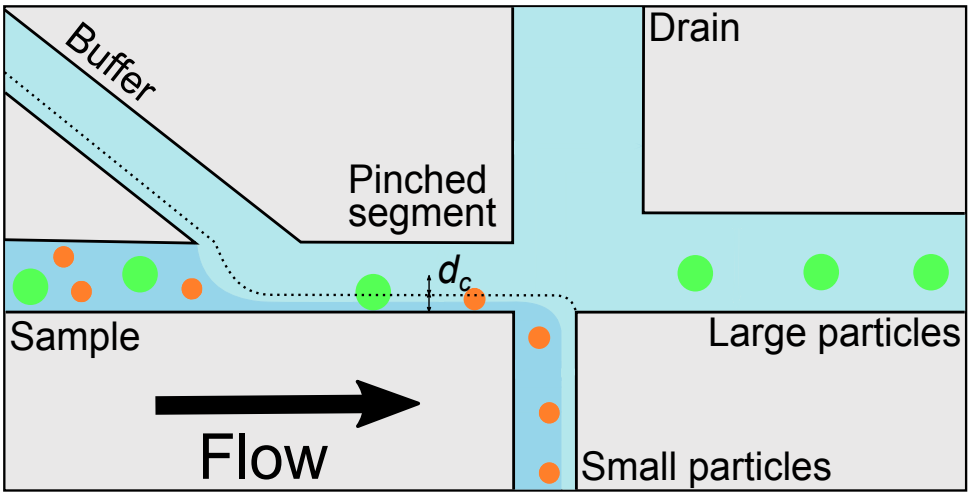

Figure 1.5: Sketch illustrating the principle of PFF. The particles are forced to align along the side wall in the pinched segment from where they are split into different outlets. The dotted line represents a streamline going just between the two particle outlets. Twice the distance from the pinched segment wall to the streamline is called the critical diameter, d_c, and it determines which outlet the particles will go to. Particles smaller than d_c flow towards the small particle outlet and particles larger than d_c flow towards the large particle outlet. On the sketch is also featured a third drain outlet, which collects some of the buffer solution to minimise dilution of the sorted samples.

separation of RBCs and WBCs [47], and detection of single nucleotide polymorphisms [48].

For this thesis, PFF designs were developed for CTC separation. All the PFF designs have three outlets as in Figure 1.5. One outlet collects particles with diameters smaller than the critical diameter, named d_c, another outlet collects particles with diameters larger than d_c, and the third outlet collects as much buffer solution as possible. The developed designs exploit the general size difference between CTC's and blood cells so that blood cells are collected in the small particle outlet, CTC's are collected in the large particle outlet, and the buffer solution is collected in the drain, which is particle free.

As with all the other passive separation techniques PFF has the advantage that it is driven solely by external pressures. Since the critical diameter depends on the hydraulic resistance of the outlet channels, PFF also has the advantage that d_c can be adjusted by applying a pressure to any of the outlets. Thus any PFF device can be adjusted to separate a wide range of samples, which is not possible for any of the other mentioned passive separation techniques.

There are also some disadvantages to PFF. The separation only works for laminar flow, so the sample throughput is limited. Previously reported sample flow rates have been to be in the range of 5,000 particles/min. to 42,000 particles/min. [45, 46], which is much slower than for the inertial separation methods listed in Table 1.1. Another disadvantage is the large amount of buffer solution needed, which can dilute the output samples. Both of these disadvantages are addressed in the thesis.

1.5 State-of-the-art single cell capture

The first step towards single cell analysis is development of systems capable of single cell manipulation. Various methods already exists and have been described in several thorough reviews [49–51].

One of the most simple and well-known manipulation techniques is micropipetting. It has been used to capture, transport and release single cells and vesicles [52, 53]. Other ways to capture cells is with optical tweezers, magnetic tweezers and atomic force microscopy [54–56]. Some methods have also be combined with microfluidic systems. An example is a design made by Zhu *et al.* They used dielectrophoretic forces to attract cells towards regions with parallel narrow structures where the cells were immobilised [57]. Microfluidic systems are advantageous because small liquid samples can be handled and the channel size is typically around the size of a single cell, which greatly simplifies single cell handling. However, as mentioned in the previous section, any system that requires externally applied fields is not of interest for this thesis because they have high running costs and need advanced setups.

Hydrodynamic trapping

An alternative is hydrodynamic cell trapping systems, which can be operated solely by applying pressures to control the flow. Hydrodynamic cell trapping systems were used in this thesis to capture single cancer cells, and some similar hydrodynamic devices are described in this section. An example is a device made by Rettig and Folch [58]. They used PDMS microwells with varying dimensions to capture single cells as seen in Figure 1.6A.

Cell solutions were suspended above the microwells and after cells had settled the remaining cells were flushed away from the wells. They found that the optimal well-dimensions for cell capture were a diameter of 20 μm and a depth of 21 μm, which yielded a single-cell occupancy of 92 %. This method is mostly suitable for optical investigation of the captured cells, as the cells cannot easily be retrieved from the wells.

Di Carlo *et al.* used an array of U-shaped trapping structures shown in Figure 1.6B [59]. Again the trap dimensions were varied and they found that traps with a depth of 10 μm gave the best results with a single-cell occupancy over 50 % for HeLa cells. There is a gap of 2 μm between the traps and the seal, and when a trap is occupied the cell blocks most of the flow above the trap, which prevents other cells from being captured.

A device using a similar principle was demonstrated by Kobel *et al.* [60]. They made long channels going around a cavity with a 3 μm gap as shown in Figure 1.6C. The main channel lengths vary so between 63 % and 80 % of the flow goes through the cavity and cells will therefore likely get trapped. Once a cell is trapped it blocks the flow through the cavity and the following cells flow past to the next available cavity. Kobel *et al.* measured a capture efficiency of 97.2 % for the design with 80 % flow through cavities.

Finally Tan and Takeuchi made a similar design with a build-in release system [61]. The traps were placed in series with a main channel going around the traps. Once particles were captured they could be released individually by focusing a laser next to the particle, causing local heating and bubble formation. The bubble displaces the particle, which is released from its trap and can be moved out of the chip by the main flow as shown in Figure 1.6. The optimised traps had a width of 7.5 μm and a height of 18 μm.

Although these designs are based on hydrodynamic principles, they are very different from each other. There are variations in trap dimensions and shape, and no general theory on what requirements a device must fulfil to obtain effective single cell trapping. The design requirements and flow conditions resulting in successful single cell capture will be discussed and expanded on in this thesis.

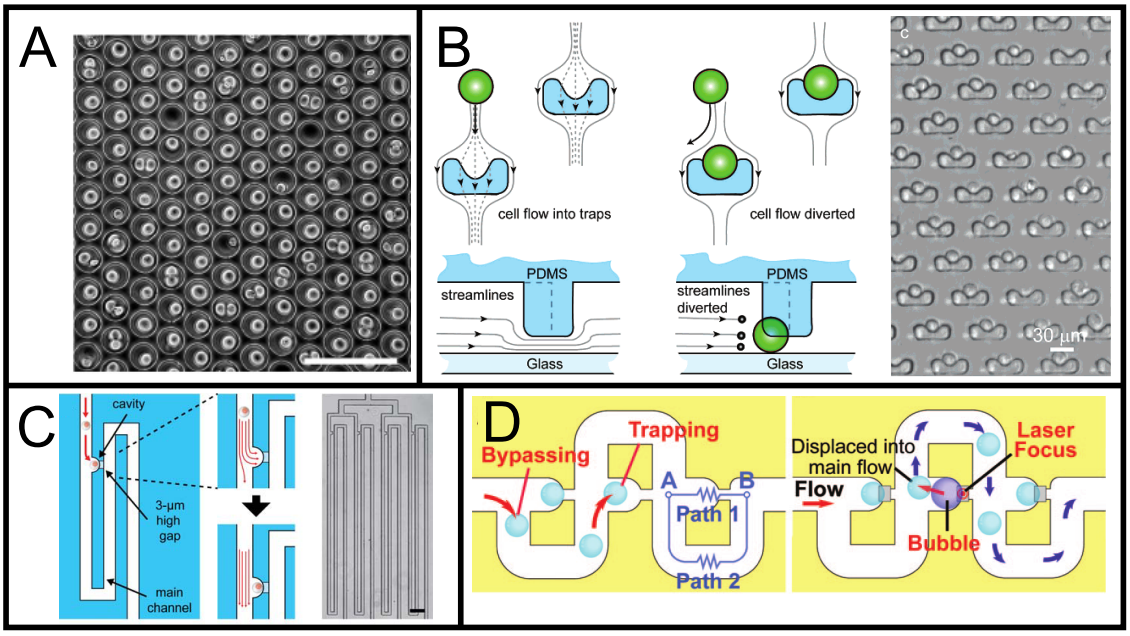

Figure 1.6: (A) Cells captured in microwells after flushing [58]. The scale bar is 100 μm. (B) Principle of cell trapping design from [59]. The left image illustrates how the flow above the structures is changed when it is occupied by a cell, which blocks the gap between the structure and seal. The image on the right shows captured HeLa cells. The scale bar is 30 μm. (C) Design by Kobel *et al.* [60]. The cavities are 3 μm high and 12 μm wide and the main channel going around them is very long so most of the flow goes through the cavities. (D) Trap-and-release system demonstrated in [61]. Again there is more flow through the trap than the main channel. Cells can be released from the trap by forming a bubble with a laser focused next to the cell. The bubble displaces the cell which again follows the main channel flow towards the outlet.

1.6 Thesis outline

LoC systems for size-based cell sorting and single cell capture are investigated in this thesis. Key elements include low chip fabrication and running costs, and easy implementation of the developed devices, so they can be setup and used in other labs. The first part of the thesis covers the elements that were identical for both LoC systems. This includes the chip fabrication process and the methods used for device characterisation, sample and chip preparation, and the experimental setups. The rest of the thesis is split in two main chapters discussing the design development, experiments and results gained from the work on cell sorting by PFF and the work on hydrodynamic cell trapping.

Chapter 2: The methods used for chip production are presented, including mask design, shim fabrication, injection moulding and thermal bonding.

Chapter 3: The techniques used for chip characterisation, sample preparations, and the setups used for cell sorting and cell trapping experiments are described.

Chapter 4: Theory, numerical simulations, design and results of the PFF experiments

are presented and discussed. Parts of the chapter are from Paper II.

Chapter 5: The design development, numerical models and results of the cell trapping experiments are presented and discussed. A section describing a method developed for investigation of sealed chips is also covered in this chapter. Parts of the chapter are from Paper III.

Chapter 6 & 7: The conclusions of the thesis are summarised and an outlook on future work is given.

Parts of the work have been moved to the Appendix to improve the flow of the thesis. The publications related to this thesis are included in Appendix A.

2 Chip fabrication

In this chapter, the chip fabrication process, from the development of a channel design to the finished LoC system, is presented. The focus is on investigations and optimisations made to produce successful batches of chips with different fabrication requirements.

Contents

2.1 Fabrication process overview

Fabrication of the polymer chips was done with injection moulding. This requires a master with the reverse channel structures that can be inserted into the injection moulder. The master is called a shim and it is fabricated in clean room facilities. Once the shim is made, thousands of polymer chips can be produced from it. After the chips have been injection moulded, their microchannels have to be sealed. This is done with a polymer foil, which is bonded to the chip using UV-assisted thermal bonding. Finally the chip reservoirs must be sealed to prevent contamination from dust particles, skin cells etc, while the chips were stored before use. The polymer chip fabrication can be divided into four steps:

1. Mask design
2. Shim fabrication
3. Injection moulding
4. Thermal bonding

All steps are described in the following sections.

2.2 Mask design

The first step in the production of LoC systems is the creation of a channel design. This design is then converted into a mask, which is used for fabrication of the shim. An example of a mask design is shown in Figure 2.1.

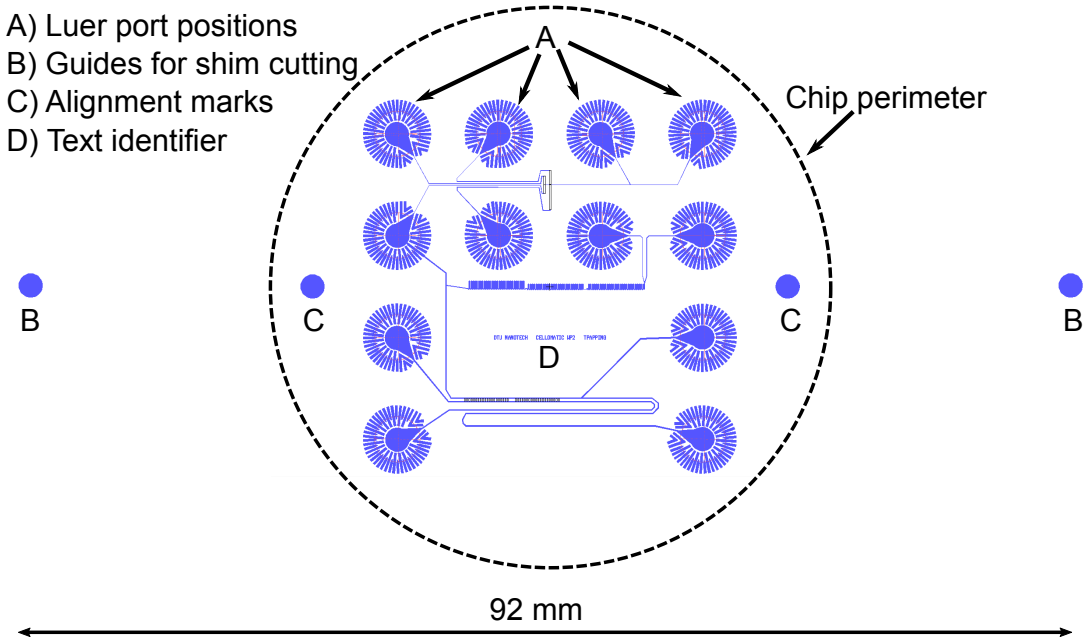

Figure 2.1: Overview of the mask design with channel structures from the first cell trapping design.

The layout of all chip designs is the same. In the injection moulding process 12 Luer-ports will be formed, and their positions are marked on the design. The Luer-ports are formed around 12 pins that are pushed onto the shim. To prevent that the pins flatten the microchannels connected to the Luer-ports, they are surrounded by support structures. The layout contains two marks at the periphery of the shim which are used as guides for cutting out the shim, so it fits in the injection moulder. There are also alignment marks for aligning the shim in the injection moulder. The name of the design is placed at a convenient position so the shim can be easily identified.

The mask designs were created with L-Edit version 15.1 software from Tanner EDA.

2.3 Shim fabrication

This part of the fabrication was done by NIL Technology ApS[1], which is one of the Cell-O-Matic partners. NIL Technology is a small DTU-based company which specialises in nano imprint lithography, and also fabricates nickel shims for injection moulding. They

[1] http://www.nilt.com/

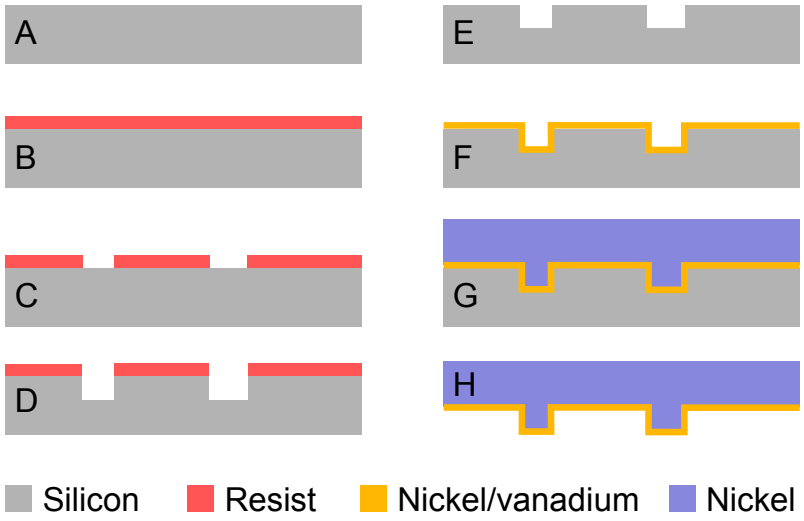

Figure 2.2: Overview of the shim fabrication process. (A) 150 mm silicon wafer. (B) Resist coating and UV lithography. (C) Resist development. (D) Reactive-ion etching. (E) Resist removal. (F) Nickel/vanadium sputtering. (G) Nickel electroplating. (H) Silicon etch leaving the nickel shim.

delivered all nickel shims used for chip production in this thesis work. The shims were fabricated using standard clean room processes [62, 63], which are briefly described in this section. The fabrication process is illustrated in Figure 2.2. It begins with a 150 mm silicon wafer which is dipped in hydrofluoric acid to remove the oxide and make the surface hydrophobic for better resist adhesion on the silicon. Next the wafer is coated with positive photo resist, which is UV-exposed under a mask with the design. The resist is then developed exposing parts of the silicon wafer. The exposed silicon is etched 30 μm using deep reactive-ion etching, a nd leftover resist is removed by plasma ashing and acetone. Then a nickel/vanadium seed layer is sputtered onto the wafer, and a nickel layer is electroplated on top. The silicon is removed with a KOH-etch leaving only the nickel shim with the reverse structures. Finally the nickel shim is cut to fit in the injection moulder.

All designs had just one layer of structures, except for the first cell trapping design. For this shim a second UV lithography step and reactive-ion etch were done, but otherwise the fabrication process was the same for all shims. The fabrication was completed in a clean room facility at DTU Danchip, and the final cut out was either done with a manual hydraulic press at a DTU lab or with a CO_2-laser at IPU[2].

2.4 Injection moulding

Injection moulding is the most widely used replication technique for fabrication of macroscopic polymer parts [64]. One of its advantages is the ability to form 3D devices that can be integrated with macroscopic equipment. Also the method has been highly automated,

[2] http://en.ipu.dk/

and equipment for large scale manufacturing is available. A disadvantage is that the polymer is exposed to high temperatures and forces, which results in high residual stresses, causing shrinkage and other defects, which are usually larger than for other replication processes such as hot embossing, PDMS-casting and thermoforming [65].

The cross section of an injection moulder is sketched in Figure 2.3A. Polymer granules are fed into a heated barrel where they melt. The melt is then injected through a nozzle into a mould. The polymer moves through a thin port called the sprue and then into a wide gate, which ensures that the polymer is evenly distributed. The mould contains a structured shim and a tool that defines the overall shape of the product. The injection is done under a high holding pressure to prevent back flow of the molten polymer. A vacuum pump is connected to the mould to get rid of air pockets. The mould can either be kept at a temperature below the glass transition temperature, T_g, of the polymer for an isotherm process, or it can be kept above T_g and cooled with the melt for a variotherm process. A typical cycle time for isotherm processes is in the order of 30 seconds to 2 minutes, whereas variotherm processes can take up to 5 minutes [65]. When the polymer has solidified the mould is opened, the product is placed on a conveyor belt, and the process starts over again.

Chips were injection moulded with an Engel Victory Tech 80/45 industrial injection moulder placed at DTU Danchip. It is placed under high-efficiency particulate air (HEPA) filters, which minimise the amount of dust particles surrounding the machine. The injection moulder is equipped with a custom designed mould tool, which produces chips with a 50 mm diameter and 2 mm thickness, containing 12 Luer-fittings. The fittings are used to connect the on-chip microchannels with macroscopic equipment used for experiments. The Luer-fittings can also be used as reservoirs and can contain 100 μL fluid when no equipment is attached. While the Luer fittings are very practical they limit the chip design as only 12 inlets/outlets can be used. An image of an injection moulded chip is seen in Figure 2.3B. The leftover polymer can easily be broken off because the gate is very thin.

For polymer injection moulding, thermoplastic polymers such as PMMA, polysterene and cyclic olefin copolymer (COC) are used. They are rigid at room temperature, and soften at T_g so they can be formed into any shape. There is typically a large difference

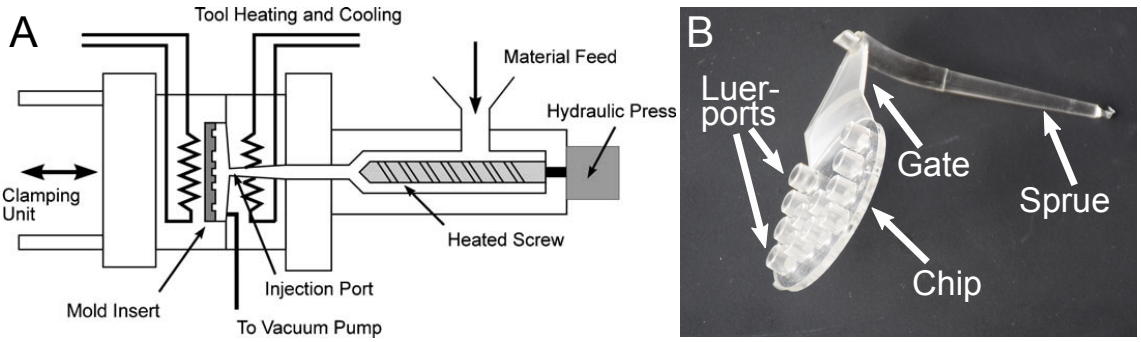

Figure 2.3: (A) Cross-sectional diagram of an injection moulder. The sketch is copied from [65]. (B) Image of a chip with the apperance it had as it came out of the injection moulder.

between their T_g and decomposition temperature, which is where the chemical bonds are broken and the material can no longer be reshaped. This allows for a large process temperature window. The COCs have become increasingly popular for microfabrication due to their favourable thermal, optical and mechanical properties [66]. The COC called TOPAS® 5013L-10 from Topas Advanced Polymers was chosen for the Cell-O-Matic project, and was therefore also used for chip fabrication in this thesis. It was chosen because it has a T_g of 134 °C [67]. The high glass transition temperature ensures that the chips can be exposed to high temperatures without deforming. This is necessary for some cell lysis procedures and for DNA amplification, which should be performed on-chip. In addition it has a high optical transparency in the visible and near UV range, and it has a low autofluorescence, which is especially important when working on stained DNA strands with a small fluorescent signal. It is also biocompatible.

The cell sorting chips were the first to be injection moulded using a recipe developed by an experienced user. The recipe is for an isotherm process, which was optimised to yield short cycle times, as described in [68]. However the sprue would sometimes break off and get stuck in the injection moulder, likely because of residual stress. It has been demonstrated that stress is caused by high pressures [69], and therefore the holding pressure was decreased from 1700 bar to 1400 bar. With the lower holding pressure, the sprue no longer broke off the injection moulded chips, and the modified recipe, named Recipe 1, was used for injection moulding of the first cell sorting and cell trapping devices. The parameters of Recipe 1 are listed in Table 2.1.

The injection cycle time with Recipe 1 is approx. 1 minute and it gives a good filling of the structures. However some defects occurred on one side of most channels, as seen in Figure 2.4. Structures in the center of the chip had no signs of stress marks, whereas structures at the edge had large stress marks with orientations pointing towards the center of the chip. This indicates that there is a center of contraction close to the center of the chips. The stress marks are not a problem for the PFF designs since their smallest dimension is around 30 μm, and there are no critical structures. Therefore these defects are not expected to influence the flow or separation efficiency of the chips, as long as the channels can be strongly sealed by thermal bonding.

For the cell trapping chips the capture efficiency depends largely on how well the walls comprising the traps are filled, and how tight the bonding is. As the cell trapping

Table 2.1: Injection moulding parameters of Recipe 1.

Parameter	Value
Nozzle temperature	270 °C
Injection speed	51.9 cm^3/s
Shot volume pressure limit	2200 bar
Holding pressure	1400 bar $\rightarrow$ 0 bar in 9.5 s
Mould temperature	120 °C
Mould cooling time	15 s

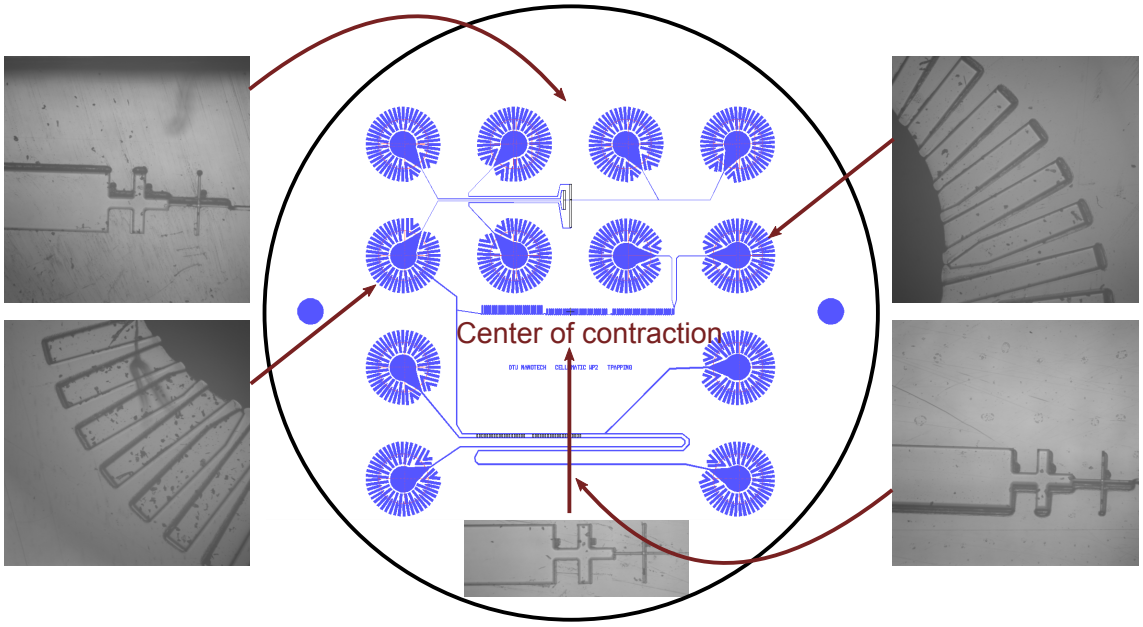

Figure 2.4: The first cell trapping design is shown in the center. Around it are images from the top, bottom, and both sides of a chip. The top and bottom structures were not present on the original design, but added by NIL Technology for characterisation purposes. The imaged structures have stress marks with orientations pointing towards the center of the chip, indicating that there is a center of contraction close to the center of the chip.

designs were optimised the injection moulding quality became more crucial, and a new set of bonding parameters was developed. It is generally accepted that the most important injection moulding parameters are holding pressure (sometimes called packing pressure), melt temperature (at the nozzle), mould temperature, and injection speed [70,71]. Residual stresses are the main cause of defects such as shrinkage and stress marks, and efforts were made to reduce the stress.

Two recipes were developed by a colleague who was also involved in the Cell-O-Matic project. The Recipes are named Recipe 2 and Recipe 3, and were originally optimised to another design. Recipe 2 turned out to worked well for one of the cell trapping designs. It has a lower nozzle temperature and a higher holding pressure, which results in chips with good filling and small stress marks. Recipe 3 has a lower holding pressure, and mould temperature and results in no stress marks, but also a poor filling. This recipe works well for designs with nano features, as stress marks usually have sizes on the micrometer scale, and therefore blocks the nano channels. On the final cell trapping design the traps were moved far away from the center of contraction and a new recipe was needed. It was made by testing recipes with a combination of parameters from Recipe 2 and Recipe 3. Three important parameters that vary between Recipe 2 and Recipe 3 are: mould temperature, holding pressure and injection rate. It was found that using the parameters of Recipe 2 with the injection rate from Recipe 3 gave the best result, found by measuring the height of the stress marks around traps. A comparison between a Recipe 2 chip and a chip

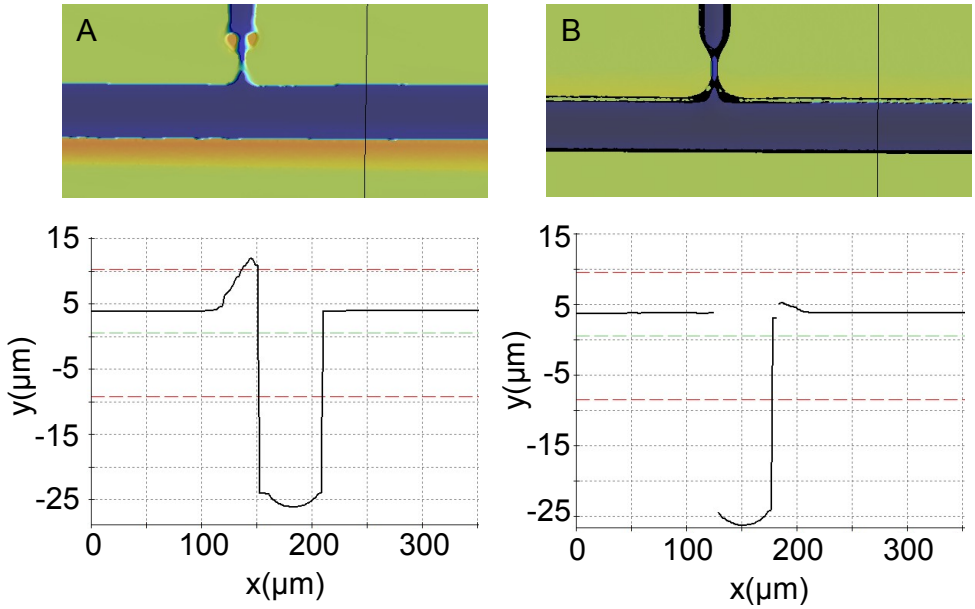

Figure 2.5: (A) Surface topology and height profile of a cell trapping chip injection moulded with Recipe 2. Blue colours represent the bottom height and red colours represent top heights. The black line indicates the position of the profile measurement. (B) Surface topology and height profile of a chip injection moulded with Recipe 4.

injection moulded with the new set of parameters, named Recipe 4, is seen in Figure 2.5. Measurements were performed with an optical profiler. The measurements show that the height of the stress marks was reduced from around 7.5 μm to 1.5 μm. The center of contraction also shifted to the other side of the traps. It is worth noting that although the structures around the triangular shape of the trap is not filled, the structures along the narrow part of the trap are completely filled.

The parameters of all injection moulding recipes are listed in Appendix B, and measurements from the optical profiler are found in Appendix C.

2.5 Thermal bonding

The microchannels have to be sealed strongly so the devices do not leak even at the maximum applied pressures (1 bar). Also the sealing process should not alter the chip structures, and the lid should not bend too much into the Luer ports or wide channels because it might partially or fully block them. The chips were sealed using UV-assisted thermal bonding, which is a popular method used for a range of microfluidic devices [72]. The chips were sealed with TOPAS®5013L-10 foils that had been cut out to fit the chips. The lids and chips were exposed to UV-light from a mercury arc lamp for approx. 30 s and were then placed in a custom made aluminium holder with holes for the Luer-fittings. A smooth nickel disc and a PDMS slice were placed on top of the lid to ensure a uniform pressure on the device surface. The stack was bonded using a P/O/Weber press, which

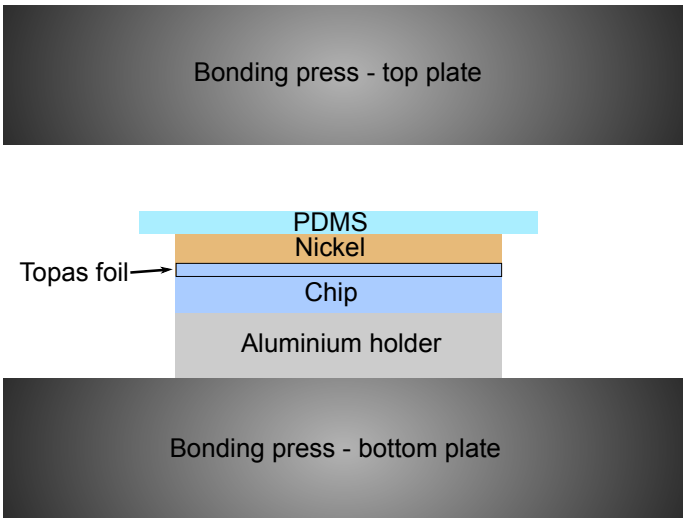

Figure 2.6: Sketch of the bonding stack used for sealing the chips. A 500 μm thick foils were used to seal the cell sorting chips, and 150 μm thick foils were used for sealing the cell trapping chips.

can apply user-defined pressures and temperatures while bonding. A sketch of the bonding stack is shown in Figure 2.6.

When choosing the lid thickness, a compromise between lid bending and magnification, when visualising the chips in a microscope, must be made. Thicker lids bend less when exposed to high temperatures and pressures, but they increase the working distance and cannot be used with high magnification objectives. The cell sorting chips were sealed with 500 μm thick lids, while cell trapping chips were bonded with 150 μm lids because high magnification is necessary for investigation of single cells and DNA. The 500 μm lids were cleaned with ethanol before bonding. This was not necessary for the 150 μm lids as they were covered in protective foil. However they were rippled and had to be flattened before bonding. The protective foil was removed and the lids were placed between smooth nickel flats and then flattened in the bonding press at 140 °C and 5.1 MPa for 10 min. The nickel flats were stuck to the lids and were not removed until the lids were used for chip bonding.

A previous study has shown that bonding at 120 °C and up to 5.1 MPa for 5 min. gives a strong seal without altering the chip structures [68], and these parameters were used as standard parameters for most chip designs. Later it was discovered that pressures of 2.5 MPa gave equally good results, and that was also used for many of the devices. Some chips were sent to partners of the Cell-O-Matic project and the final look of the chips was therefore important. While the standard parameters give a strong bonding especially at the center of the chips, the chips look somewhat unfinished. To improve this look an additional step was added to the bonding process. Chips were bonded with a thick PDMS slice at 0.5 MPa for 1 min, still at 120 °C.

The PDMS slice is flexible has holes matching the Luer-ports, so when using it for the extra bonding step, it applies an even pressure around the entire chip surface expect for at the Luer-ports, to prevent the lid from bending in towards the inlets/outlets. This final

bonding step gave the chips an even bonding on the entire surface and a nice finished look.

For some of the cell trapping designs the structures were intentionally altered by either applying higher bonding temperatures or pressures on the entire chip, or by bonding at higher temperatures only on certain parts of the device, with a small PDMS slice. The results of this alternative bonding are presented in the relevant sections. The standard bonding parameters were used for all chips unless otherwise stated.

After bonding, the Luer-fittings were covered with optical adhesive film from Applied Biosystems. The film is DNA, RNA and RNase free and prevents cross-contamination. The individual chips were placed in small plastic bags and stored until they were used for experiments. Chips were handled with gloves after injection moulding to avoid contamination. The careful chip handling was effective as almost no unwanted particles were seen in the Luer-ports or the channels.

2.6 Chapter summary

All cell separation and cell trapping designs were fabricated with standard clean room processes, and successfully injection moulded on the presented 12-Luer format. The injection moulding parameters were optimised to reduce residual stresses, and it was possible to fabricate high quality devices with maximum filling and minimal stress marks at the crucial structures. A strong and tight bonding was obtained with already published parameters, however an additional softer bonding step gave the chips the finished look of a commercialised product. Finally with careful handling of the chips it was possible to avoid contamination.

3 Methods

In this chapter characterisation methods, the setups and preparations made before any experiments are described. Image and data analysis methods are also presented.

Contents

3.1 Characterisation methods

The shims and some of the chips were investigated to check their quality before use. Two main methods were used for the characterisation: scanning electron microscopy and optical profiling. For scanning electron microscopy either a Zeiss Supra VP 40 SEM or a LEO 1550 SEM from Carl Zeiss A/S were used. Both are placed in the DTU Danchip clean room facility. Chips were covered with a 10 nm layer of either silver or gold-palladium prior to SEM characterisation to minimise charging of the polymer. The Zeiss Supra SEM was also used to investigate chips fractured after sealing. This procedure is described in Section 5.3.

A PLu Neox 3D Optical Profiler from Sensofar was used to measure the heights of channels on the shims and chips, and to visualise their surface topology. It was also used to measure the size of stress marks on injection moulded chips.

3.2 Setup

All experiments with nano- or microbeads were performed in a lab managed by the Optofluidics group at DTU Nanotech. Experiments on cell samples were carried out at a cell lab at DTU Nanotech or a cell lab at the Weatherall Institute of Molecular Medicine (WIMM) in Oxford UK, managed by Sir Walter Bodmer, who is a collaborator in the Cell-O-Matic project. Although experiments were performed at different locations, the overall elements remained the same, and in all three labs there was access to the following equipment:

- Inverted fluorescence microscope
- Charged coupled device (CCD) camera
- Flow controller
- Ultrasonic bath
- Tubing, pipettes, etc.

Figure 3.1 shows the setup in the Optofluidics lab. The equipment is described in the following section.

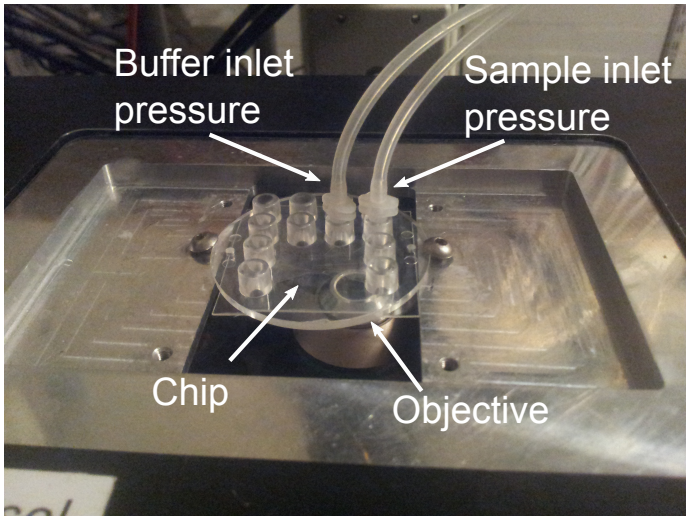

Figure 3.1: Picture of the experimental setup in the Optofluidics lab. A chip is placed in a holder for the microscope, and a flow controller is connected to the two inlets.

Fluorescence microscope

The microscope in the Optofluidics lab is an Eclipse TE2000-U inverted microscope from Nikon Instruments, which can be used for bright field or fluorescence microscopy, or a combination of both. The Nikon microscope is equipped with a halogen lamp used for

bright field imaging and a 200 W metal halide lamp used for fluorescence. It has three fluorescence filter cubes allowing for easy distinction between beads of different colours. The filters are: DAPI for violet excitation (325 nm - 375 nm) and blue emission light (435 nm - 485 nm), FITC for blue excitation (465 nm - 495 nm) and green emission light (515 nm - 555 nm), and TRITC for green excitation (525 nm - 540 nm) and orange emission light (575 nm - 650 nm).

The microscope also has a variety of objectives to choose from. For the bead experiments, air immersion objectives with 10X or 20X magnification were used. The 10X objective is good for overview images of for example beads caught in multiple traps, as it has a field of view of approx. $825\,\mu\text{m} \times 825\,\mu\text{m}$. It creates images with a pixelsize of $1.61\,\mu\text{m}$, which is too large for precisely determining the size of the microbeads, which is important for the separation experiments. Instead the 20X objective was used to take images that were later used to analyse the size of separated beads. The 20X objective takes images with a pixelsize of $0.53\,\mu\text{m}$ when an addition 1.5X magnification is added by the internal magnification module of the microscope. To check that beads lying next to each other can be distinguished from each other, the objective resolution is found using the Abbe equation [73]:

$$\delta = \frac{0.61\,\lambda}{NA}, \tag{3.1}$$

where λ is the emitted wavelength and NA is the numerical aperture of the objective. NA is 0.5 for the 20X objective. The resolution is calculated for all emission wavelengths:

$$\delta_{DAPI} = \frac{0.61 \cdot 460\,\text{nm}}{0.5} \approx 561\,\text{nm}, \qquad \delta_{FITC} = \frac{0.61 \cdot 535\,\text{nm}}{0.5} \approx 653\,\text{nm}, \tag{3.2}$$

$$\delta_{TRITC} = \frac{0.61 \cdot 612\,\text{nm}}{0.5} \approx 747\,\text{nm}. \tag{3.3}$$

Since the resolution is smaller than a micrometer it is not limiting the image analysis of microbeads. Nanobeads cannot be distinguished, but they were not imaged individually.

When imaging the beads they are typically placed in the Luer-ports. It is likely that the lid is not completely planar, but it is important for the size analysis that all beads are in focus. Thus it is advantageous that the beads are in focus in a large range of distances. This range is called the depth of field and is calculated as [73]:

$$d = \frac{\lambda}{NA^2} \tag{3.4}$$

For the three filters this results in depths of:

$$d_{DAPI} \approx 1.84\,\mu\text{m}, \qquad d_{FITC} \approx 2.14\,\mu\text{m}, \qquad d_{TRITC} \approx 2.45\,\mu\text{m}. \tag{3.5}$$

It is rather small, and it is therefore important that the beads have all settled completely at the bottom of the inlets/outlets before they are imaged.

The microscope in the Nanotech cell lab is an Axio Observer Z1 inverted fluorescence microscope from Carl Zeiss A/S. Up to 40X magnification objectives were used after experiments to take images of small objects like captured single cells.

In the Oxford lab the experiments were monitored with a Brunel SP98F inverted fluorescence microscope from Brunel Microscopes Ltd. It did not have a motorised stage and was not connected to a CCD camera, so after experiments, images were taken with an Axio Observer Z1 inverted fluorescence microscope from Carl Zeiss A/S. Images for size analysis were taken with a 20X magnification objective, which produces images with a pixelsize of 0.32 μm or 0.65 μm if binning is applied to save disk space. Binning was applied by accident on a few occasions, since many users have access to the microscope.

CCD camera

A CCD camera is a device that turns the light from an object into an electronic signal, which is then turned into an image. The CCD consists of small light-sensing elements arranged in a two-dimensional array on a semiconductor substrate. Each of these sensors correspond to a pixel. When incoming photons hit the surface of one of the pixels it generates an electron-hole pair and the electron moves to the nearest potential well. The percentage of photons that generates an electron-hole pair is called the quantum efficiency, and the number of electrons in each well corresponds to the intensity of the light. Small charges build up in the wells even when the CCD is in complete darkness because of thermal vibrations in the semiconductor substrate. This noise is called dark noise, and it creates uncertainty in the magnitude of the generated charge. Dark noise is reduced by cooling the camera. An electron multiplying (EM) CCD can, unlike a regular CCD, multiply low signals without adding any significant noise.

The camera connected to the Optofluidics microscope is a Cascade II:512 EMCCD camera from Photometrics. It has 512×512 pixels and is cooled to -70 °C. The cell lab microscope and the Oxford microscope are both connected to an AxioCam MR3 CCD camera from Carl Zeiss A/S.

Flow controller

The fluid flow was controlled by a MFCS™ FLEX from Fluigent, who are partners in the Cell-O-Matic project. The flow controller needs a steady pressure supply of 1.3 bar and can then provide pressures between 0 and 1 bar with a precision of 1 mbar. It has eight output channels, which can be controlled individually and simultaneously using the Maesflo software. The flow controller controls the applied pressure through tubing with Luer-connectors. The connectors had to be modified because they take up almost the entire Luer-port, where the samples are placed. After modification, the ports can contain approximately 80 μL of solution when connected to the flow controller. An MFCS™ FLEX was available in all labs. For some experiments additional tubing was added to enable processing of larger sample volumes without having to constantly refill the Luer-ports.

Ultrasonic bath

Air bubbles is an issue when working with microfluidics. They usually appear in areas with dead volume (almost no flow) that are difficult to fill with liquid, but they can also be in the wetting solution and completely or partially block channels, thereby changing

the flow in the device. In most cases they will ruin the experiment, and precautions must be taken to avoid air bubbles. Ultrasonic baths can be used to degas samples by placing a tubed solution in the water, and connecting it to an air pump with negative pressures. All buffer solutions were degassed in an ultrasonic bath prior to experiments. Samples with beads were also put in the bath to prevent them from sticking together.

3.3 Sample preparation

Prior to experiments, the samples and chips had to be prepared, and the protocols are described in this section.

Buffer solutions

As mentioned in the previous section, it is important that the devices are completely wetted by a buffer solution before they can be used. Since TOPAS 5013L-10 is hydrophobic the devices cannot be wetted with pure water. Instead devices were wetted with degassed Milli-Q water mixed with 0.1 % Triton X-100 (TX), which is a non-ionic surfactant with hydrophilic parts, commonly used as a wetting agent. All devices were completely wetted before any samples were introduced.

The TX solution was also used as buffer for all experiments with beads. TX cannot be used as buffer for cell experiments because it lyses the cells. Instead filtered FACSFlow from BD Biosciences was used as buffer for the cell experiments. The composition of FACSFlow is a secret, but it likely consists of phosphate-buffered saline (PBS), which is a salt solution with the same osmolarity and ion concentration as human cells. It probably also contains ethylenediaminetetraacetic acid (EDTA), which prevents cells from clumping or sticking to the chips. FACSFlow cannot be used as a wetting agent, so before cell separation experiments, devices were wetted with a degassed TX solution and then flushed with degassed FACSFlow for 5 minutes. All Luer-ports were then emptied and rinsed with FACSFlow three times to get rid of any leftover TX.

Bead mixtures

Solutions of fluorescent polystyrene nanobeads mixed with 0.1 % TX were used to characterise the flow. The nanobeads are from Duke Scientific, have an average size of 51 nm, emit green light (508 nm) and were mixed to a concentration of 1.4×10^{12} beads/mL.

Fluorescent microbeads were used to predict the behaviour of cells in the chips. For trapping experiments beads with diameters of 5 μm, 10 μm or 15 μm mixed with 0.1 % TX-100 were used. The concentrations were around 300,000 beads/mL, and beads with different sizes were not mixed.

For sorting experiments a wide range of bead sizes were mixed to resemble cell populations. The following fluorescent polystyrene beads were used for experiments: 2 μm blue from Duke Scientific, 5 μm green from Magsphere Inc, 7 μm green from Magsphere Inc, 10 μm orange from Invitrogen, and 15 μm orange from Invitrogen. Bead solutions were prepared by mixing the different beads with 0.1 % TX solutions to a total concentration

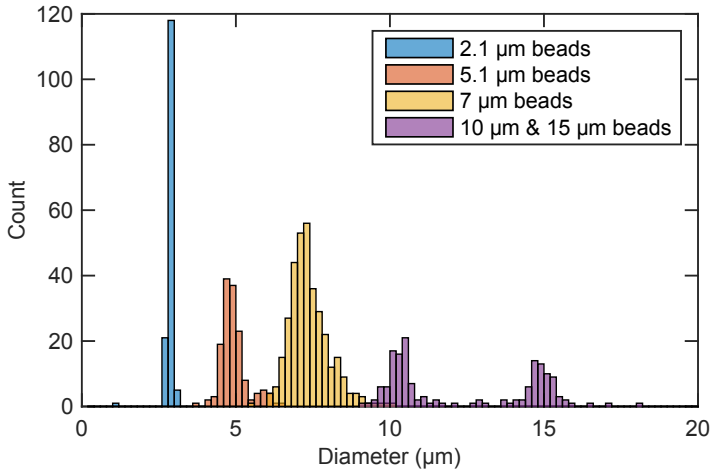

Figure 3.2: Size distribution of the microbead solution used to characterise cell sorting devices.

of 500,000 beads/mL. The solutions consisted of 15 % 2 μm beads, 20 % 5 μm beads, 40 % 7 μm beads, 20 % 10 μm beads and 5 % 15 μm beads. The size distribution of the bead mix is shown in Figure 3.2. The distribution was found by analysing fluorescence images of the bead solution.

Cell samples

The research group at the WIMM provided frozen cancer cells for testing devices at the Nanotech cell lab. In addition the author spent a total of three months in their lab in Oxford, where live cells and blood samples were provided for cell sorting and cell trapping experiments. The following description of how cells were prepared was provided by Dr. Kamila Koprowska from the WIMM.

The human colon adenocarcinoma LS174T cells were obtained from B. H. Tom (Northwestern University Medical Center, Chicago) [10]. The cell line was cultured in complete Dulbecco's Modified Eagle Medium (DMEM; Life Technologies) supplemented with 10 % heat-inactivated fetal bovine serum (FBS; Life Technologies) and 1 % penicillin/streptomycin (Invitrogen). Cells were incubated at 37 °C in a humidified environment at 10 % CO_2 and were grown to 60-80 % confluence before next passage or further experiment.

Blood specimens were drawn from healthy donors after obtaining informed consent. All specimens were collected into BD Vacutainer CPT tubes (Becton Dickinson) containing sodium heparin/Ficoll and were processed within 2 hours according to the manufacturer's protocol. Following centrifugation at 1500 x g (room temperature) for 15 min, the white blood cell suspension was collected, washed twice in PBS (1000 x g, room temperature, 10 min), and finally the cells were suspended in FACSFlow.

For separation measurements, LS174T cells were stained with calcein AM (Molecular Probes) and WBCs with either Hoechst 33342 (Thermo Scientific) or CD45-PE (Becton Dickinson), and subsequently mixed in different ratios.

For tests in the DTU cell lab the cells were frozen at the WIMM and sent to DTU, where the cells were stored at -85 °C. Cells were defrosted and centrifuged at 1200 RPM (room temperature) for 5 minutes. Then the cells were collected and suspended in FACSFlow.

In the first cell trapping experiments colorectal adenocarcinoma DLD-1 cells were used. They were prepared with the same protocol as the LS174T cells, except that they were fixed with formaldehyde after staining. Fixation leaves the cells intact, and fixed cells are more tough than live cells, and easier to work with. It was discovered that live cells were intact after separation and trapping experiments, and it was decided to use live cells for the experiments. Live LS174T cells were used for all experiments unless otherwise stated.

3.4 Software

COMSOL

The finite element simulation software COMSOL Muliphysics version 4.3 was used for all simulations. Channel structures were imported into COMSOL, and to reduce the computational power, semi-3D simulations, as described by Vig and Kristensen [74], were used. This means 2D simulations with a volume force in the opposite direction of the velocity field given by [75]:

$$\mathbf{F} = -\frac{12\eta}{H^2}\mathbf{v}. \tag{3.6}$$

All walls have the no-slip boundary condition, i.e. a velocity of zero, except for the inlet and outlet boundaries, which have varying pressures depending on the experimental conditions.

3D simulations were used to analyse shear stress experienced by cells. To minimise computational power, only parts of the design structures were simulated in 3D. Semi-3D simulations were used to determine the pressures at the beginning and end of the simulated structures and again no-slip boundary conditions were applied to all other wall segments. Obviously no volume force was needed for the 3D simulations.

Water at room temperature was used as the material for all simulations, and it was assumed that particles do not disturb the flow.

Matlab

Matlab version 2015a was used for image analysis and for creating plots and histograms. It was mainly used for analysis of the cell separation experiments. In papers reporting cell separation it is common to count the number of each cell type in the outlets after separation. However the cell sizes are not measured, so it is not known which cells are sorted correctly and which cells are not. This is important to determine how to improve the separation devices, and whether running the samples through the devices a second time should improve the separation. In this thesis the cell sizes were measured by analysing images of cells in the outlets. The script for image analysis incorporates the build-in function “imfindcircles”, which converts grey scale images to binary images and identifies any circles present. It needs a range of radii to look for, a threshold value that determines

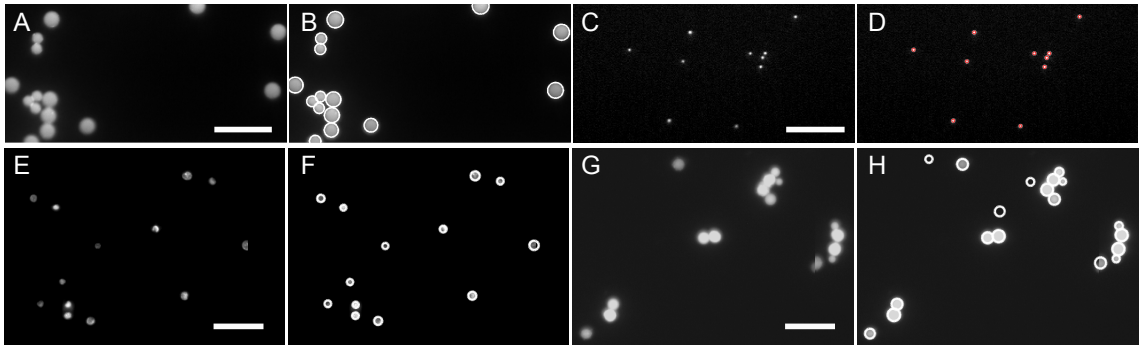

Figure 3.3: Images with and without circular fits done with the Matlab script. (A)-(B) 10 μm and 15 μm beads. (C)-(D) 2 μm beads. (E)-(F) White blood cells. (G)-(H) LS174T cancer cells. The scale bars are 50 μm.

how the image is converted, and a sensitivity value. The function then lists the center coordinates and radius of all the identified circles. Examples of images with fitted circles are seen in Figure 3.3. The size of the 2 μm beads is overestimated to an average of 3 μm because the "imfindcircles" function works better for larger particles. It is seen on Figures 3.3F-G that the cells have varying fluorescent intensities, and therefore the sensitivity value is set relatively high so most cells are found. However this means the function finds circles at positions where no cells are present. All fits were compared to the original image of the cell or bead, and any fits that were not accurate were discarded.

To check that the described image analysis gives accurate and precise cell sizes, the size distributions of cancer cells and WBCs are compared to the size distributions measured with a conventional cell counter, Cellometer® Auto T4 from Nexcelom Bioscience. Size distributions measured with both methods are shown in Figure 3.4. The mean sizes are similar, but larger for the Matlab analysis. It can be seen in Figure 3.4A that the mean size is slightly overestimated because the distribution is uneven. This comes from using the

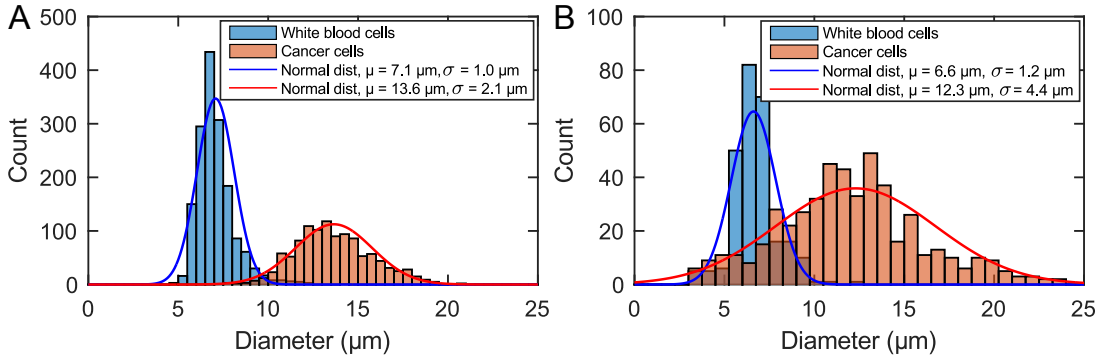

Figure 3.4: (A) Cell size distributions with fitted normal distributions found by image analysis in Matlab. The same graph was shown in Figure 1.2. (B) Cell size distributions with fitted normal distributions measured with a cell counter.

"imfindcircles" function, which needs a range of size to search for, and to avoid finding too many small objects that are not WBCs, the function is set to look for a minimum diameter of 5.2 μm. The size of the WBCs are in the same range in the two histograms, and they are in the expected range. Most of the cancer cells are between 10 μm and 15 μm on both histograms, however the standard deviation is larger for the cell counter measurements. This is likely because it also counts cell debris and it counts cell clumps as one large cell. The size distributions found from the Matlab script look as expected, and with average sizes around the average sizes measured by the cell counter, it can be concluded that the image analysis is both accurate and precise.

The image analysis is used to plot the size distributions of particles in each outlet and to determine the critical diameter, d_c, of the separation measurements. For each particle diameter the probability for going towards the large particle outlet is estimated as the proportion of particles in the large particle outlet. In the ideal case, the estimated probability could be described by a step function jumping from 0 to 1 at d_c, as illustrated in Figure 3.5. However particles with a size close to d_c have a finite probability for going towards either outlet. The reason that the particle separation does not follow the ideal case can be due to different effects such as particles disturbing the flow, particle-particle interactions or unstable flow conditions. The best estimate for d_c is determined as the size where particles have a 0.5 probability of going towards the large particle outlet, and this size is found by fitting the estimated probability to an error function modified to output values between 0 and 1:

$$f(x) = \frac{1}{2}\left(1 + \frac{\mathrm{erf}(a-x)}{b}\right), \qquad \mathrm{erf}(x) = \frac{2}{\sqrt{\pi}}\int_0^x e^{-t^2}\mathrm{d}t, \tag{3.7}$$

where a and b are fitted parameters describing position and slope of the function. The position a is equivalent to d_c. It should be noted that d_c does not depend on the size of the particles, but on the dimensions of the PFF devices. The d_c of a PFF device can only be measured with particles that have a continuous size distribution overlapping with d_c.

Matlab was used to fit the error function in Equation (3.7) to the data. For those who are interested, examples of Matlab scripts for size analysis and determination of critical diameter are found in Appendix D.

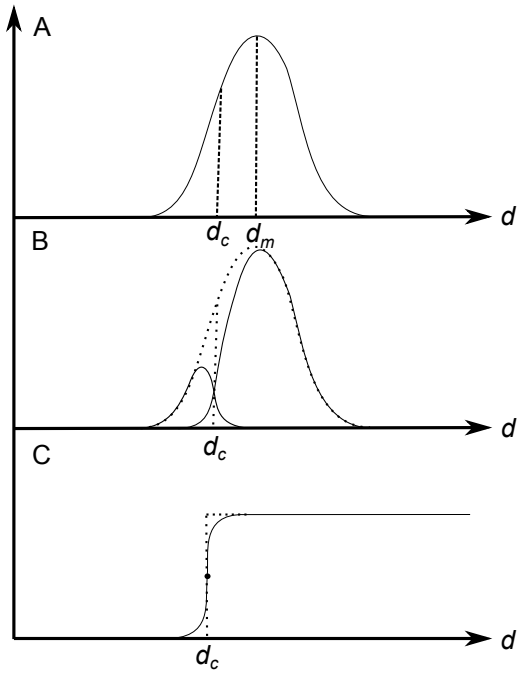

Figure 3.5: Plots illustrating the analytical method for determining the critical diameter of a measurement. (A) Distribution of particles with a mean diameter d_m. (B) Distribution of particles after separation with a critical diameter d_c. The dotted lines illustrate the ideal separation where no particles with a size above d_c go towards the small particle outlet and vice versa. The full lines represent a more realistic separation. (C) The probability for particles of a specific size to go towards the large particle outlet. Dotted lines illustrate the ideal separation, and full lines represent the realistic separation. d_c is estimated as the diameter where 50 % of the particles go towards the large particle outlet (and 50 % go towards the small).

3.5 Chapter summary

The equipment used to characterise the fabricated devices was described, as well as the setups used for the cell separation and trapping experiments. The setups are quite similar, but used for different types of experiments. All nano- and microbead experiments were performed at the Optofluidics lab, initial experiments with cells were performed at a cell lab at Nanotech, and most cell experiments were performed in Oxford, where cancer cells and human blood cells were prepared by members of the lab. The sample and chip preparation methods were also included in this chapter.

The semi-3D and 3D simulations used to predict flow behaviour were also described.

An image analysis method was presented, because to fully characterise the efficiency of size-separation, it is necessary to investigate the diameter of the separated cells. The image analysis can be used to determine the critical diameter of a measurement, and in that way it can be checked that the devices separate cells as intended, and it can be determined how the devices can be optimised to improve the separation efficiency.

4

Cell sorting with Pinched Flow Fractionation

The design, fabrication and testing of PFF devices for cancer cell isolation are described and discussed in this chapter. It includes analytical calculations and general considerations of the design requirements, characterisation of the fabrication process, and a series of experiments with samples varying from nano- or microbeads to white blood cells and cancer cells. Results of cancer cell separation are presented and compared to results gained using other LoC techniques, and potential for commercialisation of the devices is discussed.

Contents

4.1 Goal

The goal of the work carried out for this part of the thesis was to demonstrate that polymer PFF devices can be used for separation of CTCs from blood samples. This requires that at least 1 mL of whole blood can be processed within a reasonable time frame of around 8 hours. RBCs can easily be removed without expensive or user-specialised equipment

leaving the WBCs and the CTCs left to be separated. With approximately 5×10^7 cells to separate in 8 hours, a throughput of 10^5 cells/min. is required. The WBCs are roughly one million times more abundant than the CTCs. Assuming that a ratio of 1:10 CTCs to WBCs is good enough for further analysis of the CTCs, 99.999 % of the WBCs must be removed in a single step. This is practically impossible and had not been achieved at the time this thesis was written. If instead the sample could be run through several PFF devices a removal of over 90 % WBCs and a recovery of over 90 % CTCs should be enough to obtain the desired enrichment. This challenge is addressed in this chapter.

4.2 Design

The overall design space is determined by the 12-Luer platform described in Section 2.4. The microchannels must be placed in the center and lower parts of the chip and be connected to any of the 12 Luer-ports for flow control. The operation of the device should follow the protocol below:

- A cell solution is placed in one of the inlets, and a cell-free buffer solution is placed in another.
- Pressure is applied to both inlets and the cells are forced into the inlet channel and are then moved into a narrow channel, where they meet the buffer solution.
- The cells are pinched against the sidewall in the narrow channel and then follow streamlines to different outlets. Cells with a diameter below the critical diameter, d_c, flow into one of the outlets, and cells with a diameter above d_c flow into another.
- The sorted cells can then be collected from the outlet reservoirs.

This procedure only requires four Luer-ports, however to minimise dilution of the collected cell samples a third outlet which only collects buffer solution is needed. This drain outlet brings the total up to five ports pr. device, and thus with 12 Luer-ports it is possible to put two PFF devices on each chip design. Separation on the PFF chips is sketched in Figure 4.1A, and Figure 4.1B illustrates some important parameters that determine the efficiency of the separation. In the rest of this section, analytical calculations are used to optimise the microfluidic design to obtain the best flow conditions for CTC separation.

4.2.1 Channel dimensions and width of pinched segment

The PFF design only needs one channel layer, so the height was the first dimension to choose. It should be large enough to avoid cell clogging, but not so large that the flow is no longer laminar at pressures up to 1 bar, which is the maximum available pressure. The largest cell aggregates are expected to have a size around 20 μm, therefore 30 μm is the minimum dimension that can be used, to be sure there is no cell clogging. It was decided to use a channel height of 30 μm. The channel lengths have to be in the centimetre range to reach the Luer-ports and were chosen by placing the pinched segment in the middle of the chip and letting the inlet and outlet channels go straight from there to the Luer-ports.

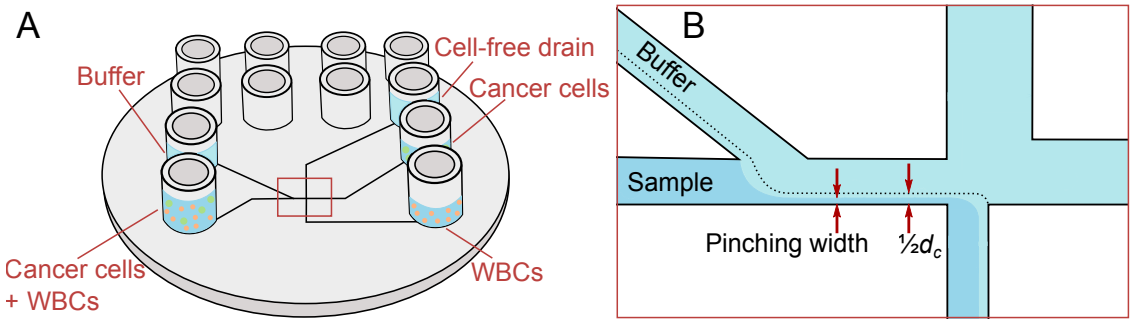

Figure 4.1: (A) Separation on PFF chips. A mix of cancer cells and WBCs is put in one inlet and a buffer in another inlet. The cells are separated and can be collected from the outlets. On outlet ideally contains all WBCs, and one contains all cancer cells. The third outlet drains the buffer fluid and is cell-free. (B) Sketch of the pinched segment, where the separation takes place. The critical diameter, d_c, and the pinching width are marked on the figure. These two important parameters determine the efficiency of the separation. The pinching width is the width of the sample stream in the pinched segment, and it determines whether particles from the sample are aligned or not.

The channel widths were then the only dimensions left to optimise. The pinched segment width is important for the separation. In the first design by Yamada *et al.* [43], the pinched segment was connected to a very broad channel, which amplified the flow and thereby also the position of the aligned particles. They suggested that particle position in the broad segment can be expressed as:

$$y = (W_p - d/2)\frac{W_b}{W_p}, \tag{4.1}$$

where d is the particle diameter and W_p and W_b are the widths of the pinched segment and broad channel, respectively. This is a very crude estimate since they assumed an even flow amplification and neglected the flow rate distribution of the outlet channels. However the tendency that a smaller W_p yields a better spread in particle positions is correct, and W_p should be as small as possible. For smaller W_p, less buffer solution should also be required to obtain full pinching of the particles. The silicon etch used when fabricating the shim is aspect-ratio dependent, and to obtain a homogeneous etch depth, 30 μm is the minimum channel width that can be used. To test these hypotheses two designs were made: Design1 with a W_p of 50 μm and Design2 with a W_p of 30 μm.

4.2.2 Critical diameter

The most important design parameter is the critical diameter. It determines which outlet cells will be sorted into after going through the pinched segment. One of the strengths of PFF is the possibility to change d_c by applying pressure at the outlets, but there are limits to how much it can be changed, so it is advantageous to chose a d_c close the desired value. It can then be optimised with applied pressures afterwards. To determine d_c in any PFF design some basic microfluidic theory is needed.

The two most fundamental equations in microfluidics are the continuity equation and the Navier-Stokes equation. They have been derived elsewhere [75] and will only be briefly described in the following. The continuity equation derives from mass conservation and states that fluid must enter a system with the same rate as it leaves the system. For the velocities and pressures used in LoC systems it can be assumed that the fluids are incompressible and the continuity equation can be written as:

$$0 = \nabla \cdot \mathbf{v}, \tag{4.2}$$

where $\nabla\cdot$ is the divergence and $\mathbf{v}$ is the velocity field.

The Navier-Stokes equation describes the motion of fluids, and is a non-linear partial differential equation. Fortunately it can be simplified by making a few assumptions. Firstly the velocities in most LoC systems are so low that the flow is laminar. Also the system can be assumed to be steady-state, and finally the dimensions of the systems are too small for gravity to have an impact, and no external forces were applied to any of the studied devices. In summary the Navier-Stokes equation for the studied LoC systems can be written,

$$0 = -\boldsymbol{\nabla} p + \eta \nabla^2 \mathbf{v}. \tag{4.3}$$

Here p is the pressure and η is the dynamic fluid viscosity. Thus only viscous effects and applied pressure contributes to the fluid motion. A fluid flow driven by a constant pressure difference in a straight channel results in a constant flow rate described by Hagen-Poiseuille's law,

$$\Delta p = RQ, \tag{4.4}$$

where Δp is the pressure drop across the channel, Q is the volumetric flow rate and R is the hydraulic resistance, which depends on the channel cross section. All studied LoC systems consists of channels with roughly rectangular or square cross sections, which have hydraulic resistances of

$$R \approx \frac{12\eta L}{(1 - 0.63H/W)H^3 W} \quad \text{for} \quad H < W, \qquad\qquad R = \frac{28\eta L}{H^4}, \tag{4.5}$$

respectively. Here L is the length, W is the width, and H is the height of the channel. The total hydraulic resistance of a series of channels is given by the sum of the individual resistances

$$R_{tot} = R_1 + R_2 + ... \tag{4.6}$$

For channels in parallel the inverse total resistance is given by the inverse sum of resistances

$$\frac{1}{R_{tot}} = \frac{1}{R_1} + \frac{1}{R_2} + ... \tag{4.7}$$

Using Equations (4.6) and (4.7) any parts of or the total resistance of a microfluidic system can be calculated.

Next the critical diameter can be calculated by considering the flow rate through the pinched segment, which must equal the sum of flow rates through the outlet channels, according to the continuity equation.

$$Q_{pinched} = Q_{small} + Q_{large} + Q_{drain}. \tag{4.8}$$

To simplify the expression, the flow rates through the large particle outlet and the drain are expressed in terms of the small particle outlet.

$$Q_{pinched} = (1 + \alpha + \beta)\, Q_{small}, \qquad \alpha = \frac{R_{small}}{R_{large}}, \qquad \beta = \frac{R_{small}}{R_{drain}}. \tag{4.9}$$

Yamada *et al.* assumed a constant velocity profile across the channels. However this assumption only holds for large channel aspect ratios, $W/H >> 1$, and not for cross sections with small aspect ratios, which is the case for the narrow pinched segment [76]. Therefore the velocity profile must be taken into account. The velocity of rectangular channels can be found numerically by solving the Navier-Stokes equation with no-slip boundary conditions at the wall ($v = 0$). This yields

$$v_x(y,z) = \frac{4H^2\Delta p}{\pi^3 \eta L} \sum_{n_{odd}}^{\infty} \frac{1}{n^3} \left(1 - \frac{\cosh(n\pi \frac{y}{H})}{\cosh(n\pi \frac{W_p}{2H})} \right) \sin\left(n\pi \frac{z}{H} \right). \tag{4.10}$$

The elements in the sum quickly vanish because of the $1/n^3$ dependency, and only the first three terms were used for calculations. The velocity profile is paraboloid-shaped with a maximum velocity in the channel center and zero velocity at the walls as sketched in Figure 4.2. The flow rates can now be calculated by integrating the velocity profile in the pinched segment across the channel width, W_p (y-direction) and the channel height, H (z-direction), and Equation (4.9) becomes,

$$\int_0^H \mathrm{d}z \int_{-W_p/2}^{W_p/2} \mathrm{d}y\, v_x(y,z) = (1 + \alpha + \beta) \int_0^H \mathrm{d}z \int_{-W_p/2}^{-W_p/2+d_c/2} \mathrm{d}y\, v_x(y,z). \tag{4.11}$$

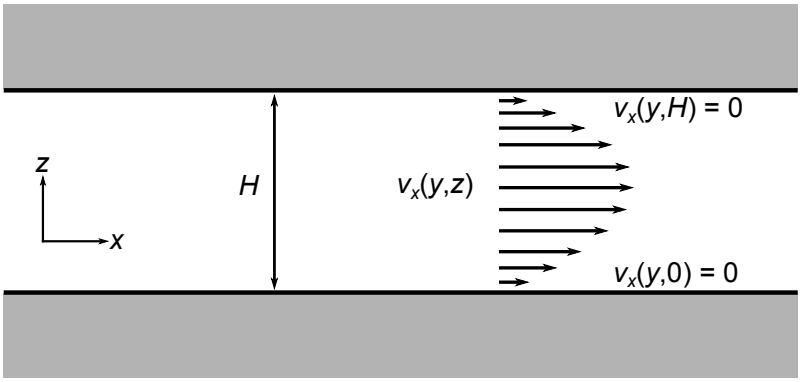

Figure 4.2: Velocity profile in rectangular channels. It has a paraboloid shape and is zero at the walls.

When the expression for velocity is put into Equation (4.11) the constant in front of the sum cancels out, so it is not necessary to know Δp. Note also that d_c appears in the equation. α and β depend on the dimensions of the outlet channels and can be set to yield any desired d_c. Many sets of dimensions can be used to get a specific d_c, some more practical than others. The widths should not be smaller than 30 μm to obtain a homogeneous etch depth, or larger than 1 mm, since that will complicate the shim fabrication, and lid bending during the bonding process will increase. Any widths within this range that result in the desired d_c can be used. It was decided to use the same width for the small particle outlet as the pinched segment width, and then optimise the other outlet widths from there.

To optimise the remaining dimensions a critical diameter must be decided upon. The pore size on filters used for CTC isolation varies from 6.5 μm for the ScreenCell® system [16] to 8 μm for ISET [15], so the optimal d_c is expected to be within that range. It is expected that a design where d_c has to be changed will give the same separation efficiency as a device where d_c was optimised by design. To test this hypothesis the two PFF designs were given different critical diameters: For Design1 it is approx. 13 μm, and for Design2 it is approx. 8 μm.

There is also a critical diameter between the large outlet and the drain, which determines the maximum size particles can have before they will flow towards the drain. This can be calculated similarly to the above calculations by considering the flow rate through the drain outlet instead of the small particle outlet. The final design parameters and calculated parameter of both designs are listed in Table 4.1.

For Design2 d_{cL} is possibly smaller than the largest cancer cells and a small additional pressure on the drain outlet might be necessary to make sure no cells flow towards the drain.

Table 4.1: Design variations in pinched segment width (W_p), ratios between hydraulic resistance of the three outlet channels (α, β), the resulting critical diameter (d_c), large critical diameter (d_cL) and total hydraulic resistance (R_{tot}).

	H [μm]	W_p [μm]	α	β	$\mathbf{d_c}$ [μm]	d_{cL} [μm]	R_{tot} [kg m^{-4}s^{-1}]
Design1	30	50	1.9	14.4	**13.1**	25.0	4.0×10^{13}
Design2	30	30	1.9	14.4	**8.3**	15.2	6.8×10^{13}

4.2.3 Validation of the laminar flow assumption

All of the above calculations are only valid as long as the flow is laminar, meaning that the fluid moves in parallel layers that never mix. The flow is laminar if viscous forces dominates over inertial forces, and the ratio between them is determined by the dimensionless Reynolds number [75]:

$$Re = \frac{\rho v L}{\eta}. \tag{4.12}$$

Here ρ is the density of the fluid, v is a characteristic velocity and L is a characteristic length of the system. For rectangular channels the characteristic length can be approximated

by the smallest dimension, i.e. the channel height. The velocity can be found using Hagen-Poiseuille's law with the maximum pressure that can be applied (1 bar) and the total resistance of the device, and then dividing the flow rate with a channel cross-sectional area. Here the cross section of the pinched segment in Design1 is used, because it has the highest velocities on the device. The velocities in Device2 are similar to the velocities in Device1.

$$Q = \frac{\Delta p}{R} = \frac{10^5\,\mathrm{Pa}}{4 \times 10^{13}\,\mathrm{kg\,m^{-4}s^{-1}}} = 2.5 \times 10^{-9}\,\mathrm{m^3/s}, \tag{4.13}$$

$$v = \frac{Q}{A} = \frac{2 \times 10^{-9}\,\mathrm{m^3/s}}{30\,\mu\mathrm{m} \times 50\,\mu\mathrm{m}} \approx 1.67\,\mathrm{m/s}. \tag{4.14}$$

The resulting Reynolds number is:

$$Re = \frac{1000\,\mathrm{kg/m^3} \times 1.67\,\mathrm{m/s} \times 30\,\mu\mathrm{m}}{10^{-3}\,\mathrm{Pa\,s}} = 50. \tag{4.15}$$

The maximum Reynolds number indicates that inertial forces cannot be completely neglected, but it is well below the critical Reynolds number of 2300, which determines when the fluid flow transitions from laminar to turbulent [77]. It is therefore reasonable to assume that the flow is laminar even at the maximum applied pressures.

4.2.4 Particles in the system

Particle behaviour is much more complicated to predict than fluid behaviour, because particles can interact with each other and the channel walls. However some tools that describes particle behaviour exist. One of these is the particle Reynolds number (Re_p), which describes particle momentum compared to viscous forces of the surrounding fluid. If Re_p is large, the particles will have enough momentum to escape the flow trajectories when they experience a rapid change [78]. The particle Reynolds number is calculated by:

$$Re_p = Re\frac{d^2}{D_h^2} = 50\frac{(10\,\mu\mathrm{m})^2}{(30\,\mu\mathrm{m})^2} \approx 5.6. \tag{4.16}$$

Here d is the particle diameter set to 10 μm, and D_h is the hydraulic diameter, which can be approximated by the channel height for rectangular channels with low aspect ratios. Whether this number is high enough for particles to deflect, depends on how rapid a change the particles experience, but it indicates that particles can deflect from the fluid trajectories when using the high end of the pressure range.

Another dimensionless number is the particle Peclet number (Pe_p), which describes whether particle motion will be dominated by diffusion or convection. It is obviously preferred that diffusion has no influence at all, since it will ruin the particle alignment in the pinched segment and thereby also the separation. It is not expected that diffusion has an influence when using the highest pressures, but when testing the devices and optimising the pressures it is more practical to use lower pressures. To check that the separation

works at lower flow rates Pe_p is calculated for velocities of 16.7 mm/s equivalent to 10 mbar pressure at the inlets.

$$Pe_p = \frac{vD_h}{D}, \qquad D = \frac{k_B T}{3\pi\eta d} \approx 4.4 \times 10^{-14}\,\mathrm{m^2/s}, \tag{4.17}$$

$$Pe_p = \frac{0.0167\,\mathrm{m/s} \times 30\,\mu\mathrm{m}}{4.4 \times 10^{-14}\,\mathrm{m^2/s}} \approx 1.1 \times 10^6. \tag{4.18}$$

D is the diffusion constant calculated by the Stokes-Einstein equation. The high Pe_p means that particle diffusion is much slower than convection, and should not influence the separation, as expected.

Cells have a density about 7 % higher than that of water [2], and will therefore slowly settle at the bottom of the channels and reservoirs. Assuming that there is a steady flow, the cells will fall with a velocity given by [79]:

$$v_0 = \frac{gd^2(\rho_c - \rho)}{18\eta} = \frac{9.8\,\mathrm{m/s^2}(10\,\mu\mathrm{m})^2(1070\,\mathrm{kg/m^3} - 1000\,\mathrm{kg/m^3})}{18 \times 10^{-3}\,\mathrm{Pa\,s}} \approx 3.8\,\mu\mathrm{m/s}. \tag{4.19}$$

where ρ_c is the density of the cell and g is the gravitational constant. Assuming that a 10 μm cell enters at a middle height of the inlet channel, it drops to the bottom of the channel in less than three seconds. This is not expected to be a problem as long as the cells are moving they should not stick to the bottom of the chips. In the reservoirs however, the cells far away from the the inlet or outlet channels are not moved and can sediment on the bottom. The reservoirs are about 1 cm high, so all cells will have settled within 45 min. This is not a problem for the experiments described in this thesis, as the cells were investigated directly in the outlets. However, in experiments where a minimal cell loss is important, the sample must be rapidly processed and continuously be removed from the outlets during separation.

4.2.5 Design layout

All channel dimensions were optimised, and it was confirmed that the requirements for separation were met with the flow conditions allowed by the setup. The final layout of Design1 and Design2 is shown in Figure 4.3. Note that the designs were placed on two different shims.

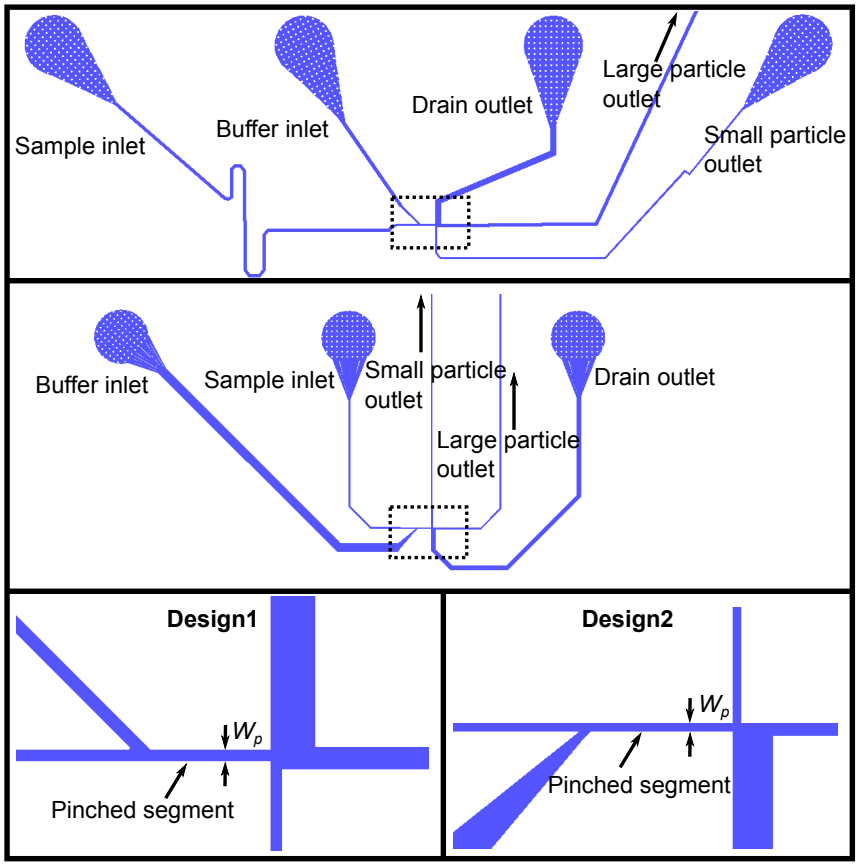

Figure 4.3: Channel structures on the cell sorting design. The device at the top shows Design1 and the middle device is Design2. Zoom-ins at the positions marked by the dotted squares are placed at the bottom and show the pinched segment, where the particle separation takes place.

4.3 Chip fabrication

SEM images of the shims are shown in Figure 4.4. The first thing to notice is that the Design1 shim is very rough. It has previously been observed that leaving a nickel shim in KOH etch for too long will result in a rough surface, as the KOH damages the vanadium in the nickel/vanadium seed layer [62]. This is likely what happened to the Design1 shim. The shim surface was investigated with an optical profiler, and a measurement is seen in Figure 4.5 together with an image of the shim, where the rough structures are clearly visible. The surface roughness might make it more likely for cells to stick to the channel walls, but otherwise it is not expected to influence the flow or the separation efficiency. Both shims have a height of approx. 30 μm. Height measurements of the Design2 shim can be seen in Appendix C.

The Design1 chips were injection moulded with Recipe 1 and bonded to 500 μm lids at the standard parameters. Images at the pinched segment of chips after bonding are seen in Figure 4.6, and they show that the roughness of the shim was transferred onto the chips.

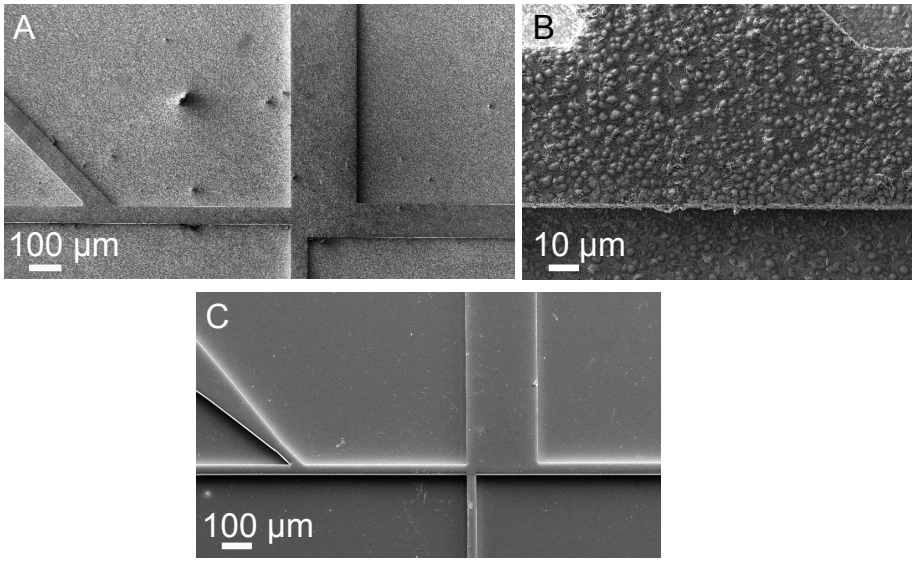

Figure 4.4: (A) SEM image of the Design1 shim at the pinched segment. (B) Zoom-in on the rough structures. (C) SEM image of the Design2 shim.

They are also rough at the bottom of the channels, but it cannot be seen on the images because the bottom is out of focus. The Design2 chips were injection moulded with Recipe 2 and had some stress marks, but with the standard parameters it was possible to obtain a tight bonding. The stress marks are not expected to have an influence on the efficiency of the chips.

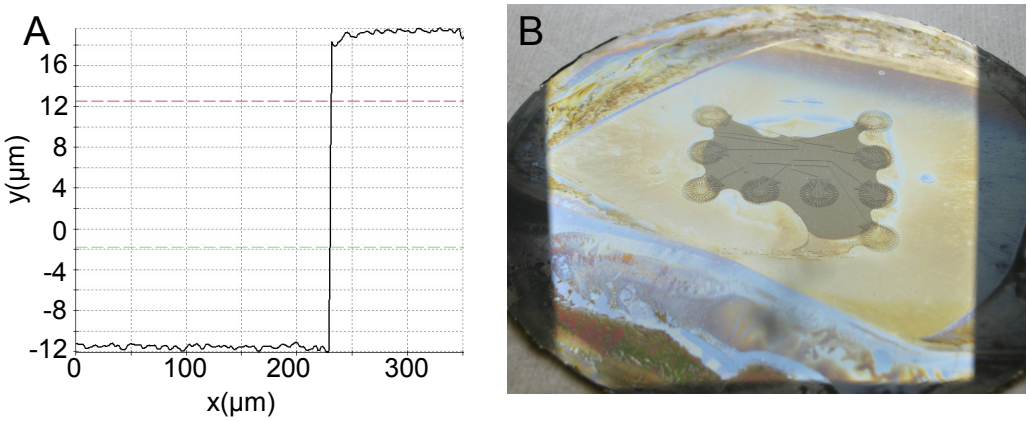

Figure 4.5: (A) Height profile of the Design1 shim showing the surface roughness. The structures vary with approx. 1 μm. (B) Photo of the shim. The rough structures are at the dark spot in the center of the shim and covers all channels.

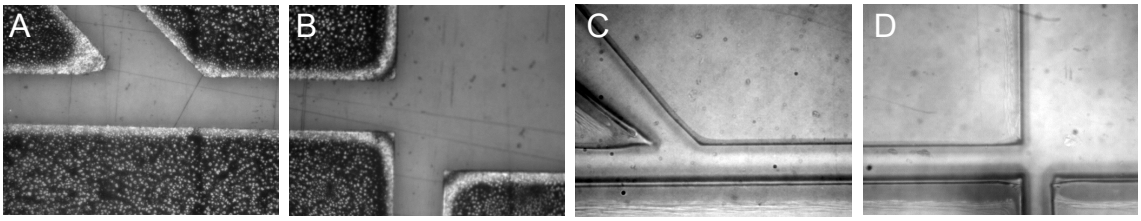

Figure 4.6: (A)-(B) Design1 chip after bonding. The roughness of the shim has been tranferred to the chips. The structures are not completely filled and therefore the lid is not in contact with the structures at the edges, especially at the corners. (C)-(D) Design2 chip after bonding. Stress marks are seen on the bottom and left side of the channels with the shown orientation. The stress marks did not affect the bonding quiality.

4.4 Experiments

This section covers the results of experiments with separation of cancer cells and WBCs. Before these experiments the PFF devices were tested with micro- and nanobeads to characterise the flow at various applied pressures, and to find the optimal pressures and flow conditions.

4.4.1 Pinching width

The first criteria for a successful separation is that the particles are aligned or pinched in the pinched segment. Particles are pinched if the width of the sample fluid in the pinched segment is smaller than or equal to the radius of the particles. The width of the sample fluid in the pinched segment is called the pinching width, and it was measured by placing a fluorescent nanobead solution in the sample inlet and a 0.1 % TX solution in the buffer inlet. Then long exposure images of the pinched segment were taken for different pressures. Images from the experiments are seen in Figure 4.7. The pressure at the buffer inlet was held at a constant value, while the pressure at the sample inlet was varied. The signal from the nanobeads can be approximated by a normal distribution, as seen in Figure 4.8A. The signal was fitted using a Matlab script, which outputs three values: the mean position of the beads, the standard deviation of the positions and a scaling factor. One way to estimate the pinching width is to calculate the full width at half maximum (FWHM) of the signal. However the nanobeads diffuse into the buffer stream, so the signal and FWHM decreases as the beads move along the pinched segment, as seen in Figure 4.8B. Also the field of depth at 30X magnification is smaller than the channel height, so a lot of the beads will be out of focus and thus contribute to a larger FWHM. Instead the pinching width was estimated as the distance from the pinched segment wall to the bead position with maximum intensity. A bright field image was used to find the position of the wall. The positions of the wall and of the maximum intensity of the nanobeads were found for 10 lines at a time in the area below the red dashed line in Figure 4.7.

The average distance to the wall versus the pressure ratio P_{Buffer}/P_{Sample} is plotted for both PFF designs in Figure 4.8C-D. Because the pinching width is estimated by the distance from the wall to the center of the intensity peak, the pinching width is probably

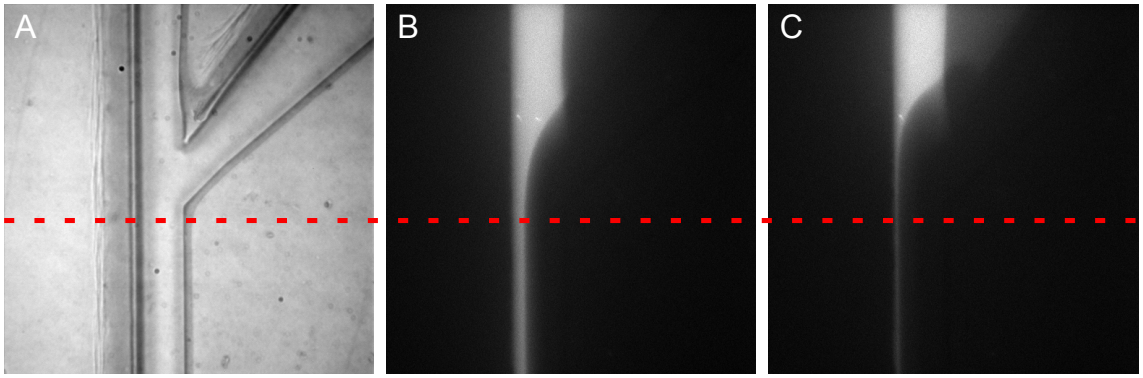

Figure 4.7: (A) Reference image of a Design2 chip used to find the position of the left wall in the pinched segment. (B) Fluorescence image of nanobeads at applied pressures of $P_{Buffer} = 100\,\text{mbar}$ and $P_{Sample} = 80\,\text{mbar}$. (C) Nanobeads at pressures of $P_{Buffer} = 100\,\text{mbar}$ and $P_{Sample} = 68\,\text{mbar}$. Measurements were performed in the area from the red dotted line to the bottom of the images. All images were taken with a 30X magnification and an exposure time of one second.

underestimated, but as the nanobeads diffuse into the buffer stream, the distribution shifts away from the wall, and the estimate might not be too crude.

The two designs need different sets of applied pressures, and a smaller pinching can be achieved with Design2, because the pinched segment is more narrow. Small pinching widths are an advantage because alignment of small particles is obtained and small variations in the applied pressures will not ruin the alignment. However the smaller the pinching width is, the smaller is the sample flow rate compared to the buffer flow rate. When choosing the pressures to operate the PFF devices a compromise must therefore be made between good particle alignment and high sample flow rates. Since the ideal critical diameter for CTC separation is between $6.5\,\mu\text{m}$ and $8\,\mu\text{m}$, it is sufficient with a pinching width of $3\,\mu\text{m}$ to $4\,\mu\text{m}$, which can be obtained with both designs. The maximum sample flow rates are found later in this chapter.

To test whether the measured pinching width depends on the fluid velocity, for example because of inertial effect on the nanobeads, the experiments were performed for two different buffer inlet pressures in a Design1 chip, as seen in fig. 4.8C. The pinching widths at the lower pressure are not significantly smaller than at the high pressure. This was expected from the low particle Reynolds number, which is even lower for nanobeads, and thus the measurements were not affected by flow velocities.

4.4.2 Critical diameter

The conditions for pinching have been established, next the critical diameter, d_c, needs to be measured and optimized. This was done with microbead solutions, because they are easier and less expensive to work with than cells. Previously, bead separation has mostly been demonstrated on solutions containing two bead types that do not overlap in size. These simple solutions do not represent biological samples very well and cannot be used to determine the critical diameter of a device. The bead solution used to determine d_c is a

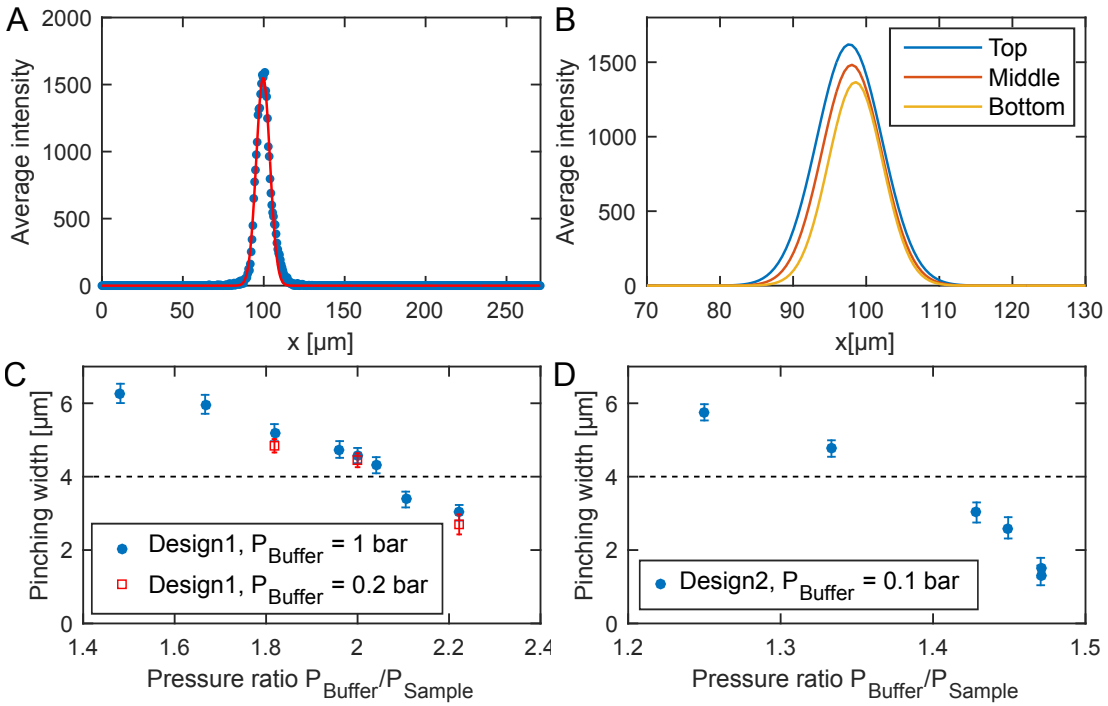

Figure 4.8: (A) Measured average intensity of nanobeads fitted to a normal distribution. (B) Fitted normal distributions at the top, middle and bottom of the same nanobead measurement. The distribution slowly moves away from the wall. (C) Measured pinching width in Design1 at two buffer inlet pressures. (D) Measured pinching width for Design2. The errorbars represent the standard deviation. The pinching width should be below the dotted lines to obtain sufficient pinching.

blend of fluorescent polymer beads with diameters from 2 μm to 15 μm, as described in Section 3.3. The size distribution of the beads is continuous, creating a good model system to determine d_c over a large range of values.

To conduct the experiments, bead solutions with a concentration of 500,000 beads/mL were pipetted into the sample inlet and pushed through the device. The experiments were monitored to check that the solution was pinched and the experiments were run until at least 1000 beads had been sorted. This is equivalent to 2 μL sample. The setup allows processing of larger samples, however, this would prevent optical visualisation of the beads in the outlets. The experiments were operated with pressures of $P_{Buffer} = 500$ mbar, $P_{Sample} = 240$ mbar and $P_{Drain} = 0$ mbar for Design1 and $P_{Buffer} = 100$ mbar, $P_{Sample} = 68$ mbar and $P_{Drain} = 0$ mbar for Design2. This is equivalent to pinching widths of approx. 3.4 μm and 1.5 μm respectively. After experiments, fluorescence images were taken of all beads in the outlets, and their size was measured using a Matlab script, as described in Section 3.4. The critical diameter was found by measuring the fraction of beads going towards the large particle outlet for each bead size, and fitting with an error function. Figure 4.9 shows the results of separation experiments on both PFF designs. The 2 μm beads were not included

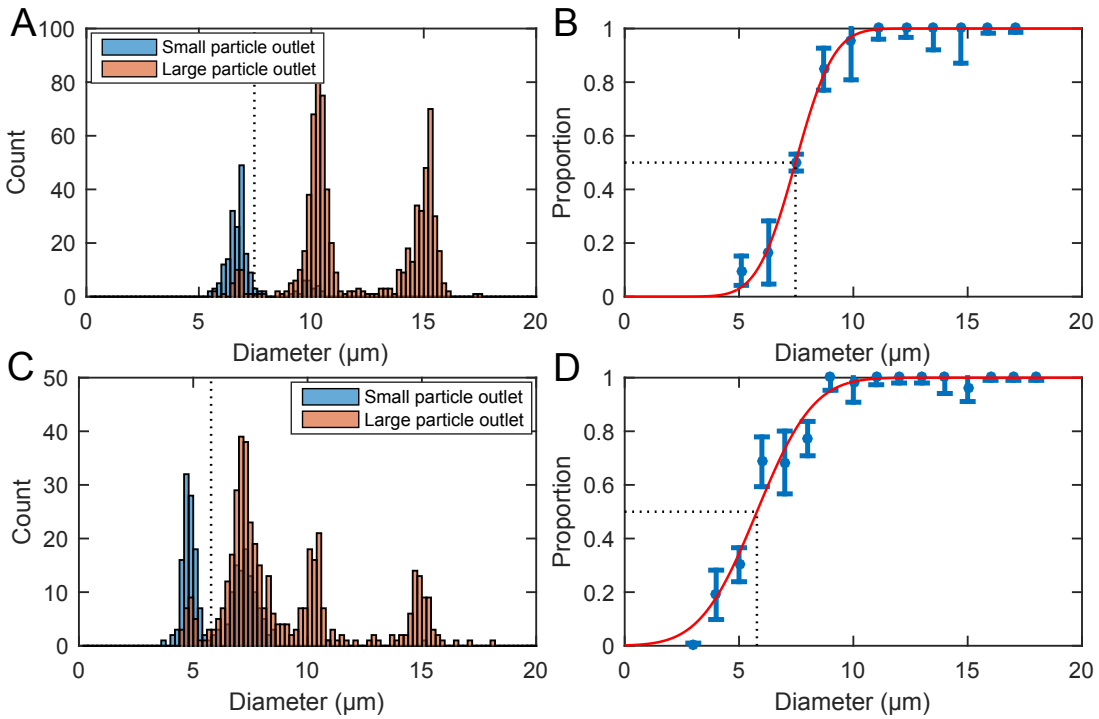

Figure 4.9: Critical diameter measurements with polymer beads. (A) Histogram with size distribution of beads in the small and large particle outlet on a Design1 chip. (B) Proportion of beads in the large particle outlet plotted as a function of size with a fitted error function. The measured critical diameter, marked by the black dashed lines, is 7.6 μm $\pm$ 0.4 μm. (C) Histogram with size distributions of beads in a Design2 chip. (D) Proportion of beads in the large particle outlet plotted as a function of size with a fitted error function. The measured critical diameter is 5.8 μm $\pm$ 0.3 μm.

because they were not fully pinched during the separation, and their size is not accurately measured.

The data fits well to the error function, and the analysis method results in d_c's of 7.6 μm and 5.8 μm for Design1 and 2, respectively. These values are much smaller than expected. The size distribution in Figure 4.9A shows that the majority of 7 μm beads are collected in the small particle outlet, while the majority of 10 μm beads are collected in the large particle outlet. It is therefore reasonable that the d_c of the Design1 chips is in the range 7 μm to 10 μm, as measured. Similarly it is seen in Figure 4.9C that most 5 μm beads went towards the small particle outlet and most 7 μm beads went towards the large particle outlet, which makes a d_c of 5.8 μm reasonable for Design2.

The bead measurements show that the critical diameter is different than the calculated value. The displacement of beads due to an effect at the end of the pinched segment described by Vig and Kristensen [74] could explain this inconsistency. Using semi-3D simulations they showed that at the corner at the end of the pinched segment, streamlines are squeezed closer to the wall than in the pinched segment. This corner effect forces

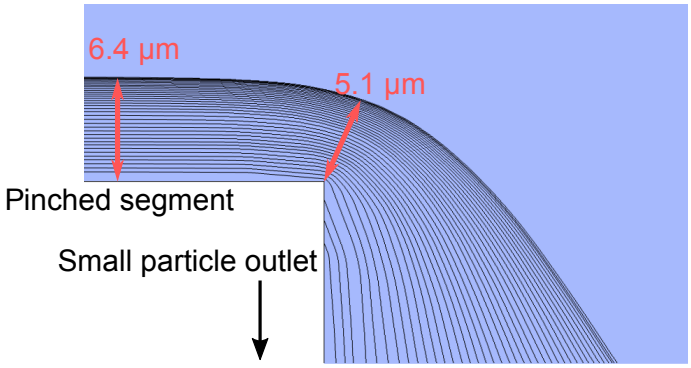

Figure 4.10: Illustration of the corner effect showing a semi-3D simulation of streamlines going towards the small particle outlet in a Design1 chip. The outermost streamline has a distance to the pinched segment wall of 6.4 μm, equivalent to a d_c of 12.8 μm. At the corner of the pinched segment the streamlines are squeezed closer together and the distance is decreased to 5.1 μm, or a modified d_c of 10.2 μm. This phenomenon is called the corner effect.

particles to follow streamlines further away from the wall, and will decrease the critical diameter. Semi-3D simulations of the designs were performed with boundary conditions at the inlets and outlets set to the applied pressures. A modified d_c was found by measuring the shortest distance from the wall to the outermost streamline going into the small particle outlet, as shown in Figure 4.10. The distance from the pinched segment wall to the outer streamline was measured as 6.4 μm, corresponding to a d_c of 12.8 μm for Design1, which is close to the value of 13 μm found from the calculations. The smallest distance from the corner to the outer streamline was 5.1 μm, corresponding to a d_c of 10.2 μm. The critical diameter between the large particle outlet and the drain is not affected by any corner effects and is 24.4 μm according to the simulations, close to the 25 μm predicted by the analytical calculations. No beads went towards the large particle outlet, so the large d_c could not be measured with the bead solution.

The same simulation was carried out on Design2, and the simulated critical diameters are summarized in Table 4.2, together with the critical diameters calculated from the geometry of the designs, and the critical diameters found with bead experiments.

The corner effect accounts for some of the difference between calculated and measured

Table 4.2: Calculated, measured and simulated critical diameter of the two PFF designs. The calculations are based on channel dimensions, the measured sizes are based on bead experiments, and the simulated values are based on semi-3D simulations, where the corner effect has been taken into account.

	Calculated d_c [μm]	Measured d_c [μm]	Simulated d_c [μm]
Design1	13.1	7.6 $\pm$ 0.4	10.2
Design2	8.3	5.8 $\pm$ 0.3	7.7

d_c, but not all. Another contributing effect could be inertial forces deflecting the particles from the streamlines shown in Figure 4.10. However the measurements were not performed at the maximum available pressures, so the particle Reynolds number would be less than the 5.6 calculated in Section 4.2.4. Other influences on the critical diameter could be particle disturbances of the flow, for example smaller beads following larger beads to the large particle outlet. The results indicate that the theoretical calculations and the simulations cannot accurately determine the critical diameter of PFF devices without expanding them to also include considerations of how particles behave and interact, which is very complicated.

The greatest advantage of PFF is that the critical diameter can be changed by applying pressure to the outlets. Using the presented image analysis method, microliter-sized bead samples can be used to find the optimal pressures, before experimenting on valuable cell samples. The Design2 devices have a critical diameter that is too small for separation of CTCs and WBCs. It can be increased by applying a pressure at the large particle outlet or the drain. Since the large critical diameter between the large outlet and the drain is only around 15 μm it was decided to apply pressure at the drain to increase both critical diameters. It was found that a pressure of 40 % of the buffer inlet pressure was suitable such that d_c is 8 μm. The Design1 devices coincidentally have a critical diameter in the expected optimal range for cancer cell separation and do not need additional applied pressures.

4.4.3 Flow rates

It is important to know the expected sample and buffer flow rates for different applied pressures, because the sample flow rate should be as high as possible to separate CTCs from clinical samples. Also it is impractical to process large amounts of buffer fluid to obtain a small pinching width. Flow rates and dilution was estimated with the same semi-3D simulations used to investigate the corner effect.

The sample flow rate, Q_{Sample}, was found for different inlet pressure ratios P_{Buffer}/P_{Sample} equivalent to pinching widths around 3 μm as seen in Figure 4.8. The simulated sample flow rates are plotted in Figure 4.11A for both devices. The ratio of buffer solution over sample solution, Q_{Buffer}/Q_{Sample}, was also simulated and is plotted in Figure 4.11B. Both simulations were carried out for $P_{Buffer} = 100$ mbar. The sample flow rate varies linearly with the applied pressure, so the flow rate can easily be calculated for higher pressures as long as the pressure ratios are constant. It is seen that the sample flow rate varies drastically as P_{Buffer}/P_{Sample} is changed, especially for Design2 devices. There is in fact only 1 mbar difference in sample inlet pressures between each data point on Figure 4.11A. It is therefore advantageous to operate the devices at higher pressures where small pressure differences have a smaller effect. It is seen in Figure 4.11 that the amount of buffer fluid needed to pinch the particles increases drastically for higher inlet pressure ratios and thus for smaller pinching widths. This is because Q_{Sample} is directly proportional to P_{Sample} and Q_{Buffer} is directly proportional to $1/P_{Sample}$, and thus the ratio Q_{Buffer}/Q_{Sample} varies as $1/(P_{Sample})^2$, assuming a constant P_{Buffer}.

It is clear that when choosing the pressures for separation experiments there is a

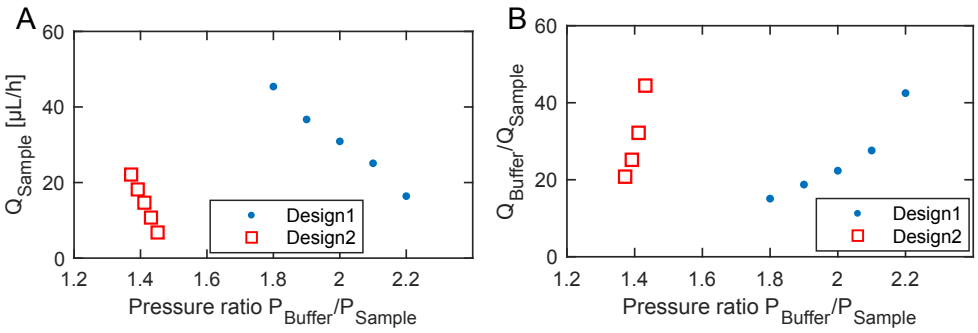

Figure 4.11: Simulations of flow rates in both PFF devices. (A) Sample flow rate at varying inlet pressure ratios. (B) Flow rate ratios at varying inlet pressure ratios.

compromise between small pinching width and sample flow rate. For CTC separation large samples must be processed and it is not practical to have to also process up to 50 times more buffer fluid than sample. Therefore the pinching width have to be chosen as the maximum possible, where small particles cannot flow towards the large particle outlet. It is also advantageous to use large pressures, both to get a higher sample throughput, and to obtain a more stable flow, which does not vary greatly with 1 mbar pressure changes, as that is the uncertainty of the flow controller. According to the simulations the highest sample flow rate that can be obtained while maintaining a pinching width below 4 μm (half the critical diameter), is 250 μL/h for the Design1 devices. Under these conditions, 28 times the amount of buffer solution is needed.

In the previous section it was discovered that the Design2 devices have to be operated with a pressure at the drain equivalent to 40 % of the buffer inlet pressure. This does not change the overall behaviour of the flow, but it does influence the exact flow rates. The highest sample flow rate with sufficient pinching is 200 μL/h for the Design2 devices. Under these conditions, 16 times the amount of buffer solution is needed. It is lower than for Design1 because the smaller pinched segment width decreases the amount of buffer needed to pinch the particles, as expected.

In summary, it is advantageous to use high applied pressure, because it will make the flow more stable. The maximum flow rate that can be achieved with the PFF designs is 200 μL/h to 250 μL/h. The Design2 devices need less buffer solution than the Design1 devices.

For all experiments in the following section the sample flow rates will be provided based on these simulations.

4.4.4 Cancer cell separation

All experiments on cancer cell separation were performed by the author at the WIMM in Oxford. Design1 chips were used to separate WBCs and cancer cells. The cancer cells and WBCs were mixed at a ratio of 1:3 to a total concentration of 400,000 cells/mL. The devices were initially run with a sample flow rate of 10 μL/h and they were monitored during the separation to ensure that the cells were pinched. The d_c was not adjusted with

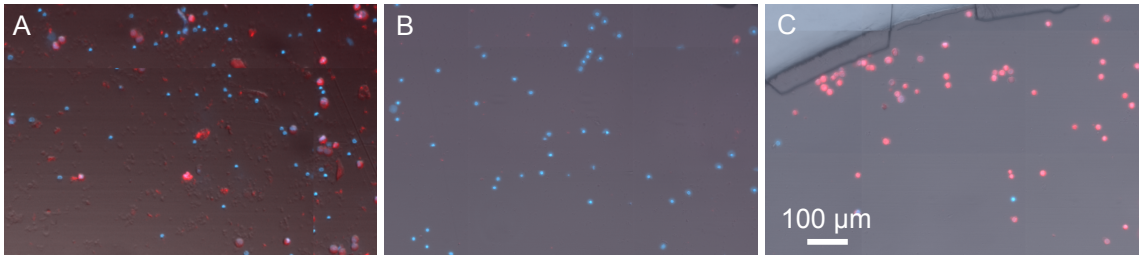

Figure 4.12: Combined fluorescence and bright field images of white blood cells and cancer cells before and after separation in a Design1 chip. The images were taken with a 20X magnification. (A) Mix of cells before separation. The blue cells are WBCs and the red cells are cancer cells. (B) Cells in the small particle outlet. (C) Cells in the large particle outlet.

additional pressures since it was measured to be 7.6 μm with polymer beads, which is within the expected optimal range. After separation the outlets were visualised with both bright field and fluorescence images, so the cell types could be distinguished. Images of cells on a chip before and after separation are shown in Figure 4.12. The cells were counted and their sizes were measured using the previously described image analysis method. The critical diameter was then determined for each cell type, and the results are shown in Figure 4.13A-D. The first observation is that the d_c measured with cancer cells is 7.9 μm,

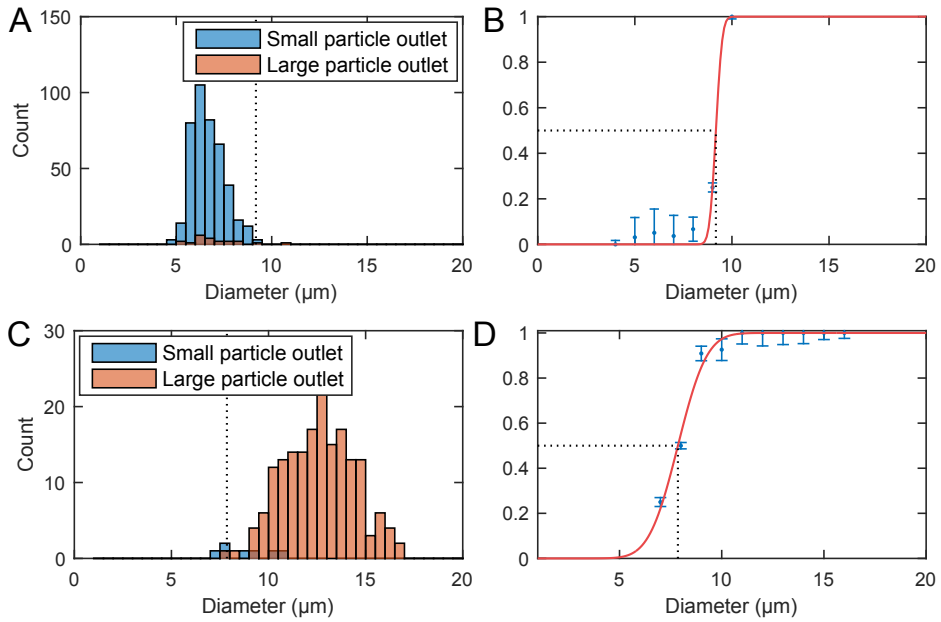

Figure 4.13: Separation of WBCs and LS174T cancer cells in a Design1 chip at 10 μL/h. (A-B) Size distribution of WBCs in each outlet after separation and corresponding critical diameter analysis. The critical diameter is marked by a black dashed line and reads 9.2 $\pm$ 2.1 μm. (C-D) Size distribution of cancer cells in each outlet after separation and corresponding critical diameter analysis. The critical diameter is marked by a black dashed line and reads 7.9 $\pm$ 0.15 μm. The recovery was 96.0 % for cancer cells with a 93.6 % removal of WBCs.

similar to the one measured with polymer beads. However, d_c measured with WBCs is 9.2 μm. This difference in critical diameter is an advantage and resulted in a recovery of 96.0 % cancer cells together with a removal of 93.6 % WBCs. This is a good separation, however, the experiment was performed at a sample flow rate of 10μL/h, which is too low for applications where larger amounts of sample must be sorted.

The effect of increased flow rates on the recovery and removal of cells was investigated. The results from a series of experiments on Design1 devices are seen in Figure 4.14A. The CTC recovery is independent of flow rates, however the WBC removal drops rapidly as the flow rate is increased. It is intuitive that a decrease in critical diameter must have lead to the lower WBCs removals, and this is verified in Figure 4.14B, where the critical diameter at the different WBC removals is plotted. The critical diameter is smaller for the low WBC removal measurements. A possible reason for the decrease in critical diameter is that the inertia of the WBCs increase with increasing flow rates, and eventually becomes large enough to deflect them from their initial trajectories. The particle Reynolds number is above 1 for the high flow rate measurements, and as larger particles have a higher inertia only the smallest WBCs would go towards the small particle outlet. This explains the lower critical diameter. It also explains why cancer cell recovery is unaffected, since the cancer cells move along straight trajectories into the large particle outlet, they are not affected by inertia. The critical diameter of the cancer cells at different recoveries is plotted in Figure 4.14C, and it is seen that the critical diameter is constant around 8 μm.

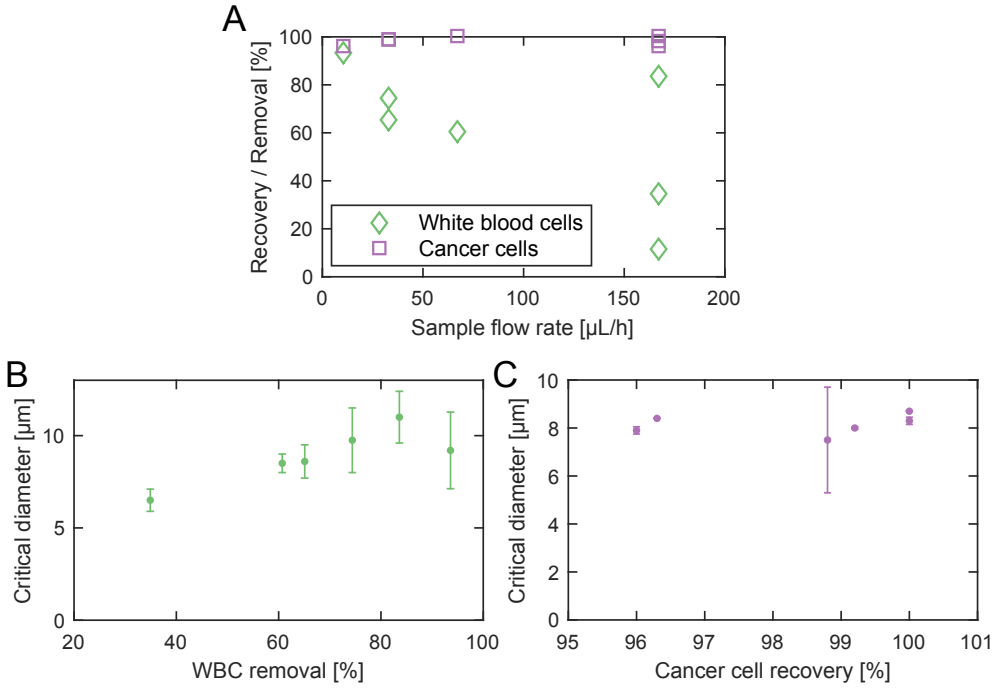

Figure 4.14: (A) Recovery of cancer cells and removal of WBCs at different sample flow rates in Design1 chips. (B) Critical diameter at different WBC removals. (C) Critical diameter vs. cancer cell recovery.

The Design2 chips were also tested with WBC samples spiked with cancer cells to test the hypothesis that the critical diameter of PFF devices can be adjusted without loss of separation efficiency. The samples were mixed 1:1 and a sample flow rate of 50 μL/h was used. The critical diameter was adjusted by applying a pressure at the drain outlet. The results are shown in Figure 4.15A-D.

The measured recovery and removal are 91.4 % and 89.7 % respectively, which is higher than to the values measured for the unadjusted Design1 devices at 50 μL/h, see Figure 4.14A. Thus PFF devices with an arbitrary critical diameter can be tuned to fit the separation of a specific sample without loss of separation efficiency.

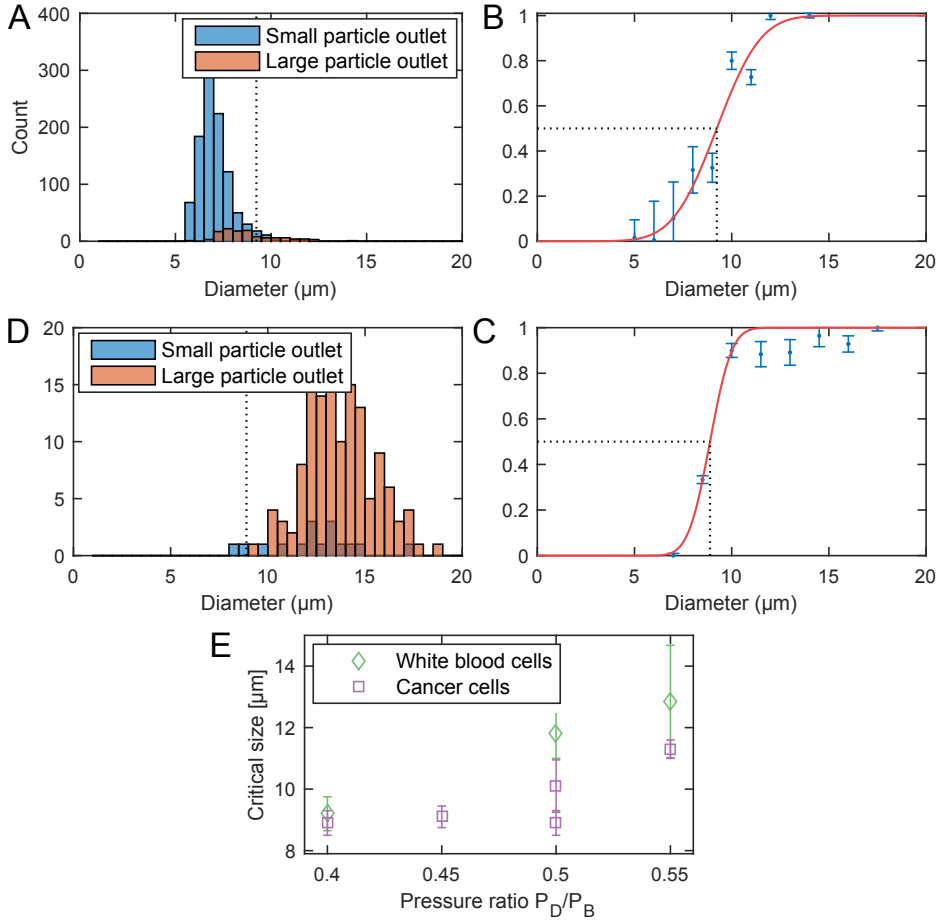

Figure 4.15: Separation of WBCs and LS174T cancer cells using Design2 chips at 50 μL/h. (A-B) Size distribution of WBCs in each outlet after separation, and corresponding critical diameter plot. The critical diameter is marked by a black dashed line and reads 9.2 $\pm$ 0.55 μm. (C-D) Size distribution of cancer cells in each outlet after separation, and corresponding critical diameter plot. The critical diameter is marked by a black dashed line and reads 8.9 $\pm$ 0.4 μm. The recovery was 91.4 % for cancer cells with a removal of 89.7 % WBCs. (E) Measured critical diameter of cancer cells and WBCs for different pressure ratios between the buffer inlet and the drain.

A difference in measured d_c between cell types was again observed as seen in Figure 4.15E. Here the critical diameter of each cell type is plotted for experiments where the pressure on the drain was changed relative to the pressure on the buffer inlet. As expected the critical diameter for both cell types increases with an increasing pressure on the drain, and the critical diameter of the WBCs stays above the critical diameter of the cancer cells, thus ensuring a high separation efficiency. The difference in critical diameter is an advantage and is exploited to get a better separation of WBCs and cancer cells than reported for most of the other passive LoC techniques, which are compared in Table 1.1.

These experiments were performed with cancer cells and WBCs mixed 1:1 - 1:3. To demonstrate that the separation also works for lower cancer cell to WBC ratios an experiment was performed on a sample mixed 1:50 to a total concentration of 700,000 cells/mL. The experiment was performed in a Device1 chip at a flow rate of 10 μL/h. Images of the outlets after the separation are shown in Figure 4.16. The cancer cell recovery was 92.3 % and the WBC removal was 92.6 %, which indicates the separation works equally well for lower cancer cell to WBC ratios. There were not enough cancer cells in both outlets to find the critical diameter.

A protocol for using the PFF devices is found in Appendix E.

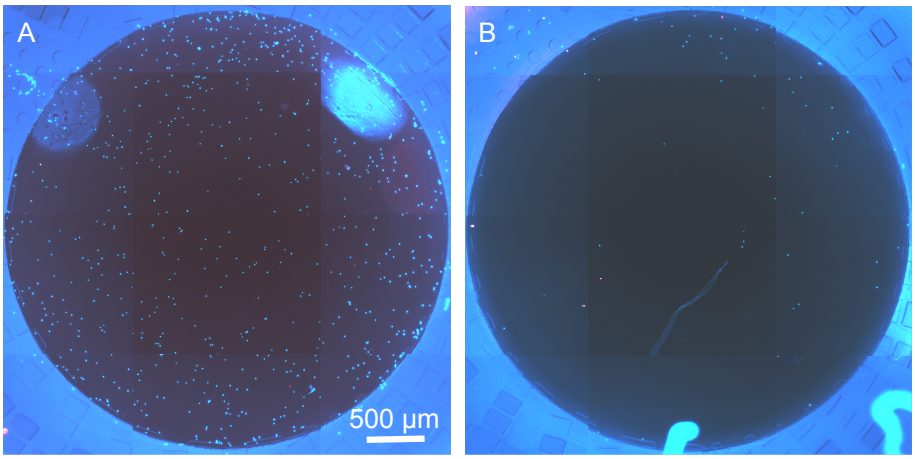

Figure 4.16: Combined fluorescence images of white blood cells and cancer cells after separation in a Design1 chip. The WBCs are blue and the cancer cells are red. (A) All cells in the small particle outlet. (B) All cells in the large particle outlet.

4.4.5 Cell deformation

It was demonstrated that the devices have a larger critical diameter for WBCs than for cancer cells. One possible explanation is that the image analysis systematically miscalculates the diameter of the cells. One source of error is that cancer cells are not perfect spheres but have a higher eccentricity. When fitting the cancer cells with circles their shortest axis is then overestimated. However, this leads to an overestimated critical diameter of the cancer cells, which would mean that the difference in critical diameter between WBCs and cancer cells is even more pronounced than measured.

Instead it is hypothesised that the difference is due to a difference in cell deformability. This would indicate that the cancer cells are more rigid than the WBCs, which also explains why they had a measured critical size closer to the one for beads. It is possible that the differences in cell deformability are due to the large rigid nucleus of the cancer cells, which has been exploited by Tang *et al.* [17]. To test this hypothesis the shear forces during PFF separation were investigated with 3D simulations. There are three possible effects in the PFF devices that could make the cell deformability influence the critical size of the cell separation:

- The elongation flow when cells move from low velocities in the sample inlet channel to high velocities in the pinched segment.
- The shear forces in the pinched segment
- The shear forces at the corner between the pinched segment and the small particle outlet channel where the corner effect occurs

The three effects are investigated by 3D simulations of the shear rate experienced by cells travelling from the sample inlet through the pinched segment. 3D simulations were used to better visualise the shear forces at the corner at the end of the pinched segment, and to minimise the computational power required to run the simulations only a small segment of the devices were simulated. The segment is the pinched segment and part of the channels connected to it in a Design1 device as shown in Figure 4.17A. The pressures at the boundaries were set to simulate a sample flow rate of $33\,\mu$L/h as used in the experiments with the lowest flow rates.

First cells meet an elongation flow when they move from the sample inlet channel to the pinched segment, where they experience an increase in velocity due to the incoming fluid from the buffer inlet. It is assumed that the cells travel at a height in the middle of the channel. The velocity along streamlines starting at different positions in the sample inlet is plotted in Figure 4.17B. The plot shows that the cells move at a constant velocity and then experience a linear velocity change as they move into the pinched segment. The change in velocity gives rise to a shear rate equal to the slope of the velocity curve found by fitting the curves in Matlab. The maximum shear rate is approx. $1{,}000\,\mathrm{s}^{-1}$. As opposed to the other cell deformation contributions, the shear rate from the elongation flow depends on the position of the cells before they are aligned. The elongation flow affects cells differently, which is a problem if it gives the highest contribution to cell deformation.

Next the shear rate in the pinched segment was estimated. A top-view 3D simulation of the pinched segment is seen in Figure 4.17A. The illustrated plane is at a middle height, and the highest shear rate is found along the wall in the pinched segment. For a sample flow rate of $33\,\mu$L/h the maximum shear rate is approx. $20{,}000\,\mathrm{s}^{-1}$. The shear is much larger than the shear rates caused by the elongation flow. Thus elongation flow is not expected to contribute to cell deformation.

Finally the largest cell deformation was at the corner at the end of the pinched segment, where the corner effect cause hard particles to change to streamlines further away from the wall, whereas soft particles deform and follow streamlines closer to the wall. The results

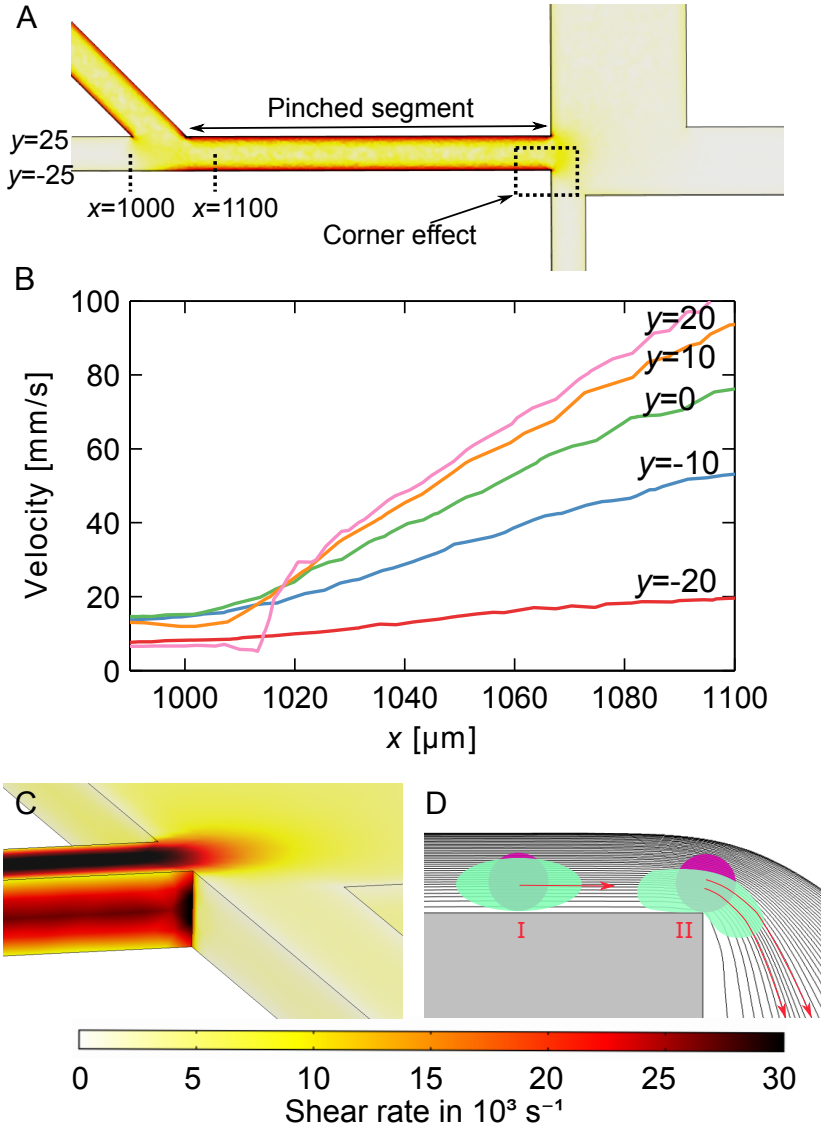

Figure 4.17: Shear rates in a Design1 chip. (A) Simulation of shear rate at a middle height in the device. The shear rare is greatest at the wall in the pinched segment. (B) Simulated flow velocity along streamlines going from the sample inlet channel to the pinched segment. All streamlines are at a middle height in the channel, and starting at different y-coordinates in the inlet channel, as marked on figure A. The plotted velocities were measured between the x-coordinates also marked on figure A. (C) Simulation at the corner between the pinched segment and the small particle outlet channel. The shear rate is constant along the wall and then increases at the corner. The color scale fits both figure A and B. (D) Illustration of the squeezing of streamlines at the transition from the pinched segment: a hard particle is forced to follow a streamline further away from the pinched segment wall because of the corner effect. A soft particle is deformed even further due to increased shear rate at the corner and follows a streamline close to the wall. This illustrates that hard and soft particles can have different d_c's. The particles were not part of the simulation.

are seen in Figure 4.17C. The shear rate is constant along the wall and then increases at the corner to approx. $30{,}000\,\mathrm{s}^{-1}$. This is much larger than the shear rates used by Beech *et al.* [80] to deform red blood cells in DLD structures. Thus the shear rates are large enough to deform soft cells, which will then get an increased critical diameter, while hard cells will get a decreased critical diameter due to the previously described corner effect. This is illustrated in Figure 4.17D. The high shear rates combined with the corner effect enhance the separation of hard and soft particles with overlapping sizes, which is very advantageous when separating cancer cells from WBCs.

The same simulations were performed on a segment of the Design2 device, and the shear rates were similar to the ones found for Design1.

The high shear rates in PFF devices can be used to improve separation of hard and soft particles. Cell deformation can also be used to improve other microfluidic size-separation devices such as DLD arrays, where shape and deformability of RBCs have already been exploited [80].

4.4.6 Conclusion on the experiments

Cancer cells and WBCs were separated at efficiencies over 90 % using injection moulded PFF devices. The size of all separated cells were measured directly in the outlets, and it was shown that there is a significant difference in critical diameter between WBCs and cancer cells. This difference likely comes from a difference in cell deformability because of the rigid nucleus of the cancer cells. The different cell deformabilities are an advantage and improve the separation efficiency. Simulations were used to investigate the cell deformation at three critical places on the devices, and the largest contribution is the shear rate at the corner of the pinched segment, just before the cells are separated.

It was demonstrated that the critical diameter of PFF devices can be changed successfully without a loss of separation efficiency. The highest separation efficiencies were obtained at sample flow rates of $10\,\mu\mathrm{L/h}$ to $50\,\mu\mathrm{L/h}$. At higher flow rates the cancer cell recovery was unaffected, whereas the WBC removal decreased. This could be because of increased inertia of the WBCs, which makes them deflect from the trajectories going towards the small particle outlet. Experiments performed at lower cancer cell to WBC ratios showed no loss of separation efficiency. The separation efficiency was higher than for previously reported state-of-the-art passive separation techniques, likely because the PFF devices exploited both differences in cell sizes and cell deformability.

The highest flow rates that can be used are $250\,\mu\mathrm{L/h}$. With a cell concentration of $700{,}000\,\mathrm{mL}^{-1}$, which was the highest concentration used for cell separation experiments, this is equivalent to a throughput of 3×10^6 cells/min. This is low compared to the inertial microfluidic separation techniques, but it is high enough to process at least 1 mL of blood after the RBCs have been removed, which was the goal for the devices. However at the increased flow rates, the WBC removal decreases. This means that the separation would either have to be done in parallel at lower flow rates, or the sample should be run through multiple PFF devices. Since the critical diameter decreases at lower flow rates, not much would be gained by running the samples through multiple times, because the smallest WBCs would be removed during the first run through. Running devices in parallel therefore

seems to be the best option, until the devices have been optimised to account for inertial effects.

4.5 Chapter summary

The development of two PFF devices was described. First analytical calculations were used to determine the optimal design dimensions, and to predict the behaviour the flow and particles in the devices. The PFF designs were successfully transferred to all-polymer chips using a fabrication process that allows for mass production of the devices.

The device operation was investigated and optimised through experiments with nano- and microbeads and with numerical simulations. A sufficient pinching width, and thus alignment of particles, could be obtained on both devices at sample flow rates up to $250\,\mu$L/h. Experiments with beads showed that the critical diameter of the first device was optimal for cancer cell separation, whereas the critical diameter of the second device had to be adjusted by applying an additional pressure. The measured critical diameter of the devices differs from the calculated, which can partly be accounted for by the described corner effect. Other effects such as particle disturbances of the flow or particle interactions can also have contributed to the deviation.

The PFF devices were tested with cancer cells spiked in WBCs at different concentrations. Separation experiments were performed at varying flow conditions, and images were taken of separated samples. A separation efficiency of over 90 % was achieved with both devices, however as the flow rates were increased the efficiency decreased. Thorough image analysis of all separated cells was performed and it was demonstrated that the cancer cells and WBCs were separated at different critical diameters, which is likely due to a difference in deformability of the cells. It was showed with 3D simulations around the pinched segment, that the cells are subjected to a range of shear stresses that have previously been used for cell deformation experiments. The difference in critical diameter is a great advantage and contributed to the high separation efficiencies.

5 Single cell trapping

Several hydrodynamic cell trapping devices were developed during this study. The final devices should enable single cell capture, on-chip cell lysis, and single cell DNA extraction to a separate uncontaminated outlet. The devices were made to be used on rare cells by researchers in another lab, so there was focus on cell trapping quality as well as user-friendliness. This created some interesting challenges, which were overcome not only with new improved designs, but also optimisation of the injection moulding process and bonding parameters. The designs, chip fabrication quality, experiments, and results related to cell trapping are presented and discussed in this chapter.

Contents

5.1 Design requirements and development

The devices are all based on hydrodynamic principles, and there were a few things to consider before creating a design. Firstly the trap dimensions must be sufficiently small so the particles do not go through the traps, but the exact dimensions needed for bead or cell capture has not been studied much in the published literature. For rigid beads it is intuitive that as long as the smallest trap dimension is smaller than the bead it cannot go through the trap. For cell capture it is not as straight forward. Cell populations can have wide spreads in size and deformability. It is still intuitive that the smallest trap dimension should be smaller than the smallest cells, but how much smaller depends on cell deformability and on the flow conditions. A larger velocity through the trap will increase the shear stress acting on the cell and thereby increase its deformation. Since the goal is to

capture only one cell per trap, the first cell should block the trap and thereby increase its hydraulic resistance so much that no more cells are captured in the same trap. Therefore the trap cross section must also be considered.

For hydrodynamic particle trapping it was proposed by Tan and Takeuchi [61] that the resistance of the trap has to be smaller than the resistance of the main channel going around it, otherwise the particles will simply flow past the trap. While it will undoubtedly increase the probability of particle capture it might not be necessary if the particles are deliberately guided close to the traps. The particles can be aligned to a channel wall by a buffer fluid stream, similar to in the PFF devices. It is hypothesised that by following the streamlines going through the traps, it can be predicted which particles will be captured. This is illustrated in Figure 5.1. Particles with a radius smaller than the distance from the wall to the outermost streamline going through the first trap will be captured, while particles with a radius larger than that distance will flow past the trap. Two times that distance is called the critical size, s_c, throughout the rest of the thesis.

From the hypothesis it follows that to obtain single particle capture, the first particle occupying a trap must reduce the critical size so that the next particle will be captured in the next trap etc. until all traps are occupied.

To summarize, the following requirements are necessary to obtain single particle trapping:

- The smallest trap dimension must be smaller than the particle diameter.
- The critical size s_c must be larger than the particle diameter.
- Once a single particle is captured it must reduce s_c, so it is smaller than the particle diameter.

A total of three generations of cell trapping chips were created for addressing different challenges, adding up to a total of eight cell trapping devices. Here follows a short summary

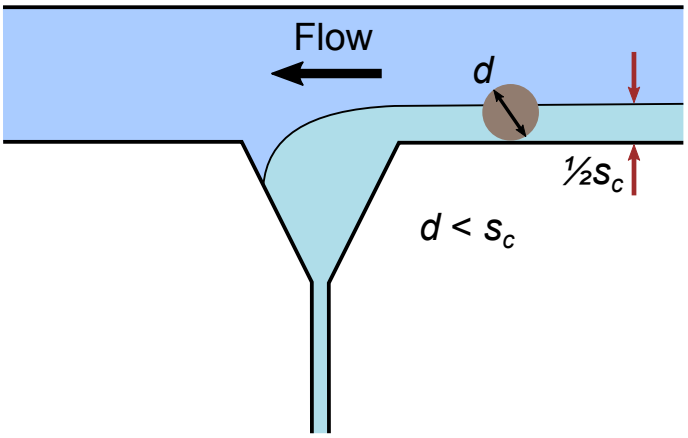

Figure 5.1: The hypothesised requirement for efficient particle capture. Particles with $d < s_c$ will be captured and particles with $d > s_c$ will not. The particles must be aligned, as in the pinched segment on PFF devices.

of all designs and shims created for this study.

First generation: Capture in traps with shared outlets.

- Device1 to 3 - Channel heights of 43 μm/10 μm. Created to test different trap dimensions and channel structures. The channel heights were supposed to be 30 μm/10 μm, so a new version was made.
- Device1 to 3 - Channel heights of 30 μm. Correct channel heights, but the 10 μm layer was skipped for a faster delivery time.

Second generation: Capture in traps with separate outlets.

- Device4 and 5 - Created to test different trap widths for capture of cells in traps with separate outlets.
- Device6 and 7 - Optimised designs for capture in traps with separate outlets.

Third generation: Final optimised design.

- Device8 - Design with optimised trap dimensions, which enabled single cell capture with a high efficiency.

The design process, fabrication quality and results will be presented and discussed for each trap design generation in the following sections.

5.2 First generation - Capture in traps with shared outlets

The purpose of the first cell trapping generation was to capture single cells in traps with shared outlets, and to narrow down which trap dimensions and channel structures to use. It was based on state-of-the-art designs, and adapted to the previously described 12 Luer chip-format. The trap dimensions were adjusted for capture of single cancer cells.

Design

Device1 to 3 were placed on one shim design shown in Figure 5.2. The shim design was made by a member of the group before the work for this thesis began. Device1 was inspired by Kobel *et al.* [60] and is the only design with two heights, 30 μm for the main channels and 10 μm for the traps. The 30 μm was chosen to prevent large cell aggregates from clogging the channels. The structure consists of one feeding channel that splits into four channels with one trap each. With a cross section of 10 μm $\times$ 10 μm the traps are the smallest on the entire shim. The main channels going around the traps have two different lengths: 1 mm and 2 mm. This is the only device where the particles are not aligned against the wall where the traps are positioned, and it therefore makes no sense to calculate the critical size. Instead the resistance ratios between the main channels and the traps are

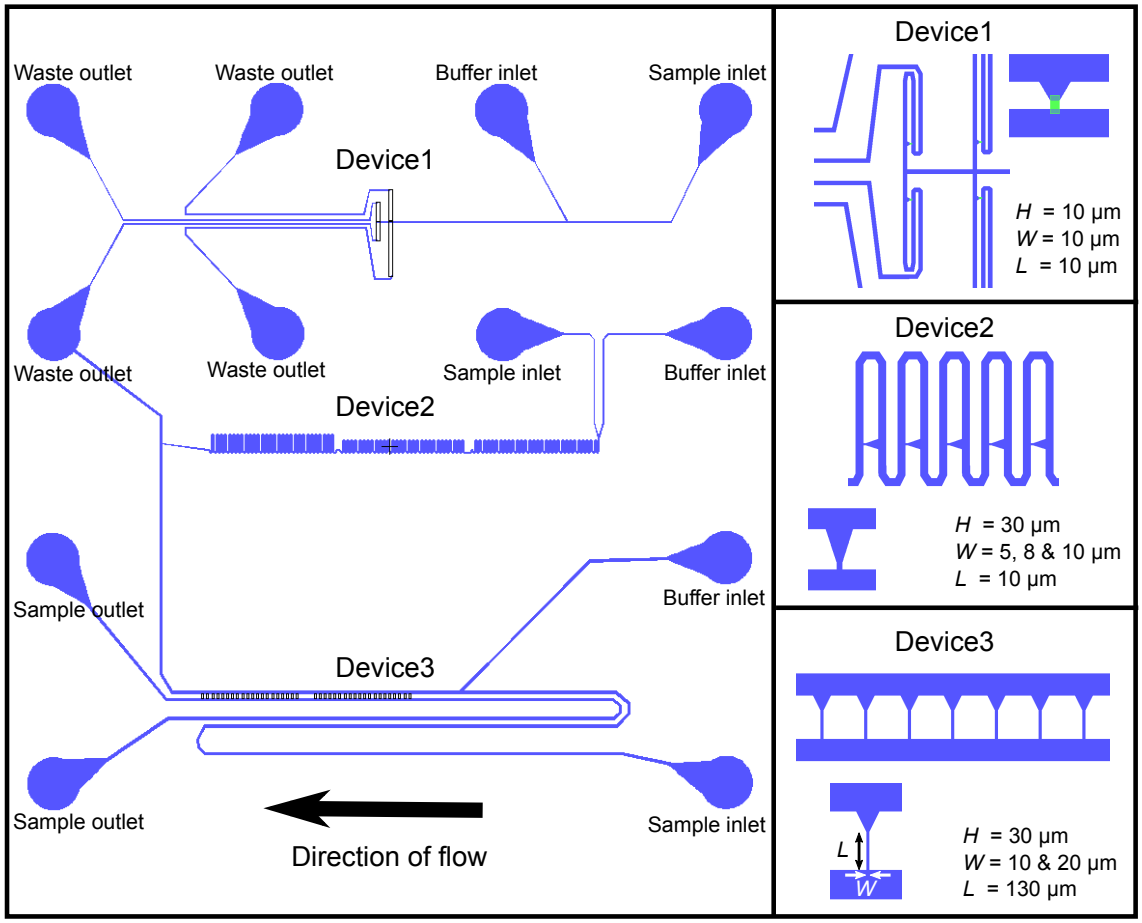

Figure 5.2: First generation cell trapping chips. It consists of three separate devices with different channel structures and trap dimensions. Zoom-ins of each design structure is shown together with an insert of a single trap and its dimensions.

calculated by using the equations for resistance of rectangular and square channels. The resistances are calculated as:

$$\frac{R_{1mm}}{R_{Trap}} \approx 1.2, \qquad \frac{R_{2mm}}{R_{Trap}} \approx 2.5. \tag{5.1}$$

Thus there is more flow going through the traps than around them, and the basic particle trapping criterion proposed by Tan and Takeuchi [61] is fulfilled.

Device 2 was inspired by Tan and Takeuchi [61] and has three times thirty traps in series along a feeding channel. There are two inlets, one for the particle solution and one for a buffer solution, which guides the particles towards the side of the feeding channel where the traps are positioned. The first series of traps are 10 μm wide, the second are 8 μm and the third are 5 μm. The 5 μm traps are the narrowest on the entire shim. The feeding channels going around the traps are 30 μm wide and have varied lengths to make up for the different trap resistances.

Device3 was inspired by Zhu *et al.* [57]. It consists of two times twenty traps in parallel positioned on the same side of a feeding channel. As in Device2 there are two inlets, and again the buffer fluid directs the particles to the side of the feeding channel where the traps are positioned. The first set of traps are 10 μm wide and the second set are 20 μm wide. These traps are the longest with a length of 130 μm. The feeding channel and outlet channels are all 100 μm wide. One advantage of Device3 is that the traps are connected to outlets that are separated from the waste outlet for the leftover particles. Thus contamination from the leftover cells is avoided and the device should enable extraction of DNA from a few cells.

The critical size of Device2 and 3 was determined by semi-3D simulations of the designs. For Device2 only the part shown in Figure 5.3A was simulated. The figure shows the simulation of the 10 μm wide trap, but the two other trap types were also simulated. The pressures applied to the Device2 simulations has no influence on s_c, which cannot be changed since the traps and feeding channel are connected to the same outlet. For Design3 the entire device was simulated and the plot in Figure 5.3B only shows part of the simulation. The pressure at all outlets was set to zero as in the experiments. As in the PFF devices, the streamlines are squeezed at the corner of the traps, as illustrated in Figure 5.3B. This gives rise to a similar corner effect, which decreases the critical size. The simulated critical sizes, when the corner effect has been taken into account, are listed in Table 5.1.

The devices with a critical size of 30 μm had streamlines going through the traps, that were wider than half the channel width, and should therefore capture all aligned particles. Both devices should capture beads and cells effectively as s_c is larger than their sizes. The critical size of the last 10 μm trap and the first 20 μm trap in Device3 is lower than the others, but it is expected to increase as the 10 μm traps gradually are being filled, and the

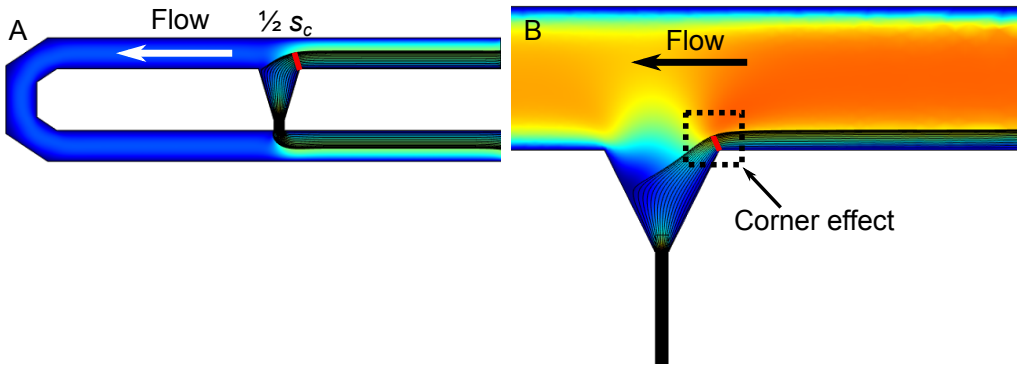

Figure 5.3: Semi-3D simulations for determining s_c. (A) Simulation of a 10 μm wide trap in Device2. Streamlines going through the trap are shown and s_c is marked with a red line. Since the streamlines take up more than half the feeding channel width all particles should go through the trap as long as they are aligned, and s_c is equivalent to the width of the feeding channel, which is 30 μm (B) Simulation of the first 10 μm trap in Device3. Only part of the simulation is shown. The corner effect decreases s_c, which is marked by a red line. The colours on the plots represent velocity but the two figures do not have the same scale, so they cannot be compared.

Table 5.1: Critical size of traps in the Device2 and Device3 designs.

	Device2			Device3			
Trap	10 μm	8 μm	5 μm	First 10 μm	Last 10 μm	First 20 μm	Last 20 μm
s_c [μm]	30	30	24.9	21.6	4.8	8.1	42.7

flow through the unoccupied traps increases. Because the critical sizes are very large it is expected that multiple particles will be captured in each trap, as it is unlikely that a single particle can decrease s_c sufficiently when occupying a trap. However the main purpose of the first generation of devices was to get some experience working with hydrodynamic cell trapping and narrow down which trap dimensions and channel structures to use for the next generations.

Chip Fabrication

As mentioned in the previous section, the first generation devices were all placed on one shim design. Two first generation shims were delivered. The first had been etched for too long, so the channels were too high. Therefore a second shim with the correct dimensions was also delivered. Both shims were used for chip fabrication and experiments, and they are characterised in this section.

Device1 to 3 - 43 μm height

Bright field images of the shim showed that the top of all channels is very rough. This is likely because the KOH etch attacked the vanadium particles in the seed layer, as on the PFF Design1 shim. Particles in the devices have little interaction with the top of the channels, but they touch the side walls when trapped. The channel walls were investigated in a SEM, which showed that the size of the rough structures is smaller than the particles and is therefore not expected to have any effect. The channel height was measured with an optical profiler, which showed that the first layer had been over-etched to a height varying from 41 μm to 45 μm, while the second layer had a height of 11 μm, which is within the specified range. Images and a height measurement are shown in Figure 5.4, and they are representative of the rest of the shim.

The shim was used for injection moulding with Recipe 1, as described in Section 2.4. The first chip batch was sealed with 500 μm thick lids using the standard parameters, i.e. 120 °C at 5.1 MPa for 5 min. Chips before and after bonding are shown in Figure 5.5. The images show that the polymer has stress marks at the traps on Device1 and 2, but not on Device3, which indicates that the center of contraction is close to the Device3 traps. The stress marks are still visible after bonding, where bright areas appear in places with no contact between chip and lid. It can be seen that the trap widths vary greatly between the top and bottom, not just because of stress marks but also because of the increased height. The large height is a problem, especially for Device1, where particles cannot be directed towards the traps. Assuming an increase in height from 30 μm to 40 μm, while all

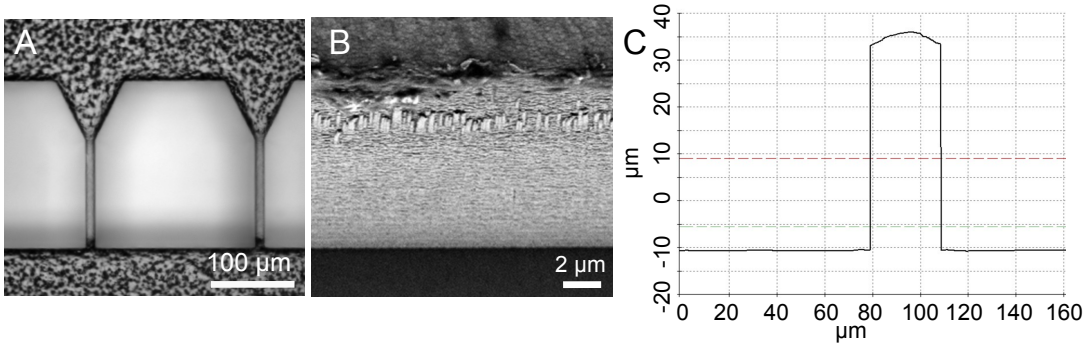

Figure 5.4: Investigation of the shim. (A) Bright field image of channels on Device3. (B) Tilted SEM image of the side wall on a Device3 trap. The rough structures are smaller than 1 μm. (C) Measurement across a 30 μm wide main channel, showing a height of 45 μm.

other dimensions are unaffected, leads to a decrease in the resistance ratios to 0.7 and 1.5 instead of the larger values from Equation (5.1). For Device2 and 3 the cross sectional area of the traps was greatly increased, but there was not much change in the critical sizes.

To compensate for the poor shim dimensions, three new sets of bonding parameters were used: one where the temperature was increased to 125 °C, one where the pressure was increased to 10.2 MPa and one where both temperature and pressure were increased. For each set of parameters the width at the top of the traps was measured on bright field images. The results are listed in Table 5.2. Images of the chips used for the measurements are located in Appendix F.

Even bonding with the standard parameters greatly reduces the trap width for Device1 and 2, and it decreases even further with the tougher bonding parameters, which all have surprisingly similar outcomes. The traps in Device3 experienced a relatively small change in trap width compared to the other devices, which indicates that the channel structures on channels without stress marks are not altered much by the tougher bonding. The reason for the reduced widths on Device1 and 2 could be that tougher bonding levels out the stress marks and reduce the gap between the chip and lid at the traps.

Table 5.2: Average trap width of chips measured at the top of the channel. Values are given in micrometers with the stated uncertainties corresponding to the standard deviation.

	Device1		Device2		Device3
Parameters	10 μm	10 μm	8 μm	5 μm	10 μm
No bonding	20.3 ± 0.7	23.2 ± 0.4	22.0 ± 1.5	21.4 ± 1.4	12.2 ± 1.3
120 °C, 5.1 MPa	16.4 ± 0.4	17.1 ± 0.7	14.8 ± 1.9	11.7 ± 0.4	11.2 ± 0.6
120 °C, 10.2 MPa	13.8 ± 0.2	13.1 ± 0.8	10.0 ± 0.9	8.5 ± 0.6	10.0 ± 0.8
125 °C, 5.1 MPa	13.5 ± 0.7	12.3 ± 0.4	11.5 ± 1.1	9.4 ± 0.7	10.1 ± 1.1
125 °C, 10.2 MPa	16.6 ± 0.1	13.0 ± 1.4	11.8 ± 0.9	9.2 ± 1.8	10.0 ± 0.7

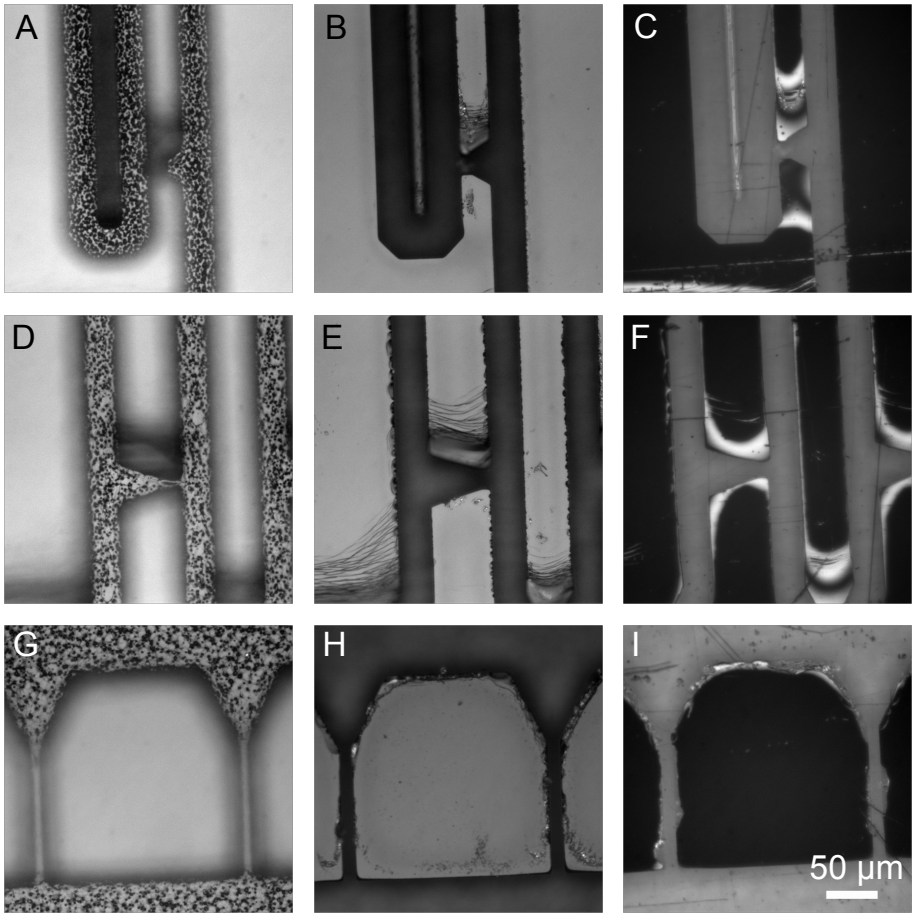

Figure 5.5: Bright field images for investigation of first generation chips before and after bonding. (A)-(B) Focus on the bottom and the top of trap in Device1 before bonding and (C) after bonding. (D)-(E) Trap in Device2 before bonding and (F) after bonding. (G)-(H) Traps in Device3 before bonding and (I) after bonding. The scale bar fits all images.

Device1 to 3 - 30 μm height

The second shim had main channel heights of 30 μm, however the 10 μm layer was skipped for a faster delivery time, leaving Device1 unusable. Height measurements confirming the channel dimensions are located in Appendix C. For these chips it was necessary to use high magnification objectives with lower working distances to investigate the captured cells, and therefore a sheet of 150 μm thickness was used for bonding. The chips were injection moulded with Recipe 1 and bonded with the standard parameters. The shim, an injection moulded chip, and a bonded chip are seen in Figure 5.6.

The injection moulded chips have stress marks at Device3, which is in agreement with Figure 2.4, where the center of contraction is in the middle of the chip, between Device2 and Device3. However, as seen on the sealed chip, the stress marks are levelled out after bonding, which was also the case for the Device2 traps. The bonded chips had the same

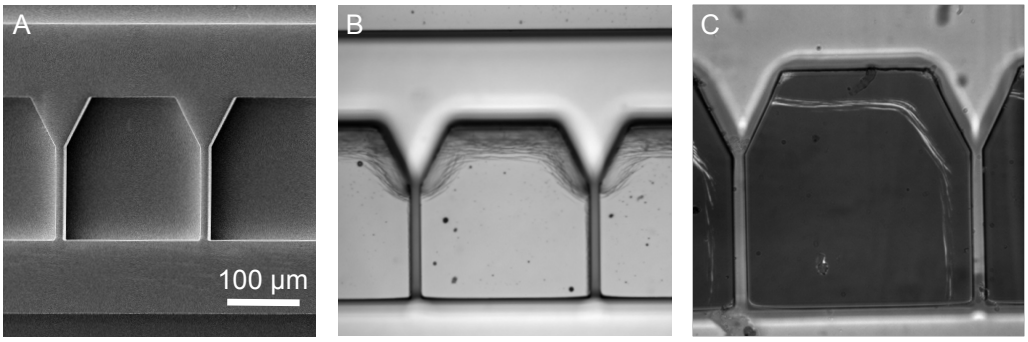

Figure 5.6: (A) SEM image of the shim with 30 μm high channels. (B)-(C) Bright field image of a chip before and after bonding.

dimensions as on the design, and will give a better qualitative description of the dimensions that are needed to capture single cells. It was decided to test chips from both designs to compare results which can be used for the next design.

Experiments

Device1 to 3 - 43 μm height

Chips bonded at 125 °C and 5.1 MPa were tested with 15 μm beads mixed to a concentration of 3×10^5 beads/mL. The pressures were approx. 10 mbar on all inlets. In Device 1 many beads passed by the traps as expected from the calculated decrease in the resistance ratios. In addition beads had a tendency to get stuck in the channels after a while, especially in the feeding channel where it splits into three channels, which decreases the velocity of the beads. To split the channel was a poor design choice and the channel structures on Device1 were generally not usable for particle trapping.

The Device2 structure captured 15 μm beads with one or two beads in most traps. During the experiments an interesting event occurred where trapped beads blocked the flow enough for other cells to skip past the trap, but at the same time let enough flow through that when the next beads reached the other side of the trap, they were pushed towards the wrong side of the channel. This event caused the beads to skip all the following empty traps, which resulted in a poor trapping efficiency. An example of this event is seen in Figure 5.7. In some occurrences it happened that a second bead would enter the occupied trap and block the flow so the next beads would fill in the following traps. If the experiment was run long enough all traps would eventually be filled with one or two beads, but this is ineffective. Beads changed position in the main channel so often that when they reached the 8 μm and the 5 μm traps they were not likely to get captured, and testing of these traps was limited.

In Device3 some 15 μm beads flowed past the traps although they were guided by the buffer. However most beads were captured, and the traps were slowly filled with multiple beads, as seen in Figure 5.8. The first couple of traps were filled with a few and then many beads, and the last traps were not occupied before all the first traps were completely filled.

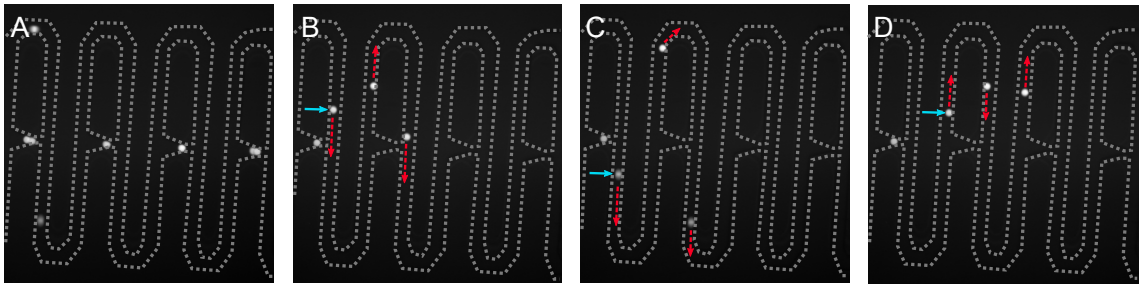

Figure 5.7: Experiment with 15 μm beads in 10 μm wide traps on Device2. The grey dotted lines represent the walls. (A) One to two beads captured in each trap. (B)-(D) The bead marked by a solid blue arrow approaches the end of a trap, and because there is still flow through it the bead is pushed towards the other side of the channel, which causes it to skip the next trap. The same had happened to the two other beads. The red dashed arrows indicate the direction of flow.

The high number of beads per trap can be caused by two things: Either the trap cross section is too large and beads do not block the traps sufficiently, or the triangular area where beads are caught creates dead volume with little flow, and other beads are therefore easily captured. No beads went through the 10 μm traps, while many beads went through the 20 μm traps before filling. It was surprising that the 20 μm traps were filled at all, but the beads could be blocked by either small variations in the trap width or unusually large beads, or a combination of the two. Indeed the beads got stuck halfway through one trap in Figure 5.8E, which points to the first explanation, while one bead blocking one of the other traps seems to be rather large, which points to the other explanation.

The chips bonded with 120 °C at 10.2 MPa, showed the same overall particle behaviour, but with a lower trapping efficiency for Device2. Chips bonded with 125 °C at 10.2 MPa were not tested.

The chips bonded with 125 °C at 5.1 MPa were also tested with cells. Fixed DLD-1 cells were used because the experiments were carried out before it was decided to use LS174T cells as the standard. It was evident that Device1 did not work better with cells than with beads, and again cells were stuck in the feeding channel. Device2 worked well for 10 μm

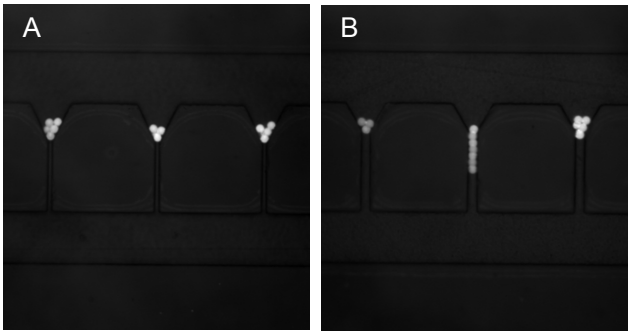

Figure 5.8: (A) Beads captured in 10 μm wide traps on Device3. (B) Beads captured in 20 μm wide traps on Device3.

traps, which captured one to two cells in each, as seen in Figure 5.9. The cells were easier to capture than the beads and only few flowed past the traps. The observed phenomena with beads being pushed towards the other side of the channel was not observed with cells. It can be explained by the cell deformability, which cause them to take the shape of the trap and block a larger area of the trap cross section than the beads. However the cells had a tendency to clump together and block the feeding channel. This should be avoided with a wider feeding channel.

Device3 captured too many DLD-1 cells in both the 10 μm and 20 μm traps, and many cells also went trough the 20 μm traps. Device3 was also tested with defrosted LS174T cells. These experiments went better and only one or two cells were captured in each trap. The most probable cause is a difference in cell deformability because fixed cells are more rigid than live cells. The LS174T cells were captured with pressures of 10 mbar on both inlets, but at higher pressures some cells slowly started moving through the traps, and at 20 mbar most cells would go through. Images from the experiments are shown in Figure 5.9.

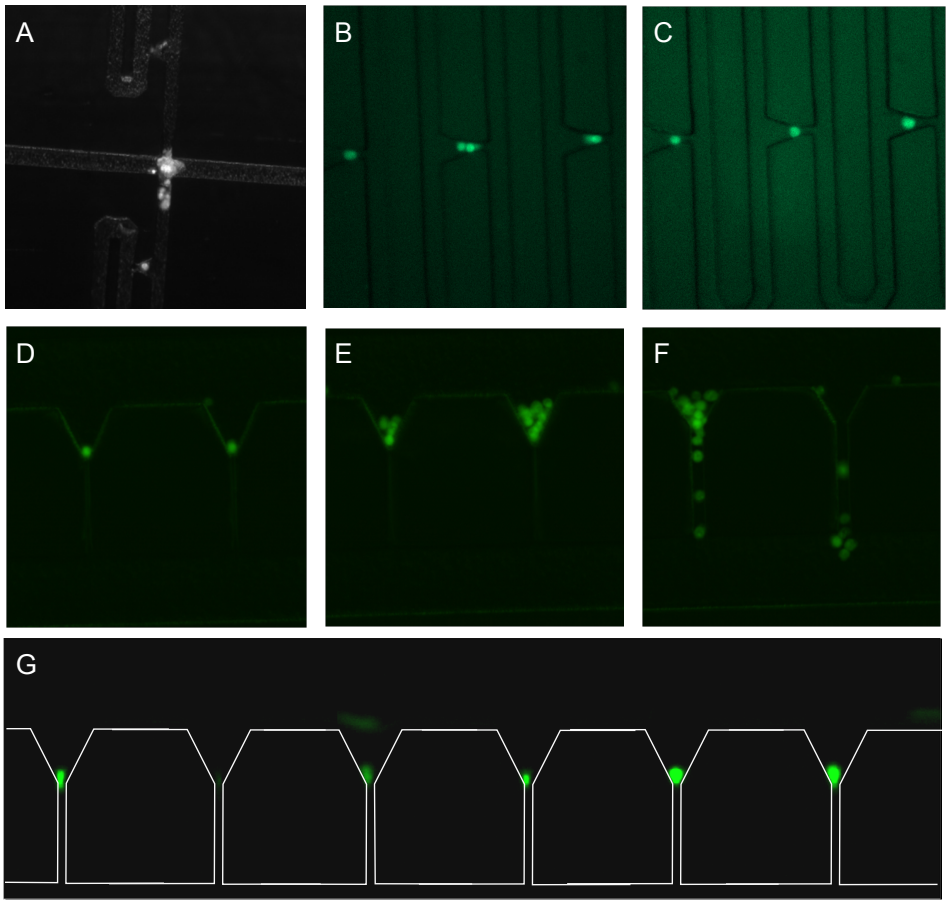

Figure 5.9: Cells in chips with 43 μm high channels. (A) Cells blocking the main channel in Device1. (B)-(C) Single or double DLD-1 cells captured in 10 μm wide traps on Device2. (D)-(E) Single or a few DLD-1 cells captured in 10 μm wide traps and (F) many cells in 20 μm traps on Device3. (G) Defrosted LS174T cells in 10 μm traps on Device3.

Design1 to 3 - 30 μm

The second shim was first tested with 15 μm beads. Device2 trapped beads more efficiently with few beads skipping the traps, however up to seven beads were captured in each trap, and it is clear that beads do not block the flow through traps very well. The 10 μm traps in Device3 were also filled with 15 μm beads, while beads went straight through the 20 μm traps. Images from experiments are seen in Figure 5.10. Note that the trapped cells are all in focus, indicating that they are trapped in the same height, probably at the bottom of the chip. Most of the beads therefore do not contribute with additional trap blockage, which explains the high number of beads in each trap. Although the trap cross sections on this shim should be smaller, traps were occupied by as many or more beads than traps on the first shim.

Tests were performed with defrosted LS174T cells in Device3. A concentration of 300,000 cells/mL was used with applied pressures of 5 mbar. As seen on the images in Figure 5.11 multiple cells were captured in most of the traps and although smaller pressures were used, the cells moved further into the traps than cells did in the traps from the first shim, as seen in Figure 5.9G. At higher pressures cells would move further into the traps and eventually go through, as observed with chips from the first shim.

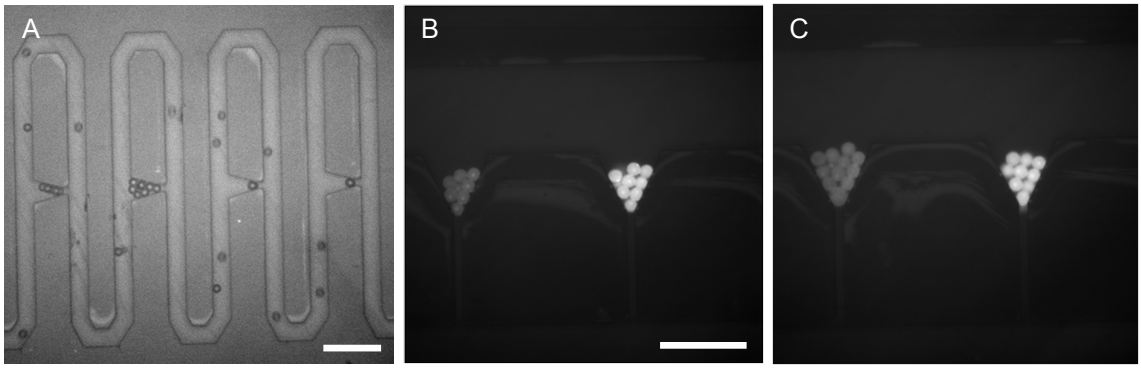

Figure 5.10: 15 μm beads in chips from the second shim. (A) Several beads captured in 10 μm wide traps on Device2. (B)-(C) Many beads captured in 10 μm wide Device3 traps. The scale bars are 100 μm.

Conclusion

The experiments with fluorescent beads and cells showed some interesting differences between the two. The cells clump together and are more sticky than the beads. Single cells were easier to capture than single beads, likely because cells are deformable and therefore block the traps more efficiently. Most devices captured multiple beads. The captured beads are settled at the bottom of the channels and does not contribute much to blocking of the traps, which therefore allows more beads to be captured in the same trap.

From the experiments on devices with both channel heights it can be concluded that the overall structure of Device3 is the best to work with. It is easy to wet without bubble formation, and cells rarely get stuck in the wide feeding channel. It also has the advantage

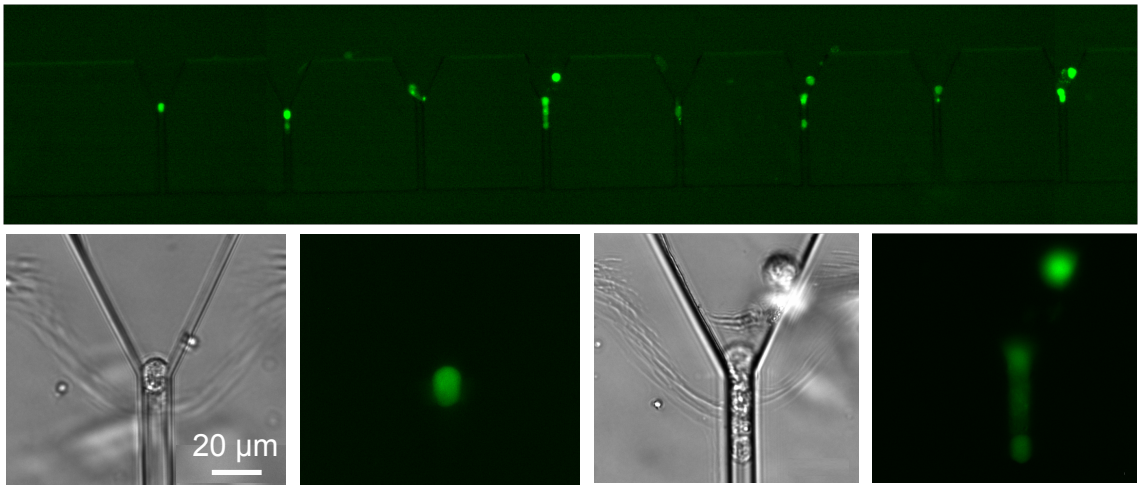

Figure 5.11: Cell experiments on the second shim. LS174T cells were captured in 10 μm traps on Device3. The bright field and fluorescence images below are zoom-ins of the first and fourth trap from the left. Cells have moved further into the traps than on Figure 5.9G.

that the traps are connected to an outlet different from the waste, which means the design is easier to adjust to single cell capture in traps with separate outlets. Cells flowed through the Device3 traps at pressures above 10 mbar, and in the devices with lower heights multiple cells were captured. Single cells were captured with a high efficiency in the 10 μm wide traps on Device2, and those trap dimensions are better suited for cell capture.

The goal of capturing single cells in traps with a shared outlet was achieved with chips from the first shim. However their exact trap dimensions were unknown. Also traps on the two first generation shim captured cells different. The first shim captured more single cells, and the captured cells did not easily move into the traps, as on the second shim. Therefore it was concluded that a better method for investigation of sealed chips was needed to determine the dimensions of traps that captured single cells, and to understand why the cell capture between the different shims varied.

A method for cleaving polymer chips and visualising the channel cross sections is described in the next section.

5.3 Freeze-fracture investigation

A method for investigation of structures and bonding quality of sealed chips was needed to determine which dimensions are needed for single cell capture and how bonding parameters affect the trap structures. The developed technique is illustrated in Figure 5.12. First a hacksaw is used to saw from the edge of the sealed chip to a point close to the traps. The chip is then cut from two sides to help guide the break and a scalpel is used to make a shallow cut on the top and bottom side of the chip where it should break. Next the entire chip is immersed in liquid nitrogen until it is cooled and it is then quickly placed in a bench clamp and split in two. After freeze-fracture the two parts are coated with a 10 nm layer

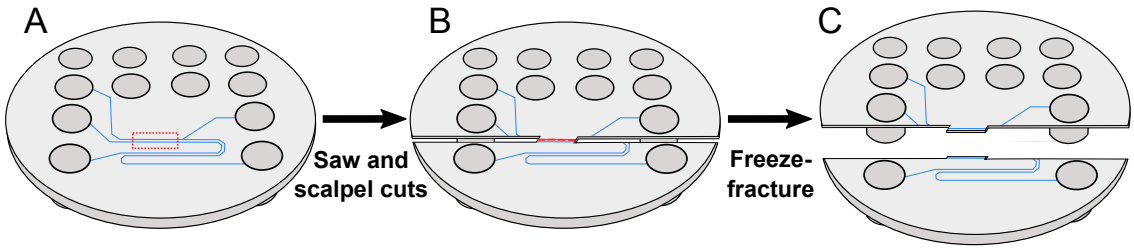

Figure 5.12: Sketch of the freeze-fracture method. (A) A sealed chip with traps of interest marked by the red dotted square. (B) The chip after it has been cut with a hacksaw and a scalpel, marked by the red dotted line. (C) After freeze-fracture the cross sections are exposed on the two parts.

of either silver or gold-palladium to enable SEM imaging with minimal charging. Images were taken with the inlense detector at low working distances.

The freeze-fracture method was used to investigate cross sections of Device3 traps. A freeze-fractured 43 μm high chip bonded at 125 °C and 5.1 MPa is shown in Figure 5.13 together with a 30 μm chip bonded with the standard parameters. The first thing to notice is that the scalpel cut is visible and the chip therefore broke at the intended position and enabled visualisation of many trap cross sections. The cross sections of the 43 μm chip reveal that the channel walls are very rough, likely because the polymer was sticking to the small structures on the shim and then got stretched during the separation. It can also be seen that the trap walls bend slightly towards the middle of the trap, whereas the walls on the 30 μm chip are straight and smooth. On both shims the sealing is complete, so any stress marks have been levelled out. To determine why the 43 μm chips captured single cells more effectively the height, smallest width and cross sectional area of the 10 μm traps were measured, and the average values are listed in Table 5.3.

The traps on the 43 μm high chips are more narrow but also higher and with a larger cross section than the traps on 30 μm high chips. The dimensions were used to estimate the hydraulic resistance of the traps. The trap on Figure 5.13B is roughly rectangular, but the smallest width is not representative. Instead the resistance is estimated as the resistance of a rectangular channel with the same height and cross section, i.e. with a width of $W = 285\,\mu\text{m}^2/37.3\,\mu\text{m} = 7.6\,\mu\text{m}$. This yields:

$$R_{43\,\mu\text{m}} \approx 1.1 \times 10^{14}\,\text{kgm}^{-4}\text{s}^{-1}. \tag{5.2}$$

The trap on Figure 5.13D have straight walls and the resistance is calculated using the

Table 5.3: Average trap height, smallest width and cross sectional area of 10 μm traps on Device3. The uncertainties correspond to standard deviations.

	Bonding parameters	Smallest width [μm]	Height [μm]	Cross sectional area [μm^2]
43 μm chip	125 °C, 5.1 MPa	6.8 ± 0.9	37.3 ± 0.6	285 ± 31
30 μm chip	120 °C, 5.1 MPa	8.8 ± 0.8	28.3 ± 1.3	257 ± 18

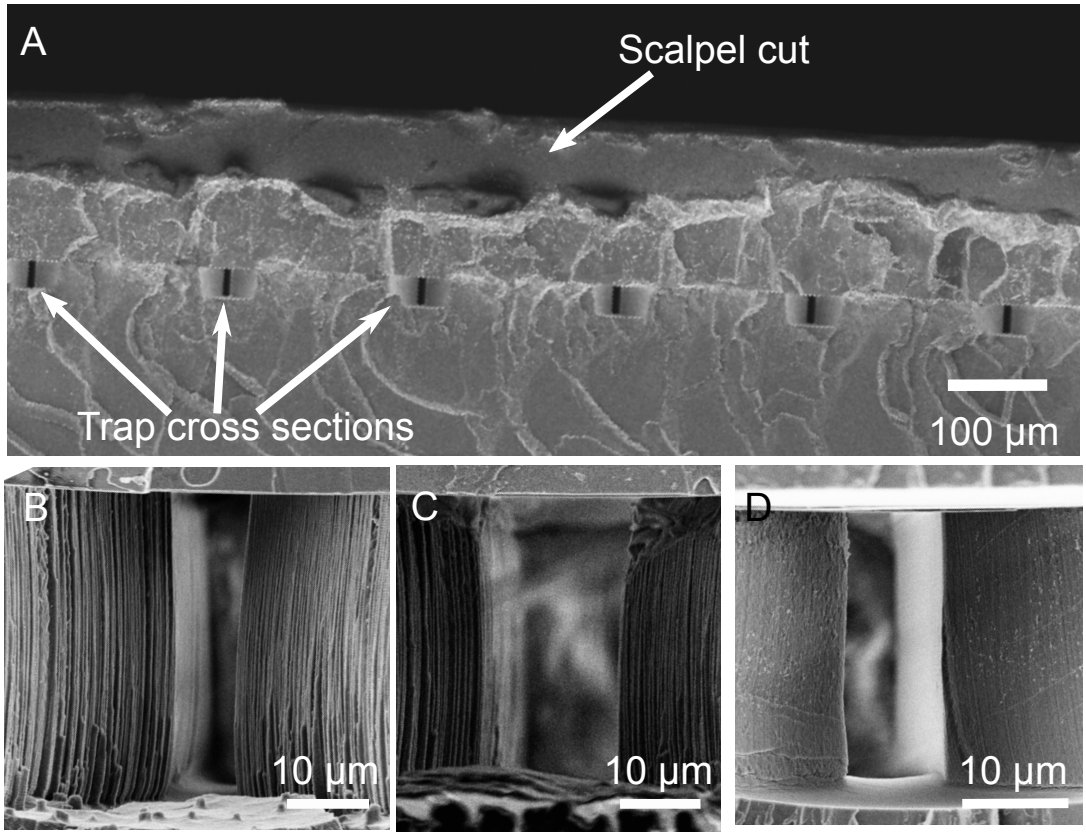

Figure 5.13: SEM images of freeze-fractured chips. (A) Overview of chip with many visible trap cross sections and a scalpel cut. (B)-(C) 10 μm and 20 μm traps on a 43 μm high chip bonded 125 °C and 5.1 MPa. (D) 10 μm trap on a 30 μm high chip bonded at 120 °C and 5.1 MPa.

equation for rectangular channels:

$$R_{30\,\mu\mathrm{m}} \approx \frac{12\eta L}{(1-0.63W/H)W^3H} \approx 1.0\times10^{14}\,\mathrm{kgm^{-4}s^{-1}}. \tag{5.3}$$

The resistance of the traps from the 43 μm high chips is larger, but only by about 10 %, which is not enough to explain the difference between the shims. It is more likely that the wall structures increase the cell-wall friction and thus prevent cells from moving through the chips.

Since multiple beads were captured in all traps, it would be interesting to find out which trap dimensions are necessary for single bead capture. To see whether it is possible to obtain single bead capture on Device3 chips, the trap dimensions were deliberately altered with high temperature bonding. From a fabrication point-of-view it is also interesting to investigate how one-layered structures can be altered. One-layered designs are preferable because both fabrication costs and complexity are increased significantly for each added layer. One-layered designs however have some limitations as high-aspect ratio channels are difficult to fabricate reliably [81]. A reduction of the cross sections will result in less flow

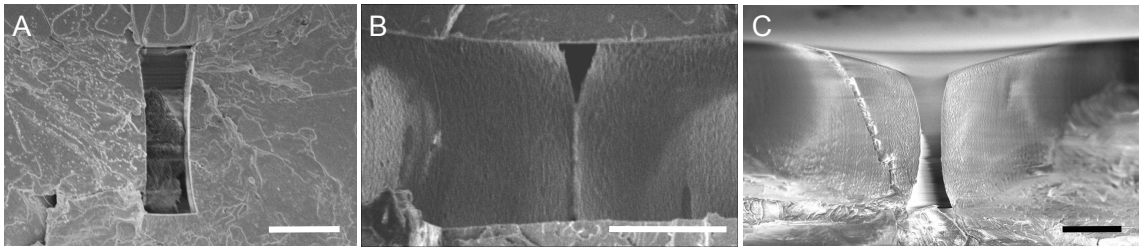

Figure 5.14: Freeze-fractured chips showing 10 μm traps on Device3. (A) Chips bonded at 125 °C and 5.1 MPa, (B) 128 °C and 2.5 MPa and (C) 120 °C and 2.5 MPa at the entire chip surface and then 128 °C and 0.5 MPa on the traps. The scale bars are 10 μm.

through the traps which should decrease s_c and minimise the number of beads in each trap. To test this hypothesis 30 μm high chips were bonded at different temperatures close to the glass transition temperature of TOPAS 5013L-10 to intentionally alter the trap cross sections.

Trap cross sections of freeze-fractured chips bonded at different temperatures are seen in Figure 5.14.

The walls on chips bonded at 125 °C bend towards the middle of the trap, as observed on the rough chips bonded at the same temperature. On chips bonded at 128 °C the cross section is greatly reduced, however the main channels collapsed, which could be seen in an optical microscope without the use of freeze-fracture, and those chips can obviously not be used for bead capture. Chips bonded at 128 °C and 0.5 MPa directly on the traps had very narrow cross sections and no main channel collapse.

The trap dimensions on freeze-fractured chips were measured and compared to the dimensions of an unsealed chip, which was analysed with an optical profiler. The results are summarised in Table 5.4. There is no significant difference between dimensions of the unsealed chip and the chip bonded at standard parameters, which is in agreement with observations made by Matteucci *et al.* [68], who claimed that these parameters yield a strong bonding without altering the injection moulded structures.

Chips bonded at 128 °C on the traps have a significantly decreased cross sectional area.

Table 5.4: Average height, smallest width and cross sectional area measured on an unsealed chip and chips bonded with different parameters. The uncertainties correspond to standard deviations.

Bonding parameters	Smallest width [μm]	Height [μm]	Cross sectional area [μm^2]
No bonding	8.9 ± 0.4	28.8 ± 0.3	256 ± 10
120 °C, 5.1 MPa	8.8 ± 0.8	28.3 ± 1.3	257 ± 18
125 °C, 5.1 MPa	6.7 ± 0.3	25.9 ± 0.5	192 ± 9
128 °C, 2.5 MPa	0	16.1 ± 1.3	15.5 ± 6.4
120 °C, 2.5 MPa + 128 °C, 0.5 MPa	3.3 ± 0.2	21.5 ± 3.0	91 ± 25

The trap resistance was estimated by calculating the resistance of a rectangular channel with the same measured height and cross section. This gives a resistance of:

$$R_{128\,^\circ\mathrm{C}} \approx 1.1 \times 10^{15}\,\mathrm{kgm^{-4}s^{-1}}, \tag{5.4}$$

which is around ten times higher than for the traps bonded at 120 °C and 5.1 MPa. To obtain such a high resistance of rectangular traps on a one-layered design with a 30 μm height would require a trap width of only 3.7 μm. This large increase of resistance should have a large effect on the critical size, which can be determined now that the trap dimensions are known. Semi-3D simulations of a Device3 device with the modified trap dimensions were carried out, and a s_c of 7.4 μm was measured. According to the hypothesis, the chips should not be able to capture 15 μm beads because they are larger than s_c. They should instead capture fewer 5 μm beads as the beads only have to decrease s_c by 2.4 μm.

The altered chips were initially tested with 15 μm fluorescent beads, but they flowed past the traps and were not captured, as predicted. Instead the chips were tested with 5 μm beads, and the results are seen in Figure 5.15. It was observed that only one or two beads were captured in each trap, which is a great improvement and demonstrates that traps with smaller critical sizes indeed capture fewer beads.

The freeze-fracture investigation revealed some interesting features of sealed chips, and was used to enable visualisation of structures that had been altered by high temperature bonding. The method is used throughout this chapter to investigate trap cross sections on bonded chips.

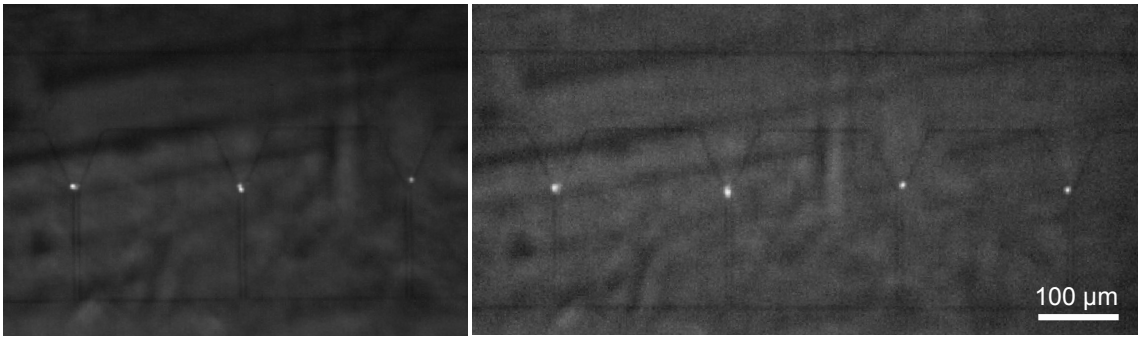

Figure 5.15: Combined bright field and fluorescence images of 5 μm beads in traps bonded at 128 °C and 0.5 MPa on the traps. Single particles are captured because s_c was decreased by the high temperature bonding, as seen in Figure 5.14C.

5.4 Second generation - Capture in traps with separate outlets part 1

The next goal was trapping of single cells in traps with separate outlets. This required a new cell trapping design, and the Device4 design was developed for that purpose.

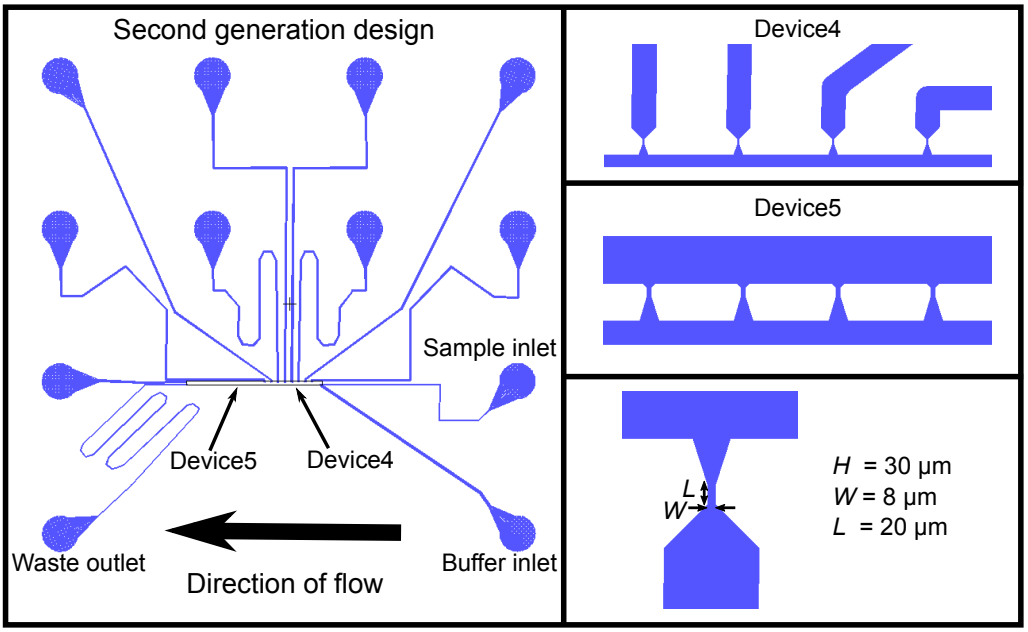

Figure 5.16: Second generation shim design. It consists of two devices in parallel, Device4 and 5. Zoom-ins of each design structure is shown together with an insert of a single trap and its dimensions.

Design

The second generation shim consists of two devices in parallel, both with parallel traps similar to Device3. All channels are 30 μm high and their structure is shown in Figure 5.16. The devices have two shared inlets, one for particles and one for a buffer which aligns the particles and keeps them in the traps after capture. Device4 has eight traps in parallel with the same dimensions as the Device2 traps. They have a width of 8 μm, a length of 20 μm and are positioned with a pitch of 400 μm. The triangular area where particles are caught has also been decreased to avoid creating a dead volume around the trapped particles, where particles can get caught. It is made to fit a 20 μm sphere, which is the largest expected cell size. The traps are connected to separate outlets through outlet channels that all have equal lengths and widths, and therefore also the same resistance.

Device5 has 15 traps in parallel with a shared outlet. Obviously this device cannot capture single cells in separate outlets, instead it serves as a backup. A lot of dimensions were changed from the first to the second design generation, and in the case Device4 does not work, it can either be because of the trap dimensions or the channel structure. If Device5 captures single cells, it is the channel structures that must be improved, and if Device5 fails it can be concluded that the trap dimensions should be changed. The traps all have the same dimension as traps in Device4. All main channels are at least 50 μm wide to prevent cell clogging.

Semi-3D simulations were used to determine s_c for both devices, and the results are listed in Table 5.5. The critical size increases drastically from the first to the last trap of

Table 5.5: Critical size of traps in the Device2 and Device3 designs.

	Device4		Device5	
Trap	First	Last	First	Last
s_c [μm]	22.4	33.7	22.6	47.1

each device. This is because as the fluid moves along the feeding channel past the traps there are fewer paths leading to the outlets, so a larger percentage of the fluid will move through the traps. The s_c is again too large to capture single beads, but the traps in Device3 had similar critical sizes and were able to capture single cells because they block the flow through traps more efficiently.

Chip fabrication

The chips were injection moulded with Recipe 1 and bonded at standard parameters to 150 μm thick foils. Images of the shim, an injection moulded chip and a sealed chip are shown in Figure 5.17.

The shim had smooth structures with a height of 30 μm in all channels, except for the traps where the height is 26 μm, because the silicon etching process is aspect-ratio dependent. The stated height measurements are documented in Appendix C. Some stress marks were observed, but they were very small compared to the channel dimensions and did not have an effect on the bonding quality. The stress marks are not expected to have an influence on trapping efficiency.

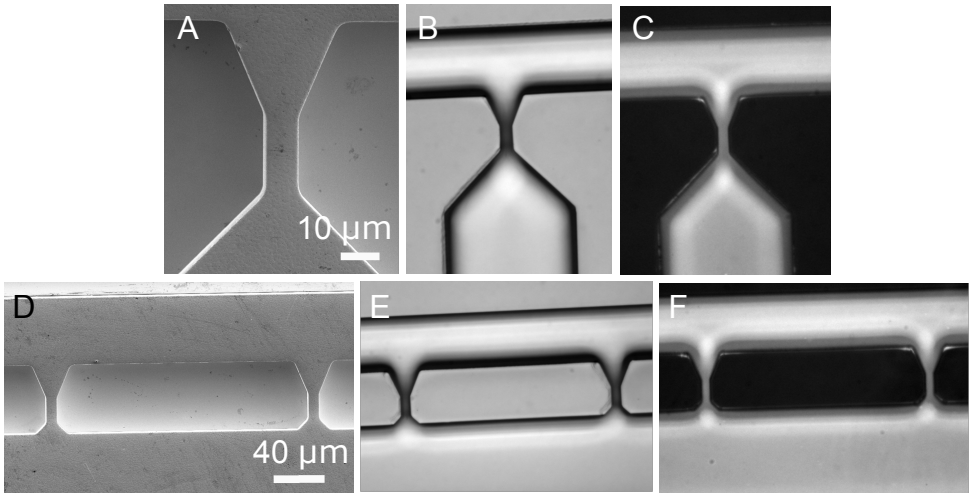

Figure 5.17: (A) SEM image of Device4 on the shim. (B)-(C) Bright field images of Device4 on an injection moulded chip before and after bonding. (D) SEM image of Device5 on the shim. (E)-(F) Bright field images of Device5 on an injection moulded chip before and after bonding.

Experiments

The chips were characterised with fluorescent 10 μm beads mixed to a concentration of 3×10^5 beads/mL. The results are shown in Figure 5.18, which shows that many beads were captured in each trap, and they even went outside the triangular area in Device4. The trapping efficiency was greatly increased and only few beads skipped the traps. As expected the s_c is too large for single bead capture.

The chips were then tested with LS174T cells at the WIMM in Oxford. A concentration of 300,000 cells/mL was used since it gave a good flow of cells, where individual cells were easy to follow. All cells went through the traps on Device4. They deformed and then quickly squeezed through the traps, and cells even went through at applied pressures as low as 2 mbar. The cells went through the first traps and never made it to Device5, and it could not be determined whether cells would also go through these traps.

Freeze-fracture investigation had shown that chips bonded at 128 °C on the traps experienced a 10 times increase in hydraulic resistance and a large decrease in critical size. Second generation chips bonded with those parameters were also tested with LS174T cells, and the results are shown in Figure 5.19. Large cells and cell clumps slowly squeezed through the traps or were in some rare cases trapped. Cells also went through traps in Device5 and it was concluded that this set of trap dimensions would not be able to capture single cells.

The Device4 traps have dimensions similar to the Device2 and 3 traps that captured cells, and they fulfil all the requirements for successful trapping, but they did not work as intended. It is evident that cells go through traps in Device4 because they deform, which could be because of high velocities of the fluid going through the traps. Semi-3D

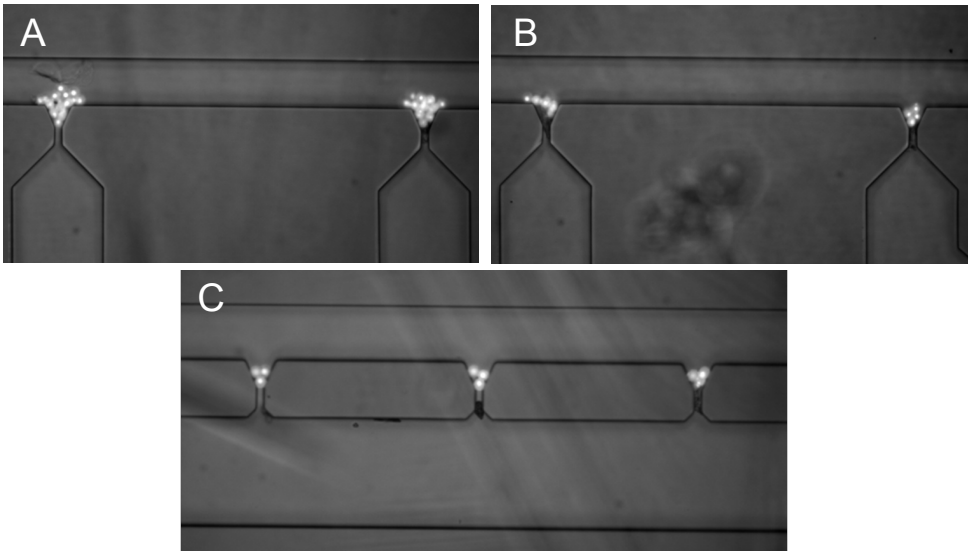

Figure 5.18: Combined fluorescence and bright field images of 10 μm beads in second generation chips. (A)-(B) Beads captured in Device4. (C) Beads captured in Device5. Multiple beads were captured as expected.

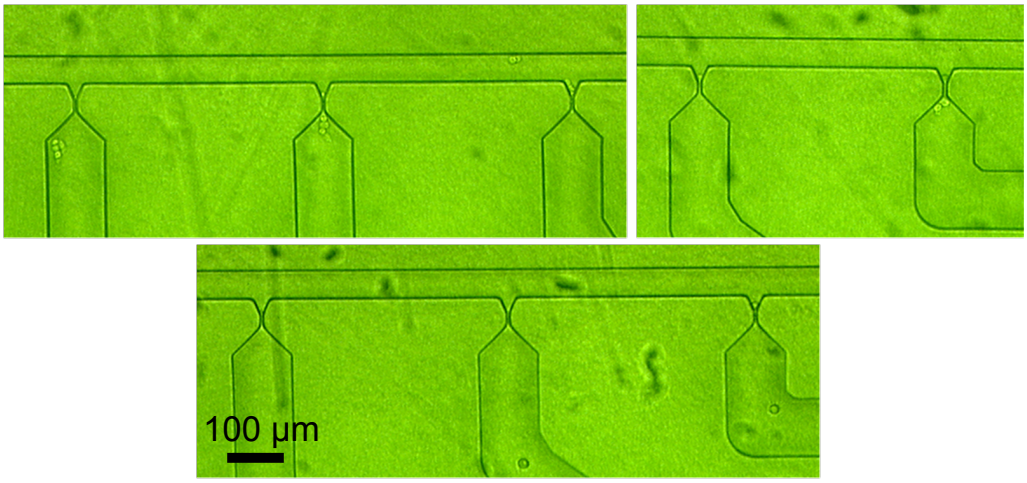

Figure 5.19: Bright field images of cells in Device4 chips bonded at 128 °C directly on the traps. Cells that have squeezed through the traps are clearly visible and larger than the trap widths.

simulations of Device3 and 4 were made to investigate and compare the flow conditions and check whether the velocity is indeed higher in Device4 chips. Figure 5.20 shows the velocity at the first traps on both designs. To mimic the experimental conditions, an inlet pressure of 10 mbar for Device3, and 2 mbar for Device4, were used. The outlet pressures were set to 0 mbar and the no slip condition was used for all other boundaries. The highest velocity in both simulations is at the traps. For Device3 it is 4.7 mm/s and for Device4 it is 6.1 mm/s. It was shown that cells in Device3 chips would slowly move through the traps at applied pressures above 10 mbar, and since the trap dimensions of Device3 and 4 chips are similar it is reasonable to assume that cells experiencing a velocity above 4.7 mm/s will go through the traps. This explains why cells are not captured in Device4 chips since even at 2 mbar pressures the velocity is too high.

Conclusion

The bead capture efficiency was improved with the second generation chips because the critical size was increased, but multiple beads were captured in each trap. Cells went through the traps on both devices, so the trap dimensions or overall channel structure are not suited for cell capture. The most likely cause of the unsuccessful capture is the length of the traps and the high fluid velocity through the traps. In Device3 chips it was observed that cells moved into the trap. This does not work for cells in Device4, where the trap length is only 20 μm, which make it easier for the cells to squeeze through the traps. Simulations showed that the fluid velocity through the Device4 traps is higher than on Device3 even at 2 mbar pressure, which cause cells to deform enough to go through the traps. In conclusion it is not enough to make the smallest trap dimension smaller than the cells, and thus cell deformation must be taken into consideration when designing cell capture chips.

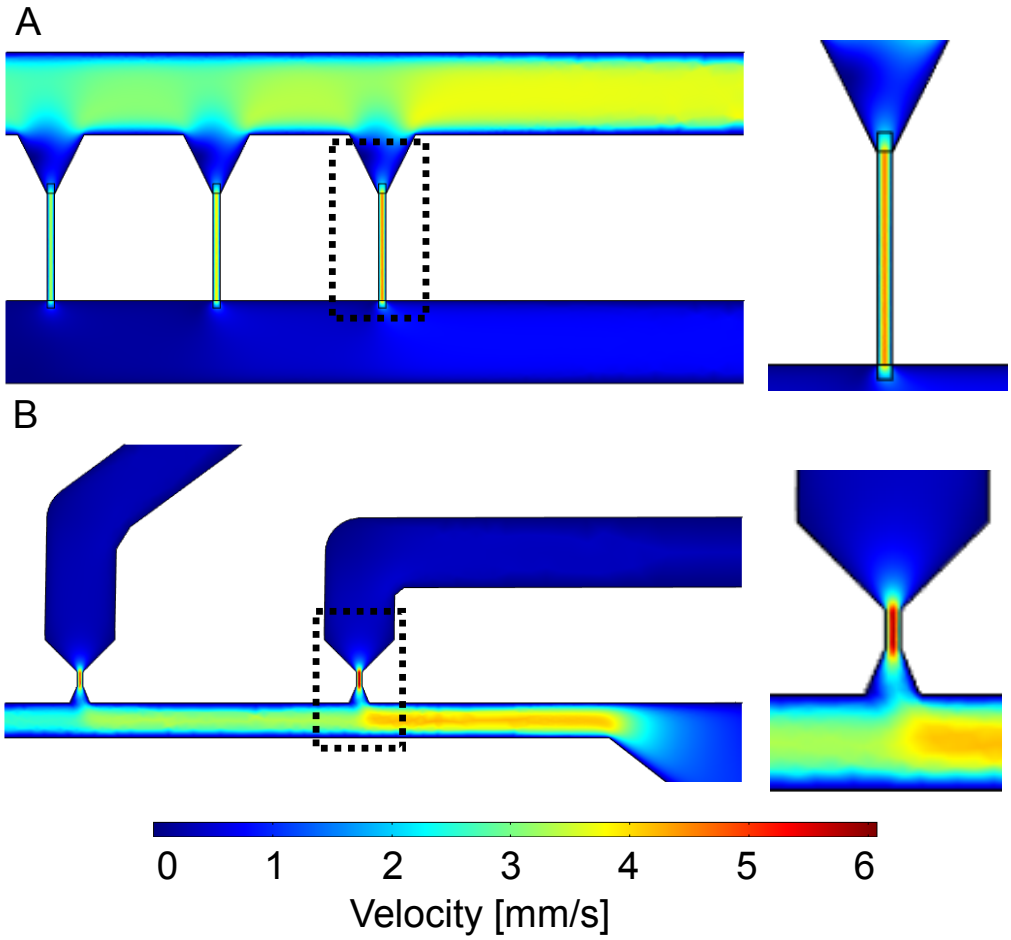

Figure 5.20: Semi-3D simulation of fluid velocity in the cell trapping designs. (A) Velocity in Device3 on chips bonded at the standard parameters with an inlet pressure of 10 mbar. (B) Velocity in Device4 chips bonded at standard parameters with an inlet pressure of 2 mbar. The positions of the zoom-ins are marked with dotted squares. The colour scale fits both plots.

5.5 Second generation - Capture in traps with separate outlets part 2

A new shim with two devices was created for single cell trapping in traps with separate outlets. The devices are named Device6 and Device7.

Design

The design consists of two separate devices with parallel traps. Both designs have two inlet channels and a waste outlet. Device6 has four traps with separate outlets, while Device7 has four times twenty traps in parallel with combined outlets. The trap cross sections are smaller than on Device4 and 5, so cells will not squeeze through as easily, and the traps are

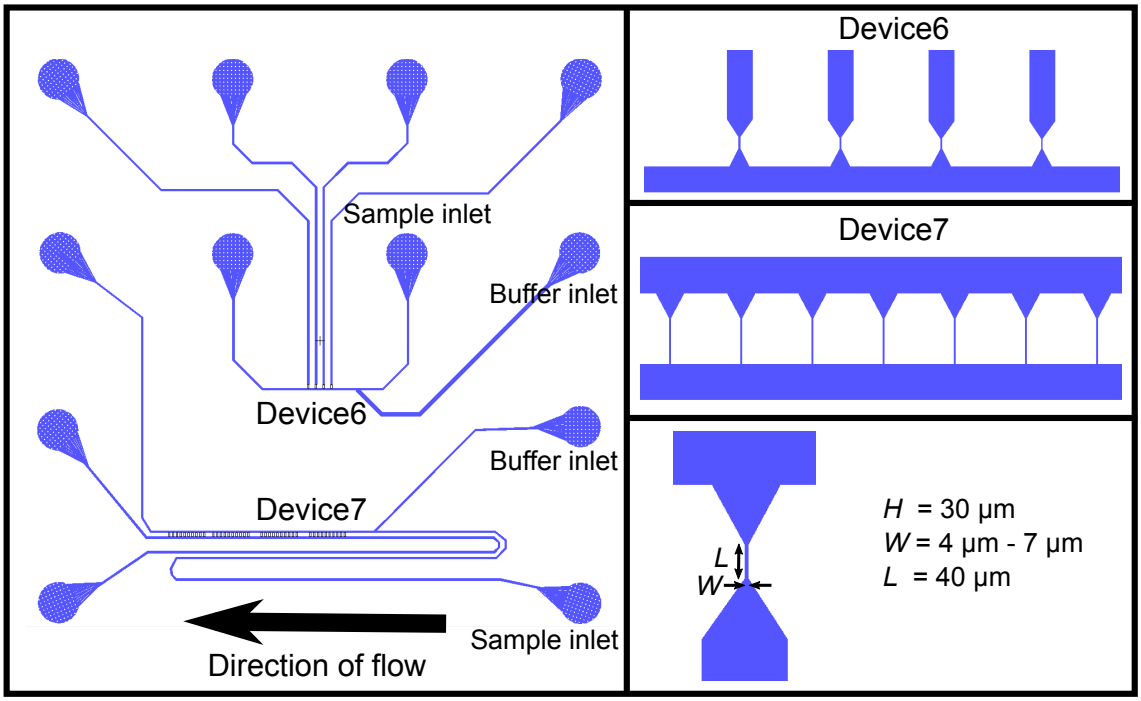

Figure 5.21: The Design6 and 7 shim design. The devices are separated and both have parallel traps. Zoom-ins of each design structure is shown together with an insert of a trap and its dimensions.

also longer. The smallest trap width is 4 μm, which is about the smallest width possible to fabricate on a 30 μm one-layered design. The channel structure is seen in Figure 5.21. The traps have widths of 4 μm, 5 μm, 6 μm and 7 μm and lengths of 40 μm. Device8 was analysed with simulations to find the critical size of the four traps. The velocity through the traps at 2 mbar applied pressure was also found, and the results are listed in Table 5.6. The critical size of the first two traps is close to the 21.7 μm for Trap1 traps that captured single cells, and the velocities are smaller, so cells should not squeeze through the traps. It is possible that the device can be driven at higher pressures since the trap cross sections are smaller.

Table 5.6: Simulated critical size and maximum velocity through traps in Trap3 with applied pressures of 2 mbar.

Trap width [μm]	s_c [μm]	Max. velocity [mm/s]
4	18.2	3.6
5	25.9	4.4
6	32.0	4.4
7	35.6	3.6

Chip fabrication

On the shim the main channels are 30 μm high, and the traps are 22 μm to 24 μm high and 1 μm wider than on the design. The measurements are documented in Appendix C. Chips were initially injection moulded with Recipe 1, but large stress marks around the traps were observed, and they interfered with the bonding, which was not complete around the traps. Instead Recipe 2 and Recipe 3 described in Section 2.4 were used. The first showed smaller stress marks and good filling for some chips, while others had very large stress marks. Recipe 3 chips had no stress marks, but also had poor filling. The shim and examples of injection moulded and bonded chips are seen in Figure 5.22. Both Recipe 2 and Recipe 3 chips were used for cell trapping experiments.

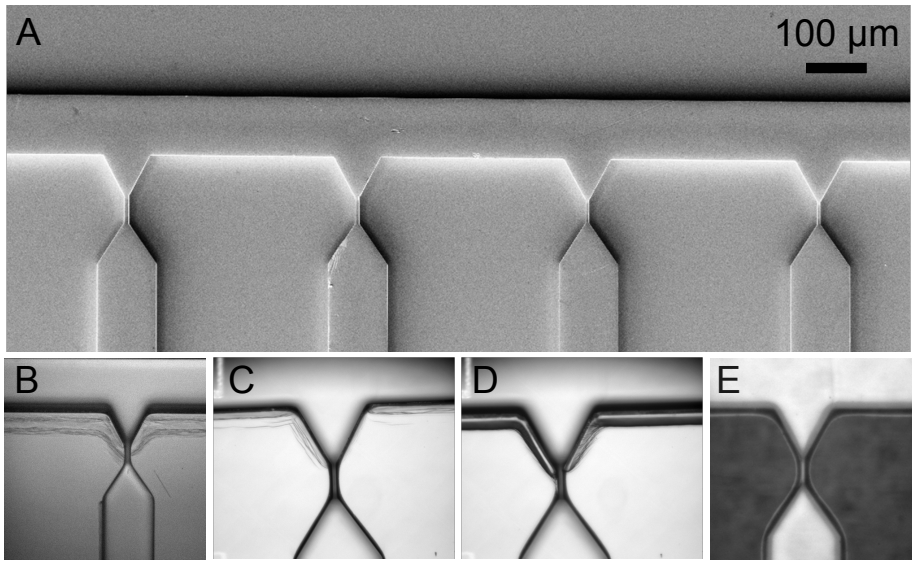

Figure 5.22: Images of Device6. (A) SEM image of traps on the shim. (B) Chip injection moulded with Recipe 1 and (C)-(D) Recipe 2, which was unstable and had variations in the stress marks. (E) Recipe 3 chip after bonding.

Experiments

Chips were tested with LS174T cells at the WIMM and with defrosted LS174T cells in a cell lab at DTU Nanotech. Images of experiments are seen in Figure 5.23. The cells were captured at 5 mbar pressure on both outlets. This is equivalent to trap velocities of 9 mm/s to 11 mm/s, and proves the hypothesis that traps with smaller cross sectional area can trap cells at higher velocities. The three most narrow traps captured both fresh and defrosted cells effectively, while many cells went through the widest trap before one was captured. In most traps either single or double cells were trapped. The cells were either stuck together before entering the trap or a second cell entered an occupied trap. Cells were trapped at applied pressures of 5 mbar. At 15 mbar pressure cells would go through all traps, so there is a large range of pressures that cannot be used. The Recipe 2 chips

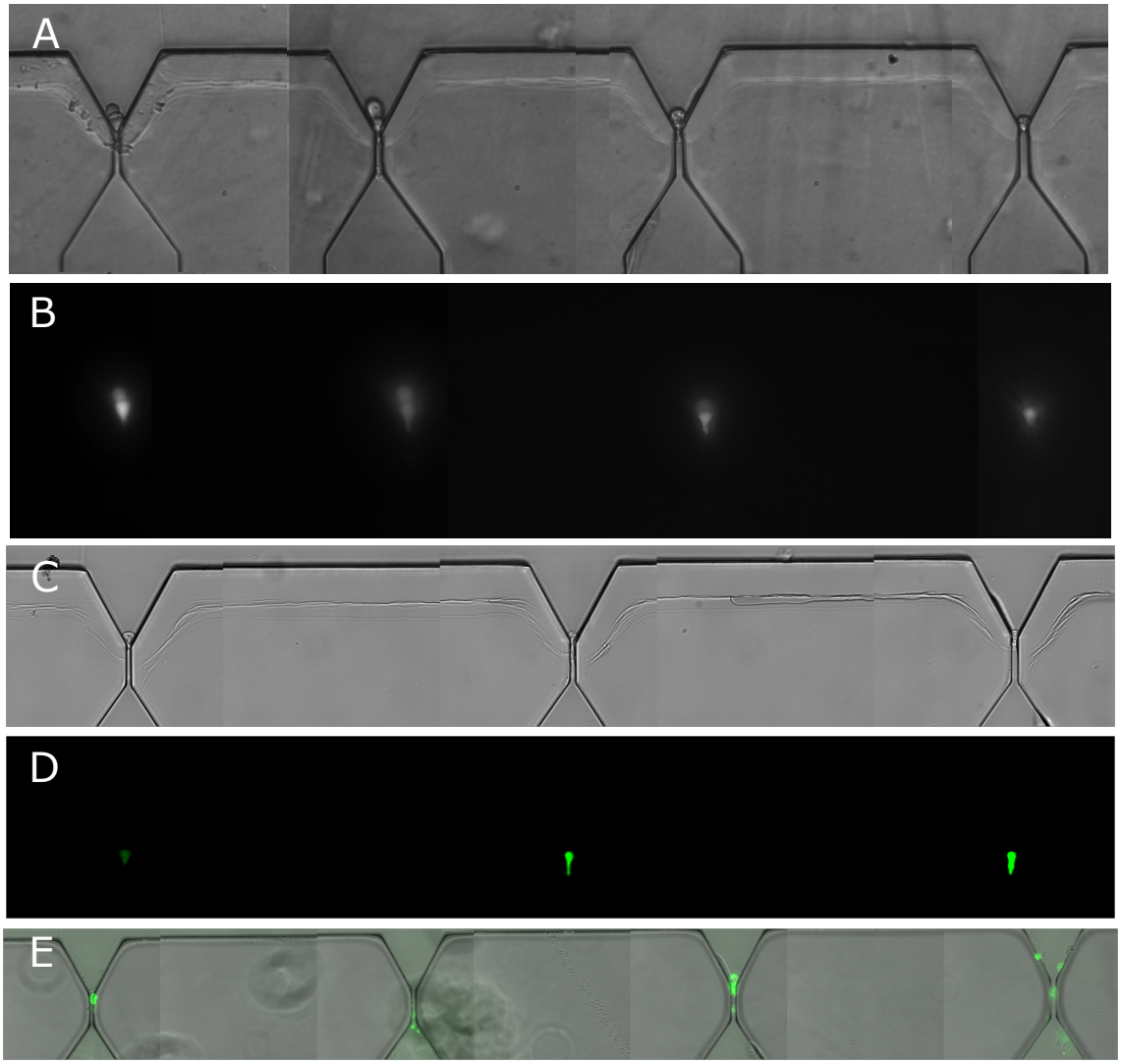

Figure 5.23: Cell capture on Device6. The traps on the left are the narrowest. (A)-(B) Bright field and fluorescence images of live cells trapped with chips injection moulded with Recipe 2. (C)-(D) Bright field and fluorescence images of defrosted cells trapped in a Recipe 2 chip. (E) Combined bright field and fluorescence image of cells trapped in a Recipe 3 chip.

trapped single cells efficiently. In chips injection moulded with Recipe 3 cells could go through the traps and multiple cells were trapped. Some cells were caught between the chip and lid, as seen in Figure 5.23E.

The overall purpose of the traps is to capture single cells and then either push them through to the outlets or extract their DNA and push that into the outlets. In an experiment it was demonstrated that cells can be captured and then intentionally be pushed through the traps. If the cells have been in the traps for about ten minutes (the time it takes to take images of all captured cells), they stick to the chip surface, and applying a pressure

of 15 mbar is no longer enough, as seen in Figure 5.24. Here cells were captured, the cell inlet pressure was turned off to prevent other cells from entering the device, and the buffer inlet pressure was increased to 15 mbar. The captured cells in the two widest traps went through to the outlets, and the other cells stayed. However by replacing the FACSFlow solution with a solution containing the enzyme Trypsin, the rest of the cells were also pushed through. Trypsin is commonly used by cell biologist to re-suspend cells that have adhered to a surface.

Once cells were caught they could sit in the traps for several hours without loss in their fluorescence signal and the device therefore have other applications for example as an array for single cell analysis. Since Device6 worked, it was not necessary to test Device7, which cannot be used for single cell analysis, since the traps have a shared outlet.

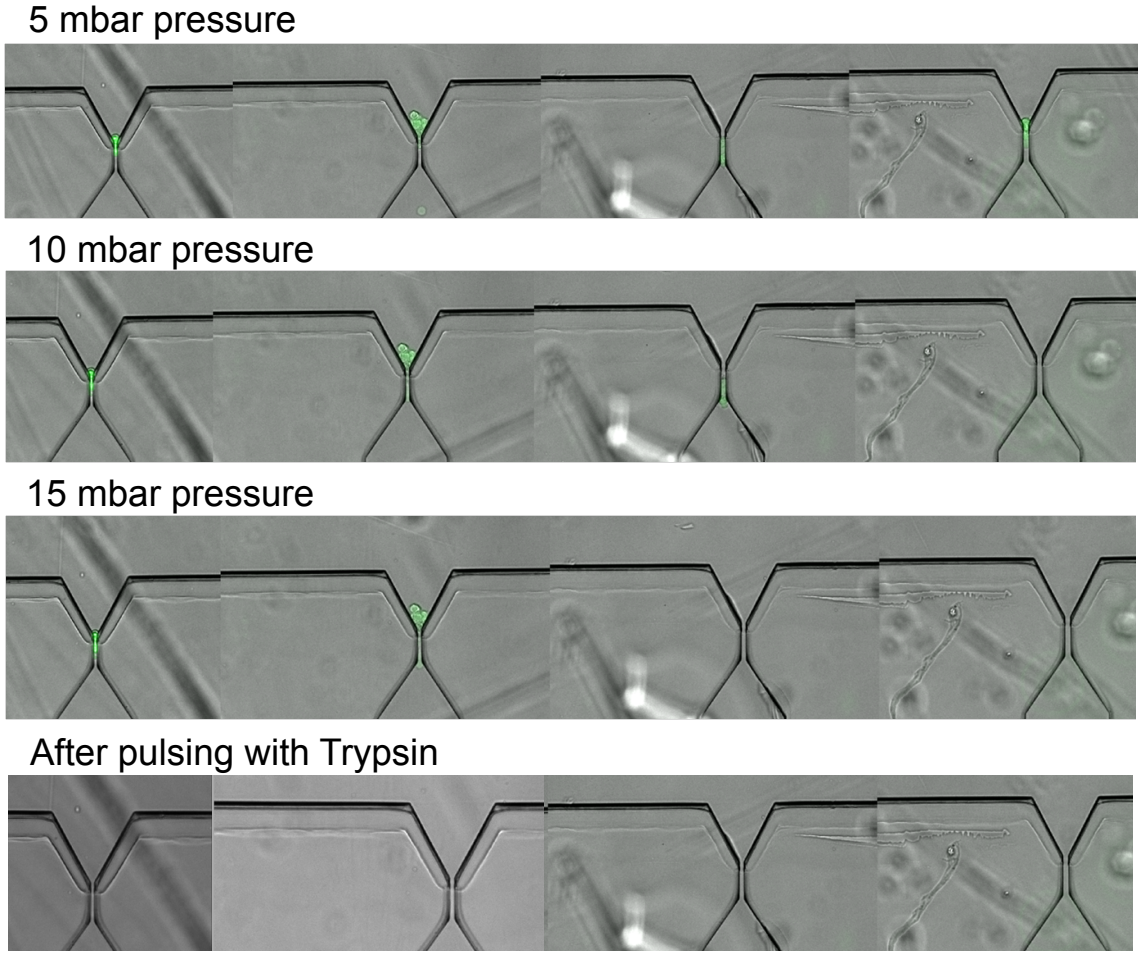

Figure 5.24: Experiments where defrosted cells were captured and then pushed through to the outlets for further treatment. Cells where captured at 5 mbar pressure. The cell inlet pressure was turned off and the buffer inlet pressure increased to 10 mbar and then 15 mbar. Cells did not go through the narrowest traps, so the FACSFlow solution was replaced with Trypsin, which enabled the cells to go through, and all traps were emptied.

Conclusion

Single cells were efficiently captured in the Device6 as predicted by the hypothesised particle trapping requirements. The chips injection moulded with Recipe 3 were unable to capture single cells because the channels were not completely filled during injection moulding. The trap widths were only 1 μm apart, yet many cells went through the widest trap, few went through the second widest and no cells went through the narrowest traps at 5 mbar pressure. However cells went through all traps at 15 mbar pressures. The experiments demonstrate that cell trapping is limited to a small range of trap dimensions and fluid velocities, and the quality of the injection moulding is very important for the cell trapping outcome.

5.6 Third generation - Final design

The third and final design generation has the purpose of capturing single cells reliably so the chips can be used for single cell analysis by researchers in a biology lab.

Design

The Device8 design has one device with eight parallel traps that have the same dimensions as the smallest trap in Device6, i.e. a width of 4 μm and a length of 40 μm. The device structure is similar to the previous designs, but with an additional inlet for adding lysis buffer once the cells are trapped. In this way the lysis buffer can be added directly to the third inlet while there is still pressure on the buffer inlet. This removes the risk of backflow that can cause the trapped cells to move out of the traps. The channel structure is seen in Figure 5.25. Some of the traps are placed far from the outlets, which results in large resistances of the outlet channels and a smaller critical size. Therefore the width of the feeding channel was decreased to 50 μm compared to 100 μm in Device6, thereby increasing the critical size.

The design was investigated with semi-3D simulations, and the results are listed in Table 5.7. The critical size has generally decreased, but should still be large enough to trap

Table 5.7: Simulated critical size and maximum velocity through all traps in Device8 with applied pressures of 8 mbar to 10 mbar.

Trap no. from inlet	s_c [μm]	Max. velocity [mm/s]
1	14.3	9.0
2	15.8	9.5
3	12.2	5.5
4	13.7	6.0
5	13.8	5.5
6	13.1	4.5
7	18.8	7.5
8	18.7	6.5

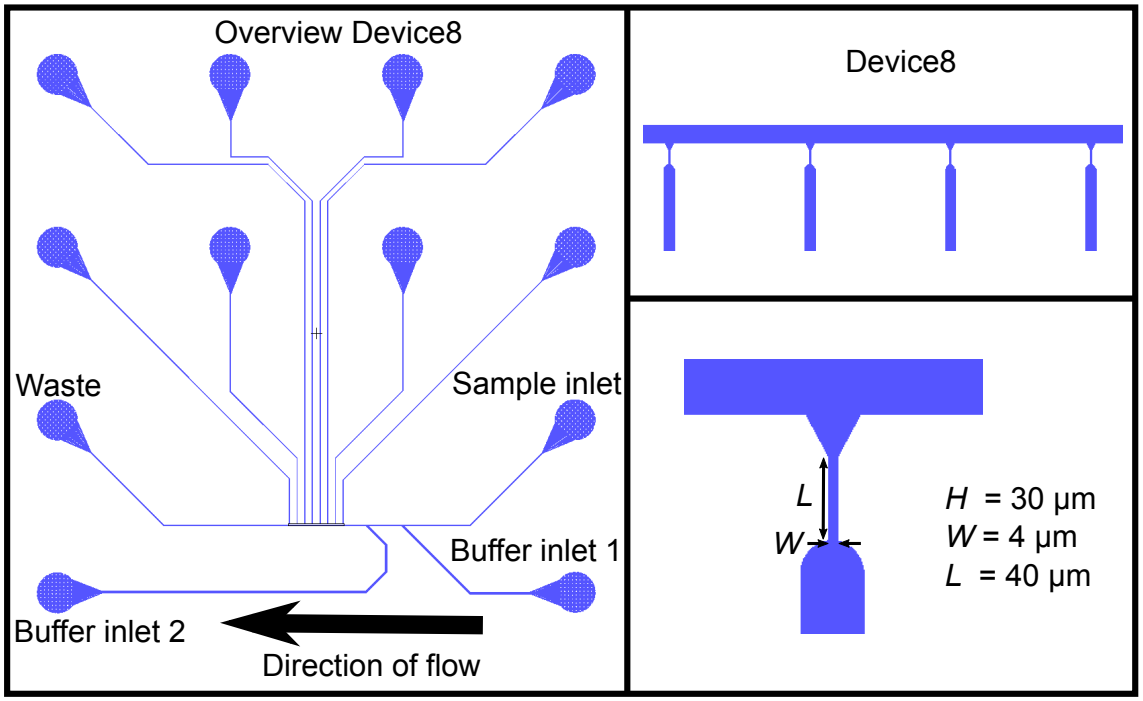

Figure 5.25: The Device8 design. It has one device with eight parallel traps. A zoom-in of the trapping structures is shown together with an insert of a trap and its dimensions.

cancer cells. The velocities are in the same range or smaller than in Device6, so cells are not expected to go through any of the traps. The total resistance of the channel system is increased, which gives a larger range of applied pressures to use and makes the devices easier to use. User-friendliness is important since the devices are made to be used in labs where microfluidics is not necessarily the main research area.

Chip Fabrication

The shim was fabricated with the usual clean room process and again a difference between main channel height and trap height was observed. The main channels were approx. 31 μm high, while the traps were 22 μm high with a width of 4.5 μm. Measurements of the shim dimensions are included in Appendix C. Chips were initially injection moulded with Recipe 2, and the result is shown in Figure 5.26 together with the shim. The traps were positioned in a lower area of the chip to make all Luer-ports available for the device. This meant that the traps were located further away from the center of contraction, which resulted in large stress marks around the traps. On Figure 5.26C it is clear that the bonding is not tight around the traps, which could influence the trapping quality as observed with the Device6 chips. Also these chips should be delivered to collaborators in another lab, and the stress marks gave the chips a somewhat unappealing and unfinished look. It was necessary to optimize the injection moulding, which resulted in a new set of bonding parameters called Recipe 4, as discussed in Section 2.4.

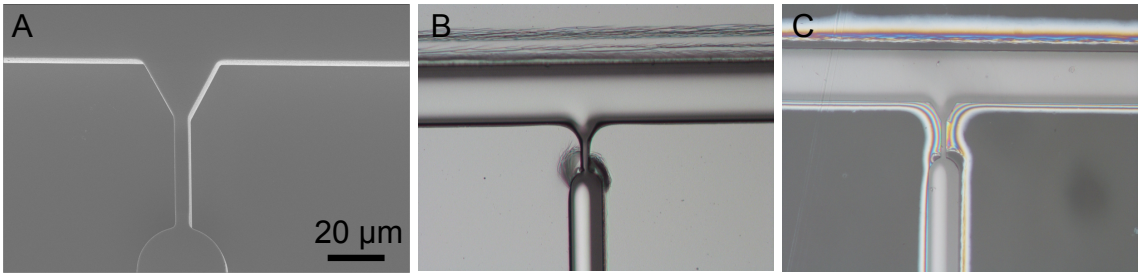

Figure 5.26: (A) SEM image of a trap on the third generation shim. (B)-(C) Bright field images of Device8 chips injection moulded with Recipe 2, before and after bonding.

Chips were bonded at 120 °C and 2.5 MPa for 5 min. and then 0.5 MPa for 1 min. The final small pressure ensures that the sealing is completed even around the edges of the chip, and was introduced mainly to improve the overall look of the chips.

To be sure the final chips had a good bonding quality they were freeze-fractured and the traps were visualised in a SEM as shown in Figure 5.27. It was observed that the structures were filled and the sealing was tight around the trap. The bright field image in Figure 5.27B shows a bonded chip, which looks much nicer and more finished than the chip in Figure 5.26C. A few Device8 chips were freeze-fractured and they all revealed trap cross sections, meaning that the freeze-fracture method described in Section 5.3 has a precision of at least 60 μm, which is the length of the trap including the triangular area.

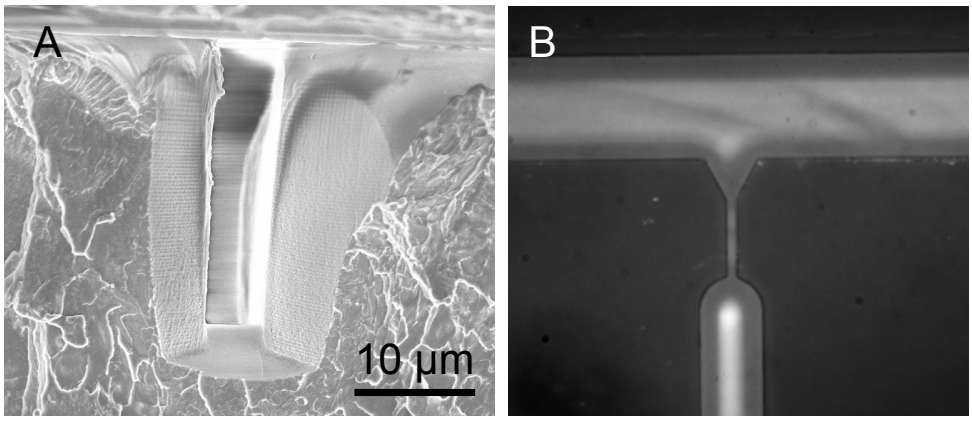

Figure 5.27: (A) Freeze-fracture on Recipe 4 chip with almost completely filled structures. (B) Final bonded chip showing that the bonding is tight around the trap.

Experiments

Before sending the Device8 chips to the collaborators, the devices were quickly tested with defrosted LS174T cells as shown in Figure 5.28. Pressures of 10 mbar were applied to the cell and buffer inlets with 8 mbar on the third inlet to ensure the flow is directed towards the outlets. All traps except one were occupied with cells, and no cells went through

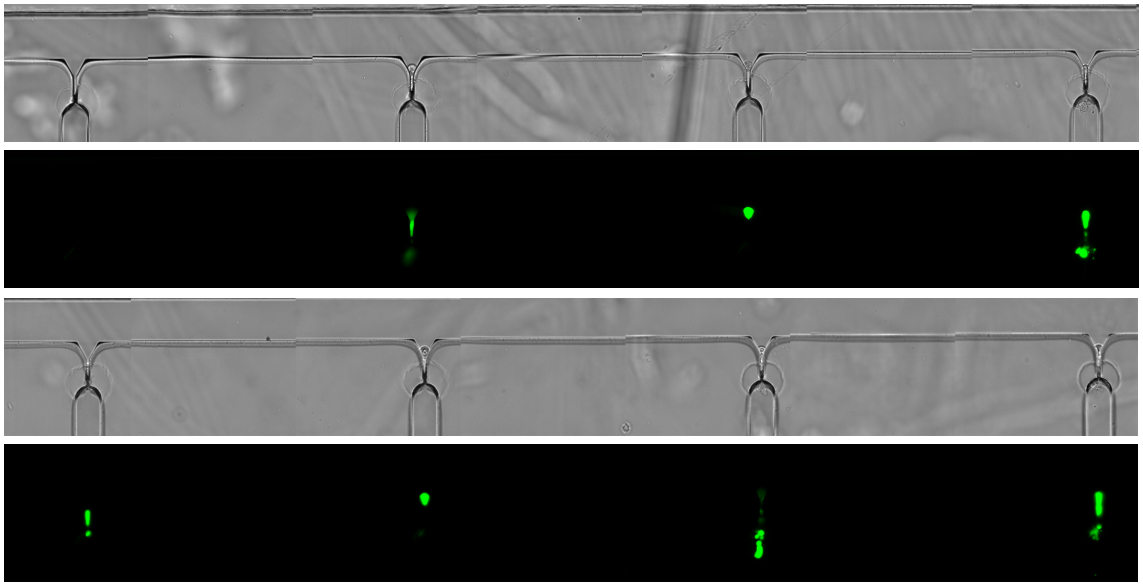

Figure 5.28: Bright field and fluorescence images of defrosted cells captured in a Device8.

the traps. Single cells were captured in two of the traps and cell aggregates in the rest. Defrosted cells are more prone to clumping and it is expected that a higher ratio of single cells will be captured when using fresh cells. A protocol for using Device8 is found in Appendix E.

The chips were delivered to the collaborators who used the chips with great success. They reported a capture of six to eight single cells for each experiment and they are currently using the chips for on-chip extraction of DNA. They then amplify the extracted DNA directly in the outlets after which they pipette it out for off-chip analysis.

Conclusion

Devices for single cell trapping were fabricated and delivered to another research lab, where they are still used for analysis of DNA from single cells. The devices were optimized with regards to flow conditions such as total resistance of the system and velocities through the traps. The injection moulding parameters were also optimised with focus on completely filling the traps while minimising the stress marks so they did not interfere with the bonding quality. Finally the bonding process was optimised to give the chips a finished look. Single cell capture was demonstrated with the optimised device, which can capture up to eight single cells in parallel.

5.7 Chapter summary

Hydrodynamic single cell trapping was accomplished through development of increasingly improved designs. The first design captured single cells in traps with shared outlets, next single cell capture in traps with separate outlets was obtained, and finally a device for

parallel capture of eight single cells was produced and used for successful DNA extraction from single cells.

During the design development, new demands to the injection moulding and bonding arose, and both processes were optimised. It was possible to obtain a satisfactory trap quality, where the structures were completely filled and tightly sealed, so the desired trap dimensions were realised. A method for investigation of sealed chips was presented. The freeze-fracture method does minimal change to the chip structures and was shown to have a precision of at least 60 μm. Freeze-fracture was used to confirm that the trap dimension are unaltered by the standard bonding procedure, and to investigate how structures can be altered intentionally to improve the capture efficiency of cell trapping devices.

The trap dimensions and resistance are not enough to determine a design's particle capture capability, instead the critical size of traps was introduced. It determines the maximum particle size that will be captured in traps with known dimensions, and can be optimised to trap either single cells or single beads of a certain size, by setting the device dimensions such that the critical size is just above the particle size. Chips were optimised to trap LS174T cells, and have not been tested on other cell lines. It is expected that cell lines with different physical characteristics like average size and deformability require other trap dimensions.

6 Conclusion

LoC devices for rare cell separation and single cell trapping have been developed and tested. The device functionality was based on hydrodynamic principles and they were fabricated in thermoplastics using injection moulding from a nickel master, and sealed with UV-assisted thermal bonding to a plastic foil. The injection moulding process parameters were optimised for different designs, and high quality structures were obtained. The fabrication process ensures potential for mass production of the devices. The 12 Luer-format used for injection moulding of the chips enables easy connection to common lab equipment and thus the chips have potential for commercialisation.

Separation of cancer cells and WBCs was realised with the passive size-based microfluidic PFF technique. Two PFF devices were developed and tested for cell separation. The devices were characterised through a combination of analytical calculations, numerical simulations and experiments with nano- and microbeads to optimise channel dimensions and flow conditions on the chips. Finally the devices were tested with LS174T cancer cells spiked into WBCs. The goal of a simultaneous recovery of over 90 % of the cancer cells and removal of over 90 % of the WBCs was obtained on both PFF devices. It was suggested that the high separation efficiencies were obtained because of differences in cell size as well as cell deformability. It was demonstrated that the cell types behave differently in the devices leading to a significant difference between the critical diameters of the WBCs and the cancer cells, which is highly advantageous. Cell deformability is a limiting factor for other passive separation techniques, but can be exploited to improve the separation in PFF devices. The samples were processed at throughputs up to 3×10^6 cells/min, which is comparable to flow rates of other passive separation techniques, however the high sample flow rates resulted in reduced WBC removal because of inertial effect. The PFF technique has shown great potential for rare cell separation, and with some improvements it can possibly be used to isolate CTCs from clinical samples.

Capture of single cells was realised with hydrodynamic trapping devices. Several designs were developed with increased improvement in capture efficiency. Many channel layouts and trap dimensions were tested and a final optimised design for parallel capture of eight single cells was created. It was demonstrated that the chips can be used to obtain uncontaminated DNA from single cells. The amount of parallel traps was limited by the chip format, and can potentially be increased to any number of traps. Requirements for single particle trapping were presented and demonstrated through several microbead and cancer cell experiments. A critical size of the traps was introduced and determined by numerical

simulations of each design. It was shown that the critical size can be optimised to obtain single particle capture. It is expected that it can be used to optimise any hydrodynamic trapping devices.

A method for investigation of sealed chips was developed and used to determine trap cross sections on the cell capture devices. The freeze-fracture method was used to investigate structures that had been altered intentionally by high temperature bonding. The altered devices were used for single particle capture and had an improved efficiency compared to the unaltered structures. It was also used to verify that the thermal bonding process does not alter the microstructures at the standard bonding parameters used for sealing of chips in this thesis.

With the devices developed in this thesis LoC systems have become one step closer to commercialisation of devices for rare cell isolation and single cell trapping. This combination has the potential to increase the understanding of differences between individual cells. An understanding, which is necessary for improving cancer cell treatment.

7 Outlook

The injection moulding process was shown to give a good replication of the designed devices. Some of the recipes were however unstable, and chips from the same batch did not always have the same quality. It is possible that the injection moulding could be improved by using a variotherm process.

While the cycle process was about one minute per device for the injection moulding, the chip sealing took almost ten minutes for each device. It would be advantageous if several chips could be bonded in parallel with the same quality as described in the thesis.

The total resistance of both PFF devices was relatively low, meaning that small variations in the applied pressure has a great effect on flow conditions such as pinching width, sample flow rate and the amount of buffer vs. sample fluid needed to operate the devices. This means that the devices are very unstable and cannot and has to be monitored during the entire experiment. To increase the stability of the devices, the total hydraulic resistance can be reduced by placing meander-shaped segments at all inlet or outlet channels. This would lead to a lower maximum throughput, but the devices could instead be run in parallel without having to monitor the separation.

The efficiency of the devices could be improved by minimising the impact of inertial effects as the sample flow rates are increased. The sharp corner that cells has to flow past to get into the small particle outlet could be smoother, so the change in the cell trajectories would be smaller, and cells would be less likely to deflect from it. The corner contributes to the shear rate experienced by cells, but cells experience a shear rate of the same order of magnitude in the pinched segment, so soft cells would likely still deform during the separation. With these improvements the PFF technique would have a great potential for separation of clinical samples.

The cell trapping devices were limited by the 12 Luer-format, but should easily be adapted to other formats allowing a greater amount of single cells to be captured in parallel. It should also be possible to operate multiple Device8 chips in parallel for a larger cell trapping throughput.

Bibliography

[1] Shu Chien, Shunuchi Usami, Robert J Dellenback, and Magnus I Gregersen. Shear-dependent deformation of erythrocytes in rheology of human blood. *American Journal of Physiology–Legacy Content*, 219(1):136–142, 1970.

[2] Palaniappan Sethu, Aaron Sin, and Mehmet Toner. Microfluidic diffusive filter for apheresis (leukapheresis). *Lab on a Chip*, 6(1):83–89, 2006.

[3] Bruce Wetzel and Harry Schaefer. Scanning electron microscope image of blood cells. https://visualsonline.cancer.gov/details.cfm?imageid=2129, 1982.

[4] Subra Suresh. Biomechanics and biophysics of cancer cells. *Acta Materialia*, 55(12):3989–4014, 2007.

[5] Ann F Chambers, Alan C Groom, and Ian C MacDonald. Metastasis: dissemination and growth of cancer cells in metastatic sites. *Nature Reviews Cancer*, 2(8):563–572, 2002.

[6] Patrizia Paterlini-Brechot and Naoual Linda Benali. Circulating tumor cells (ctc) detection: clinical impact and future directions. *Cancer letters*, 253(2):180–204, 2007.

[7] Tannishtha Reya, Sean J Morrison, Michael F Clarke, and Irving L Weissman. Stem cells, cancer, and cancer stem cells. *nature*, 414(6859):105–111, 2001.

[8] Massimo Cristofanilli, G Thomas Budd, Matthew J Ellis, Alison Stopeck, Jeri Matera, M Craig Miller, James M Reuben, Gerald V Doyle, W Jeffrey Allard, Leon WMM Terstappen, et al. Circulating tumor cells, disease progression, and survival in metastatic breast cancer. *New England Journal of Medicine*, 351(8):781–791, 2004.

[9] TG Ntouroupi, SQ Ashraf, SB McGregor, BW Turney, A Seppo, Y Kim, X Wang, MW Kilpatrick, P Tsipouras, T Tafas, et al. Detection of circulating tumour cells in peripheral blood with an automated scanning fluorescence microscope. *British journal of cancer*, 99(5):789–795, 2008.

[10] Baldwin H Tom, Lynne P Rutzky, Milda M Jakstys, Ryoichi Oyasu, Celia I Kaye, and Barry D Kahan. Human colonic adenocarcinoma cells. *In vitro*, 12(3):180–191, 1976.

[11] Catherine Alix-Panabières and Klaus Pantel. Technologies for detection of circulating tumor cells: facts and vision. *Lab on a Chip*, 14(1):57–62, 2014.

[12] Sabine Riethdorf, Herbert Fritsche, Volkmar Müller, Thomas Rau, Christian Schindlbeck, Brigitte Rack, Wolfgang Janni, Cornelia Coith, Katrin Beck, Fritz Jänicke, et al. Detection of circulating tumor cells in peripheral blood of patients with metastatic breast cancer: a validation study of the cellsearch system. *Clinical Cancer Research*, 13(3):920–928, 2007.

[13] Shannon L Stott, Chia-Hsien Hsu, Dina I Tsukrov, Min Yu, David T Miyamoto, Belinda A Waltman, S Michael Rothenberg, Ajay M Shah, Malgorzata E Smas, George K Korir, et al. Isolation of circulating tumor cells using a microvortex-generating herringbone-chip. *Proceedings of the National Academy of Sciences*, 107(43):18392–18397, 2010.

[14] Emre Ozkumur, Ajay M Shah, Jordan C Ciciliano, Benjamin L Emmink, David T Miyamoto, Elena Brachtel, Min Yu, Pin-i Chen, Bailey Morgan, Julie Trautwein, et al. Inertial focusing for tumor antigen–dependent and–independent sorting of rare circulating tumor cells. *Science translational medicine*, 5(179):179ra47–179ra47, 2013.

[15] Giovanna Vona, Abdelmajid Sabile, Malek Louha, Veronique Sitruk, Serge Romana, Karin Schütze, Frédérique Capron, Dominique Franco, Mario Pazzagli, Michel Vekemans, et al. Isolation by size of epithelial tumor cells: a new method for the immunomorphological and molecular characterization of circulating tumor cells. *The American journal of pathology*, 156(1):57–63, 2000.

[16] Isabelle Desitter, Bella S Guerrouahen, Naoual Benali-Furet, Janine Wechsler, Pasi A Jaenne, Yanan Kuang, Masahiko Yanagita, Lilin Wang, Jillian A Berkowitz, Robert J Distel, et al. A new device for rapid isolation by size and characterization of rare circulating tumor cells. *Anticancer research*, 31(2):427–441, 2011.

[17] Yadong Tang, Jian Shi, Sisi Li, Li Wang, Yvon E Cayre, and Yong Chen. Microfluidic device with integrated microfilter of conical-shaped holes for high efficiency and high purity capture of circulating tumor cells. *Scientific reports*, 4, 2014.

[18] David R Parkinson, Nicholas Dracopoli, B Gumbs Petty, Carolyn Compton, Massimo Cristofanilli, Albert Deisseroth, Daniel F Hayes, Gordon Kapke, Prasanna Kumar, J Sh Lee, et al. Considerations in the development of circulating tumor cell technology for clinical use. *J Transl Med*, 10(1):138, 2012.

[19] Ali Asgar S Bhagat, Hansen Bow, Han Wei Hou, Swee Jin Tan, Jongyoon Han, and Chwee Teck Lim. Microfluidics for cell separation. *Medical & biological engineering & computing*, 48(10):999–1014, 2010.

[20] Daniel R Gossett, Westbrook M Weaver, Albert J Mach, Soojung Claire Hur, Henry Tat Kwong Tse, Wonhee Lee, Hamed Amini, and Dino Di Carlo. Label-free cell separation and sorting in microfluidic systems. *Analytical and bioanalytical chemistry*, 397(8):3249–3267, 2010.

[21] Andreas Lenshof and Thomas Laurell. Continuous separation of cells and particles in microfluidic systems. *Chemical Society Reviews*, 39(3):1203–1217, 2010.

[22] P Sajeesh and Ashis Kumar Sen. Particle separation and sorting in microfluidic devices: a review. *Microfluidics and nanofluidics*, 17(1):1–52, 2014.

[23] Anne Y Fu, Charles Spence, Axel Scherer, Frances H Arnold, and Stephen R Quake. A microfabricated fluorescence-activated cell sorter. *Nature biotechnology*, 17(11):1109–1111, 1999.

[24] Xiaoyuan Hu, Paul H Bessette, Jiangrong Qian, Carl D Meinhart, Patrick S Daugherty, and Hyongsok T Soh. Marker-specific sorting of rare cells using dielectrophoresis. *Proceedings of the National Academy of Sciences of the United States of America*, 102(44):15757–15761, 2005.

[25] Nicole Pamme and Claire Wilhelm. Continuous sorting of magnetic cells via on-chip free-flow magnetophoresis. *Lab on a Chip*, 6(8):974–980, 2006.

[26] T Franke, S Braunmüller, L Schmid, A Wixforth, and DA Weitz. Surface acoustic wave actuated cell sorting (sawacs). *Lab on a chip*, 10(6):789–794, 2010.

[27] Hisham Mohamed, James N Turner, and Michele Caggana. Biochip for separating fetal cells from maternal circulation. *Journal of Chromatography A*, 1162(2):187–192, 2007.

[28] Timothy A Crowley and Vincent Pizziconi. Isolation of plasma from whole blood using planar microfilters for lab-on-a-chip applications. *Lab on a Chip*, 5(9):922–929, 2005.

[29] Kevin Loutherback, Joseph D'Silva, Liyu Liu, Amy Wu, Robert H Austin, and James C Sturm. Deterministic separation of cancer cells from blood at 10 ml/min. *AIP advances*, 2(4):042107, 2012.

[30] Masumi Yamada and Minoru Seki. Hydrodynamic filtration for on-chip particle concentration and classification utilizing microfluidics. *Lab on a Chip*, 5(11):1233–1239, 2005.

[31] Sungyoung Choi, Taeyun Ku, Seungjeong Song, Chulhee Choi, and Je-Kyun Park. Hydrophoretic high-throughput selection of platelets in physiological shear-stress range. *Lab on a Chip*, 11(3):413–418, 2011.

[32] Sungyoung Choi, Seungjeong Song, Chulhee Choi, and Je-Kyun Park. Continuous blood cell separation by hydrophoretic filtration. *Lab on a Chip*, 7(11):1532–1538, 2007.

[33] Ali Asgar S Bhagat, Sathyakumar S Kuntaegowdanahalli, and Ian Papautsky. Inertial microfluidics for continuous particle filtration and extraction. *Microfluidics and nanofluidics*, 7(2):217–226, 2009.

[34] Soojung Claire Hur, Nicole K Henderson-MacLennan, Edward RB McCabe, and Dino Di Carlo. Deformability-based cell classification and enrichment using inertial microfluidics. *Lab on a Chip*, 11(5):912–920, 2011.

[35] Ali Asgar S Bhagat, Han Wei Hou, Leon D Li, Chwee Teck Lim, and Jongyoon Han. Pinched flow coupled shear-modulated inertial microfluidics for high-throughput rare blood cell separation. *Lab on a Chip*, 11(11):1870–1878, 2011.

[36] TM Geislinger, B Eggart, S Braunmüller, L Schmid, and T Franke. Separation of blood cells using hydrodynamic lift. *Applied Physics Letters*, 100(18):183701, 2012.

[37] Soojung Claire Hur, Albert J Mach, and Dino Di Carlo. High-throughput size-based rare cell enrichment using microscale vortices. *Biomicrofluidics*, 5(2):022206, 2011.

[38] Jiashu Sun, Chao Liu, Mengmeng Li, Jidong Wang, Yunlei Xianyu, Guoqing Hu, and Xingyu Jiang. Size-based hydrodynamic rare tumor cell separation in curved microfluidic channels. *Biomicrofluidics*, 7(1):011802, 2013.

[39] Han Wei Hou, Majid Ebrahimi Warkiani, Bee Luan Khoo, Zi Rui Li, Ross A Soo, Daniel Shao-Weng Tan, Wan-Teck Lim, Jongyoon Han, Ali Asgar S Bhagat, and Chwee Teck Lim. Isolation and retrieval of circulating tumor cells using centrifugal forces. *Scientific reports*, 3, 2013.

[40] Jochen Guck, Stefan Schinkinger, Bryan Lincoln, Falk Wottawah, Susanne Ebert, Maren Romeyke, Dominik Lenz, Harold M Erickson, Revathi Ananthakrishnan, Daniel Mitchell, et al. Optical deformability as an inherent cell marker for testing malignant transformation and metastatic competence. *Biophysical journal*, 88(5):3689–3698, 2005.

[41] Jason S Kuo, Yongxi Zhao, Perry G Schiro, Laiying Ng, David SW Lim, J Patrick Shelby, and Daniel T Chiu. Deformability considerations in filtration of biological cells. *Lab on a Chip*, 10(7):837–842, 2010.

[42] Xi Qin, Sunyoung Park, Simon P Duffy, Kerryn Matthews, Richard R Ang, Tilman Todenhöfer, Hamid Abdi, Arun Azad, Jenny Bazov, Kim N Chi, et al. Size and deformability based separation of circulating tumor cells from castrate resistant prostate cancer patients using resettable cell traps. *Lab on a Chip*, 15(10):2278–2286, 2015.

[43] M. Yamada, M. Nakashima, and M. Seki. Pinched flow fractionation: continuous size separation of particles utilizing a laminar flow profile in a pinched microchannel. *Analytical chemistry*, 76(18):5465–5471, 2004.

[44] J. Takagi, M. Yamada, M. Yasuda, and M. Seki. Continuous particle separation in a microchannel having asymmetrically arranged multiple branches. *Lab Chip*, 5(7):778–784, 2005.

[45] Y. Sai, M. Yamada, M. Yasuda, and M. Seki. Continuous separation of particles using a microfluidic device equipped with flow rate control valves. *Journal of chromatography A*, 1127(1-2):214–220, 2006.

[46] Xinyu Lu and Xiangchun Xuan. Inertia-enhanced pinched flow fractionation. *Analytical chemistry*, 87(8):4560–4565, 2015.

[47] Claudio Cupelli, Thorsten Borchardt, Thomas Steiner, Nils Paust, Roland Zengerle, and Mark Santer. Leukocyte enrichment based on a modified pinched flow fractionation approach. *Microfluidics and nanofluidics*, 14(3-4):551–563, 2013.

[48] Asger Vig Larsen, Lena Poulsen, Henrik Birgens, Martin Dufva, and Anders Kristensen. Pinched flow fractionation devices for detection of single nucleotide polymorphisms. *Lab on a chip*, 8(5):818–821, 2008.

[49] Xin Lu, Wei-Hua Huang, Zong-Li Wang, and Jie-Ke Cheng. Recent developments in single-cell analysis. *Analytica Chimica Acta*, 510(2):127–138, 2004.

[50] Huabing Yin and Damian Marshall. Microfluidics for single cell analysis. *Current opinion in biotechnology*, 23(1):110–119, 2012.

[51] Keir C Neuman and Attila Nagy. Single-molecule force spectroscopy: optical tweezers, magnetic tweezers and atomic force microscopy. *Nature methods*, 5(6):491–505, 2008.

[52] Clyde F Wilson, Garth J Simpson, Daniel T Chiu, Anette Strömberg, Owe Orwar, Nestor Rodriguez, and Richard N Zare. Nanoengineered structures for holding and manipulating liposomes and cells. *Analytical chemistry*, 73(4):787–791, 2001.

[53] Stanislav S Rubakhin, Rebecca W Garden, Robert R Fuller, and Jonathan V Sweedler. Measuring the peptides in individual organelles with mass spectrometry. *Nature biotechnology*, 18(2):172–175, 2000.

[54] Hu Zhang and Kuo-Kang Liu. Optical tweezers for single cells. *Journal of The Royal Society Interface*, 5(24):671–690, 2008.

[55] Andreas R Bausch, Winfried Möller, and Erich Sackmann. Measurement of local viscoelasticity and forces in living cells by magnetic tweezers. *Biophysical journal*, 76(1):573–579, 1999.

[56] Shuhei Nishida, Yutaka Funabashi, and Atsushi Ikai. Combination of afm with an objective-type total internal reflection fluorescence microscope (tirfm) for nanomanipulation of single cells. *Ultramicroscopy*, 91(1):269–274, 2002.

[57] Zhen Zhu, Olivier Frey, Diana Silvia Ottoz, Fabian Rudolf, and Andreas Hierlemann. Microfluidic single-cell cultivation chip with controllable immobilization and selective release of yeast cells. *Lab on a Chip*, 12(5):906–915, 2012.

[58] Jacqueline R Rettig and Albert Folch. Large-scale single-cell trapping and imaging using microwell arrays. *Analytical chemistry*, 77(17):5628–5634, 2005.

[59] Dino Di Carlo, Nima Aghdam, and Luke P Lee. Single-cell enzyme concentrations, kinetics, and inhibition analysis using high-density hydrodynamic cell isolation arrays. *Analytical chemistry*, 78(14):4925–4930, 2006.

[60] Stefan Kobel, Ana Valero, Jonas Latt, Philippe Renaud, and Matthias Lutolf. Optimization of microfluidic single cell trapping for long-term on-chip culture. *Lab on a Chip*, 10(7):857–863, 2010.

[61] Wei-Heong Tan and Shoji Takeuchi. A trap-and-release integrated microfluidic system for dynamic microarray applications. *Proceedings of the National Academy of Sciences*, 104(4):1146–1151, 2007.

[62] Simone Tanzi, Peter Friis Østergaard, Marco Matteucci, Thomas Lehrmann Christiansen, Jiri Cech, Rodolphe Marie, and Rafael Taboryski. Fabrication of combined-scale nano-and microfluidic polymer systems using a multilevel dry etching, electroplating and molding process. *Journal of Micromechanics and Microengineering*, 22(11):115008, 2012.

[63] Pawel Utko, Fredrik Persson, Anders Kristensen, and Niels B Larsen. Injection molded nanofluidic chips: Fabrication method and functional tests using single-molecule dna experiments. *Lab on a Chip*, 11(2):303–308, 2011.

[64] M Heckele and WK Schomburg. Review on micro molding of thermoplastic polymers. *Journal of Micromechanics and Microengineering*, 14(3):R1, 2004.

[65] Holger Becker and Claudia Gärtner. Polymer microfabrication technologies for microfluidic systems. *Analytical and bioanalytical chemistry*, 390(1):89–111, 2008.

[66] Pedro S Nunes, Pelle D Ohlsson, Olga Ordeig, and Jörg P Kutter. Cyclic olefin polymers: emerging materials for lab-on-a-chip applications. *Microfluidics and nanofluidics*, 9(2-3):145–161, 2010.

[67] Topas datasheets. http://www.topas.com/tech-center/datasheets.

[68] Marco Matteucci, Thomas Lehrmann Christiansen, Simone Tanzi, Peter Friis Østergaard, Simon Tylsgaard Larsen, and Rafael Taboryski. Fabrication and characterization of injection molded multi level nano and microfluidic systems. *Microelectronic Engineering*, 111:294–298, 2013.

[69] WF Zoetelief, LFA Douven, and AJ Housz. Residual thermal stresses in injection molded products. *Polymer Engineering & Science*, 36(14):1886–1896, 1996.

[70] KMB Jansen, DJ Van Dijk, MH Husselman, et al. Effect of processing conditions on shrinkage in injection molding. *Polymer Engineering and Science*, 38(5):838–846, 1998.

[71] Du-Soon Choi and Yong-Taek Im. Prediction of shrinkage and warpage in consideration of residual stress in integrated simulation of injection molding. *Composite Structures*, 47(1):655–665, 1999.

[72] Chia-Wen Tsao and Don L DeVoe. Bonding of thermoplastic polymer microfluidics. *Microfluidics and Nanofluidics*, 6(1):1–16, 2009.

[73] D.G. Brandon, W.D. Kaplan, and D. Brandon. *Microstructural characterization of materials*. Wiley Online Library, 1999.

[74] Asger Laurberg Vig and Anders Kristensen. Separation enhancement in pinched flow fractionation. *Applied Physics Letters*, 93(20):203507, 2008.

[75] H. Bruus. *Theoretical Microfluidics*. Oxford University Press, 2008.

[76] Karsten B Andersen, Simon Levinsen, Winnie E Svendsen, and Fridolin Okkels. A generalized theoretical model for "continuous particle separation in a microchannel having asymmetrically arranged multiple branches". *Lab on a Chip*, 9(11):1638–1639, 2009.

[77] Gh Mohiuddin Mala and Dongqing Li. Flow characteristics of water in microtubes. *International Journal of Heat and Fluid Flow*, 20(2):142–148, 1999.

[78] Zhigang Wu, Ben Willing, Joakim Bjerketorp, Janet K Jansson, and Klas Hjort. Soft inertial microfluidics for high throughput separation of bacteria from human blood cells. *Lab on a Chip*, 9(9):1193–1199, 2009.

[79] HS Allen. Xxxi. the motion of a sphere in a viscous fluid. *The London, Edinburgh, and Dublin Philosophical Magazine and Journal of Science*, 50(304):323–338, 1900.

[80] Jason P Beech, Stefan H Holm, Karl Adolfsson, and Jonas O Tegenfeldt. Sorting cells by size, shape and deformability. *Lab on a Chip*, 12(6):1048–1051, 2012.

[81] Banqiu Wu, Ajay Kumar, and Sharma Pamarthy. High aspect ratio silicon etch: a review. *Journal of applied physics*, 108(5):051101, 2010.

A
Publications

The three publications related to this thesis are included in this chapter.

Paper I
Injection molded pinched flow fractionation device for enrichment of somatic cells in cow milk

Appendix A. Publications

Microelectronic Engineering 124 (2014) 53–57

Contents lists available at ScienceDirect

Microelectronic Engineering

journal homepage: www.elsevier.com/locate/mee

Injection molded pinched flow fractionation device for enrichment of somatic cells in cow milk

Marie Pødenphant [a], Rodolphe Marie [a,*], Tom Olesen [b], Marco Matteucci [a], Anders Kristensen [a]

[a] Technical University of Denmark, Department of Micro and Nanotechnology, Ørsteds Plads Building 345E, Kongens Lyngby, Denmark
[b] Unisensor A/S, Gydevang 42, Allerød, Denmark

ARTICLE INFO

Article history:
Received 28 October 2013
Received in revised form 21 March 2014
Accepted 9 April 2014
Available online 18 April 2014

Keywords:
Pinched flow fractionation
Microfluidics
Injection molding
Somatic cells
TOPAS

ABSTRACT

In this paper the continuous microfluidic separation technique pinched flow fractionation is applied to the enrichment of somatic cells from cow milk. Somatic cells were separated from the smallest fat particles and proteins thus better imaging and analysis of the cells can be achieved. The enrichment was performed using an all-polymer pinched flow fractionation device fabricated by injection molding. The polymer chips were bonded to a 500 μm polymer foil using UV assisted thermal bonding. The quality of the final devices was reproducible and the injection molding process combined with the use of cheap materials ensures the possibility for device mass production.

© 2014 Elsevier B.V. All rights reserved.

1. Introduction

Dairy production is a large industry and the milk quality depends strongly on the animal health. Milk quality is measured by the concentration of somatic cells, which are cells from the animal that naturally are found in the milk. In the EU, milk is discarded if the number of somatic cells is above 400,000 mL^{-1} [1]. The majority of the somatic cells found in milk are white blood cells, which can be divided into several types. The quantity of white blood cells increases and the cell type distribution changes in response to an animal getting an infection. Other somatic cells found in milk are less important to the animal health. To test the milk quality dairy farmers use commercial cell counters where nuclear DNA is stained, and fluorescence detection is used to estimate the cell count. This method only allows to assess cell counts corresponding to milk quality below standards. Measurements on not just the amount of somatic cells, but also the percentage of each type would instead provide dairy farmers with valuable information to prevent milk waste. Optical imaging of somatic cells could allow such early diagnostics of animal infections. However, optical detection of cell types is very difficult because of the blur and contrast reduction induced by fat particles and proteins found in milk samples. There is therefore an interest in a method for enrichment of somatic cells in milk to allow for in-line optical characterization of the white blood cell distribution. This can for example be done by separating fat cells and proteins from the somatic cells. Fat particles vary in size from 1 μm to 15 μm, with the highest occurrence around 4 μm [2], and proteins are even smaller. Most white blood cells have sizes between 8.5 μm and 10 μm [3]. This size difference can be exploited by lab-on-a-chip (LOC) based separation techniques.

In recent years the interest in LOC systems for cell handling has increased. LOC devices can be produced at a low cost and enable label-free detection to be combined with single cell handling, which can be important when investigating cell biology. Several microfluidic techniques have been developed for cell separation and sorting [4] including deterministic lateral displacement [5], hydrophoretic separation [6], use of hydrodynamic lift forces [7] and pinched flow fractionation (PFF) [8]. These methods have for example been used for enrichment of circulating tumor cells [5] and separation of platelets and red blood cells [6,7]. Other LOC techniques for separation relying on applied external fields have been developed. These include, among others, dielectrophoresis [9], magnetophoresis [10], acoustophoresis [11] and centrifugal disk platforms [12], but are not relevant for somatic cell separation because of increased sample preparation time and running costs compared to the method described in this paper.

LOC microfluidic separation devices are often operated by applying a pressure-driven flow and use either a passive or active control of the cut off size. Passive devices are attractive as they require no other actuation than a source of pressure or vacuum.

* Corresponding author. Tel.: +45 4525 5753.
E-mail address: rodolphe.marie@nanotech.dtu.dk (R. Marie).

http://dx.doi.org/10.1016/j.mee.2014.04.018
0167-9317/© 2014 Elsevier B.V. All rights reserved.

However they have the disadvantage that they cannot be adjusted to different samples because the cut off value is fixed by the device geometry. Recently, a flow displacement device was fabricated where the cut off value is adjusted by deforming the device made of elastomeric PDMS [13]. The devices presented in this paper use the pinched flow fractionation principle. In this size separation device, the cut off size can be adjusted by varying the pressures applied to the drain outlet, thus the separation can be adjusted to different samples. Furthermore, PFF devices are passive microfluidic devices that can be mass produced using the plastic industry standard method injection molding.

PFF is a continuous microfluidic size separation method. A sample containing particles of different sizes is injected into a microfluidic system and enters a narrow channel called the pinched segment, where the particles are aligned against the channel wall because of high flow from a buffer fluid, see Fig. 1a. Next the aligned particles enter a broader channel where they follow a streamline according to their center of mass. In the broader segment the particles of different radii (r and R in Fig. 1a) are positioned at different distances to the wall (dr and dR respectively) thus they can be collected in different outlets. In the fabricated devices there are two outlets for separation of the sample, so that particles bigger than a critical radius r_c are separated from smaller particles.

PFF was first demonstrated in 2004 [8] and has been used extensively for size separation of polymer beads from the microscopic to the sub-micrometer range. The designs have become increasingly advanced using different geometries with several separation outlets or microvalves to precisely control the flow rates [14,15]. It has also been shown that PFF can be used for sorting of non-solids such as oil emulsions [16] and it has been used for a few applications for diagnostics, such as detection of single nucleotide polymorphisms for fast genotyping [17] and separation of red blood cells and white blood cells [18].

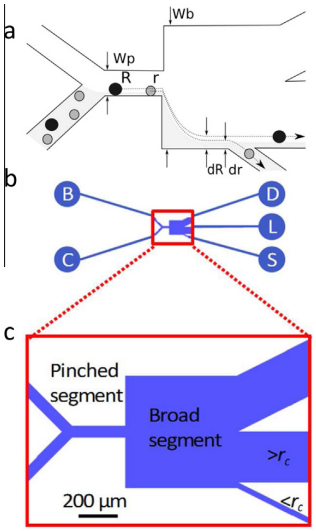

Fig. 1. (a) Sketch of the PFF principle, where two particles of different radii are aligned in the pinched segment and separated into the outlet for small and large particles respectively. (b) The inlets and outlets on the PFF devices. Inlet C is for the cell sample, inlet B is for the buffer, outlet S (L) is for collecting small (large) cells with a radius below (above) the critical radius r_c, and outlet D is a drain for collection of the buffer. (c) Zoom in at the pinched and broad segment. The height of all channels is 30 µm. The width of the pinched segment W_p is 100 µm and the width of the broad segment W_b is 1000 µm.

In this paper we demonstrate that PFF devices that can be cheaply mass produced by injection molding can be used to enrich somatic cells from milk by separating them from the smallest fat particles and proteins, thus enabling optical characterization of the somatic cells.

2. Materials and methods

2.1. Chip design

A sketch of the channel design is shown in Fig. 1b–c. The PFF device has two inlets, a pinched and broad segment and three outlets. The first two outlets are for separating the sample into particles smaller and larger than r_c and the third is used as a drain for most of the buffer solution injected from inlet B in order to pinch the sample in the pinched segment. The height of all channels is 30 µm such that particles as big as 25 µm can be handled.

2.2. Fabrication

A nickel shim for injection molding of the chips was fabricated using standard clean room processes [19,20]. A four inch silicon wafer was treated with hydrofluoric acid and coated with positive photo resist for I-line photolithography. The resist was developed creating an etch-mask. The silicon wafer was etched 30 µm using deep reactive-ion etching and the leftover resist was removed by plasma ashing and acetone. A nickel seed layer was sputtered onto the wafer thus a 30 µm thick nickel layer could be electroplated. Finally the silicon was removed using a KOH etch leaving only the nickel shim. The final shim was imaged in a scanning electron microscope (SEM) before injection molding, see Fig. 2a.

The microchannels were injection molded in the polymer TOPAS 5013 using a tool temperature of 140 °C and a cooling time of 90 s. A chip was imaged in a SEM after injection molding, see Fig. 2b.

2.3. Thermal bonding

The channels were sealed with a 500 µm thick TOPAS 5013 foil using UV assisted bonding. The chips were bonded at 120 °C and a pressure of 51 bar for 5 min using a P/O/Weber press. Prior to bonding the polymer device and lid had been exposed to UV light from a mercury arc lamp for 30 s. A similar bonding process has previously been shown to yield a high strength sealing, meaning the chips can withstand high applied pressures [21]. An image of a bonded chip is shown in Fig. 2c. Due to the molding parameters, the top edge of the microchannels is rounded, causing the bonding of the foil to be incomplete at the edge of the channel. The resulting shallow gap around the channels is visible on the optical images (Fig. 2c), however this is not expected to affect the fluid flow.

2.4. Sample preparation

Fluorescent beads were used to test the PFF device and to set r_c before experiments with milk. Two bead sizes were used: Green fluorescent (468/508) 5 µm polystyrene beads from Duke Scientific and orange fluorescent (540/560) 10 µm FluoSpheres® polystyrene beads from Invitrogen. The beads were mixed with 0.1% Triton X-100 in Milli-Q water to a concentration of 300,000 mL^{-1}. Cow milk supplied from a dairy farmer was mixed with 0.1% Triton X-100 in Milli-Q water to concentrations between 5 vol% and 10 vol%. Milk samples were kept in a refrigerator before use and were no more than two days old. The concentration of somatic cells was measured before and after experiments using a DeLaval cell counter (DCC) [22]. The DCC works by sucking approx. 60 µL

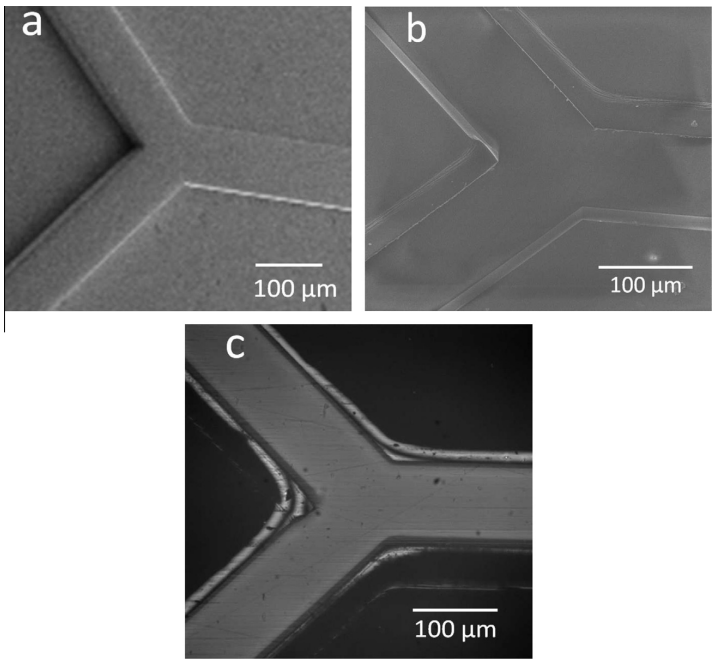

Fig. 2. (a) SEM image of the nickel shim. (b) SEM image of an injection molded chip. (c) Optical image of a chip after thermal bonding.

of sample into a cassette, where cell DNA is stained with a fluorescent dye. The cassette is then inserted in the DCC and the cells in 1 μL of sample are counted. Before counting cells from the outlets of the PFF device, the volume of collected solution was adjusted to at least 60 μL by adding buffer when necessary.

2.5. Experimental procedure

The channels of the PFF device were completely wetted with a solution of 0.1% Triton X-100 mixed with Milli-Q water before inserting the milk samples in the chips. Next the device was flushed with 1 mg/mL BSA in PBS for 10 min at flow rates of approx. 20 μL/min. Finally the 5 μm or 10 μm bead solutions were used to set the r_c between 2.5 μm and 5 μm. A microfluidic flow control system (MFCS) from Fluigent was used to control the fluid flow through the chips. The air pressure at inlet C, B and outlet S were controlled separately. The applied pressures were in the range 5 mbar–25 mbar. A Nikon Eclipse TE2000-U inverted microscope connected to an EMCCD camera from Photometrics was used to take images during experiments and the images were analysed using ImageJ software.

3. Results

3.1. Bead separation

The PFF devices were initially tested with polymer beads of sizes 5 μm and 10 μm mixed together. The flow rates in the sample and buffer inlets were approx. 0.5 μL min^{-1} and 5.2 μL min^{-1} ensuring the pinching of the 5 μm beads in the pinched segment. Images were recorded during the separation of beads in the broad channel where it is split into channels leading to outlets S and L. Fig. 3a and b shows 200 video frames converted into average intensity images of the fluorescent beads. They show the separation of the two bead sizes, where the 5 μm went towards outlet S for small particles and the bigger 10 μm beads went towards outlet L for large particles. The number of beads going to each outlet is shown in Fig. 3c.

All the 10 μm beads were collected in outlet L while 99% of the 5 μm beads were collected in outlet S, showing that the fabricated PFF devices work for samples with size ratio 1:2. The separation efficiency is equivalent to other PFF devices fabricated in silicon or by PDMS casting.

3.2. Somatic cell enrichment

Beads were used to set r_c and the milk sample was then added to the device inlet. The flow rate in the sample and buffer inlet was approx. 0.5 μL min^{-1} and 5.2 μL min^{-1} respectively to ensure optimal pinching of the smaller particles in the pinched segment and that optical images could be recorded.

During the experiment the somatic cells and fat particles could not be distinguished, and to confirm the enrichment of samples collected in outlet L the solution was pipetted out from the outlets and analysed with the DCC. Table 1 summarizes the cell counts from three separate experiments. Listed are the reference cell concentrations measured in the milk sample before enrichment, the measurements after separation for each outlet, the total volume of sample after dilution and the amount of cells in each outlet. Cell counting analysis was also performed on samples from outlet D and confirmed that no cells were collected in the drain outlet of the device.

The cell count analysis shows that between 62.5% and 82.9% of the somatic cells were collected in the outlet for particles with radii larger than r_c. During experiments it was observed that most of the visible particles in the samples were redirected to outlet S, confirming that most of the proteins and fat from the milk went to the outlet for particles with radii smaller than r_c, as expected from the size distribution of proteins and fat [2]. There is indeed an overlap in the size distributions of the fat and somatic cells thus

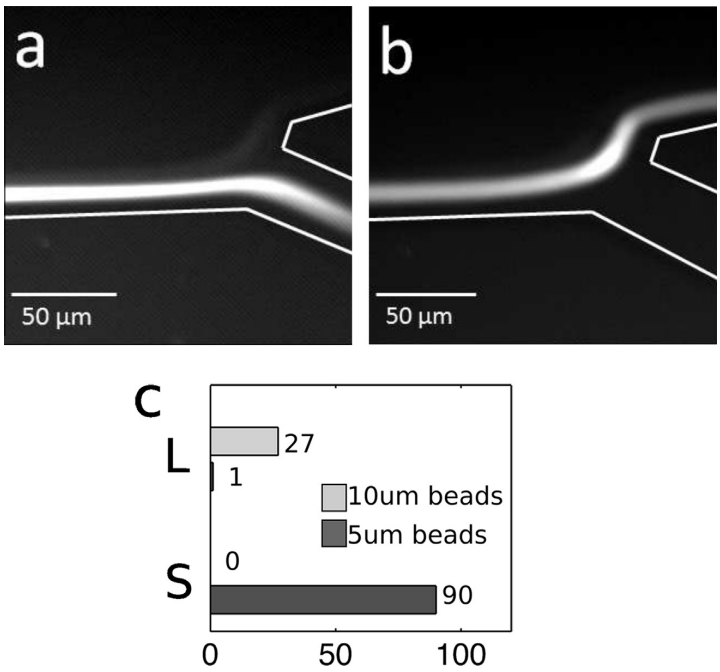

Fig. 3. (a) Average fluorescent image of 5 µm beads going to outlet S. The 10 µm beads going to outlet L can also be seen but with less intensity because the filter is set to fit the green 5 µm beads. (b) The 10 µm beads going to outlet L. The 5 µm beads cannot be seen on the image. White lines represent the channel walls. (c) Counts of 5 µm and 10 µm beads going into the outlet for large particles (L) and small particles (S).

Table 1
Summary of cell counts in the solution collected from outlet for small (S) and large (L) particles after enrichment of somatic cells from milk.

Sample	Ref. conc. (μL^{-1})	Conc. S:L (μL^{-1})	Volume S:L (μL)	Cell count S:L (%)
10 vol% milk	219	2.5:7	96:166	17.1:82.9
10 vol% milk	1010	7:6	90:175	37.5:62.5
5 vol% milk	1327	2:4	96:113	29.8:70.2

they cannot be completely separated. Nevertheless the cell counts combined with the observations during experiments show that the PFF devices can be used to enrich somatic cells because the proteins and most of the fat particles have been removed.

The results in Table 1 show very low cell counts after separation, which is due to dilution from the buffer fluid. The buffer flow rate was around ten times larger than the sample flow rates to ensure pinching of the particles. The majority of the visible particles flowed to outlet S meaning that they experienced a low dilution, while particles flowing to outlet L were very diluted by the buffer. Limiting the dilution in the PFF device can be achieved by designing the drain outlet channel to collect more buffer fluid by reducing its hydraulic resistance.

Finally, while low sample flow rates were necessary to obtain images during experiments for proof of concept, flow rates and milk concentration could be increased to achieve larger volumes and cell counts in the sample collected from the device outlets. For industrial applications the samples must be processed fast, which can be done by parallelisation of the separation using multiple devices at once. This can be done relatively cheap because of the low fabrication and running costs of the devices.

4. Conclusion

A PFF device was fabricated in polymer by injection molding in an industrial compatible way ensuring the possibility of mass production. The quality of the devices were reproducible and similar results were obtained on different devices. The separation results obtained with fluorescent beads are similar to results obtained with PFF devices made of more expensive materials, and showed up to 99% separation efficiency. The devices were also used for separation of somatic cells and small fat particles with separation of up to 82.9% of the somatic cells. The results are promising and indicates that the PFF devices can be used for somatic cell enrichment to obtain better milk quality analysis.

Acknowledgements

The authors gratefully acknowledge funding from the European Commission under the Seventh Framework Programme (FP7/2007–2013) under grant agreements number 278204 (Cellomatic).

The authors thank NIL Technology ApS for fabrication of the shim for injection molding.

References

[1] Council of the european communities council directive 92/46/eec of 16 June 1992 laying down the health rules for the production and placing of the market of raw milk, heat treated milk and milk-based products, 1992.
[2] M. Michalski, M. Ollivon, V. Briard, N. Leconte, C. Lopez, Chem. Phys. Lipids 132 (2004) 247–261.
[3] P. Sethu, A. Sin, M. Toner, Lab Chip 6 (2006) 83–89.
[4] D. Gossett, W. Weaver, A. Mach, S. Hur, H. Tse, W. Lee, H. Amini, D. Di Carlo, Anal. Bioanal. Chem. 397 (2010) 3249–3267.
[5] K. Loutherback, J. D'Silva, L. Liu, A. Wu, R.H. Austin, J.C. Sturm, AIP Adv. 2 (2012) 042107.
[6] S. Choi, T. Ku, S. Song, C. Choi, J. Park, Lab Chip 11 (2011) 413–418.

Appendix A. Publications

[7] T. Geislinger, B. Eggart, S. Braunmuller, L. Schmid, T. Franke, Appl. Phys. Lett. 100 (2012) 183701.
[8] M. Yamada, M. Nakashima, M. Seki, Anal. Chem. 76 (2004) 5465–5471.
[9] X. Hu, P.H. Bessette, J. Qian, C.D. Meinhart, P.S. Daugherty, H.T. Soh, Proc. Natl. Acad. Sci. USA 102 (2005) 15757–15761.
[10] N. Pamme, C. Wilhelm, Lab Chip 6 (2006) 974–980.
[11] A. Lenshof, A. Ahmad-Tajudin, K. Järås, A.-M. Swärd-Nilsson, L. Åberg, G. Marko-Varga, J. Malm, H. Lilja, T. Laurell, Anal. Chem. 81 (2009) 6030–6037.
[12] S. Haeberle, T. Brenner, R. Zengerle, J. Ducrée, Lab Chip 6 (2006) 776–781.
[13] J.P. Beech, J.O. Tegenfeldt, Lab Chip 8 (2008) 657–659.
[14] J. Takagi, M. Yamada, M. Yasuda, M. Seki, Lab Chip 5 (2005) 778–784.
[15] Y. Sai, M. Yamada, M. Yasuda, M. Seki, J. Chromatogr. A 1127 (2006) 214–220.
[16] H. Maenaka, M. Yamada, M. Yasuda, M. Seki, Langmuir 24 (2008) 4405–4410.
[17] A. Larsen, L. Poulsen, H. Birgens, M. Dufva, A. Kristensen, Lab Chip 8 (2008) 818–821.
[18] C. Cupelli, T. Borchardt, T. Steiner, N. Paust, R. Zengerle, M. Santer, Microfluid. Nanofluid. (2013) 1–13.
[19] S. Tanzi, P.F. Østergaard, M. Matteucci, T.L. Christiansen, J. Cech, R. Marie, R. Taboryski, J. Micromech. Microeng. 22 (2012) 115008.
[20] P. Utko, F. Persson, A. Kristensen, N.B. Larsen, Lab Chip 11 (2011) 303–308.
[21] M. Matteucci, T.L. Christiansen, S. Tanzi, P.F. Østergaard, S.T. Larsen, R. Taboryski, Microelectron. Eng. 111 (2013) 294–298.
[22] C. Gonzalo, B. Linage, J. Carriedo, L. De La Fuente, J. Dairy Sci. 91 (2008) 3114–3118.

Paper II

Separation of cancer cells from white blood cells by pinched flow fractionation

Journal Name

ARTICLE TYPE

Cite this: DOI: 10.1039/xxxxxxxxxx

Separation of cancer cells from white blood cells by pinched flow fractionation

Marie Pødenphant,[a] Neil Ashley,[b] Kamila Koprowska,[b] Kalim U. Mir,[c] Maksim Zalkovskij,[d] Brian Bilenberg,[d] Walter Bodmer,[b] Anders Kristensen[a] and Rodolphe Marie*[a]

Received Date
Accepted Date

DOI: 10.1039/xxxxxxxxxx

www.rsc.org/journalname

In this paper, the microfluidic size-separation technique pinched flow fractionation (PFF) is used to separate cancer cells from white blood cells (WBCs). The cells are separated at efficiencies above 90 % for both cell types. Circulating tumor cells (CTCs) are found in the blood of cancer patients and can form new tumors. CTCs are rare cells in blood, but they are important for the understanding of metastasis. There is therefore a high interest in developing a method for the enrichment of CTCs from blood samples, which also enables further analysis of the separated cells. The separation is challenged by the size overlap between cancer cells and the 10^6 times more abundant WBCs. The size overlap prevents high efficiency separation, however we demonstrate that cell deformability can be exploited in PFF devices to gain higher efficiencies than expected from the size distribution of the cells.

1 Introduction

Circulating tumour cells (CTCs) are cells that have been shed from a tumour and entered the blood circulation. When shed from the primary tumour following adaptation to and colonization of the microenvironment of a secondary site, they form metastases which are responsible for over 90 % of solid tumour-related deaths.[1] CTCs, obtained through a simple venipuncture, can serve as a "liquid biopsy" to monitor tumour characteristics in real-time, including inter- and intratumoural heterogeneity. However, CTC isolation and subsequent characterization are technically challenging due to the low numbers among an abundance of white blood cells. A wide range of analytical methods for CTC detection, enrichment and isolation has been developed. They exploit CTC-specific properties, either biological such as surface marker expression or physical e.g. size, density or stiffness. Most of the available platforms utilize immunomagnetic capture using antibodies targeting the epithelial cell adhesion molecule-1 (EpCAM). Subsequent CTC detection is based on either direct antibody-based methods such as immunocytochemistry (ICC), immunofluorescence (IF) and fluorescence-activated cell sorting (FACS), or indirect nucleic acid-based methods which measure mRNA transcripts by reverse transcriptase-polymerase chain reaction (RT-PCR), or direct DNA isolation and sequencing.[2] So far the only Food and Drug Administration (FDA) approved technology for the clinical monitoring of CTC counts in cancer patients is the CellSearch® system (Veridex). This system is based on an initial step of immunomagnetic enrichment of EpCAM-positive cells. Subsequent enumeration of CTCs is done using fluorescent microscopy to identify DAPI-positive, cytokeratin-positive and CD45-negative cells.[3] AdnaTest® (AdnaGen AG) is an example of a system combining immunomagnetic enrichment of epithelial (EpCAM-positive) cells with multiplex RT-PCR to identify putative gene transcripts.[4] Another strategy for the identification of CTCs is to enumerate and analyze proteins specifically secreted by viable tumour cells by use of EPISPOT (EPIthelial ImmunoSPOT). First CTCs are enriched by negative depletion using CD45 and subsequently cultured on a membrane coated with antibodies that capture secreted proteins such as cytokeratin 19, mucin 1, prostate-specific antigen or fibroblast growth factor 2.[5] All antibody-based capture technologies have limitations as they likely capture only a subpopulation of the CTCs. Furthermore, most of them have high initial and running costs and require user specialization which limits wide spread use of these systems. In contrast passive size-separation in microfluidic devices is an alternative approach that is label-free and can potentially be performed on cost-effective single use devices, if they can be mass-produced. Microfluidic separation devices are also easy to operate and have low running costs especially if a simple pressure-driven

[a] *DTU Nanotech, Ørsteds Plads Building 345east, 2800 Kgs. Lyngby, Denmark. Fax: XX XXXX XXXX; Tel: +45 4525 5753; E-mail: rodolphe.marie@nanotech.dtu.dk*
[b] *Weatherall Institute of Molecular Medicine, Department of Oncology, John Radcliffe Hospital, Headington, Oxford OX3 9D5, United Kingdom.*
[c] *Genotype2Phenotype LLC (G2P), One Mifflin Place, Cambridge, MA 02138, USA.*
[d] *NIL Technology ApS, Diplomvej 381, 2800 Kgs. Lyngby, Denmark.*

This journal is © The Royal Society of Chemistry [year]

flow is used to operate the device.[6–9]

Rare cells have been separated from red blood cells (RBCs) and WBCs using different continuous label-free size-separation techniques. A successful separation is usually characterized by high recovery of the cancer cells, high removal of WBCs and RBCs,[†], and high sample throughput. Another important aspect to consider is the characteristics of the cell line used to mimic CTCs, especially the cell size has a great influence on the results.

Geislinger *et al.* used non-inertial lift forces to sort MV3 skin cancer cells and RBCs with recoveries up to 100 % for the cancer cells and a removal of 98 % to 99 % of the red blood cells.[10] This was done at a throughput in the order of 10^6 cells/min. The MV3-cell line has an average size of $14\,\mu\text{m} \pm 2\,\mu\text{m}$, which is within the size range of WBCs, however in this study the removal of WBCs was not investigated. Loutherback *et al.*[11] used deterministic lateral displacement arrays to separate MDA-MB-231 breast cancer cells from diluted whole blood. They measured a recovery of 86 % at 10 mL/min, but with a blood cell removal of only 75 %. Bhagat *et al.*[12] used inertial microfluidics to separate MCF-7 and MDA-MB-231 breast cancer cells spiked in whole blood with a recovery over 80 % at a throughput of 10^8 cells/min. They measured a removal of both WBCs and RBCs of over 99 %. The MCF-7 and MDA-MB-231 cell lines are relatively large with an average diameter of approx. $18\,\mu\text{m}$,[12] consequently there is no size-overlap between these cancer cells and WBCs and it is not surprising that Loutherback *et al.* and Bhagat *et al.* measured such high recoveries and blood cell removals. The average diameter of CTCs is approx. $15\,\mu\text{m}$, but can be smaller, depending on their origin, which increases the size-overlap between WBCs and CTCs and is thus a challenge for any size-separation technique.

We use pinched flow fractionation (PFF) to separate WBCs from LS174T colon cancer cells. We chose LS174T cell as a convenient well characterised colorectal cancer derived cell line to model CTCs. PFF is a continuous size-separation technique first presented by Yamada *et al.*[13] The principle of our PFF devices is shown in Fig. 1. Briefly, a sample containing particles of different sizes is placed in one inlet and a carrier solution is placed in the other inlet. The solutions from both inlets are then pushed into the device, where they meet at a narrow channel called the pinched segment. The particles then get aligned against the channel side-wall under the high flow from the carrier solution, and they follow streamlines according to the position of their center of mass. Downstream, the pinched segment is split into three outlet channels: a small and large particle outlet channel, and a drain channel. Particles with a diameter below and above the critical diameter, d_c, will flow towards the small and large particle outlet respectively, while the drain collects most of the buffer fluid to prevent dilution. The critical diameter d_c can be adjusted by applying a pressure to the drain outlet and thus the devices can be adapted to any sample. We refer to this operation of the device as *adjustable*-PFF in the following. The PFF technique was first used to separate microbeads of different sizes using increasingly refined designs.[14,15] PFF has also been applied to biological samples and used for separation of RBCs and WBCs,[16] and detection of single nucleotide polymorphisms.[17] Recently we used PFF to remove fat particles from cow milk samples for improved cell analysis.[18]

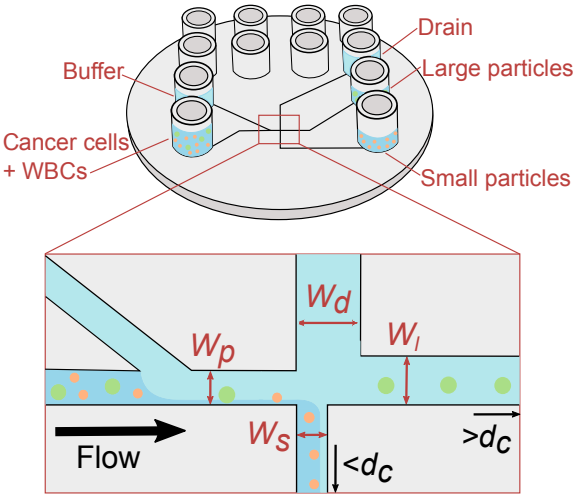

Fig. 1 Sketch of the PFF device fabricated by injection molding with five Luer fittings used as inlets and outlets. (close up) The principle of PFF, where particles are aligned and then sorted by size into different outlets. Particles with a diameter smaller than the critical diameter, d_c, flow towards the small particle outlet, and particles larger than d_c flow towards the large particle outlet. The drain collects most of the carrier solution. Channel dimensions that affect the critical diameter are shown. The four widths denote width of: the pinched segment (W_p), the small particle outlet channel (W_s), the large particle outlet channel (W_l), and the drain channel (W_d).

In this paper, we perform the separation of LS174T cancer cells from WBCs using PFF in order to mimic the isolation of CTCs from WBCs. Whole blood samples can rapidly be centrifuged to separate WBCs and CTCs from the remaining blood cells, and separating CTCs from WBCs is thus critical in isolating CTCs. We use LS174T colorectal adenocarcinoma cells as models for CTCs. They have a measured average size of $12.3 \pm 0.15\,\mu\text{m}$, which is closer in size to CTCs than the often used breast cancer cell-lines. The LS174T cells have a large size overlap with WBCs, which varies in size from $5\,\mu\text{m}$ to $15\,\mu\text{m}$. We demonstrate that a difference in cell deformability is the most likely reason for the unexpected separation efficiency, and show that we can exploit the apparent relatively large deformability of the WBCs to achieve both a cancer cell recovery and a WBC removal over 90 %, which is better than expected from the size distribution of each cell type.

2 Materials and methods

2.1 Design

The PFF devices have two inlets and three outlets. The first outlet is for particles with a diameter below d_c, the second for particles

[†] Recovery is calculated as the percentage of cancer cells in the targeted outlet compared to the total number of cancer cells in all outlets. Removal is the percentage of blood cells removed from the targeted outlet compared to the total number of blood cells in all outlets.

This journal is © The Royal Society of Chemistry [year]

with a diameter above d_c, while the third works as a drain for the buffer solution. A sketch of the designs is seen in Fig. 1.

The channel dimensions were optimized to ensure good separation of WBCs and cancer cells. It has previously been reported that filters with a size of 8 μm work well for cancer cells enrichment,[19] thus 8 μm was expected to be the ideal critical diameter.

The designs were optimized by deriving an expression for the critical diameter as a function of channel dimensions. This was done by considering the flow rates in the pinched segment and the three outlet channels. The flow rate through the pinched segment must equal the sum of flow rates through the outlet channels, due to mass conservation.

$$Q_{pinched} = Q_{small} + Q_{large} + Q_{drain}. \quad (1)$$

To simplify the expression, the flow rates through the large particle outlet and the drain are expressed in terms of the small particle outlet.

$$Q_{pinched} = (1 + \alpha + \beta)\, Q_{small}, \quad (2)$$

where α and β are the ratios of hydraulic resistances between the small particle outlet and the respective other outlet (R_s/R_l and R_s/R_d). It is often assumed that microfluidic channels have a constant flow profile, however Andersen *et al.*[20] pointed out that this assumption only holds for large channel aspect ratios, $H/W >> 1$ and $W/H >> 1$, and not for cross sections with small aspect ratios as in the pinched segment. Therefore the velocity profile, $v_x(y,z)$, must be taken into account, and the flow rates are calculated by integrating the velocity profile in the pinched segment across the channel width (y-direction) and the channel height (z-direction).Thus Eq. (2) becomes,

$$\int_0^H \mathrm{d}z \int_{-W_p/2}^{W_p/2} \mathrm{d}y\, v_x(y,z) = (1+\alpha+\beta) \int_0^H \mathrm{d}z \int_{-W_p/2}^{-W_p/2+d_c/2} \mathrm{d}y\, v_x(y,z). \quad (3)$$

Note that the critical diameter, d_c, appears in the equation. The velocity of rectangular channels can be found numerically by solving the Navier-Stokes equation with no-slip boundary conditions at the wall.[21] The optimal hydraulic resistance ratio (α) was then calculated by inserting the expression for the velocity in Eq. (3) and solving for α.

There are many sets of dimensions that yield the desired critical diameter, some more practical than others. The largest cell aggregates are expected to have a size of around 20 μm, therefore the channel height was chosen to be 30 μm to avoid clogging. The lengths were chosen by letting the outlet channels go straight from the pinched segment to the outlets. The injection molded chip has a diameter of 5 cm, so the channel lengths have to be in the centimeter range. Therefore only the channel widths were left to be optimized using Eq. (3). We prepared two designs: one where the flow does not have to be adjusted, and one where the critical diameter is too small, to demonstrate adjustable-PFF where d_c has to be tuned. The final design parameters are listed in Tab. 1.

Table 1 Channel height (H), pinched segment width (W_p) and ratios between hydraulic resistances of the three outlet channels, and the resulting critical diameter d_c for both designs.

	H [μm]	W_p [μm]	α (R_s/R_l)	β (R_s/R_d)	d_c [μm]
Non-adjusted PFF	30	50	1.9	14.4	13.1
Adjustable PFF	30	30	1.9	14.4	8.3

2.2 Fabrication

A nickel shim for injection molding was fabricated using standard clean room processes.[22,23] A 150 mm silicon wafer was treated with hydrofluoric acid and coated with positive photoresist. The resist was developed and the silicon wafer was etched 30 μm using deep reactive-ion etching. The leftover resist was removed by plasma ashing and acetone. A nickel-vanadium seed layer was sputtered onto the wafer, and a 30 μm thick nickel layer was electroplated on top. Finally the silicon was removed using a KOH etch and the shim was cut out to fit in the injection molder. The devices were injection molded using the polymer TOPAS® 5013L-10 at a mold temperature of 120 °C, a holding pressure of 1500 bar and an injection rate of 20 cm^3/s to 45 cm^3/s. The total injection and cooling time was around 70 s pr. device. The injection molder was equipped with a tool that creates 12 Luer fittings on each chip, which ensures easy connection to the equipment. Finally the microchannels on each chip were sealed with a 500 μm thick TOPAS® 5013L-10 foil using UV-assisted bonding. The chips and lids were exposed to UV-light from a mercury arc lamp for 30 s and then bonded at 120 °C and a pressure of 51 bar for 5 min. using a P/O/Weber press.

2.3 Cell culture and sample preparation

The following fluorescent polystyrene beads were used for experiments: 2.1 μm blue (Duke Scientific), 5.1 μm green (Magsphere Inc.), 7 μm green (Magsphere Inc.), 10 μm orange (Invitrogen), and 15 μm orange (Invitrogen). Bead solutions were prepared by mixing the different beads with Milli-Q water and 0.1 % Triton X-100 to a total concentration of 5×10^5 particles mL^{-1}. The solutions consisted of 15 % 2.1 μm beads, 20 % 5.1 μm beads, 40 % 7 μm beads, 20 % 10 μm beads and 5 % 15 μm beads. All solutions were degassed in an ultrasonic bath before experiments. Milli-Q water and 0.1 % Triton X-100 was used to wet the devices before the sample was introduced, and as buffer solution for all experiments with beads.

The human colon adenocarcinoma LS174T cells were obtained from B. H. Tom (Northwestern University Medical Center, Chicago).[24] The cell line was cultured in complete Dulbecco's Modified Eagle Medium (DMEM; Life Technologies) supplemented with 10 % heat-inactivated fetal bovine serum (FBS; Life Technologies) and 1 % penicillin/streptomycin (Invitrogen). Cells were incubated at 37 °C in a humidified environment at 10 % CO_2 and were grown to 60-80 % confluence before next passage or further experiment.

Blood specimens were drawn from healthy donors after obtaining informed consent. All specimens were collected into BD Vacutainer CPT tubes (Becton Dickinson) containing sodium hep-

arin/Ficoll and were processed within 2 hours according to the manufacturer's protocol. Following centrifugation at 1500 x *g* (room temperature) for 15 min, the white blood cell suspension was collected, washed twice in PBS (1000 x *g*, room temperature, 10 min), and finally the cells were suspended in FACSFlow.

For separation measurements, LS174T cells were stained with calcein AM (Molecular Probes) and WBC's with either Hoechst 33342 (Thermo Scientific) or CD45-PE (Becton Dickinson), and subsequently mixed in a ratio of 1:1.

Before cell separation experiments devices were wet with degassed Milli-Q water and 0.1 % Triton X-100 and then flushed with degassed buffer solution (FACSFlow, BD). All Luer fittings were then emptied and rinsed with FACSFlow to get rid of leftover Triton X-100. FACSFlow was used as buffer solution for all cell experiments.

2.4 Separation measurements

In this study, either solutions containing hard polystyrene spheres or WBCs spiked with LS174T cancer cells were used. In our study we perform an experiment with polymer beads to determine the critical diameter of a PFF separation for hard spheres. Previously, bead separation has mostly been demonstrated on simple solutions containing two bead types that do not overlap in size. These simple solutions do not represent biological samples very well and cannot be used to determine the critical diameter of a system. The bead sample is a blend of fluorescent polymer beads with diameters from 2.1 μm to 15 μm. The size distribution of the beads is continuous and there are small overlaps between beads of different colors, creating a good model system to determine the critical diameter of the separation over a continuous range of values.

To conduct separation experiments, samples were pipetted into the Luer fittings on chip and pushed through the device using a pressure-driven flow controller (Fluigent MFCS-EZ). Experiments were monitored using an inverted fluorescence microscope (Nikon Eclipse TE2000-U) coupled to an EMCCD camera (Photometrics Cascade II:512) or a Brunel SP98F inverted fluorescence microscope (Brunel Microscopes Ltd). After experiments, images were taken of all particles in the two outlets and the drain. The images were analyzed using a script in MATLAB version R2013b software to extract the size distribution of each bead or cell type from the fluorescence images. The size of each particle was found by fitting circles to the beads/cells and calculating the corresponding diameter.

2.5 Critical diameter measurements

The separation efficiency of the cancer cell measurements was evaluated by calculating the recovery of cancer cells and the removal of WBCs, which we define as the number of cells in the targeted outlet divided by the total number of cells, $R = \frac{N_x}{N_{small}+N_{large}+N_{drain}}$, where N_x is set to N_{small} for WBC removal and N_{large} for cancer cell recovery. No particles went to the drain for most of the pressure settings used in the experiments except for particles appearing very large such as aggregates of cells. After experiments we measured the size of all particles in the outlets, and used the size distributions to determine the critical diameter, d_c. For each particle size the probability for going towards the large particle outlet is estimated as the proportion of particles in the large particle outlet. In the ideal case the estimated probability could be described by a step function jumping from 0 to 1 at d_c. However particles with a size close to d_c have a finite probability for going towards either outlet. The best estimate for d_c is determined as the size where particles have a 0.5 probability of going towards the large particle outlet, and this size is found by fitting the estimated probability to an error function modified to output values between 0 and 1:

$$f(x) = \frac{1}{2}\left(1 + \frac{\mathrm{erf}(a-x)}{b}\right) \ , \ \mathrm{erf}(x) = \frac{2}{\sqrt{\pi}}\int_0^x e^{-t^2}\mathrm{d}t, \qquad (4)$$

where a and b are fitted parameters describing position and slope of the function. MATLAB was used to fit the error function to the data. The stated uncertainties in measured parameters correspond to half the distance from the upper to the lower bounds on the 95 % confidence interval. Error bars on plots represent the standard deviation.

2.6 Simulations

The devices were simulated in the finite element simulation software COMSOL version 4.3. The critical diameter of the devices was determined using semi-3D simulations as described by Vig and Kristensen.[25] Effects relating to cell deformation were investigated using 3D simulations of a section around the pinched segment. No-slip boundary conditions were applied to all channel walls, and the pressures at the inlets and outlets were set to values used in the experiments. Furthermore it was assumed that particles do not disturb the flow.

3 Results and discussion

3.1 Hard sphere measurements

A blend of polymer beads with a broad size distribution was separated by size through the device in order to test the method for determining the critical diameter d_c. For the initial experiments the sample flow rates were 30 μL/h to 50 μL/h depending on the design, and the flow was not adjusted by any pressure at the outlets. The experiments were run until at least 1000 beads had been sorted, equivalent to 2 μL of sample. The setup allows processing of larger samples, however, this would prevent optical visualization of beads in the outlets. All beads were counted and analyzed, and we extracted the critical diameter of the separation using our described method. Fig. 2 shows the result of a separation in an adjustable PFF device. The 2 μm beads are not represented on the figure because they were not fully pinched.

The data fits well to the error function, but the analysis method results in a critical diameter of 5.8 μm $\pm$ 0.3 μm, which is much smaller than the expected diameter of 8.6 μm. The size distribution in Fig. 2 shows that the majority of 5 μm beads are collected in the small particle outlet, while the majority of 7 μm beads are collected in the large particle outlet. It is therefore reasonable that the critical diameter is in the range 5 μm to 7 μm, as measured.

The bead measurements show that the critical diameter is dif-

This journal is © The Royal Society of Chemistry [year]

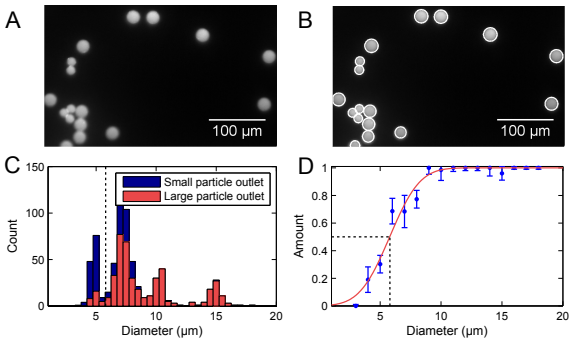

Fig. 2 Critical diameter measurement with polymer beads. (A) Fluorescence images of 10 μm and 15 μm beads. (B) The original image with white circles showing the fit to each bead. (C) Histogram with size distributions of beads in the small and large particle outlet. (D) Proportion of beads in the large particle outlet plotted as a function of size, and a fitted error function. The measured critical diameter, marked by the black dashed lines, is 5.8 μm $\pm$ 0.3 μm.

ferent from the calculated value. The displacement of beads due to an effect at the end of the pinched segment described by Vig and Kristensen[25] could explain this discrepancy. Using semi-3D simulations they showed that at the corner at the end of the pinched segment, streamlines are squeezed closer to the wall than in the pinched segment. This corner effect forces particles to follow streamlines further away from the wall, and will decrease the critical diameter. We made similar semi-3D finite element simulations, and found a modified critical diameter, by measuring the shortest distance from the wall to the outer streamline going into the small particle outlet.

The distance from the pinched segment wall to the outer streamline was measured as 4.2 μm, corresponding to a critical diameter of 8.4 μm, which is close to the value of 8.3 μm found from the calculations. The smallest distance from the corner to the outer streamline was 3.85 μm, corresponding to a critical diameter of 7.7 μm. The same simulation was carried out on both designs, and the simulated critical diameters are summarized in Tab. 2, together with the critical diameters calculated from the geometry of the designs, and the critical diameters determined from bead experiments.

Table 2 Calculated, measured and simulated critical diameter of the two PFF designs. The calculations are based on channel dimensions, the measured sizes are based on bead experiments, and the simulated values are based on semi-3D simulations, where the corner effect has been taken into account.

	Calc. d_c [μm]	Measured d_c [μm]	Simulated d_c [μm]
Non-adjusted PFF	13.0	7.6 $\pm$ 0.4	10.2
Adjustable PFF	8.3	5.8 $\pm$ 0.3	7.7

The corner effect accounts for some of the difference between calculated and measured critical diameter. Other influences on the critical diameter include deviations in the replication of the design during the fabrication and particle disturbances of the flow. The results indicate that the measurement of the critical diameter presented in figure 2 is more accurate than the theoretical calculations and the simulations. An advantage of PFF is that the critical diameter can be changed by applying pressure to the outlets. Using our new analysis method, microliter-sized bead samples can be used to find the optimal flow conditions, before experimenting on valuable cell samples.

The adjustable PFF devices have a critical diameter that is too small for separation of CTCs and WBCs. It can be increased by applying a pressure at the drain, and it was found that a pressure of 40 % of the buffer inlet pressure was suitable such that the critical diameter for hard spheres is 8 μm.

3.2 Cancer cell separation by PFF

We used non-adjusted PFF devices to separate WBCs and cancer cells. We have measured the critical diameter of the device to be 7.6 μm with polymer beads. The devices were initially run with a sample flow rate of 10 μL/h, and the results are shown in Fig. 3A-D.

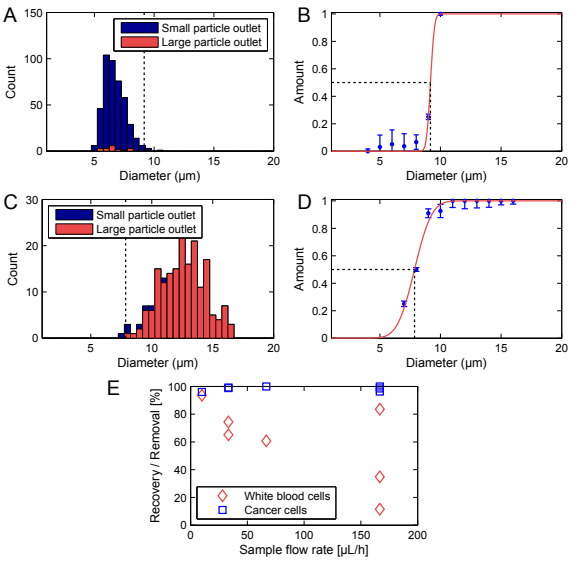

Fig. 3 Separation of WBCs and LS174T cells in a PFF device with a fixed critical diameter at 10 μL/h. (A-B) Size distribution of WBCs in each outlet after separation and corresponding critical diameter analysis. The critical diameter is marked by a black dashed line and reads 9.2 $\pm$ 2.1 μm. (C-D) Size distribution of cancer cells in each outlet after separation and corresponding critical diameter analysis. The critical diameter is marked by a black dashed line and reads 7.9 $\pm$ 0.15 μm. The recovery was 96.0 % for cancer cells with a 93.6 % removal of WBCs. (E) Recovery of cancer cells and removal of WBCs at different sample flow rates.

The first observation is that the critical diameter for cancer cells is 7.9 μm $\pm$ 0.15 μm, similar to polymer beads. However, the critical diameter for WBCs is larger, 9.2 μm $\pm$ 2.1 μm. This difference in critical diameter is an advantage and resulted in a recovery of 96 % cancer cells together with a removal of 93.6 % WBCs.

This is a good separation that should allow for isolation of CTCs, however, the experiment was performed at sample flow rates that are too low for applications where at least 10 mL of sample must be sorted. We investigated how increasing flow rates affect the recovery and removal of cells. The results from a series of experiments are seen on Fig. 3E. The CTC recovery is independent of flow rates, however the WBC removal drops rapidly as the flow rate is increased. A possible reason is that the inertia of the WBCs increase with increasing flow rates, and eventually becomes large enough to deflect them from the streamlines going around the corner and into the small particle outlet. This also explains why cancer cell recovery is unaffected, since the cancer cells move along straight trajectories into the large particle outlet.

3.3 Cancer cell separation by adjustable-PFF

The adjustable-PFF devices were also tested with WBC samples spiked with cancer cells to demonstrate that the critical diameter of PFF devices can be adjusted without loss of separation efficiency. A sample flow rate of 50 μL/h was used, and the critical diameter was adjusted by applying a pressure at the drain outlet. The results are shown in Fig. 4A-D.

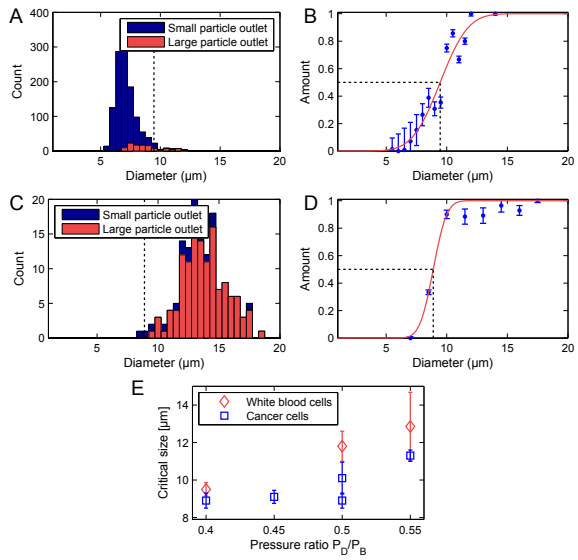

Fig. 4 Separation of WBCs and LS174T cells using adjustable-PFF devices at 50 μL/h. (A-B) Size distribution of WBCs in each outlet after separation, and corresponding critical diameter plot. The critical diameter is marked by a black dashed line and reads 9.5 $\pm$ 0.35 μm. (C-D) Size distribution of cancer cells in each outlet after separation, and corresponding critical diameter plot. The critical diameter is marked by a black dashed line and reads 8.9 $\pm$ 0.4 μm. The recovery was 91.4 % for cancer cells with a removal of 89.7 % WBCs. (E) Measured critical diameter of cancer cells and WBCs vs. the pressure ratio between the buffer inlet and the drain.

The measured recovery and removal are comparable to the values measured for the non-adjusted PFF devices at equivalent flow rates, see Fig. 3E. Thus we show that PFF devices with an arbitrary critical diameter can be tuned to fit the separation of a specific sample.

A difference in critical diameter between cell types was again observed in the measurements as seen in Fig. 4E. Here the critical diameter of each cell type is plotted for experiments where the pressure on the drain was changed relative to the pressure on the buffer inlet. As expected the critical diameter for both cell types increases with an increasing pressure on the drain, and the critical diameter of the WBCs stays above the critical diameter of the cancer cells, thus ensuring that the overall separation efficiency is high. The difference in critical diameter is an advantage and is exploited to get a better separation than expected from the overlapping size distributions.

3.4 How cell deformability influences PFF

We demonstrated that WBCs have a larger critical diameter than cancer cells in a PFF device. A possible source of error is that cancer cells are expected to be less spherical than WBCs. This would lead to an overestimation of the shortest axis of the cancer cells when measured by fluorescence imaging. The critical diameter of cancer cells would then be overestimated, which would mean that the difference in critical diameter between WBCs and cancer cells is indeed even more pronounced that we observe here. We hypothesize instead that the difference in critical diameter is due to a difference in deformability. This would indicate that the cancer cells are more rigid than the WBCs, which also explains why they had a measured critical size closer to the one for beads. It is possible that the differences in cell deformability are due to the large nucleus of the cancer cells. This has already been exploited by Tang *et al*, who used microfilters to separate cancer cells from whole blood. They observed that WBCs were able to deform and squeeze through 6.5 μm filters, while cancer cells were caught because of their rigid nucleus.[26]

We investigated three possible effects in the PFF devices that could make the cell deformability influence the critical size of the cell separation: The elongation flow when cells move from the sample inlet channel to the pinched segment, the shear rate in the pinched segment, and squeezing at the corner between the pinched segment and the outlet channels.

We model the shear rate experienced by cells when travelling from the inlet to the pinched segment by finite element simulations, as seen in Figure 5A. The largest cell deformation is expected to be at the corner at the end of the pinched segment, where the corner effect cause hard spheres or cells to change to streamlines further away from the wall, whereas soft cells can deform and follow the streamlines they occupy in the pinched segment. We estimated the shear rates at the corner between the pinched segment and the small particle outlet channel using 3D simulations. The results from the simulations are seen in Fig. 5B. The shear rate is constant along the wall and then increases at the corner to approx. 30,000 s^{-1} for a sample flow rate of 33 μL/h. This is much larger than the shear rates used by Beech *et al.*[27] to deform red blood cells in lateral displacement structures. Thus the shear rates are large enough to deform soft cells, which will then get an increased critical diameter, while hard cells will get

This journal is © The Royal Society of Chemistry [year]

a decreased critical diameter due to the so-called corner effect. This is illustrated in Fig. 5C. The high shear rates combined with the corner effect enhance the separation of hard and soft particles with overlapping sizes, which is very advantageous when separating cancer cells from WBCs.

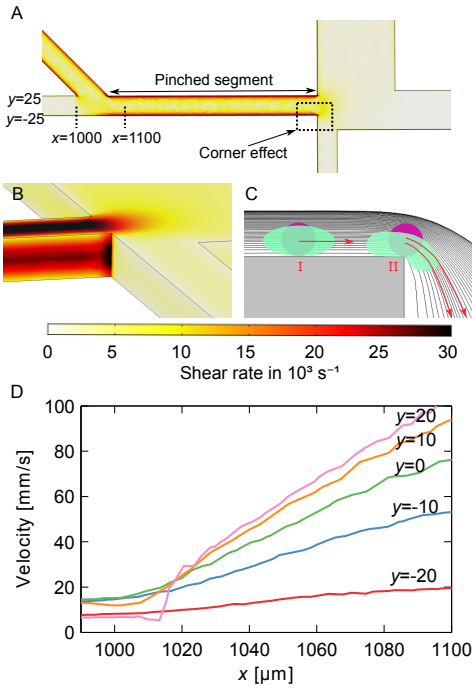

Fig. 5 Shear rates in the PFF device. (A) Simulation of shear rate at a middle height in the PFF device. The shear rare is greatest at the wall in the pinched segment. (B) 3D simulation at the corner between the pinched segment and the small particle outlet channel. The shear rate is constant along the wall and then increases at the corner. The color scale fits both figure A and B. (C) Illustration of the squeezing of streamlines at the transition from the pinched segment: a hard particle is forced to follow a streamline further away from the pinched segment wall because of the corner effect. A soft particle is deformed even further due to increased shear rate at the corner and follows its initial streamline. The particles are included to illustrate the different behaviours of soft and hard particles and were not part of the simulation. (D) Simulated flow velocity along streamlines going from the sample inlet channel to the pinched segment. All streamlines are at a middle height in the channel, and starting at different y-coordinates in the inlet channel, as marked on figure A. The plotted velocities were measured between the x-coordinates also marked on figure A.

We have also estimated the shear rate in the pinched segment. A top-view 3D simulation of the pinched segment is seen in Fig. 5A. The illustrated plane is at a middle height, and the highest shear rate is found along the wall in the pinched segment. For a sample flow rate of 33 μL/h the maximum shear rate is approx. 20,000 s^{-1}. It is in the same order of magnitude as the shear rate at the corner and is expected to contribute to cell deformation as well.

Finally when cells move from the sample inlet channel to the pinched segment, they experience an increase in velocity due to the incoming fluid from the buffer inlet. Simulations were used to investigate this elongation flow. It is assumed that the cells travel at a height in the middle of the channel. The velocity along streamlines starting at different positions in the sample inlet is plotted in Fig. 5D. The plot shows that the cells move at a constant velocity and then experience a linear velocity change as they move into the pinched segment. The change in velocity gives rise to a shear rate equal to the slope of the velocity curve. As opposed to the other cell deformation contributions, the shear rate from the elongation flow depends on the position of the cells before they are aligned. This could therefore decrease the separation efficiency. However the maximum shear rate is approx. 1,000 s^{-1}, which is much smaller than the shear rates along the wall and at the corner of the pinched segment. Thus elongation flow is not expected to contribute to cell deformation.

The cell viability is not expected to decrease since Hur *et al.*[28] did not see a significant change when using inertial focusing with high shear stresses to classify cells according to deformability.

We have shown that the high shear rates in PFF devices can be used to improve separation of hard and soft particles. Cell deformation can also be used to improve other microfluidic size-separation devices such as deterministic lateral displacement arrays, where morphology and deformability of RBCs has already been exploited.[27]

4 Conclusion

We have separated cancer cells and WBCs at efficiencies over 90 % using injection molded PFF devices. We measured the size of all separated cells and showed that there is a significant difference in critical diameter between WBCs and cancer cells. We suggest this comes from a difference in cell deformability, which improves the separation efficiency. We have used finite element simulations to investigate the cell deformation at three critical places on the devices, and the largest contribution is the shear rate at the corner of the pinched segment, just before the separation.

We have demonstrated that the critical diameter of PFF devices can be changed successfully without a loss of separation efficiency. The highest separation efficiencies were obtained at sample flow rates of 10 μL/h. At higher flow rates the cancer cell recovery was unaffected, whereas the WBC removal decreased. We believe the WBC trajectories changed because of increased inertia of the cells. Further investigations are needed to determine the exact cause and improve the PFF design, so a higher sample throughput can be accomplished without a decrease in WBC removal.

5 Acknowledgements

The authors gratefully acknowledge funding from the European Commission under the Seventh Framework Programme (FP7/2007−2013) under grant agreements number 278204 (Cell-o-matic).

References

1 A. F. Chambers, A. C. Groom and I. C. MacDonald, *Nature Reviews Cancer*, 2002, **2**, 563–572.

2 C. Alix-Panabières and K. Pantel, *Lab on a Chip*, 2014, **14**, 57–62.

3 S. Riethdorf, H. Fritsche, V. Müller, T. Rau, C. Schindlbeck, B. Rack, W. Janni, C. Coith, K. Beck, F. Jänicke *et al.*, *Clinical Cancer Research*, 2007, **13**, 920–928.

4 T. Fehm, O. Hoffmann, B. Aktas, S. Becker, E. F. Solomayer, D. Wallwiener, R. Kimmig and S. Kasimir-Bauer, *Breast cancer res*, 2009, **11**, R59.

5 C. Alix-Panabières, J.-P. Vendrell, M. Slijper, O. Pellé, E. Barbotte, G. Mercier, W. Jacot, M. Fabbro and K. Pantel, *Breast Cancer Res*, 2009, **11**, R39.

6 D. Gossett, W. Weaver, A. Mach, S. Hur, H. Tse, W. Lee, H. Amini and D. Di Carlo, *Analytical and Bioanalytical Chemistry*, 2010, **397**, 3249–3267.

7 X. Zhe, M. L. Cher and R. D. Bonfil, *American journal of cancer research*, 2011, **1**, 740.

8 L. R. Huang, E. C. Cox, R. H. Austin and J. C. Sturm, *Science*, 2004, **304**, 987–990.

9 H. W. Hou, M. E. Warkiani, B. L. Khoo, Z. R. Li, R. A. Soo, D. S.-W. Tan, W.-T. Lim, J. Han, A. A. S. Bhagat and C. T. Lim, *Scientific reports*, 2013, **3**, 1259.

10 T. M. Geislinger and T. Franke, *Biomicrofluidics*, 2013, **7**, 044120.

11 K. Loutherback, J. D'Silva, L. Liu, A. Wu, R. H. Austin and J. C. Sturm, *AIP advances*, 2012, **2**, 042107–042107.

12 A. A. S. Bhagat, H. W. Hou, L. D. Li, C. T. Lim and J. Han, *Lab on a Chip*, 2011, **11**, 1870–1878.

13 M. Yamada, M. Nakashima and M. Seki, *Analytical chemistry*, 2004, **76**, 5465–5471.

14 J. Takagi, M. Yamada, M. Yasuda and M. Seki, *Lab on a Chip*, 2005, **5**, 778–784.

15 Y. Sai, M. Yamada, M. Yasuda and M. Seki, *Journal of chromatography A*, 2006, **1127**, 214–220.

16 C. Cupelli, T. Borchardt, T. Steiner, N. Paust, R. Zengerle and M. Santer, *Microfluidics and Nanofluidics*, 2013, 1–13.

17 A. Larsen, L. Poulsen, H. Birgens, M. Dufva and A. Kristensen, *Lab on a Chip*, 2008, **8**, 818–821.

18 M. Pødenphant, R. Marie, T. Olesen, M. Matteucci and A. Kristensen, *Microelectronic Engineering*, 2014, **124**, 53–57.

19 G. Vona, A. Sabile, M. Louha, V. Sitruk, S. Romana, K. Schütze, F. Capron, D. Franco, M. Pazzagli, M. Vekemans *et al.*, *The American journal of pathology*, 2000, **156**, 57–63.

20 K. B. Andersen, S. Levinsen, W. E. Svendsen and F. Okkels, *Lab on a Chip*, 2009, **9**, 1638–1639.

21 H. Bruus, *Theoretical microfluidics*, Oxford University Press, USA, 2008, vol. 18.

22 S. Tanzi, P. F. Østergaard, M. Matteucci, T. L. Christiansen, J. Cech, R. Marie and R. Taboryski, *Journal of Micromechanics and Microengineering*, 2012, **22**, 115008.

23 P. Utko, F. Persson, A. Kristensen and N. B. Larsen, *Lab on a Chip*, 2011, **11**, 303–308.

24 B. H. Tom, L. P. Rutzky, M. M. Jakstys, R. Oyasu, C. I. Kaye and B. D. Kahan, *In vitro*, 1976, **12**, 180–191.

25 A. L. Vig and A. Kristensen, *Applied Physics Letters*, 2008, **93**, 203507.

26 Y. Tang, J. Shi, S. Li, L. Wang, Y. E. Cayre and Y. Chen, *Scientific reports*, 2014, **4**, 6052.

27 J. P. Beech, S. H. Holm, K. Adolfsson and J. O. Tegenfeldt, *Lab on a chip*, 2012, **12**, 1048–1051.

28 S. C. Hur, N. K. Henderson-MacLennan, E. R. McCabe and D. Di Carlo, *Lab on a Chip*, 2011, **11**, 912–920.

This journal is © The Royal Society of Chemistry [year]

Paper III

Optimization of thermally sealed all-polymer microfluidic devices for hydrodynamic single particle trapping

Optimization of thermally sealed all-polymer microfluidic devices for hydrodynamic single particle trapping

Marie Pødenphant,[1] Brian Bilenberg,[2] Anders Kristensen,[1] and Rodolphe Marie[1, a)]

[1)] *DTU Nanotech, Ørsteds Plads Building 345east, 2800 Kgs. Lyngby, Denmark.*

[2)] *NILT Technology ApS, Diplomvej 381, 2800 Kgs. Lyngby, Denmark.*

(Dated: 7 September 2015)

We optimize the geometry of a microfluidic device based on a simple constriction for the trapping of single particles. In order to reduce fabrication costs, a one-layered design is replicated in a thermoplastic material by injection molding. As a consequence the maximum aspect ratio of the microfluidic constriction is limited by the dry etching of the master substrate for a given channel depth. To allow trapping of particles 5 μm in diameter the cross section of the constriction was reduced by thermally sealing the channels at temperatures close to the glass transition temperature of the polymer. The internal dimensions of the constriction were imaged by scanning electron microscopy after controlled freeze-fracture of the device. We show how the cross section of 10 μm-wide constrictions can be lowered by deformation to reach the flow conditions allowing single 5 μm polymer beads to be reliably captured.

[a)] Electronic mail: rodolphe.marie@nanotech.dtu.dk

Appendix A. Publications

I. INTRODUCTION

Single cell analysis is a powerful tool for the understanding of many biological processes[1–3]. Recently there has been a growing interest for the manufacturing of microfluidic devices for single cell trapping,[4] in particular the devices that achieve passive trapping of cells, as opposed to active devices based on an external force such as electrical[5] or optical[6] trapping. Various hydrodynamic trapping devices have been developed for different applications. Wang *et al.* created a cell sieve array for cytotoxicity analysis[7]. They successfully tested it on three different cell types and captured approx. 10 cells in each sieve. Tan and Takeuchi designed a trap and release system for microarray applications[8]. They used it to capture cells contained in hydro-gel beads, and demonstrated an optical-based release mechanism. The same group also made a hydrodynamic microarray device for observation of cell-cell interactions, which they demonstrated on microbeads[9] Kobel *et al.* made a two-layered single cell trapping device for cell cultivation[10]. It was tested on a T-cell lymphoma cell line with a capture efficiency of 97 %. Ultimately, each trap should capture a single cell.

Our design is inspired by a cultivation device made by Zhu *et al.*[11], who used it to capture 8 μm beads and yeast cells. On the designs mentioned above the trapped and retrieved cells go to the same outlet as the leftover cells, whereas on the design of Zhu *et al.* the leftover cells that are not captured go to a separate outlet. In this way trapped cells can be pushed through the traps to an uncontaminated outlet, where they can be extracted for further analysis.

For the sake of reducing the fabrication cost of the final device, we chose to use injection molding for the replication of a single-layer design in a thermoplastic cyclic olefin copolymer (COC). Thermoplastic polymers have become increasingly popular for fabrication of microfluidic devices due to low material costs and their mechanical and optical properties[12,13]. In the injection molding process, a microfluidic structure is defined as trenches in a silicon master that is later electroplated as a Nickel shim which is then used to replicate polymer parts[14]. A range of polymer fabrication techniques exist, such as hot embossing, thermoforming and injection molding[15–18]. Regardless of which replication technique is used, the maximum aspect ratio of the final microfluidic structure is limited by the etch process used to define the initial microfluidic structure in the silicon master, assuming a single layer design. In addition the microfluidic channels must be sealed with a lid and the bonding process is

crucial for the quality of the finalized devices. For most applications it is important that the bonding process does not alter the fabricated structures. However this can be a challenge because bonding is often done at high temperatures or pressures to get the highest bonding strength[19]. We propose to optimize the internal dimension of the microfluidic constriction by controlled alteration of the injection molded part under a thermal bonding at a temperature close to the glass transition temperature, T_g, of the COC polymer. Such optimization requires measurements of the final internal dimensions of the device at critical locations (the microfluidic constriction).

It can be done by cleaving the device with a diamond tipped cutting blade or cutting and polishing the device[20,21]. Instead we present a simpler method based on freeze-fracture. The polymer device is cooled with liquid nitrogen before fracture, thus a minimum deformation is achieved. We used freeze-fracture to investigate how bonding temperature and pressure affect the outcome of internal dimensions on injection molded devices for particle trapping. The devices were sealed with thin foils using UV-assisted thermal bonding at temperatures below T_g. UV surface treatment has previously yielded strong bonds between thermoplastic substrates without deformation of the microstructures[20,22]. We show that even though the devices were bonded at temperatures below T_g, narrow channels ($\approx 10\,\mu$m wide) experienced a large decrease in cross-sectional area. We demonstrate trapping of single polymer beads in the altered microfluidic structures.

II. MATERIALS AND METHODS

A. Particle trapping design

The device consists of a feeding channel where particles are introduced, and a buffer channel that guides the particles to the side of the feeding channel, where the traps are positioned. An overview of the device structure is seen in Figure 1. The traps have a triangular shape where particles get caught when trying to move through the long narrow channels. In this study we want to minimize the trap cross section such that when a particle occupies the trap, the flow through the trap is insufficient for a second particle to be trapped, and thus all traps get occupied by single particles, while leftover particles go towards a waste outlet. All the traps are connected to an outlet different from the waste outlet. The one-

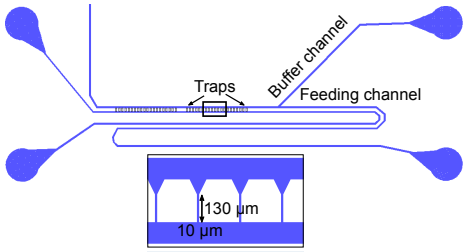

FIG. 1. Layout of the trapping design with a close-up of the traps. The large circles represent the position of inlets and outlets on the injection molded device. The particle flow is from right to left. The structure is a one-layered design with 30 μm deep channels.

layer design impose some restrictions on the trap dimensions. For single particle trapping the channels must have a height of at least 30 μm to prevent large particles or clumps from clogging the device. Therefore the traps have to be quite narrow to block the particles and long to minimize the flow through them. The traps are 10 μm wide, 130 μm long and located at a pitch of 200 μm.

B. Fabrication

A nickel shim for injection molding was fabricated using standard clean room processes[23]. The devices were injection molded with the COC polymer TOPAS®grade 5013 using a mold temperature of 120 °C, a holding pressure of 1400 bar and a cooling time of 15 s. The injection molder was equipped with a tool that creates 12 Luer fittings on each device. The Luer fittings are used to connect flow controllers to the microstructures on the device.

C. UV-assisted thermal bonding

The channels on each device were sealed with a 150 μm thick TOPAS®grade 5013 foil using UV-assisted thermal bonding. The devices and lids were exposed to UV-light from a mercury arc lamp for 30 s and then placed in an aluminum holder that fits to the Luer fittings. A smooth nickel disc and a thin PDMS plate were placed on top of the lid to ensure a uniform pressure on the device surface. A previous study has shown that devices bonded at 120 °C and up to 5.1 MPa for 5 minutes experience a strong bonding[24]. These parameters

were used as well as higher temperatures up to 128 °C, since T_g of TOPAS®5013 is 130 °C. We also applied pressure locally at the traps to prevent the inlets and microchannel network from collapsing during bonding. This was done by placing a small thick PDMS slice on top of the 150 μm foil at the position of the traps. The stack was bonded using a P/O/Weber press. Images of the nickel shim, an injection molded device and a sealed device are shown in Figure 2.

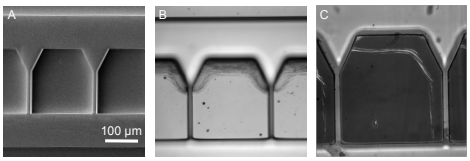

FIG. 2. (A) SEM image of traps on the nickel shim. (B) Bright field image of an injection molded device. (C) Bright field image of a device after bonding at 120 °C and 5.1 MPa.

D. Freeze-fracture

The freeze-fracture procedure is sketched in Figure 3. First a hacksaw is used to saw from the edge of the bonded device to a point close to the traps. The device is cut from two sides to help guide the break. Then a scalpel is used to make a superficial cut on the top and bottom side of the device across the traps. This should increase the likelihood that the device fractures at the cuts. Next the entire device is immersed in liquid nitrogen until it is cooled and then rapidly placed in a bench clamp and split in two. Finally the two

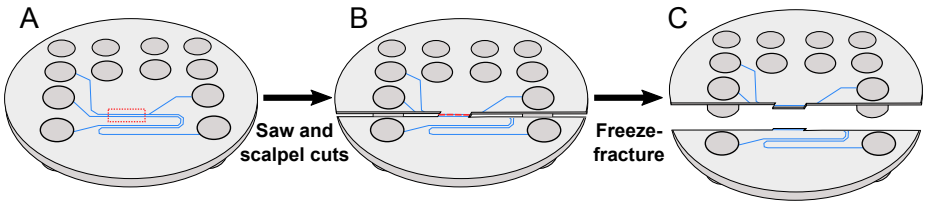

FIG. 3. Sketch of the freeze-fracture process. (A) Sealed device with traps of interest marked by the red dotted square. (B) The device after it has been cut with a hacksaw and a scalpel (red dashed line). (C) The device after freeze-fracture. The trap cross sections are exposed and can be imaged.

pieces are coated with an approx. 10 nm layer of either silver or palladium-gold to enable SEM imaging. Traps were exposed on all fractured devices, and the method therefore has a precision of at least 130 μm, which is the length of the traps.

The fractured pieces were imaged in a Zeiss Supra VP 40 SEM (Carl Zeiss AG) at low voltages (2 kV-4 kV) and low working distances (<10 mm) using an inlens detector. The images were used to measure dimensions and cross-sectional area of the traps.

E. Fluorescent bead solutions

Fluorescent polystyrene beads of 5 μm (Duke Scientific) and 15 μm (Invitrogen) diameters were used. Bead solutions were prepared by mixing the beads with Milli-Q water and 0.1 % Triton X-100 to a total concentration of 3×10^5 beads mL^{-1}. The bead solutions were degassed in an ultrasonic bath before experiments. Milli-Q water and 0.1 % Triton X-100 was used to wet the devices before the sample was introduced.

To conduct trapping experiments, bead samples were pipetted into the inlets on the device and pushed through the channels using a pressure-driven flow controller (Fluigent MFCS-EZ). Experiments were monitored using an inverted fluorescence microscope (Nikon Eclipse TE2000-U) coupled to an EMCCD camera (Photometrics Cascade II:512).

Pressures in the range of 5 mbar - 10 mbar were applied, corresponding to sample flow rates of 2.9 μL/h - 5.7 μL/h.

F. Simulations

The device was simulated with COMSOL version 4.3, using semi-3D simulations as described by Vig and Kristensen[25]. No-slip boundary conditions were applied to all channel walls, and the pressures at the inlets and outlets were set to values used in the experiments. It was assumed that particles have no influence on the flow.

III. RESULTS

A. Freeze-fracture investigation

The effects of bonding temperature and pressure were investigated using the freeze-fracture method. Bonding at 120 °C and 5.1 MPa is used as the reference because the microchannel dimensions are not altered under those conditions. We compare the result of other bonding conditions by visualizing the trap cross sections. SEM images of freeze-fractured devices are seen in Figure 4. The device in Figure 4A fractured at the scalpel cut and exposed several trap cross sections. There is a great variation in trap cross sections of devices bonded at a few degree's difference. At the reference bonding, the cross section is $257\,\mu\text{m}^2 \pm 18\,\mu\text{m}^2$ (Fig. 4B). Bonding above 120 °C (Fig. 4C-E) causes the microchannel side walls to bend inwards and the trap cross section is reduced to $15.5\,\mu\text{m}^2 \pm 6.4\,\mu\text{m}^2$ (Fig. 4D). At the highest temperature, the deformation of the microchannel is such that not only the trap is critically deformed. We therefore obtain a functional device by applying pressure only on the trap area at the highest temperature (Fig. 4E) while bonding of the overall microchannel structure is obtained at the reference parameters.

B. Bead trapping experiments

In our design, incoming particles are aligned against the microchannel wall where the microfluidic constrictions are placed (i.e. the traps). A particle is thus placed on a streamline according to its radius r, see Fig. 5A. For each trap, a fraction of liquid from the feeding channel enters the trap downstream corresponding to a distance from the wall r_c. We call r_c the critical radius. A condition for the bead to enter the next trap is that it is on a streamline that enters the traps or $r < r_c$. Successful single particle trapping occurs if $r_c > r$ when the trap is unoccupied and $r_c < r$ when the trap is occupied with a single particle, thus the incoming bead passes by and enters the next trap.

Particle trapping was tested with fluorescent beads to assess the functionality of devices prepared under different bonding conditions. The device bonded at reference parameters (without deformation of the constriction, see figure 4B) was able to capture 15 μm beads however, multiple beads were trapped because the hydrodynamic resistance of the constriction is not reduced significantly by the presence of a single particle. This can be seen in

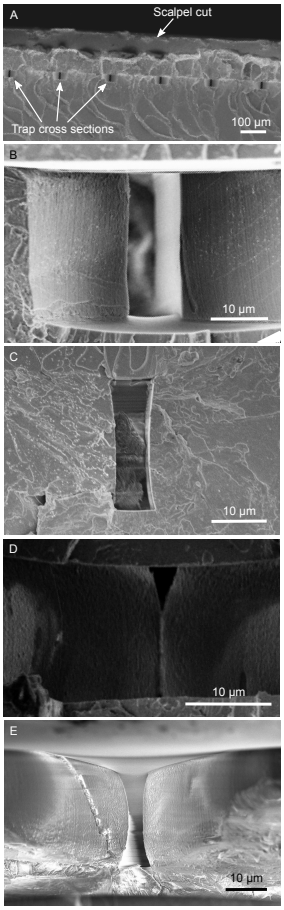

FIG. 4. (A) SEM image of a freeze-fractured device showing an overview of trap cross sections where the scalpel cut can be seen. (B) close-up of trap cross section on a device bonded at 120 °C and 5.1 MPa. These constrictions have an average cross-sectional area of $257\,\mu m^2 \pm 18\,\mu m^2$. (C) Trap bonded at 125 °C and 5.1 MPa. The average cross-sectional area is $192\,\mu m^2 \pm 9\,\mu m^2$. (D) Trap bonded at 128 °C and 2.5 MPa with an average cross-sectional area of $15.5\,\mu m^2 \pm 6.4\,\mu m^2$. (E) Trap bonded at 120 °C and 2.5 MPa and then 128 °C and 0.5 MPa. The average cross-sectional area is $91\,\mu m^2 \pm 25\,\mu m^2$.

Figure 6A.

Reducing the constriction cross section to $91\,\mu m^2$ under bonding at 128 °C and 0.5 MPa (Fig. 4E) enables single capture of 5 μm particles in adjacent traps (Fig. 6B). The devices

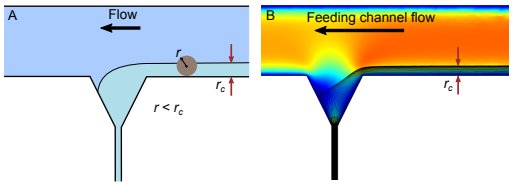

FIG. 5. (A) Microfluidic conditions for particle trapping. (B) Semi-3D simulation showing streamlines going through the first trap of the device bonded at reference conditions. The lateral position of the outermost streamline entering the trap shows the maximum radius a particle can have before it is no longer captured. The critical radius r_c is marked by the red solid line.

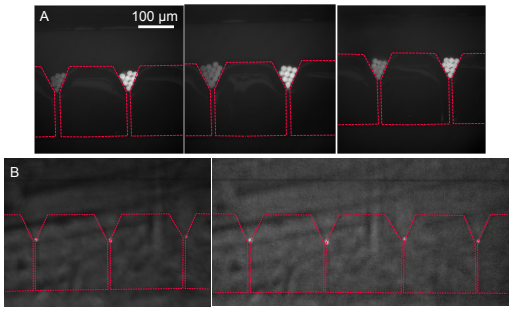

FIG. 6. Combined bright field and fluorescence image of (A) several 15 μm beads in traps bonded at 120 °C and 5.1 MPa and (B) 5 μm beads in traps bonded at 120 °C and 2.5 MPa and then 128 °C and 0.5 MPa. The red dashed lines represent the approximate positions of the channel walls. Single particle trapping was possible because the trap cross sections were altered by high temperature bonding, as seen in Figure 4E.

were also tested with 15 μm beads, however they flowed past the traps and could not be captured.

We use 3D simulations to confirm that for the optimised trap geometry (i) 5 μm beads enter unoccupied traps (ii) 5 μm beads do not enter a trap already occupied by one bead and (iii) 15 μm beads cannot be trapped in the device. Streamlines going through the first trap in a device bonded at reference parameters are visualized in Figure 5B. In this design, r_c, the distance from the wall to the outermost streamline going through the trap, is 10.8 μm according to the simulation. This is much larger than the radius of the 15 μm beads (7.5 μm), and explains why multiple beads were captured. For the optimised geometry

(Fig. 4E) we simulate a r_c of just 3.7 μm. The difference between r_c and the radius of 5 μm beads (2.5 μm) is smaller. We estimate with simulations that the 5 μm beads must block the trap cross section by 40 % to obtain single bead capture, which seems reasonable from the trap geometry. The 15 μm beads are not captured since they have a radius larger than the simulated r_c.

In our design reducing the microfluidic trap cross section by deforming the microchannel is successful at creating flow conditions for single particle trapping. We estimate that the hydraulic resistance of the trap was increased 10 fold by the deformation during bonding[26]. Such a high resistance of rectangular traps on a one-layered design with a 30 μm height would require a trap width of 3.7 μm, which is challenging to fabricate.

We find that the conditions needed for successful single microparticle capture are traps where the smallest dimension is smaller than the particles, and a critical radius which is slightly larger than the particle radius, so that a single particle can sufficiently reduce the flow through the trap.

IV. CONCLUSION

We have fabricated a disposable all-polymer one-layer particle trapping device by injection molding and UV-assisted thermal bonding. The limitations in the one-layer design were compensated for by sealing the devices at temperatures close to the glass transition temperature to deliberately decrease the trap cross sections. The sealed channels were characterized using a precise and easy method for breaking channels based on freeze-fracture. The method can be used to check the bonding quality of particularly sensitive structures as well as to optimize the outcome of channel dimensions in general. We showed that trapping devices with altered structures had an improved trapping efficiency compared to structures sealed with standard parameters. We explained the improved trapping efficiency by finding the critical radius, which determines whether particles of a given size are trapped or not. The simulations were consistent with the bead capture results, and we showed that to capture single particles the critical radius should be just above the particle size.

V. ACKNOWLEDGEMENTS

The authors gratefully acknowledge funding from the European Commission under the Seventh Framework Programme (FP7/2007−2013) under grant agreements number 278204 (Cell-o-matic).

REFERENCES

[1]C. Zong, S. Lu, A. R. Chapman, and X. S. Xie, Science **338**, 1622 (2012).

[2]J. Gole, A. Gore, A. Richards, Y.-J. Chiu, H.-L. Fung, D. Bushman, H.-I. Chiang, J. Chun, Y.-H. Lo, and K. Zhang, Nature biotechnology **31**, 1126 (2013).

[3]S. S. Dey, L. Kester, B. Spanjaard, M. Bienko, and A. van Oudenaarden, Nature biotechnology (2015).

[4]J. Nilsson, M. Evander, B. Hammarström, and T. Laurell, Analytica chimica acta **649**, 141 (2009).

[5]J. Voldman, Annu. Rev. Biomed. Eng. **8**, 425 (2006).

[6]K. Ramser and D. Hanstorp, Journal of biophotonics **3**, 187 (2010).

[7]Z. Wang, M.-C. Kim, M. Marquez, and T. Thorsen, Lab on a Chip **7**, 740 (2007).

[8]W.-H. Tan and S. Takeuchi, Lab on a Chip **8**, 259 (2008).

[9]T. Teshima, H. Ishihara, K. Iwai, A. Adachi, and S. Takeuchi, Lab on a Chip **10**, 2443 (2010).

[10]S. Kobel, A. Valero, J. Latt, P. Renaud, and M. Lutolf, Lab on a Chip **10**, 857 (2010).

[11]Z. Zhu, O. Frey, D. S. Ottoz, F. Rudolf, and A. Hierlemann, Lab on a Chip **12**, 906 (2012).

[12]H. Becker and C. Gärtner, Analytical and bioanalytical chemistry **390**, 89 (2008).

[13]P. S. Nunes, P. D. Ohlsson, O. Ordeig, and J. P. Kutter, Microfluidics and nanofluidics **9**, 145 (2010).

[14]P. Utko, F. Persson, A. Kristensen, and N. B. Larsen, Lab on a Chip **11**, 303 (2011).

[15]M. Heckele and W. Schomburg, Journal of Micromechanics and Microengineering **14**, R1 (2004).

[16]H. Becker and U. Heim, Sensors and Actuators A: Physical **83**, 130 (2000).

[17]R. Truckenmüller, S. Giselbrecht, N. Rivron, E. Gottwald, V. Saile, A. Van den Berg, M. Wessling, and C. Van Blitterswijk, Advanced Materials **23**, 1311 (2011).

[18]J. Giboz, T. Copponnex, and P. Mélé, Journal of Micromechanics and Microengineering **17**, R96 (2007).

[19]C.-W. Tsao and D. L. DeVoe, Microfluidics and Nanofluidics **6**, 1 (2009).

[20]A. Bhattacharyya and C. M. Klapperich, Lab on a Chip **7**, 876 (2007).

[21]Y. Sun, Y. C. Kwok, and N.-T. Nguyen, Journal of Micromechanics and Microengineering **16**, 1681 (2006).

[22]C. Tsao, L. Hromada, J. Liu, P. Kumar, and D. DeVoe, Lab on a Chip **7**, 499 (2007).

[23]S. Tanzi, P. F. Østergaard, M. Matteucci, T. L. Christiansen, J. Cech, R. Marie, and R. Taboryski, Journal of Micromechanics and Microengineering **22**, 115008 (2012).

[24]M. Matteucci, T. L. Christiansen, S. Tanzi, P. F. Østergaard, S. T. Larsen, and R. Taboryski, Microelectronic Engineering **111**, 294 (2013).

[25]A. L. Vig and A. Kristensen, Applied Physics Letters **93**, 203507 (2008).

[26]Calculated using the expression for hydraulic resistance of rectangular channels of equivalent height and cross section ($21.5\,\mu$m, $91\,\mu$m^2 and $28.3\,\mu$m, $257\,\mu$m^2 for the deformed and un-deformed traps respectively). The cross section of the traps on devices bonded at 120 °C have an estimated hydraulic resistance of $10^{14}\,\mathrm{kg\,m^{-4}s^{-1}}$, and traps bonded at 128 °C and 0.5 MPa have an estimated resistance of $10^{15}\,\mathrm{kg\,m^{-4}s^{-1}}$.

B

Injection moulding recipes

Parameters of all injection moulding recipes are listed in this part of the Appendix.

Table B.1: Injection moulding parameters of Recipe 1 & 2.

Parameter	Recipe 1	Recipe 2
Nozzle temperature	270 °C	250 °C
Injection speed	51.9 cm^3/s	51.9 cm^3/s
Shot volume pressure limit	2200 bar	2200 bar
Holding pressure	1400 bar → 0 bar in 9.5 s	1500 bar → 0 bar in 5 s
Mould temperature	120 °C	120 °C
Mould cooling time	15 s	60 s

Table B.2: Injection moulding parameters of Recipe 3 & 4.

Parameter	Recipe 3	Recipe 4
Nozzle temperature	250 °C	250 °C
Injection speed	20 cm^3/s - 45 cm^3/s	20 cm^3/s to 45 cm^3/s
Shot volume pressure limit	2200 bar	2200 bar
Holding pressure	1000 bar → 0 bar in 6 s	1500 bar → 0 bar in 5 s
Mould temperature	115 °C	120 °C
Mould cooling time	20 s	60 s

C

Optical profiler measurements

This part of the Appendix includes height measurements of all nickel shims used in this project. Some measurements on injection moulded chips are also included.

Measurements on the two shims with PFF devices are seen in Figure C.1. It can be seen that the surface of the Design1 shim is very rough, and the impurities at the top and bottom of the shim vary with approximately 1 μm. These structures were also transferred to the chips. The structures on both shims have a height of 30 μm.

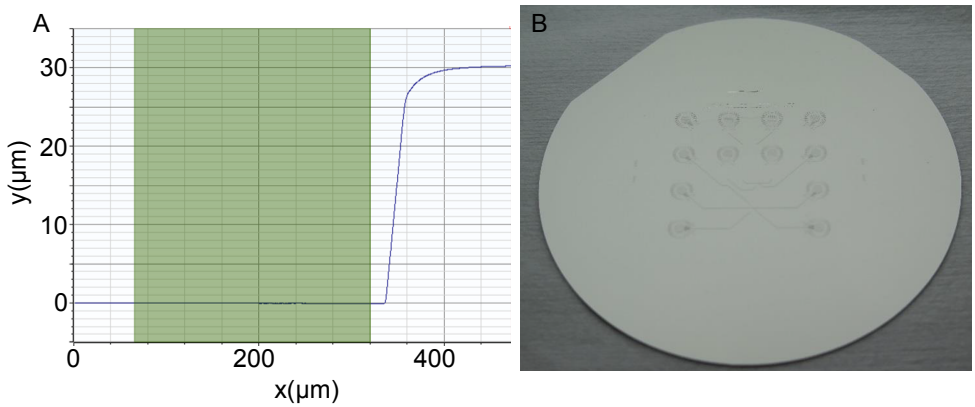

Figure C.1: (A) Height profile of the Design2 shim. The structures are much smoother than on the Design1 shim. (B) Photo of the Design2 shim. Both images are from NIL Technology.

Height measurements on the first generation cell trapping shim containing Design1-3 are seen in Figure C.2. The main channels are 32 μm high.

Height measurements on the second generation cell trapping shim containing Design4 and Design5 are seen in Figure C.3 together with a measurement on one of the chips. The main channels are 30 μm high and the traps are 26 μm.

Height measurements on the second generation cell trapping shim containing Design6 and Design7 are seen in Figure C.4. The traps are 22 μm to 24 μm high, while the main channels are 30 μm high according to NIL Technology. The traps are 1 μm wider than on the design.

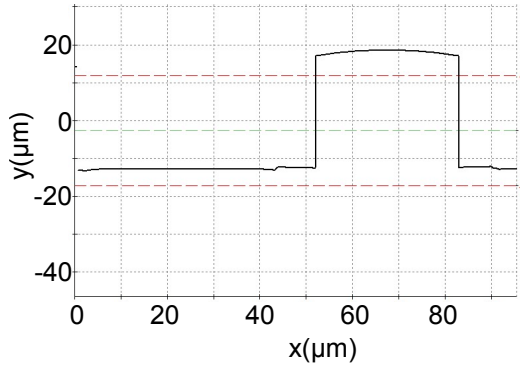

Figure C.2: Height profile of the smooth Design1-3 shim.

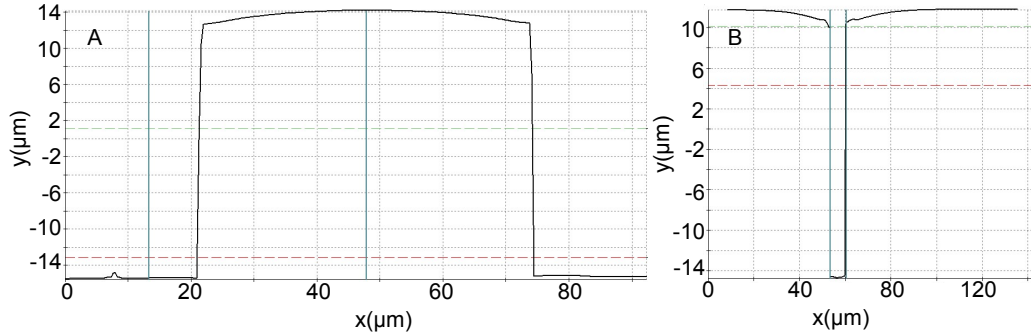

Figure C.3: (A) Height profile of the shim with Design4 and Design5. (B) Height profile of a Design4 trap on a chip injection moulded with Recipe 1.

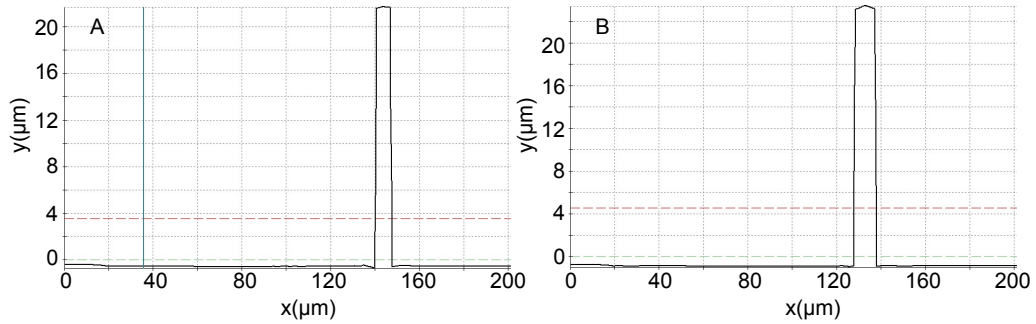

Figure C.4: Height profiles of the shim with Design6 and Design7. (A) 4 μm wide trap on Design6. (B) 7 μm wide trap on Design6.

Figure C.5 shows height measurements of the third generation cell trapping chips injection moulded with different recipes. The chips injection moulded with Recipe 4 had the smallest stress marks and it was therefore used to fabricate Device8. The main channels are 31 μm high, whereas the traps are 22 μm high and 4.5 μm wide.

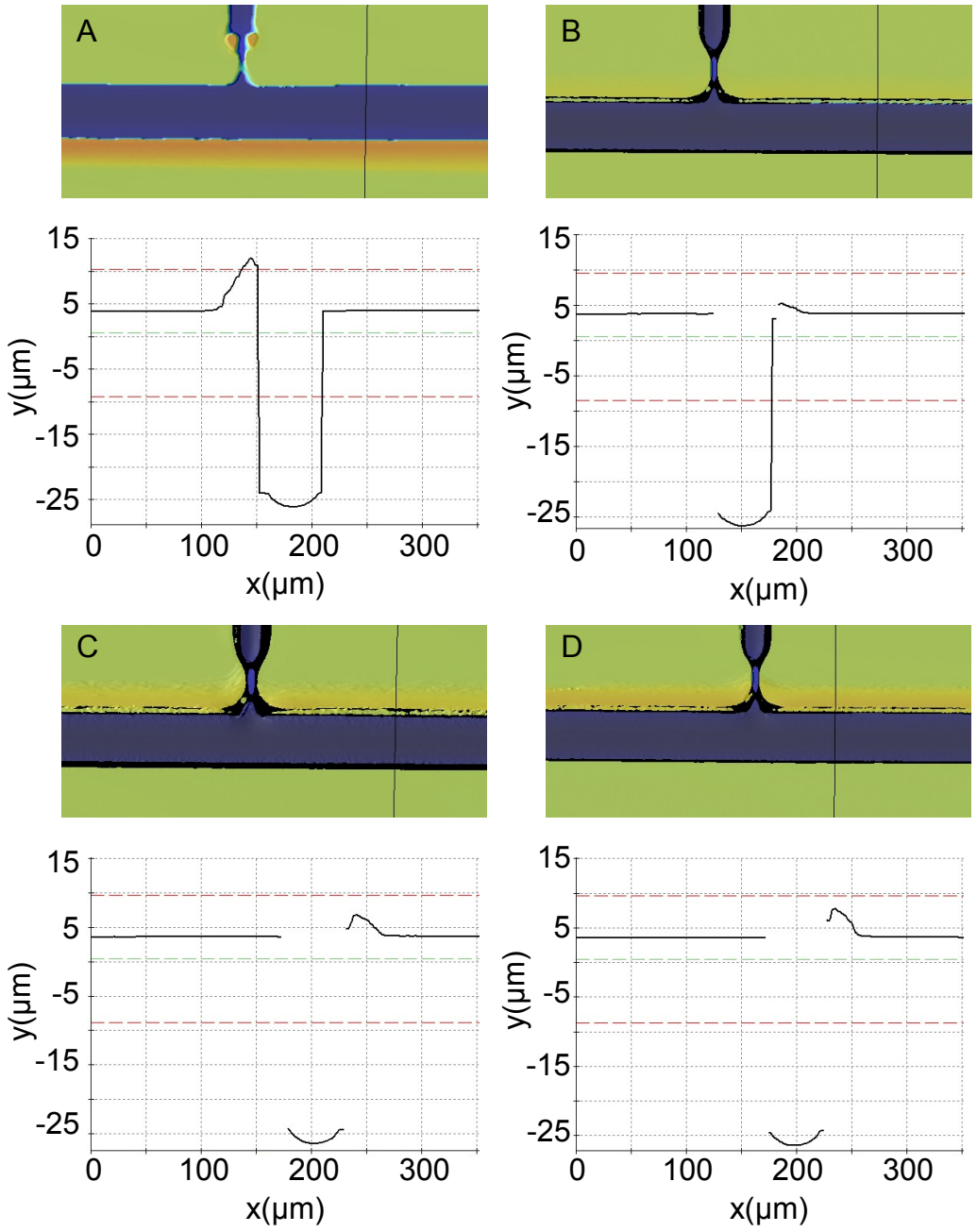

Figure C.5: (A) Surface topology and height profile on a chip injection moulded with Recipe 2. Blue colours represent the bottom height and red colours represent top heights. The black line indicates the position of the profile measurement.(B) Surface topology and height profile of chip injection moulded with the optimized Recipe 4. (C) Surface topology and height profile on a chip injection moulded with Recipe 2, except for a mould temperature of 115 °C. (D) Surface topology and height profile of chip injection moulded with Recipe 2, except for a holding pressure of 1000 bar.

D
Matlab scripts

This part of the Appendix includes Matlab scripts used for image analysis of separated samples.

Cancer cell separation

This is the Matlab script template used to determine recovery/removal and the critical diameter of a measurement. Paths to folders containing the cell images are simply inserted, and the script should work.

```
clear all; clc; close all;
startup

%% Analysis of images after separation ChipXX

% Small particle outlet 20x image WBC's

% Original images S Outlet
% Image 1-107 = both colours, image 108-214 = WBC's, image 215-321 = CC's
% and image 322 - 428 = BF
imgPath = 'C:....'; %Input directory with images
imgType = '*.png';
images  = dir([imgPath imgType]);
ImSmall = cell(1,428);
for i = 1:length(images);
    ImSmall{i} = imread([imgPath images(i).name]);
end


%%

path = 'C:...'; %Input path were images for investigation should be saved

k = 0; %counter
for i = 108:214; %Images with WBC's (blue fluorescence)
```

```
26      [centers, radii] = imfindcircles(ImSmall{1,i},[7 20], ...
27          'Edgethreshold', 0.25,'Sensitivity', 0.93);
28
29      for j = 1:length(radii);
30          k = k+1;
31          radii_2(k) = radii(j);
32
33          %Create and save images for visual inspection
34          figure;
35          subplot(1,3,1)
36          FigCrop = imcrop(ImSmall{1,i},[centers(j,1)-30 centers(j,2)-30 ...
                60 60]);
37          imshow(FigCrop,[])
38          viscircles([30 30], radii(j),'EdgeColor','b');
39          subplot(1,3,2)
40          FigCropBF = imcrop(ImSmall{1,i+214},[centers(j,1)-25 ...
                centers(j,2)-25 60 60]);
41          imshow(FigCropBF)
42          subplot(1,3,3)
43          FigCropColour = imcrop(ImSmall{1,i-107},[centers(j,1)-30 ...
                centers(j,2)-30 60 60]);
44          imshow(FigCropColour)
45
46          set(gcf,'inverthardcopy','off')
47          saveas(gcf,fullfile(path, strcat('WBC_Small_',num2str(k))),'png')
48      end
49
50      close all
51  end
52
53  % After visual inspection, some measurements are disregarded
54  x = 1:length(radii_2);
55  w = [];  %Input measurements to be disregarded (because of bad circular ...
        fit, not a cell etc.)
56  x = setdiff(x,w);
57
58  for j = x;
59      radii_final(j) = radii_2(j);
60  end
61
62  % Histogram with sizes of WBC
63  DSmall = radii_final*2*0.32; %0.32 = Pixelsize
64  xcenters = 0:0.5:35;
65  figure
66  mstyle
67  histogram(DSmall,xcenters)
68  xlabel('Diameter (\mu m)')
69  ylabel Count
70  title('Size Distribution, WBC small cell outlet')
71  xlim([4 25])
72
73  mexport('_Hist_SmallWBC'); %Save histogram
74
75  % Count number of WBC's in small particle outlet
```

```
76  N = DSmall > 0;
77  N_WBCS = sum(N)+XX; %Add number of cells that were removed from ...
        measurements because of bad fit
78
79
80  %% Large outlet 20x image WBC's
81
82  % Original images L Outlet
83  % Image 1-105 = WBCs', image 106-210 = CC's, image 211-315 = BF
84  % and image 316 - 420 = both colours
85  imgPath = 'C:...';
86  imgType = '*.png';
87  images  = dir([imgPath imgType]);
88  ImLarge = cell(1,420);
89  for i = 1:length(images);
90      ImLarge{i} = imread([imgPath images(i).name]);
91  end
92
93  %%
94  k = 0; %counter
95  radii_2 = [];
96  for i = 1:105;
97      [centers, radii] = imfindcircles(ImLarge{1,i},[7 20], ...
98          'Edgethreshold', 0.25,'Sensitivity', 0.93);
99
100     for j = 1:length(radii);
101         k = k+1;
102         radii_2(k) = radii(j);
103
104         figure;
105         subplot(1,3,1)
106         FigCrop = imcrop(ImLarge{1,i},[centers(j,1)-30 centers(j,2)-30 ...
                60 60]);
107         imshow(FigCrop,[])
108         viscircles([30 30], radii(j),'EdgeColor','b');
109         subplot(1,3,2)
110         FigCropBF = imcrop(ImLarge{1,i+210},[centers(j,1)-25 ...
                centers(j,2)-25 60 60]);
111         imshow(FigCropBF)
112         subplot(1,3,3)
113         FigCropColour = imcrop(ImLarge{1,i+315},[centers(j,1)-30 ...
                centers(j,2)-30 60 60]);
114         imshow(FigCropColour)
115
116         set(gcf,'inverthardcopy','off')
117         saveas(gcf,fullfile(path, strcat('WBC_Large_',num2str(k))),'png')
118     end
119
120     close all
121 end
122 %%
123 x = 1:length(radii_2);
124 w = [];  %Input measurements to be disregarded
125 x = setdiff(x,w);
```

```
126
127 radii_final = [];
128 for j = x;
129     radii_final(j) = radii_2(j);
130 end
131
132 % Histogram with WBCs in large particle outlet
133 DLarge = radii_final*2*0.32;
134 figure
135 mstyle
136 histogram(DLarge,xcenters)
137 xlabel('Diameter (\mu m)')
138 ylabel Count
139 title('Size Distribution, WBC large cell outlet')
140 xlim([4 25])
141
142 mexport('_Hist_LargeWBC');
143
144 % Count number of WBC's in large outlet
145 N = DLarge > 0;
146 N_WBCL = sum(N)+XX;
147
148 %% Large outlet 20x image cancer cells
149
150 k = 0; %counter
151 radii_2 = [];
152 for i = 106:210;
153     [centers, radii] = imfindcircles(ImLarge{1,i},[11 40], ...
154         'Edgethreshold', 0.25,'Sensitivity', 0.93);
155
156     for j = 1:length(radii);
157         k = k+1;
158         radii_2(k) = radii(j);
159
160         figure;
161         subplot(1,2,1)
162         FigCrop = imcrop(ImLarge{1,i},[centers(j,1)-50 centers(j,2)-50 ...
                100 100]);
163         imshow(FigCrop,[])
164         viscircles([50 50], radii(j),'EdgeColor','b');
165         subplot(1,2,2)
166         FigCropBF = imcrop(ImLarge{1,i+105},[centers(j,1)-50 ...
                centers(j,2)-50 100 100]);
167         imshow(FigCropBF)
168
169         set(gcf,'inverthardcopy','off')
170         saveas(gcf,fullfile(path, strcat('CC_Large_',num2str(k))),'png')
171     end
172
173     close all
174 end
175 %%
176 x = 1:length(radii_2);
177 w = [];
```

```
178 x = setdiff(x,w);
179
180 radii_final = [];
181 for j = x;
182     radii_final(j) = radii_2(j);
183 end
184
185 % Histogram with sizes of cancer cells in large particle outlet
186 DCells = radii_final*2*0.32;
187 xcenters = 0:1:35;
188 figure
189 mstyle
190 histogram(DCells,xcenters)
191 xlabel('Diameter (\mu m)')
192 ylabel Count
193 title('Size Distribution, Cancer cells large cell outlet')
194 xlim([4 25])
195
196 mexport('_Hist_LargeCC');
197
198 % Count number of cancer cells in large outlet
199 N = DCells > 0;
200 N_CCL = sum(N)+XX;
201
202 %% Small outlet 20x image cancer cells
203
204 k = 0; %counter
205 radii_2 = [];
206 for i = 215:321;
207     [centers, radii] = imfindcircles(ImSmall{1,i},[11 40], ...
208         'Edgethreshold', 0.25,'Sensitivity', 0.93);
209
210     for j = 1:length(radii);
211         k = k+1;
212         radii_2(k) = radii(j);
213
214         figure;
215         subplot(1,2,1)
216         FigCrop = imcrop(ImSmall{1,i},[centers(j,1)-50 centers(j,2)-50 ...
                100 100]);
217         imshow(FigCrop,[])
218         viscircles([50 50], radii(j),'EdgeColor','b');
219         subplot(1,2,2)
220         FigCropBF = imcrop(ImSmall{1,i+107},[centers(j,1)-50 ...
                centers(j,2)-50 100 100]);
221         imshow(FigCropBF)
222
223         set(gcf,'inverthardcopy','off')
224         saveas(gcf,fullfile(path, strcat('CC_Small_',num2str(k))),'png')
225     end
226
227     close all
228 end
229 %%
```

```
x = 1:length(radii_2);
w = [];
x = setdiff(x,w);

radii_final = [];
for j = x;
    radii_final(j) = radii_2(j);
end

% Histogram with sizes of cancer cells
DSCells = radii_final*2*0.32;
figure
mstyle
histogram(DSCells,xcenters)
xlabel('Diameter (\mu m)')
ylabel Count
title('Size Distribution, Cancer cells small cell outlet')
xlim([4 25])

mexport('_Hist_SmallCC');

% Count number of cancer cells in small outlet
N = DSCells > 0;
N_CCS = sum(N)+XX;

%%
% Analysis of combined WBC data

% Combined histogram of WBCs in both outlets.
figure
mstyle
xcenters = 1:0.5:25;
histogram(DSmall,xcenters)
hold on
histogram(DLarge,xcenters)
xlabel('Diameter (\mu m)')
ylabel('Count')
legend('Small particle outlet', 'Large particle outlet')
xlim([0 20])
ylim([0 150])
hold on %Line showing critical diameter found later in script
line([9.174 9.174], [0 150],'linewidth',2,'color','k','linestyle',':');
hold off

mexport('_Hist_WBC');

%WBCs in small vs large outlet
xcenters = 4:1:25;
counthistdataS = histcounts(DSmall,xcenters);
counthistdataL = histcounts(DLarge,xcenters);

%Amount of WBCs in the large particle outlet for each size
data_perc = counthistdataL./(counthistdataL+counthistdataS);

```

```
% Error bars based on number of counts pr. bin
N = counthistdataS+counthistdataL;
EB = sqrt(N.*(1-N/sum(N)))/100;

xcenters = 4:1:24;
% Put x and y-values together and remove columns where data_perc is NaN
M = [xcenters; data_perc]';
N = M(~any(isnan(M),2),:);
% Error function fit
ft = fittype('errorfun( x, a, b)');
[f,gof] = fit(N(:,1),N(:,2),ft, 'StartPoint', [10, 2])

% For plotting the fitted function
xrange = 0:0.1:xcenters(end);

% Plot binned data with fit and errorbars
figure
mstyle
errorbar(xcenters,data_perc,EB,'.');
xlim([0 20])
ylim([0 1])
xlabel('Diameter (\mu m)')
ylabel('Amount')
legend('off')
hold on
plot(xrange,f(xrange),'linewidth',2)
hold on
line([9.174 9.174], [0 0.5],'linewidth',2,'color','k','linestyle',':');
hold on
line([0 9.174], [0.5 0.5],'linewidth',2,'color','k','linestyle',':');
hold off

mexport('_Plot_WBC');

%% Analysis of combined cancer cell data

% Combined histogram of cancer cells in both outlets.
xcenters = 1:0.5:30;
figure
mstyle
histogram(DSCells,xcenters)
hold on
histogram(DCells,xcenters)
xlabel('Diameter (\mu m)')
ylabel('Count')
legend('Small particle outlet', 'Large particle ...
    outlet','Location','northwest')
xlim([0 20])
ylim([0 30])
hold on
line([7.857 7.857], [0 30],'linewidth',2,'color','k','linestyle',':');
hold off

mexport('_Hist_CC');
```

```
337
338 %Cancer cells in small vs large outlet
339 xcenters = 4:1:30;
340 counthistdataS = histcounts(DSCells,xcenters);
341 counthistdataL = histcounts(DCells,xcenters);
342
343 data_perc = counthistdataL./(counthistdataL+counthistdataS);
344
345 % Error bars
346 N = counthistdataS+counthistdataL;
347 EB = sqrt(N.*(1-N/sum(N)))/100;
348
349 xcenters = 4:1:29;
350 % Put x and y-values together and remove columns where data_perc is NaN
351 M = [xcenters; data_perc]';
352 N = M(~any(isnan(M),2),:);
353
354 % Fit to error function
355 ft = fittype('errorfun( x, a, b)');
356 [f,gof] = fit(N(:,1),N(:,2),ft, 'StartPoint', [10, 3])
357
358 % For plotting the fitted function
359 xrange = 0:0.1:xcenters(end);
360
361 % Plot binned data with fit and errorbars
362 figure
363 mstyle
364 errorbar(xcenters,data_perc,EB,'.');
365 xlim([1 20])
366 ylim([0 1.01])
367 xlabel('Diameter (\mu m)')
368 ylabel('Amount')
369 legend('off')
370 hold on
371 plot(xrange,f(xrange),'color',colour(2,:),'linewidth',2)
372 hold on
373 line([7.857 7.857], [0 0.5],'linewidth',2,'color','k','linestyle',':');
374 hold on
375 line([0 7.857], [0.5 0.5],'linewidth',2,'color','k','linestyle',':');
376 hold off
377
378 mexport('_Plot_CC');
```

In the above script a function was used to fit the data to an error function. This is the script with the function:

```
1 function y = errorfun(x, a, b)
2 % Fitting parameters a,b. a is the critical diameter (center of the
3 % distribution), b determines the slope of the function.
4 y = 0.5*(erf((x-a)/b)+1);
5
6 end
```

E

Device protocols

This par of the Appendix includes protocols for how to operate different devices.

Cell sorting protocol

The Design1 and Design2 chips are very similar and are operated in the same way, except that they need different pressures to obtain sufficient pinching.

1. Place 50 μL of degassed 0.1 % TX mixed with PBS or Milli-Q water in the sample and buffer inlets.
2. Apply pressure to the two inlets until the entire device is filled. There should be no air bubbles. It can help to pulsate the pressures.
3. Remove the TX solution from all inlets/outlets.
4. Pipette 50 μL of FACSFlow into all inlets/outlets, mix and then remove.
5. Repeat two more times for the inlets.
6. Place 50 μL of FACSFlow in the inlets and apply 40 mbar for five to ten minutes to replace all the TX.
7. Pipette 50 μL of FACSFlow into all outlets, mix, remove and repeat.
8. Empty the sample inlet and completely fill the buffer inlet with FACSFlow.
9. Put 50 μL of cells suspended in FACSFlow into sample inlet.
10. Apply pressure at the buffer inlet, waste outlet and sample inlet in that order so cells are always pinched. For Design1 the pressure at the sample inlet should be 40 % to 45 % of the buffer inlet pressure, and there should be no pressure on the waste outlet. For Design2 the pressure at the waste outlet should be 40 %, and the sample inlet pressure should be 80 % of the buffer inlet pressure.

11. Always monitor the experiments to make sure the cells are pinched. Keep an eye on the buffer inlet as it runs dry within minutes. Refill it by turning down the sample inlet pressure by a few mbar and turn off all pressures simultaneously. When refilling the buffer inlet it is also a good idea to mix the cells in the sample inlet to avoid cells from settling at the bottom of the inlet, and to empty the waste outlet as it fills up quickly.

12. When the experiment is done turn off all pressures, remove the cell solution from the sample inlet and fill the buffer inlet with FACSFlow to avoid sorted cells from flowing back into the chip.

Illustrations of the PFF designs can be seen in Figure 4.3.

Cell trapping protocol

The protocol for the optimised Device8 chips is listed below. The first steps are similar to the cell trapping protocol.

1. Place 50 μL of degassed 0.1 % TX mixed with PBS or Milli-Q water in the sample inlet and the first buffer inlet.

2. Apply pressure to the two inlets until the entire device is filled. There should be no air bubbles. It can help to pulsate the pressures.

3. Remove the TX solution from all inlets/outlets.

4. Pipette 50 μL of FACSFlow into all inlets/outlets, mix and then remove.

5. Repeat two more times for the two inlets.

6. Place 50 μL of FACSFlow in the inlets and apply 40 mbar for five to ten minutes to replace all the TX.

7. Pipette 50 μL of FACSFlow into all outlets, mix, remove and repeat.

8. Empty the sample inlet and fill the two buffer inlets with FACSFlow.

9. Put 20 μL of cells suspended in FACSFlow into the sample inlet. The sample should have a concentration of approx. 10^5 cells/mL.

10. Apply 5 mbar to 10 mbar pressure at all inlets, and monitor the traps.

11. When all or a sufficient number of traps ore occupied by cells, immediately turn off the pressure at the sample inlet and the second buffer inlet and turn the pressure at the first buffer inlet down to 5 mbar.

12. To extract DNA from the cells, empty the second buffer inlet and fill it with lysis buffer.

13. Apply a pressure of 5 mbar to the second buffer inlet and turn of the pressure on the first inlet. The cells are lysed once they have lost their fluorescence signal.

14. Turn up the pressure at both buffer inlets to push the DNA into the outlets. From there the DNA can be amplified directly in the reservoirs.

An illustration of the Device8 design can be seen in Figure 5.25

F

Images of cell trapping chips

Images used to determine the trap widths listed in Table 5.2 are included in this part of the Appendix.

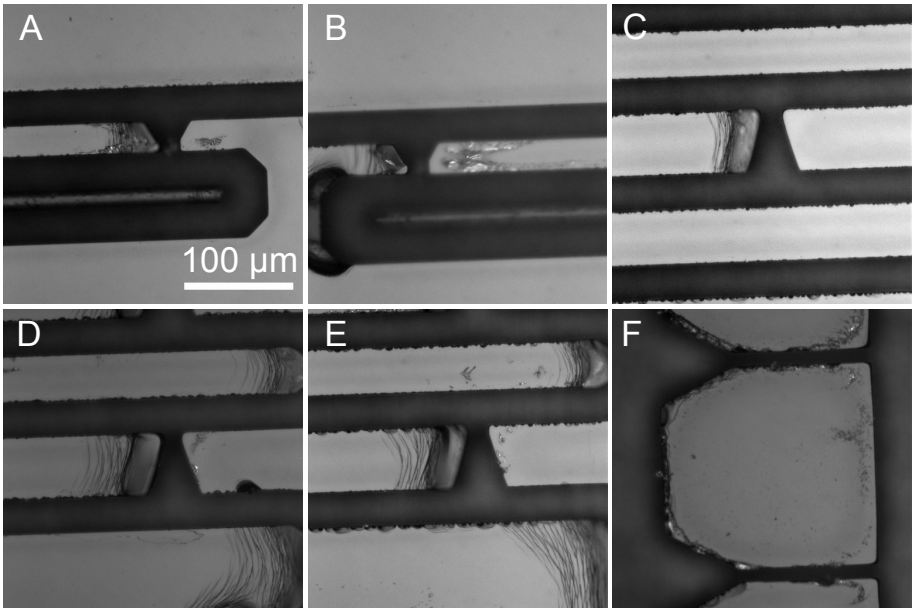

Figure F.1: Bright field images of a first generation cell trapping chip from the first shim. The images were taken with a 30X magnification before the chip was bonded. (A)-(B) 10 μm traps on Device1. (C)-(E) 10 μm, 8 μm and 5 μm traps on Device2. (F) 10 μm traps on Device3.

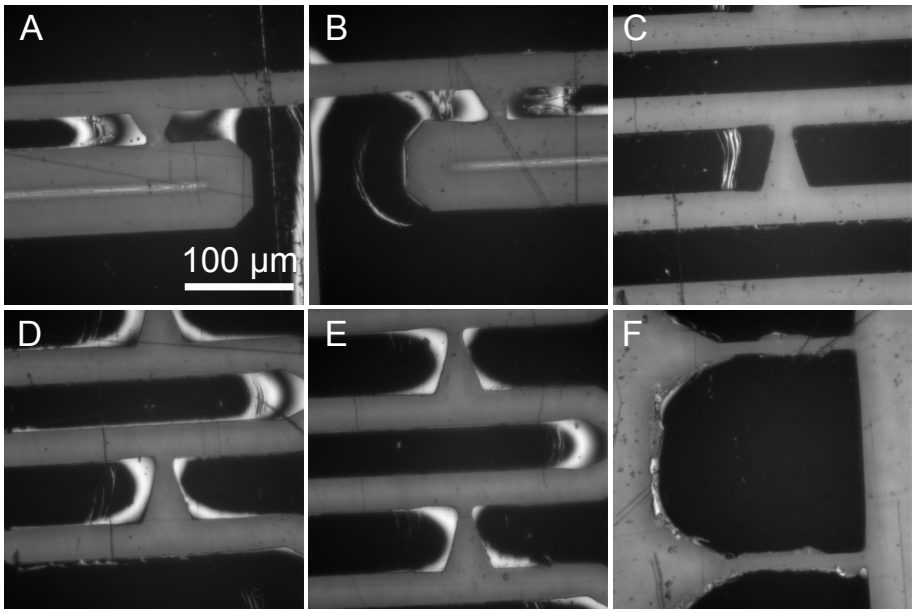

Figure F.2: Bright field images of the first generation cell trapping chip from the first shim. The chip was bonded with the standard parameters. (A)-(B) 10 μm traps on Device1. (C)-(E) 10 μm, 8 μm and 5 μm traps on Device2. (F) 10 μm traps on Device3.

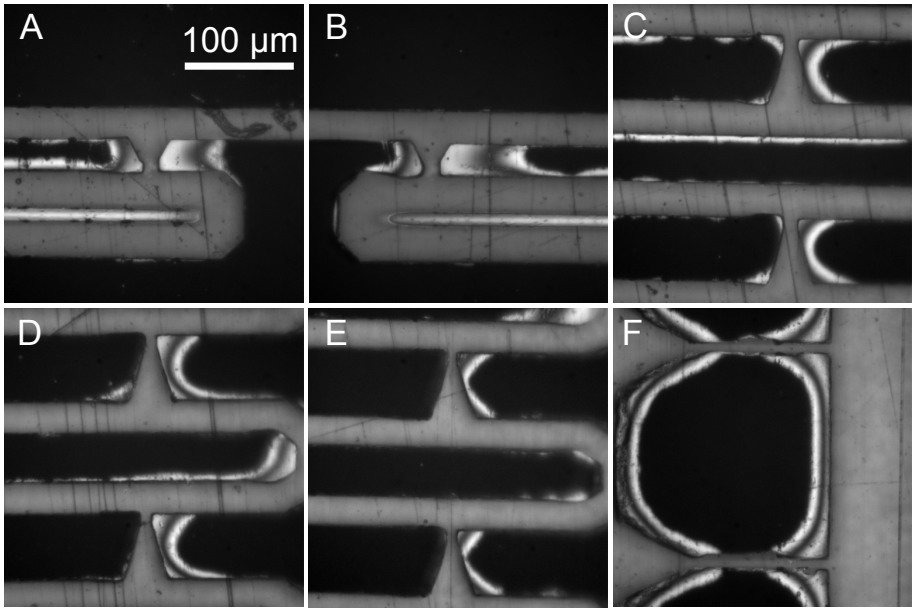

Figure F.3: Bright field images of a chip bonded at 125 °C and 5.1 MPa. (A)-(B) 10 μm traps on Device1. (C)-(E) 10 μm, 8 μm and 5 μm traps on Device2. (F) 10 μm traps on Device3.

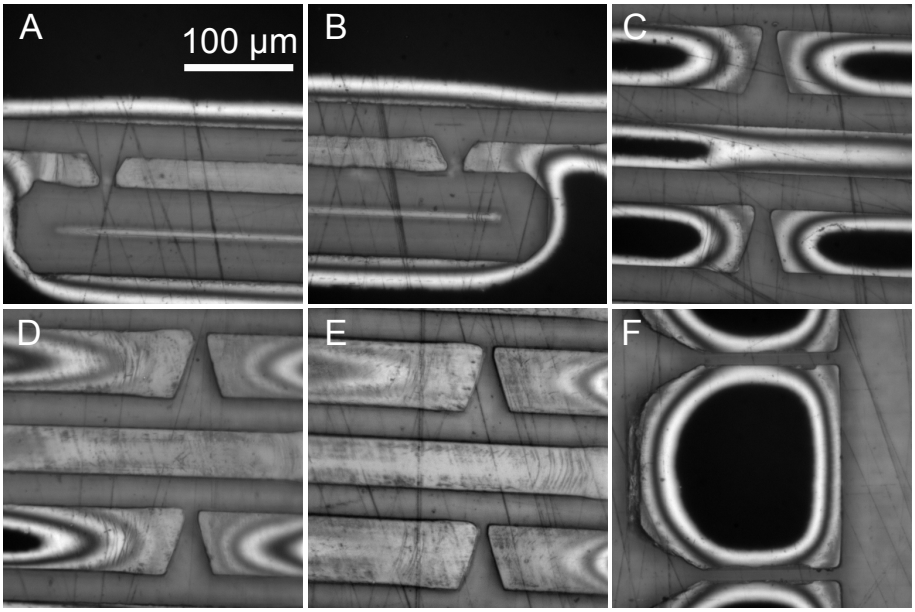

Figure F.4: Bright field images of a chip bonded at 120 °C and 10.2 MPa. (A)-(B) 10 μm traps on Device1. (C)-(E) 10 μm, 8 μm and 5 μm traps on Device2. (F) 10 μm traps on Device3.

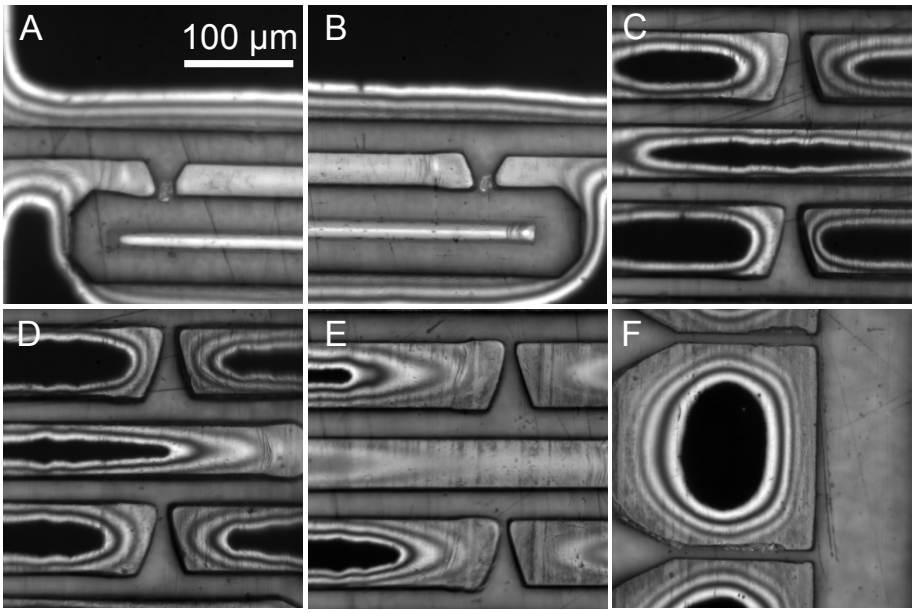

Figure F.5: Bright field images of a chip bonded at 125 °C and 10.2 MPa. (A)-(B) 10 μm traps on Device1. (C)-(E) 10 μm, 8 μm and 5 μm traps on Device2. (F) 10 μm traps on Device3.

Copyright: Marie Pødenphant Jensen
All rights reserved

Published by:
DTU Nanotech
Department of Micro- and Nanotechnology
Technical University of Denmark
Ørsteds Plads, building 345B
DK-2800 Kgs. Lyngby